Studies in lunar geology using existing remote sensing datasets and new orbital X-ray fluorescence spectroscopy from C1XS on Chandrayaan-1

Shoshana Zoë Weider

Birkbeck College
University of London

Thesis submitted for the degree Doctor of Philosophy

January 2011

Signed declaration

I, Shoshana Zoë Weider, confirm that the work presented in this thesis is my own. Where information has been derived from other sources, I confirm that this has been indicated in the thesis.

Signed: ..... Date: .....

Abstract

The main focus of this thesis is the C1XS (Chandrayaan-1 X-ray Spectrometer) instrument and its dataset, which is used to study the geochemistry of the lunar surface in combination with other existing remote sensing results, particularly from the Clementine and Lunar Prospector missions.

The overall context for lunar studies is described and the C1XS instrument design and development are discussed. Laboratory XRF (X-ray fluorescence) experiments are conducted as an analogue to the C1XS (or other planetary XRF) mission. Samples which aim to replicate the lunar regolith in a simple manner are measured with varying grain-sizes and at a range of phase angles. The results from these experiments are used to investigate the magnitude of previously reported phase angle and grain-size effects on planetary XRF data, and to test the ability of an abundance determination algorithm to accurately model the major element composition of a known rock sample.

The RAL abundance algorithm is used to model XRF spectra obtained by C1XS during two solar flare events. These periods of data acquisition represent the only sampling of basaltic regions of the Moon (Mare Serenitatis and Oceanus Procellarum), throughout the entire C1XS mission. Modelled Mg and Al abundances for a number of regions of interest are expressed in terms of MgO/SiO_2 and Al_2O_3/SiO_2 ratios, and are compared to lunar sample and Lunar Prospector compositions. The C1XS results are in better agreement with the sample compositions.

The same two lunar maria are studied using Clementine multispectral data. Observable differences in the composition of small impact crater ejecta and lava flow units are used to estimate the depth of surface deposits and thus their volume and emplacement flux. Together, these C1XS and Clementine studies highlight how the Moon's volcanic history and thermal evolution can be studied using geochemical remote sensing methods.

Acknowledgments

First of all, my sincere thanks go to my supervisors Ian Crawford and Katie Joy, whose support, teaching and guidance over the past three years have been invaluable. Also to Chris Howe, whose help and humour got me through my long months of work at RAL, and who only sometimes laughed at my ignorance to all things engineering.

Extreme thanks also go to Barry Kellett for helping me understand XRF a little bit better, for being very patient in trying to teach me IDL, and for weaving his magic with the C1XS data. Thank to you Bruce Swinyard for trusting me with his modelling code and letting me play around with it. Also to the rest of the C1XS team, especially Brian Maddison and Mattias Wallner at RAL who helped with setting up RESIK so that I could do my experiments, and to Jason Gow and David Smith at Brunel for that side of the experimental campaign. Thanks to Jim Davy for help obtaining my SEM images and to Ben Lishman who got the UCL laser profilometer up and running again.

Thank you to David Kring and the LPI, as well as my fellow interns, for giving me the opportunity to participate in the Lunar Exploration Summer Intern Program, and allowing me an enjoyable and very educational summer in Houston. I thank STFC, the UCL Graduate School, the NLSI, the Barringer Crater Company and ESA for my funding over the past three years and for helping me attend numerous conferences on both sides of the Atlantic.

Thanks to the RPIF crew: Adam, Aidan, Ceri, Claire, Dominic, Helen, Lewis, Lottie, Lucy, Oliver Peter and Terry for keeping me amused and (relatively) sane, and especially to Josh for all kinds of technical and aesthetic help and good Moon chats. Thank you to all my friends who have provided me with perspective, quality time away from my work and endless fun: Tikva, Daniel, Nina, Rachel, Andrew, Jeremy, Becca, Zan, Gabriel (I think I might just have won, but thanks for the competition!), Dani, Dalia, Yoni, my fellow UESLESS girls (Kate, Hannah, Tamryn, Paola, Suraya), and all at the London City Singers, who have brought beautiful harmonies to my life and give me a chance to exercise my vocal chords once a week.

To Don Fraser, who took a chance on me eight years ago and from whom I learnt so much.

Lastly, to my family and my parents (who don't really understand) who have never pushed, but who always support me along whichever path I choose.

The Present

Michael Donaghy

For the present there is just one moon,
though every level pond gives back another.

But the bright disc shining in the black lagoon,
perceived by astrophysicist and lover,

is milliseconds old. And even that light's
seven minutes older than its source.

And the stars we think we see on moonless nights
are long extinguished. And, of course,

this very moment, as you read this line,
is literally gone before you know it.

Forget the here-and-now. We have no time
but this device of wantonness and wit.

Make me this present then: your hand in mine,
and we'll live out our lives in it.

Contents

Table contents

Figure contents

Chapter 1: Introduction to lunar datasets, geology and geochemical remote sensing techniques

1.1. Overview

The sight of a full Moon hanging low in a clear, dark sky is always awe-inspiring, making mankind's age-old fascination with it unsurprising. Although previous generations ascribed all kinds of spiritual and religious powers to our nearest heavenly neighbour, it was not until the first telescopic observations of the Moon were made in the 17th century, and the success of the robotic and manned-era of lunar exploration, that its scientific study truly began.

The huge scientific harvest from the early lunar missions of the 1960s (Ranger, Surveyor, Apollo), as well as subsequent missions (e.g. Clementine, Lunar Prospector), demonstrated the importance and need of studying the Moon in an organised and sustained manner. The Moon's ancient crust is perhaps unique in its ability to preserve a pristine record of early (inner) solar system history, and thus the conditions in which life on Earth originated and evolved. By studying the geological evolution of the Moon, knowledge of the intimate Earth-Moon system, as well as the Earth itself, can be improved. Comparisons between the geologically active Earth and the geologically extinct Moon provide insights into the formation and diverse evolution of terrestrial planets. The relative accessibility of the Moon means that its scientific study can be advanced in an educated and methodical manner due to the comparatively frequent missions that make it their target. It also provides an arena for learning how to live and work for extended periods on another planetary body (e.g. Mars), an essential step in sating man's curiosity and basic need to explore the universe (National Research Council, 2007).

In this chapter, the current datasets available for studying the Moon are described and the current understanding of lunar geology and geological evolution is outlined in order to provide a foundation and context for the studies described further on in this thesis that aim to combine existing remote sensing lunar datasets with new results from the Chandrayaan-1 X-ray spectrometer (C1XS).

1.2. Lunar datasets

1.2.1. *Earth-based telescopic studies*

Although Earth-based telescopic observations of the Moon's nearside may now be practically obsolete and superseded by the higher quality orbital datasets, for hundreds of years these provided the only high-resolution information regarding the surface features of the Moon. The major landforms were first distinguished in this way and the nomenclature thus coined has remained in use ever since; i.e. the most major lithological distinction, between the lunar *mare* and *terrae*, which were originally perceived as areas of sea and land respectively. These 'dark' and 'light' regions are now known as the mare basalts and the anorthositic highlands. Telescopic observations of the Moon are still conducted in certain fields of study, e.g. the observations of flashes caused by meteoroid impacts (Dunham et al., 2000; Ortiz et al., 2000; Suggs et al., 2008) and ground-based radar investigations of lunar cryptomaria (Campbell & Hawke, 2005) and polar deposits (Stacy et al., 1997; Margot et al., 1999).

1.2.2. *Luna missions*

Between 1959 and 1976 the USSR sent fifteen successful robotic probes to the Moon as either flyby, orbital or lander missions that were part of their Luna program. These were designed to gather information about the lunar surface and its environment for both scientific and future mission planning purposes. Some of the highlights of these missions include: the first images of the lunar farside taken by Luna 3 in July 1959; the first soft landing mission on the Moon (Luna 9 in 1966); three sample return missions (Luna 16, Luna 20 and Luna 24; Figure 1.1) which yielded a total of 0.362 kg of material (Vaniman et al., 1991) and added diversity to the Apollo returned sample collection (see section 1.2.4); and two Lunokhod rovers that were emplaced on the Moon during Luna 17 and Luna 21, these carried a variety of scientific payloads including XRF spectrometers, X-ray telescopes and radiation detectors (National Space Science Data Center; website reference 1).

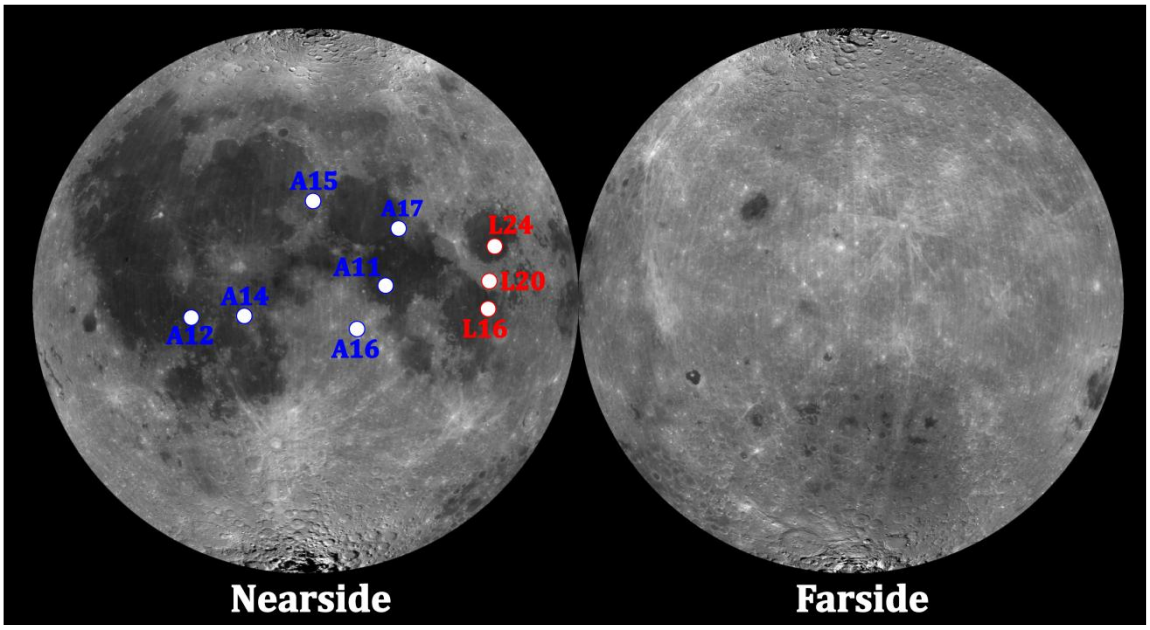

Figure 1.1. Clementine albedo (750 nm) image of the Moon showing the landing sites from which samples have been returned to Earth; Apollo sites are marked in blue, Luna sites in red. These locations are all on the nearside and in broadly equatorial regions (basemap image obtained from http://www.spudislunarresources.com/Images_Maps/Moon%20albedo%20near%20far.jpg).

1.2.3. *Apollo precursors*

Ranger & Surveyor

The early NASA lunar missions were primarily 'scouting' endeavours sent to garner knowledge about the physical characteristics of the lunar surface, essential in learning how to land a manned module safely. Ranger 7, in 1964, returned the first close-up images of the Moon and in total, more than 4,300 pictures of Mare Cognitum, into which it crashed, were transmitted (Wilhelms, 1993). The last of the pictures were taken from an altitude of 1.6 km and reveal a landscape dominated by craters; features about a metre across can be distinguished in the best of the pictures (Wilhelms, 1993). It was deduced (Hall, 1977) that the lunar surface is subject to a process that later became known as *gardening*; the continuous overturning of material due to impacts (see section 1.2.4). The three successful Ranger missions (7, 8 and 9) fulfilled their main objectives, ascertaining that typical slopes were gentle and that surfaces are smooth and strong enough to support successful manned landings (Wilhelms, 1993).

The main objective of the soft-lander Surveyor program was to investigate the upper surface layer, or the lunar *regolith*, described in section 1.2.4 (Wilhelms, 1993). Seven Surveyor spacecraft were launched between May 1966 and January 1968, with five successfully returning almost 88,000 high-resolution surface images (e.g. Figure 1.2), three chemical analyses from alpha-scatter instruments, and a number of tests of the mechanical properties of the lunar surface (Wilhelms, 1993). The general chemical model of the Moon generated from the results of the final three Surveyors was later confirmed by the Apollo scientific yield (Koppes, 1982).

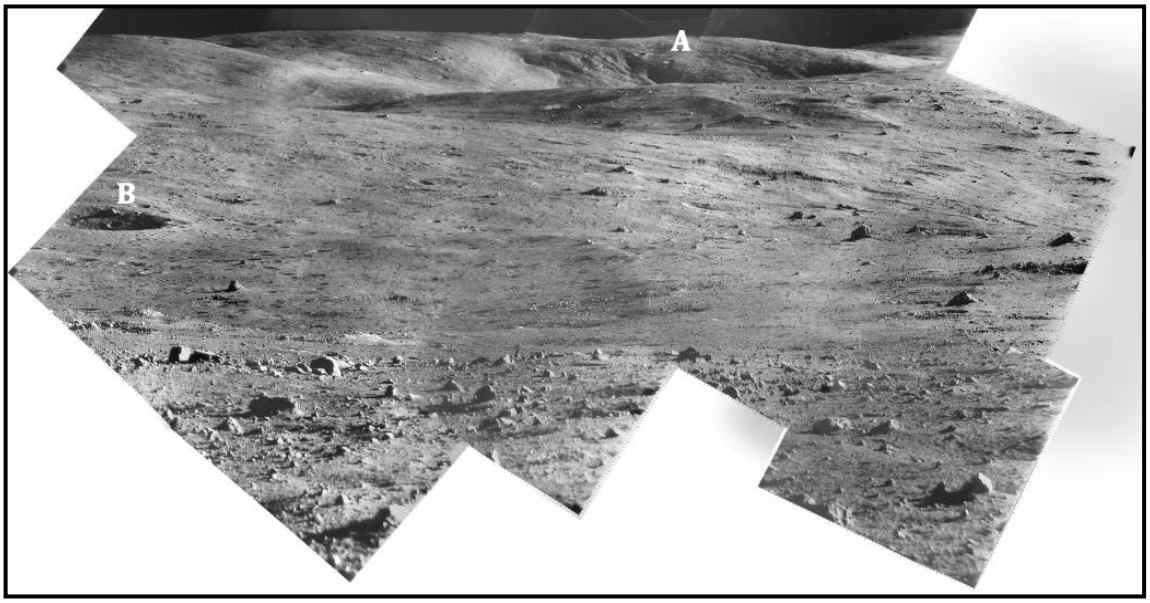

Figure 1.2. A composite of Surveyor VII narrow-angle pictures looking approximately north from the landing site within the northern ejecta of the crater Tycho (40.95°S, 11.41°W). To give an indication of the scale, the ridge labelled A and the crater labelled B are about 21 km and 590 m away from the spacecraft respectively (courtesy of P. Stooke, University of Western Ontario and the Lunar and Planetary Institute, Houston).

Lunar Orbiter

NASA launched five unmanned Lunar Orbiter probes between 1966 and 1967, which had three main objectives: (i) obtain high-resolution photographs required for planning the future Apollo landings; (ii) geodesy, in order to accurately map the gravitational field of the Moon; and (iii) measure the lunar radiation and micrometeoroid environment (Spudis & Pieters, 1991). The first three missions were dedicated to imaging potential Apollo landing sites; the fourth and fifth had broader scientific objectives and were flown in polar orbits to

increase their total coverage (Spudis & Pieters, 1991). In total, the five missions photographed 99% of the lunar surface at a resolution of ~60 m (Becker et al., 2008). The images generated have been invaluable in photogeologically mapping the Moon's major landforms and stratigraphy, and in producing high-resolution geological maps (e.g. McCauley, 1967; Wilhelms et al., 1987). The coverage and quality of the Lunar Orbiter dataset have only lately been surpassed by the most recent fleet of lunar orbital missions.

1.2.4. *Apollo missions*

Sample return

The six successful Apollo Moon landings between 1969 and 1972 returned a total of 382 kg of rock and soil samples (Vaniman et al., 1991), the landing sites from which these rocks were returned are shown in Figure 1.1. This material can be organised into broad categories that are described in the following sections.

Pristine non-mare (crustal) rocks

Examples of non-basaltic, unaltered (pristine) highlands material (remnant primary crust as well as secondary crustal material from intruded magmatic products) within the sample collection are rare, but provide vital pieces of information about the origin and early history of the Moon. A typical classification scheme is shown in Figure 1.3. These pristine rocks are identified on the basis of their texture, composition and mineralogy (Warren & Wasson, 1977; 1978; 1979), but distinguishing them from some rocks produced by large impacts can be problematic. They are rarely found with their plutonic-rock, coarsely-crystalline textures preserved, instead they tend to occur as fragments (clasts) in polymict breccias (see breccia section below). These rocks can be divided into four main groups:

Primary crust anorthosites

The ferroan anorthosites (FAN) are composed mostly of plagioclase feldspar, with a typical plagioclase mineral ($CaAl_2Si_2O_8$) composition of An_{96} (where An is defined as: plagioclase

mineral atomic Ca/[Ca+Na+K]*100). This value is much more calcic than that of terrestrial rocks (typically An_{35} to An_{65} in massif anorthosites), thus reflecting the Moon's apparent depletion in volatile elements such as sodium (Lucey et al., 2006; Wieczorek et al., 2006). Other minor minerals include olivine, but more commonly pyroxene, which are more ferroan (iron-rich) than terrestrial rocks with similar plagioclase compositions and other nonmare lunar rocks (Lucey et al., 2006). Figure 1.4 illustrates that the concentration of FeO and incompatible trace elements (e.g. Th) in FAN is very low compared to other lunar rocks (Lucey et al., 2006). Their coarse-grained textures indicate that they formed intrusively and, furthermore, the high concentration of plagioclase feldspar suggests that they are cumulate rocks, i.e. were produced by the separation and amalgamation of newly formed crystals that were possibly products of a primary lunar magma ocean (Lucey et al., 2006).

Although in the past it was thought that the lunar highlands were dominated by FAN, this idea has been reconsidered since the discovery of feldspathic lunar meteorites (see section 1.2.5), as well as additional compositions suggested by remote-sensing data and samples from Apollo 16, Apollo 17 and Luna 20 (Arai et al., 2008). Feldspathic lunar meteorites tend to be more mafic than typical feldspathic material (Korotev 1996; 1997; Korotev et al. 2003); geochemical remote sensing studies of impact basins (e.g. Bussey & Spudis, 2000; Hawke et al., 2003) suggest that although the nearside highlands have a generally noritic composition, the farside tends to be more troctolitic in nature. Granulites and granulitic breccias (see breccia section below) are ancient (yet not pristine) rocks found mostly in the Apollo 16, Apollo 17 and Luna 20 sample collections. They are less feldspathic than FAN and can be split into two distinct groups: magnesian (Mg#[1] >70) and ferroan (Mg# <70) granulites (Lindstrom & Lindstrom, 1986) and furthermore, their bulk composition and trace element characteristics indicate that their igneous precursors cannot have been FAN, nor a mixture of FAN and Mg-suite rocks (see magnesian suite section below). Their precursor was more likely to have been plutonic anorthositic norites (Lindstrom & Lindstrom 1986; Korotev et al. 2003). Due to the combination of these lines of evidence, a more heterogeneous and asymmetric lunar crust is now envisaged (Arai et al., 2008) having implications for theories of its early evolution (see section 1.3).

[1] Mg# is the magnesium number and is defined as: atomic Mg/(Mg+Fe).

A smaller group of magnesian anorthosites have also been identified (e.g. Warner et al., 1976; Lindstrom et al., 1984). These have primitive (high Ca and Mg) silicate mineral compositions as well as high and variable rare earth element concentrations (Lindstrom et al., 1984) and are thought to be petrogenetically distinct from the magnesian suite rocks (see magnesian suite section below).

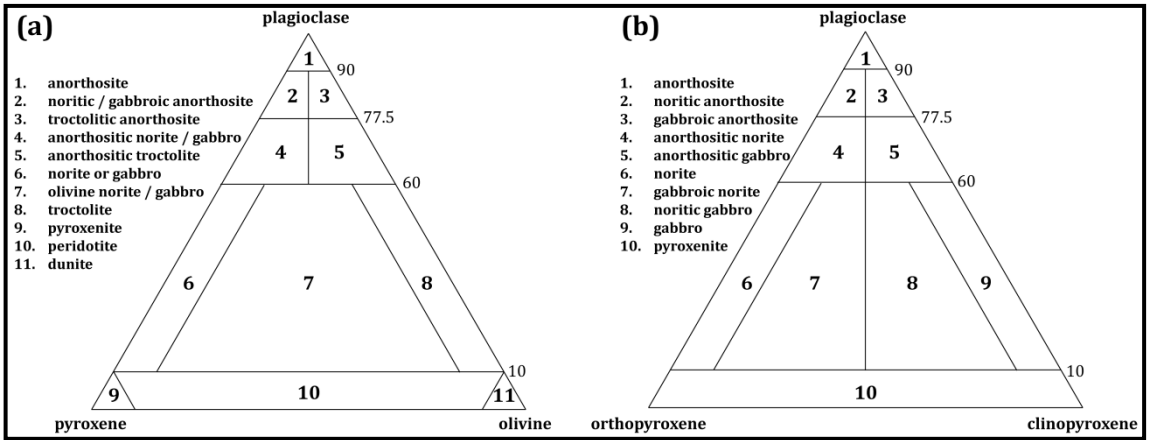

Figure 1.3. Ternary classification systems for lunar highland rocks (after Stöffler et al., 1980). (a) System based on plagioclase ($CaAl_2Si_2O_8$) – pyroxene ($[Ca,Mg,Fe]_2Si_2O_6$) – olivine ($[Mg,Fe]_2SiO_4$). (b) System based on plagioclase ($CaAl_2Si_2O_8$) – orthopyroxene ($[Mg,Fe]_2Si_2O_6$) – clinopyroxene ($[Ca,Mg,Fe]_2Si_2O_6$).

Magnesian suite (Mg-suite)

Approximately half of the pristine nonmare rocks in the sample collection are FAN, the remaining half are composed mainly of the Mg-suite of rocks (Warren et al., 1991). Although the compositional range of this group is not precisely defined, in general they have a higher modal abundance of mafic minerals than FAN samples, with the Mg# of their mafic minerals ranging from ~60 – 95, as illustrated in Figure 1.5 (Lucey et al., 2006; Wieczorek et al., 2006). The suite comprises numerous rock types, including: norites, troctolites, dunites, spinel troctolites and gabbronorites (Warren, 1993) collected from all the Apollo landing sites, but occurring most abundantly in the Apollo 14 and 17 collections (Korotev & Gillis, 2001).

Whilst petrogenetic links between similar samples at a particular site have been made, the same connections do not necessarily exist between different sites (James, 1980; James & Flohr, 1983; Papike et al., 1998). The Mg-suite is thus considered to represent intrusions

into the early FAN crust by incompatible trace element-rich parental magmas (Lucey et al., 2006; Wieczorek et al., 2006). Although the FAN samples tend to be slightly older than the Mg-suite lithologies (Borg et al., 1999; Shearer & Newsom, 2000), there is some overlap between their absolute ages (Shih et al., 1993; Borg et al., 1999; Norman et al., 2003), suggesting that whatever process led to the formation of the Mg-suite was occurring before the initial global differentiation was complete (Wieczorek et al., 2006). Based on the suggested relationship between the Mg-suite and potential *KREEP*-rich (see KREEP basalt section below for a definition) parental magmas (Snyder et al., 1995a; 1995b; Korotev, 2000) it would be expected that the occurrence of Mg-suite rocks may be controlled, to the first-order, by the early distribution of KREEP (Wieczorek et al., 2006). It has even been suggested that the KREEP basalts are actually volcanic equivalents of the Mg-suite (Snyder et al., 2000).

Alkali-suite

Rocks from the alkali-suite make only a small contribution (by mass) to the sample collection, but are found in the samples from all the landing sites (except Apollo 11) and most especially from Apollo 12, Apollo 14 and Apollo 15 (Wieczorek et al., 2006). They encompass a variety of lithologies, ranging in composition from anorthosite to norite and gabbronorite (Lucey et al., 2006; Wieczorek et al., 2006). The alkali-suite samples, as illustrated in Figure 1.5, are characterised by plagioclase that is more sodic (~An_{86}) than that found in FAN (Warren, 1993) and low-calcium pyroxene that is more ferroan than En_{70} (Snyder et al., 1995b). Those with significant silica and K-feldspar are known as quartz monzodiorite (Ryder, 1976) or monzogabbro (Jolliff et al., 1999). It has been proposed that this suite is a more mineralogically and chemically evolved set of rocks than the Mg-suite, but which have crystallised from the same KREEP basalt-like primary magma, as illustrated in Figure 1.5 (Snyder et al., 1995a; Shervais & McGee, 1998).

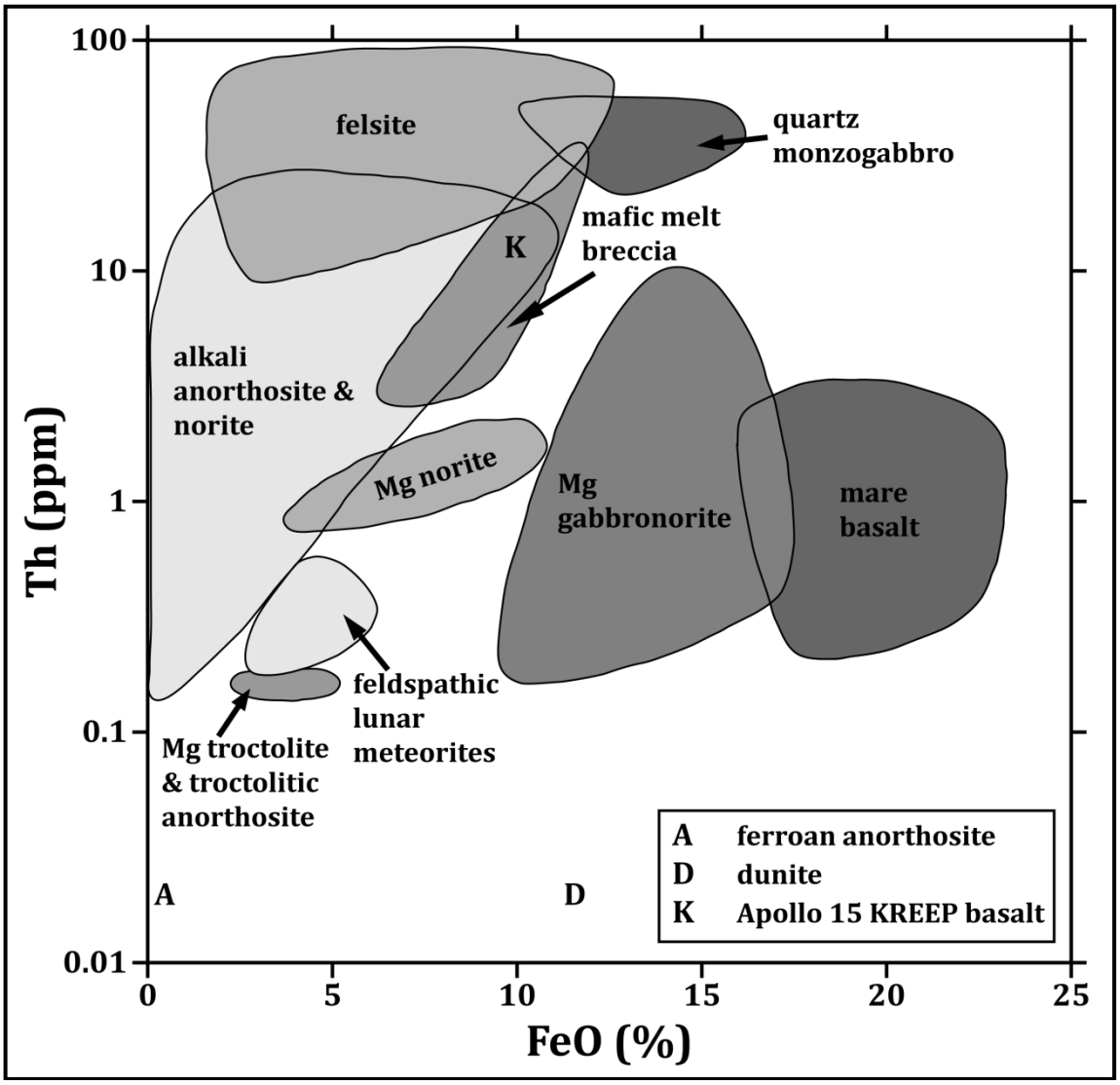

Figure 1.4. Lunar lithologies in FeO-Th element space. Felsite and quartz monzogabbro have the greatest Th concentrations among these rocks; the composition of a highly feldspathic ferroan anorthosite sample (15418) is marked as point "A" and other members of the FAN suite would plot between this point and the field for feldspathic lunar meteorites. "D" represents a dunite sample from Apollo 17 (72415-7) and "K" represents Apollo 15 KREEP basalt (adapted from Figure 2.5 of Lucey et al., 2006).

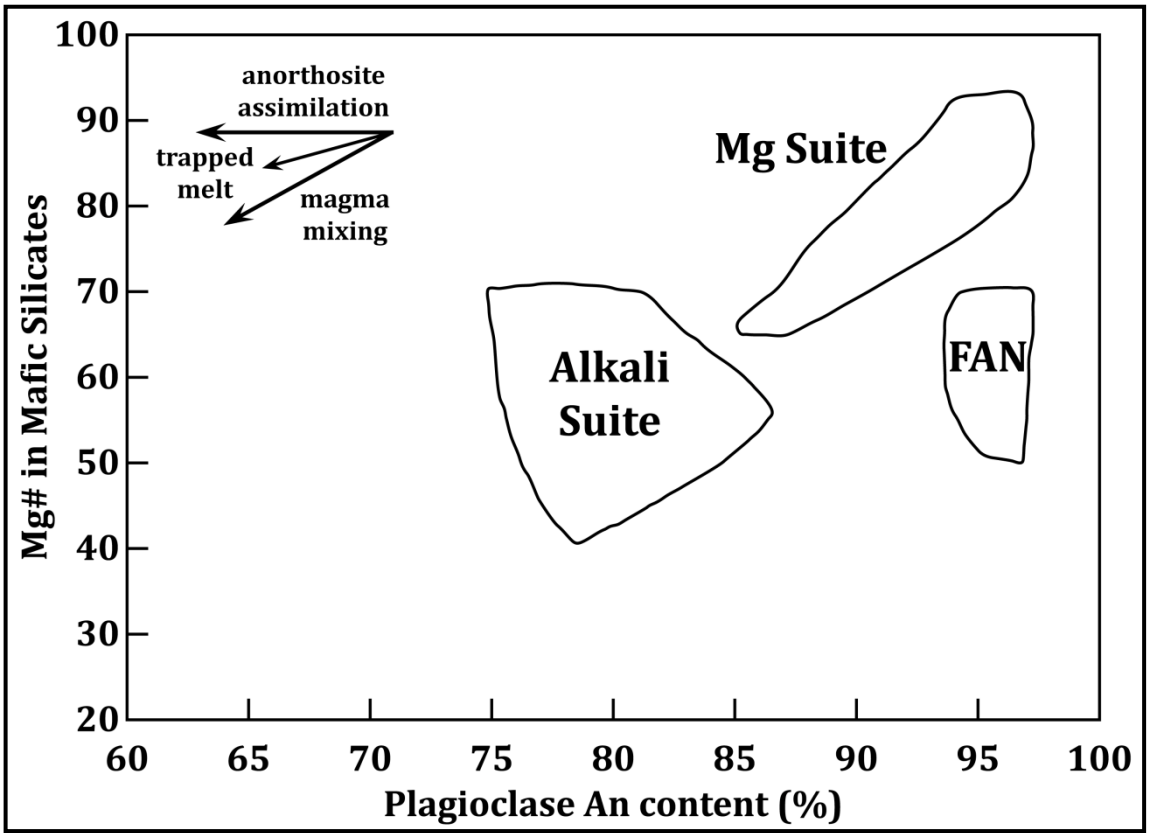

Figure 1.5. Anorthite (An) content in plagioclase versus the Mg# of coexisting mafic silicates in lunar highland rock suites. Typical trends resulting from fractional crystallisation (indicated by the arrows) suggest possible relationships between the groups. The overall trend from the upper right (Mg-suite) to lower left (alkali suite) is similar to that displayed by rocks of layered mafic intrusive bodies on Earth and by KREEP basalt minerals (Lucey et al., 2006). It is difficult to relate the Mg-suite rocks and ferroan anorthosites by a common magmatic process (adapted from Figure 4.20 of Shearer et al., 2006).

KREEP basalt

Rocks which are characteristically enriched with incompatible trace elements (typically ~100 – 150 times the concentrations of chondrites; Wieczorek et al., 2006) such as potassium (K), rare earth elements (REE) and phosphorus (P) are known as KREEP materials. Samples bearing this KREEP signature are found in the collections from all the landing sites, but the few pristine basalt samples exist predominantly in the Apollo 15 collection. These KREEP basalts are distinguished from the more abundant mare basalts by the absence of magnesian olivine, higher concentrations of plagioclase and low-Ca pyroxene, and by the presence of the characteristic KREEP signature. The KREEP basalts may have been produced by the crystallisation of impact melt, or by the assimilation fractional crystallisation of a late-stage residuum of the lunar magma ocean, known as *urKREEP* by magmas similar to those that were parental to the Mg-suite rocks (Warren &

Wasson, 1979; Warren, 1988; Nyquist & Shih, 1992). The latter hypothesis is now generally favoured because the samples have low concentrations of siderophile elements and few clasts compared to impact-melt breccias (Lucey et al., 2006). The apparently contradictory petrogenesis of a rock with high Mg# (suggesting a primitive nature) and high concentrations of silica and incompatible elements (suggesting an evolved nature) can be resolved if mixing of magnesian liquids with the urKREEP residuum, or urKREEP sinking into the mantle, occurred during a later melting episode (Warren 1988; Papike et al., 1998; Wieczorek et al., 2006). The link between the KREEP basalts and the Mg-suite (and alkali-suite) is also indicated by neodymium isotope systematics that suggest a non-chondritic, light rare-earth element enriched source (Shih et al., 1992; Wieczorek et al., 2006).

Volcanic rocks

Volcanic material on the Moon is thought to have been produced by partial melting of its solid interior (mantle) at depths between 100 and 500 km (Lucey et al., 2006). The subsequent buoyant rise of the molten rock and its eruption at the surface gave rise to at least two different types of volcanic deposit: lava flows and pyroclastic material.

Basaltic lava flows

Lunar lava flows are likely to have erupted from fissures and vents at the surface (Lucey et al., 2006). The basalts that constitute these flows have a higher abundance of iron, and a lower abundance of silicon and aluminium than terrestrial basalts. In addition, the molten lava flows are likely to have been hotter than their terrestrial compositional equivalents due to the lack of water incorporated in the material (Lucey et al., 2006). These conditions gave rise to non-viscous lavas that could form thin, widespread flows which stacked atop one another to fill impact craters and basins. The mare basalt deposits cover about 17% of the lunar surface and are thought to comprise less than 1% of the lunar crustal volume (Head, 1976; Head & Wilson, 1992). The mare basalts are found almost entirely within nearside basins, being limited to a few deposits in comparatively small and young craters on the farside (Shearer et al., 2006). This asymmetry in the distribution of mare material is

often attributed to the thicker anorthosite crust on the farside creating a barrier to erupting material (Shearer et al., 2006), but the reason for the crustal thickness asymmetry remains an important unresolved question in lunar geology.

The cooling rate of the lava flows was dependent on their thickness (dictated by parameters such as viscosity and initial composition of the lavas), thus producing a variety of mineral textures that can be observed in the sample collection. The basalts are classified primarily by their bulk sample TiO_2 wt. % content and subsequently by their Al_2O_3 wt. % content; any further subdivisions are made on the basis of their K_2O wt. % content (Neal & Taylor, 1992), with the main groups summarised in Table 1.1. Most mare basalt samples have negative europium anomalies (see Figure 1.6) in contrast to average highlands material. This pattern is due to the capability of Eu (unique among the lanthanide elements) to exist in the divalent state (Eu^{2+}), as opposed to just the trivalent ion (Eu^{3+}) and therefore substitute for Ca (and Sr) in the plagioclase structure. The negative anomalies suggest that plagioclase separated early from the magmas from which the basalts crystallised (Vaniman et al., 1991).

Pyroclastic material

Small glassy beads of a pyroclastic origin have been found in material from all the Apollo missions, but most abundantly in samples from Apollo 15 and Apollo 17 (Delano, 1986). These volcanic glasses can be distinguished from ubiquitous fragments of impact glass using criteria laid out by Delano (1986) based, for example, on their bulk composition and volatile contents. These glass beads compose the lunar pyroclastic deposits and are a product of fire-fountaining episodes, where gases within rising magmas were explosively released upon reaching the surface (Nicholis & Rutherford, 2005) and resulted in the formation of the small glassy beads with various compositions, colours and textures. On the Moon, these deposits are widely dispersed because of the weak gravitational force and their eruption into a vacuum. With multispectral remote-sensing techniques they can be distinguished from other volcanic material as deposits that are dark, due to their Ti-rich nature and the common presence of black glass spheres (Hiesinger & Head, 2006).

Table 1.1. Lunar mare basalt classification scheme based primarily on TiO_2 content, with secondary and tertiary subdivision on the basis of Al_2O_3 and K content respectively. The basaltic lunar meteorites in the collection tend to fall into the low-Ti group (adapted from Figure 5 of Neal & Taylor, 1992 using information from Lucey et al., 2006).

TiO_2	*Al_2O_3**	*K†*	*Landing Site*	*Notes*
Very low-Ti (VLT) (0 – 1 wt. %)	Low-Al	Low-K	Apollo 17, Luna 24	Possess low concentrations of rare earth elements (REE) and other incompatible trace elements (ITE). Their REE patterns are not the typical bow shape of mare basalts, instead they rise continuously from La-Lu. All but one of the Luna 24 fragments have very small negative Eu anomalies.
		High-K		
	High-Al	Low-K		
		High-K		
Low-Ti (1 – 6 wt. %)	Low-Al	Low-K	Apollo 12, Apollo 15	Apollo 12 & 15 basalts are of two main types: olivine and pigeonite (low-Ca pyroxene) basalts: - The olivine basalts tend to have more MgO and less CaO, Al_2O_3 and TiO_2 than the pigeonite basalts from the same site. - Some of the Apollo 12 samples are noticeably richer in ilmenite (designated ilmenite basalts). - REE abundances are lower than in the high-Ti basalts, although both have the bow-shaped patterns and negative Eu anomalies. - Other incompatible elements have lower concentrations in low-Ti than in high-Ti basalts. - Within the high-Al group there are samples with very high-K from Apollo 14. The Luna 16 basalts contain the most TiO_2 of any of the low-Ti, high-Al basalts and also have distinctive REE patterns, with higher concentrations of light REE (La-Sm) compared to heavier elements.
		High-K		
	High-Al	Low-K	Apollo 14, Luna 16	
		High-K	Apollo 11	
High-Ti (>6 wt. %)	Low-Al	Low-K	Apollo 11, Apollo 17	Even within these groups, the compositions of high-Ti basalts can vary widely. This is probably due to loose blocks, rather than bedrock being sampled.
		High-K	Apollo 11	
	High-Al	Low-K		
		High-K		

*Low-Al_2O_3: <11 wt. %; High-Al_2O_3: >11 wt. %; †Low-K: <2000 ppm; High-K >2000 ppm.

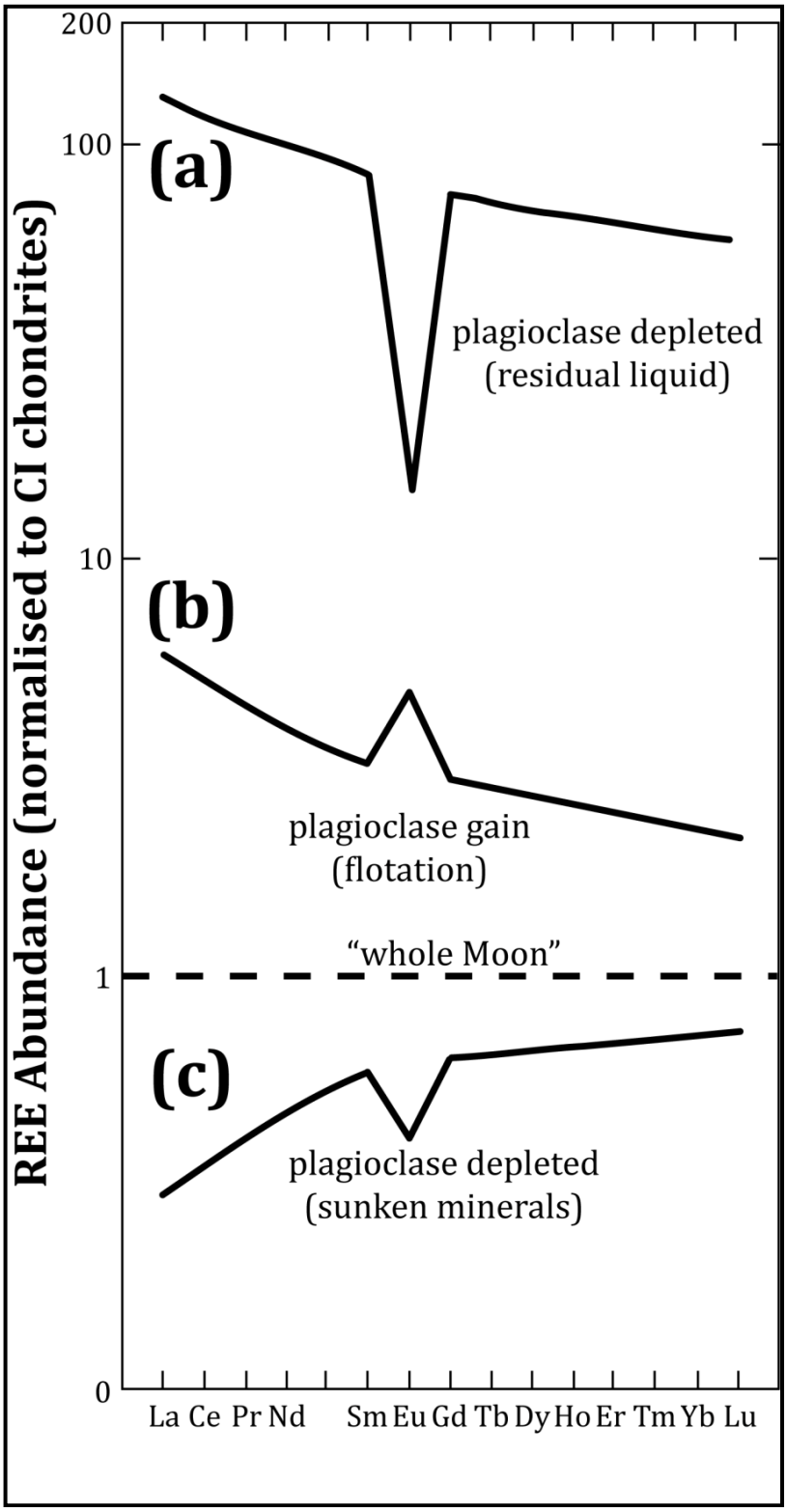

Figure 1.6. Rare Earth element (REE) concentrations and Eu anomalies in (a) the KREEP basalts from Apollo 14, (b) the plagioclase-rich lunar crust, and (c) the source regions for the low-Ti and high-Ti mare basalts. The Eu anomalies are due to excursions from smooth trends in the ratio of lanthanide element abundances of a rock compared to a model whole-Moon composition and are caused by accumulation or removal of Eu-enriched plagioclase (adapted from Figure 2.6 of Vaniman et al., 1991). The y-axis of this figure indicates REE abundance normalised to the abundance of the element in CI chondrites (according to the scheme of Evensen et al., 1978).

Regolith

As soon as fresh bedrock becomes exposed on the lunar surface, meteoroid bombardment starts to breakdown surficial material. With time, and the continuation of these impacts, the original bedrock becomes covered by a fragmental layer of broken, melted and altered debris, which has become known as the lunar regolith (McKay et al., 1991) and which is continually overturned in a process known as *gardening* (Morris, 1978; Hörz et al., 1991). Returned samples indicate that the majority of the regolith consists of particles <1 cm in size (the lunar soil), although larger cobbles and boulders are also common (McKay et al., 1991).

Lunar soil

The lunar soil is the sub-cm fraction of the regolith, with a mean grain-size range of 40 – 80 μm (McKay et al., 1991). Individual soil particles are mostly glassy bonded aggregates, known as agglutinates, but also include various rock and mineral fragments, as well as a small (<2%) meteoritic component (McKay et al., 1991). Agglutinates are small (usually <1 mm) individual particles, which are aggregates of smaller lunar soil particles that have been bonded together by small amounts of impact melt from the micrometeoroid impacts that create them. They contain droplets of very fine-grained (single domain) metallic iron and troilite (McKay et al., 1991). Their high vesicularity is caused by the release of solar-wind implanted gases (H and He) during the micrometeoroid impacts (Lucey et al., 2006) and as such they are unique to soils that develop on airless, terrestrial bodies and asteroids (McKay et al., 1991). Agglutinates constitute about 25 – 30% of the lunar soil (McKay et al., 1991), but their abundance increases with time, and is thus directly proportional to the exposure age of the soil and one of the most useful indicators of regolith maturity (McKay et al., 1991). The presence of agglutinates and the nanophase iron they contain have important implications for the analysis of multispectral remote sensing datasets for the Moon.

Breccias

Lunar breccias are complex rocks composed of fragments from older rocks that have been shattered or melted, and then reassembled by meteoroid impacts. The fragments can be single mineral grains or larger rock clasts, as well as crystallised or glassy impact melts. The clasts are set in a matrix of finer-grained material; the lithification process occurs due to the heat and shock associated with later impact events. Breccias can consist of a single rock type (monomict) that has been broken and deformed to create clasts, or of many fragments from a number of separate older rocks and impact melts (polymict). Monomict breccias tend to be strongly crushed samples of a single precursor igneous rock and can preserve some clasts with the original texture; as such they are usually included as pristine rocks. Most lunar breccias are polymict, their classification can be complicated, but the system of Stöffler et al. (2006) is often employed by subsequent workers and is outlined in Table 1.2.

Table 1.2. Classification, characteristics, and examples of non-mare polymict breccias (adapted from Stöffler et al., 1980; Lucey et al., 2006).

Breccia Class	*Main Characteristics*
Fragmental breccia	Angular clasts in porous, clastic matrix of rock, mineral and rare glass debris. Some melt clasts may be cogenetic with assembly (suevite). Most are friable.
Glassy melt breccia	Coherent glassy or devitrified glass matrix with clasts (melt breccia) or without clasts (impact glass).
Crystalline melt breccia (impact-melt breccia)	Rock or mineral clasts, or both, in an igneous (extrusive) textured matrix (ophitic, subophitic, poikilitic, dendritic, etc.). May be fine-grained or coarse-grained, and clast-poor to clast-rich.
Clast-poor impact melt	Igneous (extrusive) textured rock containing meteoritic siderophile element contamination. Textures can be slightly more heterogeneous than igneous rocks, and rare clasts may be present. Compositions can be unlike those generated by igneous processes.
Granulitic breccia (and granulite)	Rock and/or mineral clasts in an equilibrated granoblastic to poikiloblastic matrix. Clasts may not be obvious, and poikilitic textures may mimic those of, or be transitional to, plutonic rocks. Compositions reflect siderophile element contamination.
Dimict breccia	Veined texture of intrusive, dark, fine-grained crystalline melt breccia with coarser-grained light-coloured breccia consisting of plutonic or metamorphic fragments, or both. In some cases, the dark-light relationship appears mutually intrusive.
Regolith breccia	Lithified regolith. Regolith fragments including impact glass, volcanic glass and volcanic debris with a glassy matrix. Commonly retains some solar wind gases through the lithification process.

Apollo Lunar Surface Experiments Package (ALSEP)

Each of the Apollo landing missions (except Apollo 11 which deployed an earlier, less extensive package) placed a set of scientific instruments, the ALSEP, on the lunar surface. Each package was slightly different, but included: the Active Seismic Experiment (Apollo 14 and Apollo 16) and the Lunar Seismic Profiling Experiment (Apollo 17) used to investigate the uppermost structure of the crust; the Heat Flow Experiment (Apollo 15 and Apollo 17) that measured the thermal conditions of the subsurface; the Laser Ranger Retroreflectors (Apollo 11, Apollo 14 and Apollo 15) used to accurately determine the Earth-Moon distance; and the Passive Seismic Experiment (Apollo 12, Apollo 14, Apollo 15 and Apollo 16) which measured the natural *moonquakes* and therefore was used to study the lunar interior.

Apollo Command Module (CSM) payloads

All the Apollo missions that orbited the Moon conducted photography during both lunar approach and lunar orbit. The final three missions also carried two automatic cameras onboard the service module, in addition to the astronaut-operated cameras that had been used in the previous missions. These cameras produced high-resolution imagery of sunlit regions, but coverage was limited due to the near-equatorial orbits of the missions. The Apollo 15 and 16 service modules carried X-ray and gamma-ray spectrometers as part of their scientific payload. Details of these experiments can be found in sections 1.4.1 and 1.4.3.

1.2.5. *Additional lunar samples: lunar meteorites*

Meteorites originating from the Moon were first recognised by Bogard & Johnson (1983) and since then this material has become a significant part of the lunar sample collection (Korotev et al., 2003; 2009; Korotev, 2005; Lucey et al., 2006). The lunar meteorites are primarily classified according to their bulk aluminium content into three distinct groups: (i) feldspathic meteorites (with >26 wt. % Al_2O_3), (ii) intermediate mare-highland meteorites (with 13 – 26 wt. % Al_2O_3) and (iii) basaltic meteorites (with <13 wt. % Al_2O_3).

These samples provide additional diversity to the returned sample collection as their inherently random provenances must include sites away from the Apollo and Luna landing localities. Attempts have been made to determine the precise provenance of the meteorites (Gnos et al., 2004; Joy et al., 2008; Fernandes et al., 2009; Jolliff et al., 2009), but inevitably these studies will always entail large uncertainties. Therefore, it is the remote sensing datasets, from both Earth-based and satellite platforms that really provide a global view of the Moon.

1.2.6. *Post-Apollo missions*

Since the Apollo-era of lunar exploration, a number of remote-sensing missions have flown by or orbited the Moon, thus aiding its scientific study and providing a global context for the spatially and geographically limited Apollo ground truth data. These missions have revolutionised the view of the Moon in a number of ways.

Galileo, Clementine & Lunar Prospector

In 1990 and 1992 the spacecraft Galileo made two lunar flybys during its journey to Jupiter. Using images from its SSI (solid state imaging) camera (e.g. Belton et al., 1992) the first spectral investigations (in the 0.4 – 1.0 μm range) were made of the Moon, in the western and north-central nearside regions (e.g. Head et al., 1993; McEwen et al., 1993; Pieters et al., 1993a), including areas not observed during the Apollo missions.

Clementine was a joint mission between the Ballistic Missile Defense Organization (BMDO) and NASA, whose original objective was to test the space-hardiness of various spacecraft components and to make observations of both the Moon and the near-Earth asteroid, 1620 Geographos (Nozette et al., 1994). However, a spacecraft malfunction meant that the asteroid rendezvous had to be abandoned. The satellite orbited the Moon for two months in 1994, with a scientific payload consisting of five instruments, which characterised various aspects of the Moon's geochemistry and surface features (Nozette et al., 1994). These included: (i) Ultraviolet / visible camera; (ii) Near-infrared CCD camera (NIR); (iii) Laser image detection and ranging system (LIDAR); (iv) Charged particle

telescope (CPT) and; (v) High-resolution camera (HIRES). The UV-Vis and NIR datasets are described in more detail in section 1.4.2 and chapter 5.

Lunar Prospector was part of NASA's Discovery Program (Binder, 1998). The mission lasted for nineteen months between 1998 and 1999, with an objective to make a low-altitude polar orbit investigation of the Moon with its payload of five instruments (Binder, 1998): (i) Gamma ray spectrometer (GRS); (ii) Neutron spectrometer (NS); (iii) Doppler Gravity Experiment (DGE); (iv) Electron reflectometer and magnetometer (MAG/ER) and; (v) Alpha particle spectrometer (APS). The GRS dataset is described in more detail in section 1.4.3.

Together, the Clementine and Lunar Prospector missions provided the first global mapping of the lunar surface. Some of the resulting scientific highlights include: comprehensive lunar surface compositional maps; the first lunar topographic map (Spudis et al., 1994; Figure 1.7); the refinement of the lunar gravity field (Zuber et al., 1994; Lemoine et al., 1997); the discovery of a thorium-rich hotspot (Figure 1.8) on the nearside (Haskin, 1998; Lawrence et al., 1998; 2003; Haskin et al., 2000; Berezhnoy et al., 2005; Prettyman et al., 2006); evidence for the presence of hydrogen deposits at the poles (Nozette et al., 1996; Feldman et al., 1998); and the definition of different geological terranes (Jolliff et al., 2000; Figure 1.8).

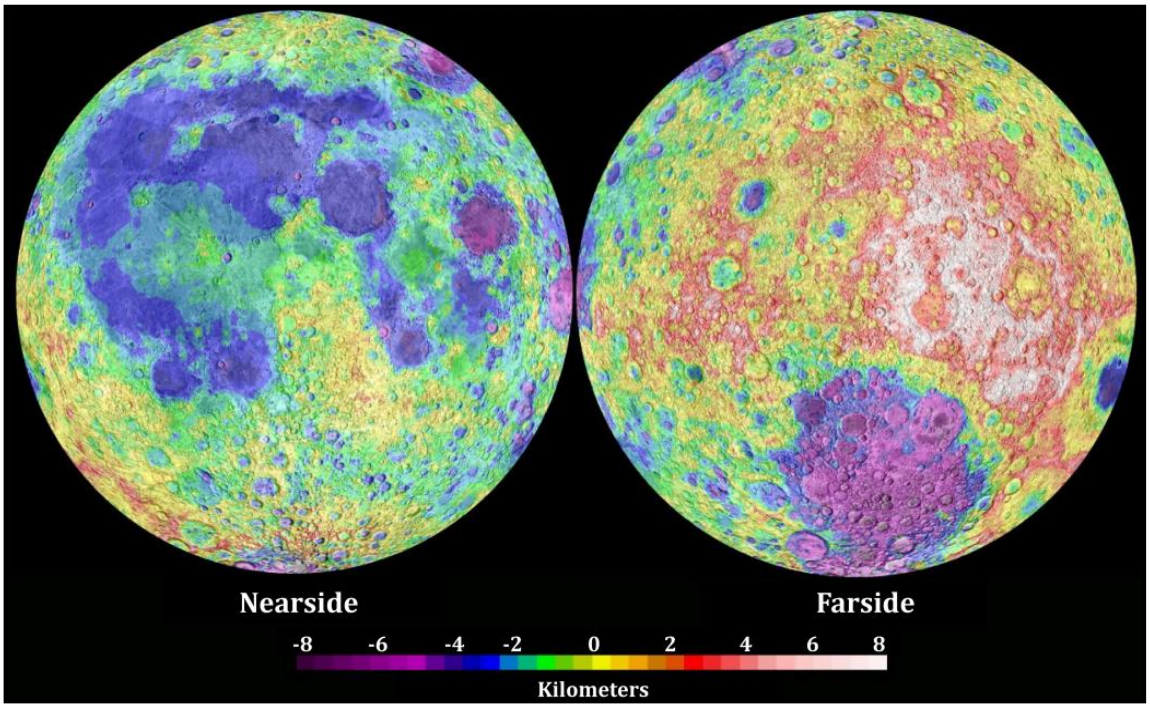

Figure 1.7. Topographic map of the Moon, constructed from Clementine Laser Altimetry data (image adapted from http://www.spudislunarresources.com/Images_Maps.htm).

SMART-1, SELENE-1 (Kaguya), Chang'e-1, Chandrayaan-1 & Lunar Reconnaissance Orbiter (LRO)

SMART-1 (Small Missions for Advanced Research in Technology), launched in 2003, was ESA's first mission to the Moon (Racca et al., 2002; Foing et al., 2006). Its payload consisted of seven technology demonstrator instruments, designed to investigate the Moon and its immediate environment, some of these included: AMIE (Advanced Moon micro-imager experiment), D-CIXS (Demonstration of a compact imaging X-ray spectrometer, see section 1.4.1 for more details), XSM (X-ray solar monitor) and SIR (infra-red spectrometer) (Huovelin et al., 2002; Grande et al., 2003; Basilevsky et al., 2004; Josset et al., 2006).

SELENE (also known as Kaguya) was a JAXA (Japanese Aerospace Exploration Agency) satellite which orbited the Moon for twenty months from September 2007. Thirteen instruments made up its scientific payload, with the objectives of obtaining scientific data relating to the origin and evolution of the Moon and of developing the technology required for future lunar exploration, these instruments included: Terrain Camera, X-ray

fluorescence Spectrometer, Spectral Profiler, Multiband Imager and Lunar Radar Sounder (Matsunaga et al., 2001; Haruyama et al., 2008a; Ohtake et al., 2008; Okada et al., 2008; Oshigami et al., 2009). Some of the major results from the mission so far include: improved lunar global topography maps (Araki et al., 2009), a detailed gravity map for the farside (Namiki et al., 2009) and the first optical observation of the permanently shadowed Shackleton crater (Figure 1.9), close to the south pole (Haruyama et al., 2008b).

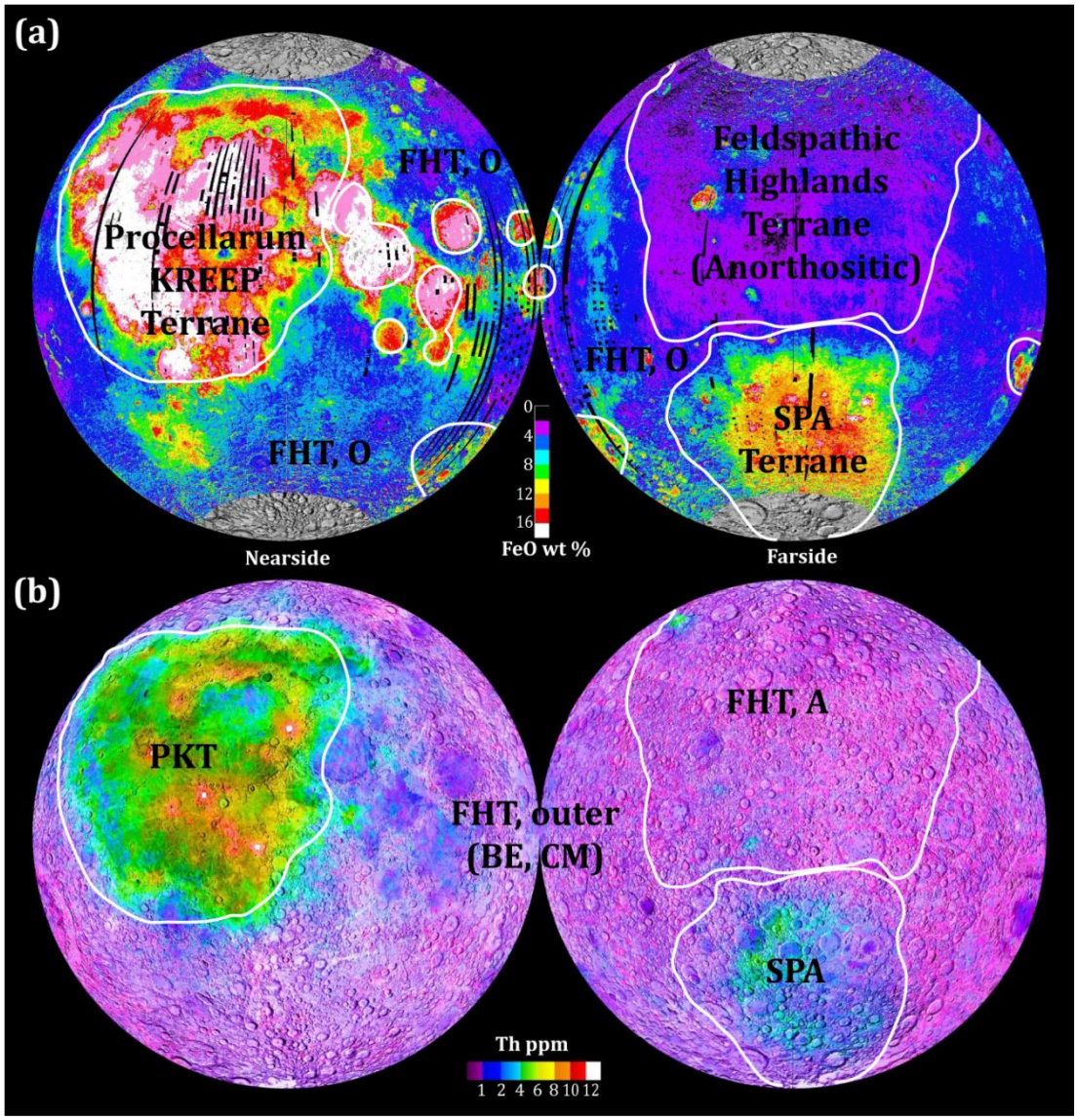

Figure 1.8. Maps of (a) Clementine FeO (Lucey et al., 1998) and (b) thorium concentration (Gillis et al., 1999) in the lunar surface, showing the locations of the major lunar crustal terranes as proposed by (Jolliff et al., 2000). The Procellarum KREEP Terrane (PKT) is the nearside region of Th-enrichment. The South Pole-Aitken Terrane (SPA) can be subdivided into an inner region of primary topographic depression and an outer region corresponding to rim and presumed proximal ejecta deposits. The Feldspathic Highlands Terrane (FHT) is defined by a central, highly anorthositic region, concentrated mainly on the farside. The outer FHT (FHT, O) consists of regions where basin ejecta (BE) or basalts (cryptomare, CM) obscure the older, presumably feldspathic surface.

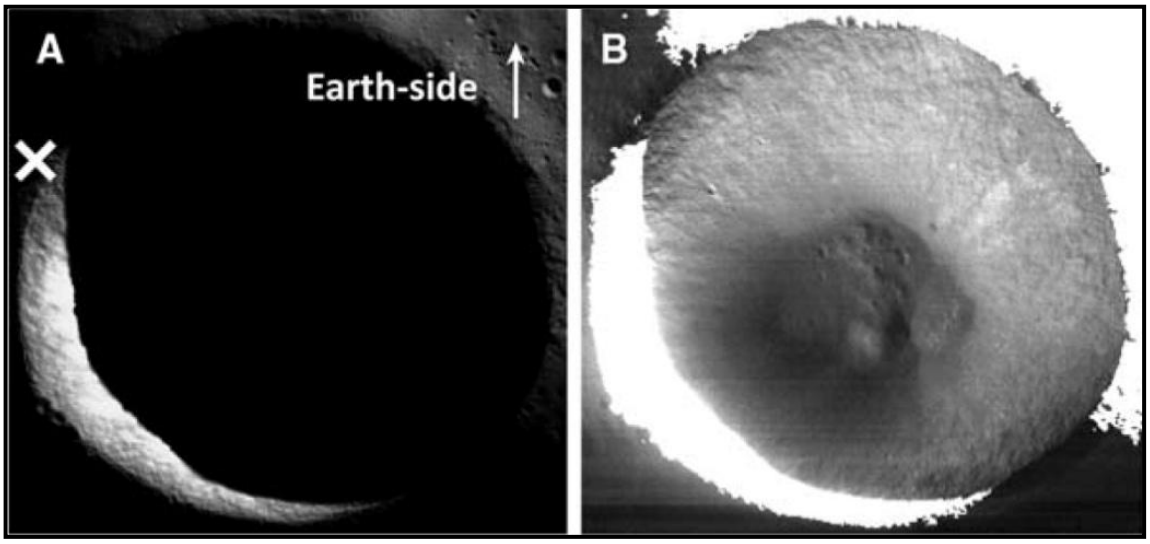

Figure 1.9. Shackleton Crater, ~20 km in diameter, close to the lunar south pole. (A) is an image of the crater taken by the SELENE Terrain Camera, the crescent is the sunlit portion of the crater's inner wall (the cross marks the location of the south pole). (B) is an enhanced image of (A), where the permanently shadowed area inside the crater has been lit by scattered light from the illuminated portion of the inner wall (from Haruyama et al., 2008b).

The China National Space Administration launched its first lunar probe, Chang'e-1 as part of its lunar exploration program in October 2007 (Zheng et al., 2008), the mission lasted until its scheduled impact in March 2009 (Chang'e-2 will continue China's lunar exploration and was launched on 1st October 2010). There were four main mission objectives: (i) to obtain 3D images of the lunar surface as a reference for future landings, (ii) analysis and mapping of the abundance and distribution of key chemical elements (K, Th, U, O, Si, Mg, Al, Ca, Te, Ti, Na, Mn, Cr and La) through a combination of gamma-ray and X-ray spectrometry, (iii) investigate the characteristics of the lunar regolith and the abundance of ^{3}He, and (iv) study the space environment between 40,000 km and 400,000 km from Earth, specifically the solar wind and the impact of solar activity on the Earth and Moon (Zheng et al., 2008).

Chandrayaan-1 was the Indian Space Research Organisation's (ISRO) first lunar mission. It was launched in October 2008 and operated until August 2009. Although this was an Indian satellite, six of the eleven scientific payloads (Figure 1.10) were provided by international space agency partners (NASA, ESA and the Bulgarian Aerospace Agency) and included the Terrain Mapping Camera (Kiran Kumar et al., 2009), C1XS (Grande et

al., 2009; see also chapter 2) and the Moon Mineralogy Mapper (Pieters et al., 2009a; see also section 1.4.2).

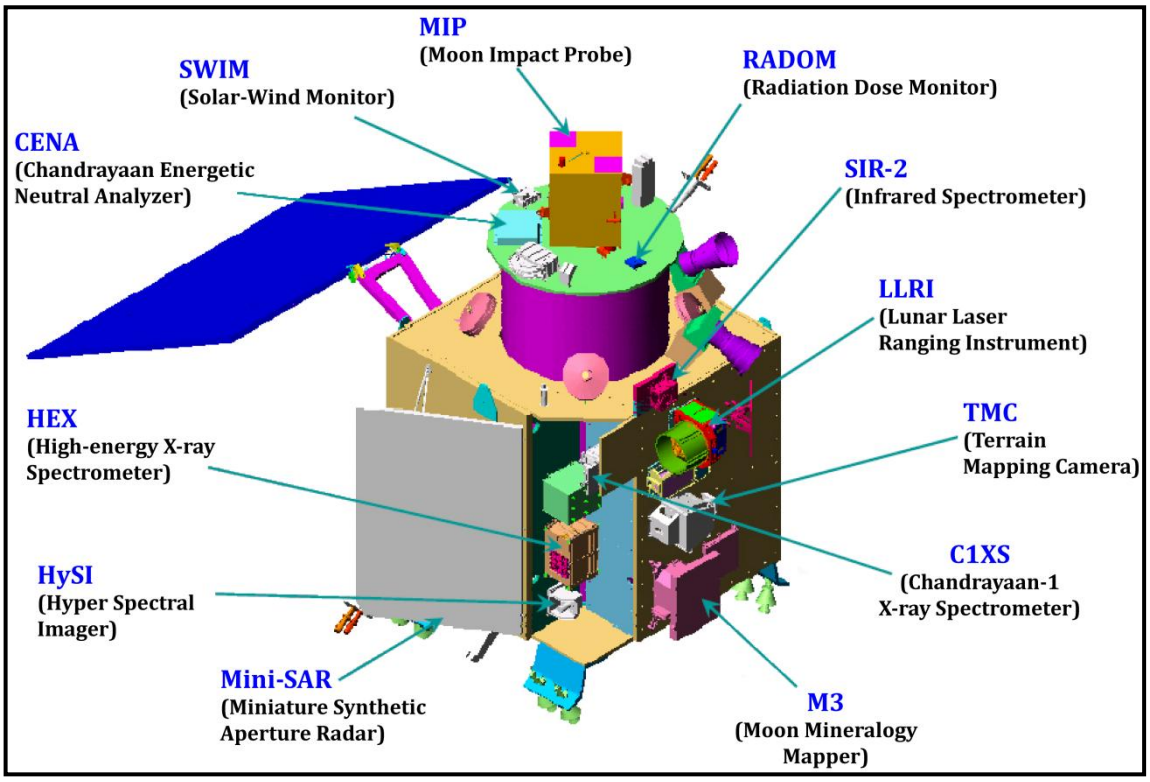

Figure 1.10. Schematic diagram of the Chandrayaan-1 satellite, showing its various payload instruments (ISRO).

Lunar Reconnaissance Orbiter (LRO) is a NASA satellite that was launched in June 2009 and is currently orbiting the Moon (as of October 2010). It is the first mission as part of the USA's Vision for Space Exploration program and within this context its objectives are to survey lunar resources, and identify possible future landing sites. Products include a 3D map of the lunar surface and high-resolution imagery (e.g. Figure 1.11) obtained from the Lunar Reconnaissance Orbiter Camera (LROC, Robinson et al., 2006), global temperature and compositional mapping from the Diviner Lunar Radiometer Experiment (Paige et al., 2009; Glotch et al., 2010; Greenhagen et al., 2010), and the search for water ice at the lunar poles with the Mini-RF (Miniature Radio Frequency) radar instrument (Spudis et al., 2009)

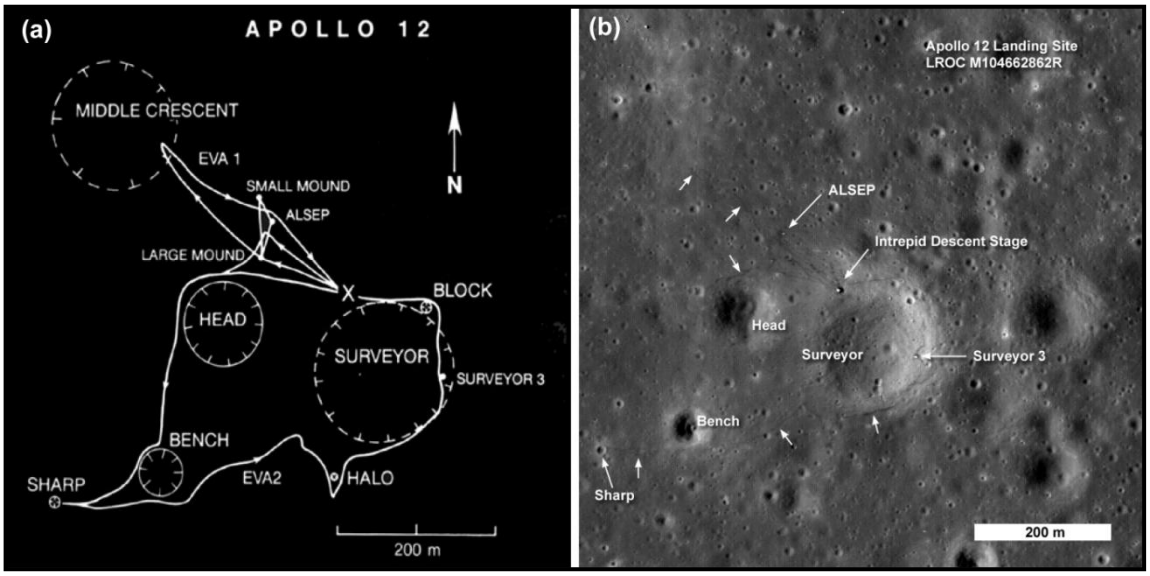

Figure 1.11. Apollo 12 landing site: (a) shows the paths traversed by the astronauts, (b) LROC NAC (narrow angle camera) image showing the same area; the tracks are visible, as are various pieces of hardware left on the surface (NASA/GSFC/Arizona State University).

1.3. Lunar geology & evolution

The synthesis of the available sample and remote sensing data described above has led to the formulation of various models for the geological evolution of the Moon; the most commonly accepted are outlined here.

1.3.1. *Formation of the Moon*

Any plausible theory of lunar formation must account for a number of fundamental and unique characteristics of the Moon (described in Canup, 2004), which include:

(i) The mass and angular momentum of the Earth-Moon system. The Moon's mass is ~1% of the Earth's, a proportion that is large in comparison to other planet-moon systems. The angular momentum of the system is also unusually high and is likely to have decreased over time (e.g. Goldreich, 1966; Kaula & Yoder, 1976; Touma & Wisdom, 1994).

(ii) The evolution of the Moon's orbit: both its orbital radius and inclination have increased significantly with time. During its early history, the Moon is thought to have been ~15 times closer to the Earth and inclined by at least 10 times its current value of ~1° to the equatorial plane (Canup, 2004).

(iii) The low lunar density is thought to be caused by a depletion of iron in the bulk Moon relative to the Earth and other inner solar system bodies (Canup, 2004).

(iv) Sufficient internal heat to cause the widespread melting required for the lunar magma ocean that is believed to have existed (section 1.3.2), but limited enough to prevent contractions in the surface caused by cooling, and which are not observed (Canup, 2004).

(v) The comparative compositions of the Earth and Moon; the Moon is more depleted in volatile elements (Jones & Palme, 2000), suggesting it has been subjected to additional thermal processing. Terrestrial and lunar materials are identical with respect to a number of isotopic systems, e.g. oxygen (Clayton & Mayeda, 1975; Wiechert et al., 2001) and tungsten (Touboul et al., 2007).

The main hypotheses for lunar formation advocated prior to the Apollo-era of lunar exploration (Wood, 1986) were:

(i) **Capture**: the Moon formed elsewhere in the solar system and later became trapped in its geocentric orbit. This was proposed in order to explain the major compositional differences between the Earth and Moon, such as the lunar iron depletion, but it is difficult to envisage the Moon's capture on a dynamic basis.

(ii) **Fission**: a rapidly spinning Earth became rotationally unstable, causing material to be siphoned off from the equator, which then recombined to form the Moon. This model would explain the lunar iron depletion if fission occurred after terrestrial core formation; it can also explain the isotopic similarities of the two bodies. However, this model requires the system to have had about four times its present angular momentum.

(iii) **Coaccretion**: the Moon formed as a companion to the Earth, undergoing similar accretion processes before entering its geocentric orbit. This model does not require a low-probability event or *ad hoc* assumptions, but fails to explain the lunar iron and volatile depletions, the system's high angular momentum, or melting that produced a magma ocean.

Following the return of lunar samples, a new model, the *giant impact hypothesis*, was proposed (Hartmann & Davis, 1975; Cameron & Ward, 1976) and thought to explain the

various constraints to a better degree. It is proposed that a planetesimal about the size of Mars impacted the early-Earth just prior to the end of its accretion. Dynamic simulations of such an impact yield proto-lunar disks with the appropriate mass and angular momentum. It has been shown that giant impact events are a natural consequence of planetary accumulation and thus a Moon-forming impact does not necessarily invoke a low-probability event (Wetherill, 1990). Models show that debris from the impact is likely to have been emplaced in an orbit around the Earth with the correct inclination (Cameron, 2000; Canup, 2004) and that it is dynamically plausible for this material to have accumulated into a single Moon (Ida et al., 1997; Canup et al., 1999).

Although the giant impact hypothesis is currently the most favoured for lunar formation, some opposition does exist. Jones & Palme (2000) claim that the expected geochemical consequences of the impact have not been observed, e.g. (i) the Moon, as a derivative of the Earth should be younger, and (ii) the thermal consequences of the impact would have resulted in a terrestrial magma ocean (Melosh, 1990; Tonks & Melosh, 1990). An alternative model in which the Moon formed from material with approximately chondritic siderophile element abundances about 35 Myr after the chondrites has been suggested (Jones & Palme, 2000). This model is incompatible with most versions of the giant impact hypothesis, they propose that it is better matched to the circum-terrestrial disk model of Weidenschilling et al. (1986), wherein silicate material was preferentially trapped in the disk over iron metal, and therefore the eventual Moon that accreted was depleted in metal.

The isotopic similarities, yet chemical differences between the Earth and Moon are difficult to explain. It has recently been proposed that liquid-vapour fractionation of the proto-lunar material during the high-temperature post-impact period may have caused the evolution of the chemical differences, alongside isotopic mixing and homogenisation (Pahlevan & Stevenson, 2009). However, Melosh (2009) noted that such isotopic equilibration would inevitably also equilibrate angular momentum, something which is not believed to be the case. If the model of Pahlevan & Stevenson (2009) is incorrect, it highlights a problem with the giant impact hypothesis that is yet to be resolved.

Long-lived isotope chronometers have been used to date the oldest lunar rocks to 4.56 – 4.29 Ga (Carlson & Lugmair, 1988; Alibert et al., 1994; Lee et al., 1997; Borg et al., 1999; Koeberl, 2006; Touboul et al., 2007; Bourdon et al., 2008), but the precise age of the Moon is uncertain. The hafnium-tungsten system is used to date the crystallisation of the lunar magma ocean to 4.527 ± 0.010 Ga, consistent with the giant impact hypothesis (Shearer & Newsom, 2000; Kleine et al., 2005; Touboul et al., 2007).

1.3.2. *Lunar differentiation – magma ocean models*

The gross differences between the mare and highland regions of the Moon provide primary evidence for a large-scale igneous differentiation event. The discovery that the oldest lunar crust, the highlands material, is anorthositic gave rise to the concept that it represents a crust of crystallised material that floated to the top of a deep 'magma ocean' (Wood et al., 1970) of denser basaltic material (Figure 1.12a). This relatively simple concept has survived since its original conception after the return of the Apollo 11 samples, although it has been challenged with new data (e.g. Longhi, 2003). Other evidence for magma ocean differentiation includes: the extremely ancient pristine non-mare rocks, and the complementary patterns of the europium anomalies in different lunar lithologies (Figure 1.6). The chemical and isotopic uniformity of the KREEP component in lunar samples suggests that these rocks were derived from a single late-stage, global residuum ('urKREEP') that became trapped between the anorthositic crust and the denser, mafic top of the mantle (Warren & Wasson, 1979).

A likely crystallisation sequence for the lunar magma ocean is: olivine → orthopyroxene + olivine → olivine + clinopyroxene + plagioclase → clinopyroxene + plagioclase → clinopyroxene + plagioclase + ilmenite (Shearer et al., 2006). It has thus been proposed that the magma ocean first fractionally crystallised a series of mafic or ultramafic cumulates that sank and formed the deep lunar mantle, which became the source areas for the mare basalts (Taylor, 1982; Warren, 1985; 1990; Papike et al., 1998; Shearer & Papike, 1999; Shearer et al., 2006); less-dense plagioclase floated to form the first stable (anorthositic) crust. Ti-oxides (i.e. ilmenite) started to crystallise from the late-stage liquid magma along with clinopyroxene and plagioclase when ~90% of the magma ocean had

solidified (Shearer et al., 2006). These Ti-cumulates were denser than the underlying olivine + pyroxene mantle and therefore it is likely that the denser material sank into the underlying mantle, where it re-melted and contributed to the source region of the high-Ti mare basalts (Ringwood & Kesson, 1976; Hess & Parmentier, 1995; Zhong et al., 2000).

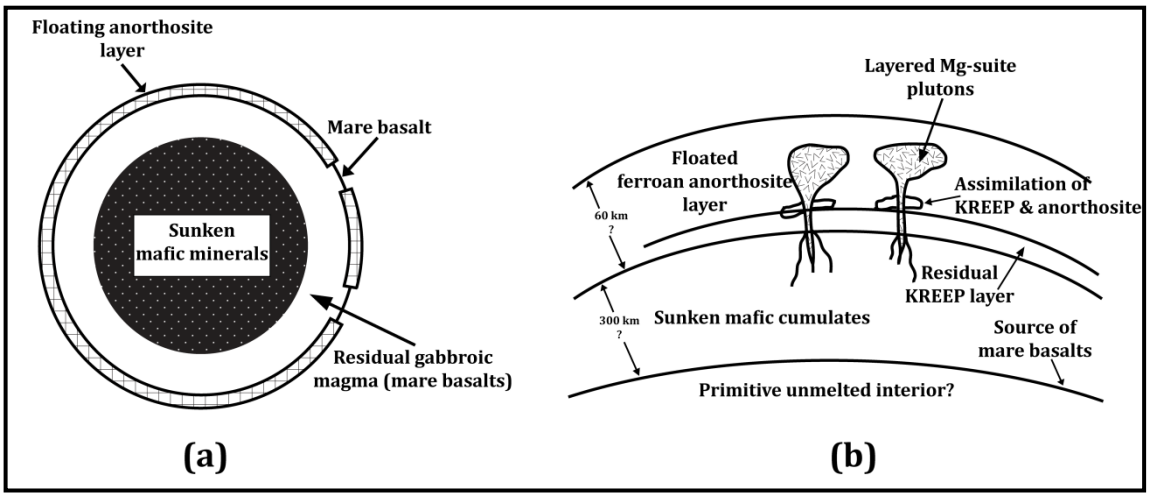

Figure 1.12. (a) An early magma ocean model (after Wood et al., 1970) where the entire Moon was initially molten and the mare basalts were parts of the chilled magma ocean exposed through holes in the crust. (b) A more recent model that allows for the ferroan anorthosites to form by flotation on the magma ocean, but accommodates a younger age for the Mg-suite rocks by formation through partial melting in the interior with assimilation of older KREEP and anorthosite compositions (adapted from Figure 2.5 of Vaniman et al., 1991).

Very late stage (after ~99% of magma ocean crystallisation) residual melts would have been rich in FeO and incompatible trace elements. As this 'urKREEP' component intruded into the lower crust it caused some partial melting and contamination of the lower crustal rocks, probably giving rise to the KREEP basalts (Vaniman et al., 1991). The total duration of the lunar magma ocean is difficult to estimate, however if KREEP material does indeed represent the last-stage residuum, then its age, 4.42 ± 0.07 Ga (Nyquist & Shih, 1992), represents the maximum period over which the magma ocean crystallised. Recent dating of a zircon in a lunar breccia to 4.417 ± 0.006 Ga provides a young age limit for the solidification of the lunar magma ocean (Nemchin et al., 2009).

The most serious alternative (Walker, 1983; Longhi & Ashwal, 1985) to the magma ocean scenario is the 'serial magmatism' model. This describes a situation where the anorthosites and other feldspathic cumulates formed from numerous magmas which had intruded into the primeval crust. An accurate determination of the plagioclase abundance in the crust

would help to determine, which, if either of these two hypotheses is correct. The serial magmatism model implies a plagioclase abundance of <55%, whereas the magma ocean hypothesis requires significantly more. Recent results from the Multiband Imager on SELENE (Ohtake et al., 2009) show a global distribution of surface rocks with very high plagioclase abundance (almost 100%), which is significantly higher than the previous estimates of 82 – 92 vol. % (Warren, 1990; Tompkins & Pieters, 1999; Wieczorek et al., 2006).

The magma ocean model provides a paradigm for the formation of the various non-mare / plutonic rock suites. The Mg-suite rocks are probably the result of melting events that postdate the magma ocean by between ~30 Myr and ~200 Myr (Longhi, 1977; Solomon & Longhi, 1977; Shearer & Newsom, 2000; Shearer et al., 2006). Magmas rising from the mantle mixed with and assimilated pockets of urKREEP (as well as ferroan anorthosite), thus explaining the KREEP-like REE patterns of the Mg-suite rocks (Warren & Wasson, 1980); differing degrees of this assimilation may have enhanced the diversity that is observed within this suite (James & Flohr, 1983). The original source of these magmas is not known, but melting may have been started by decompression caused by convective overturn of the cumulate pile, where dense Fe-rich material would originally have overlain less-dense Mg-rich material (Hess & Parmentier, 1995). Alternatively, heat from radioactive decay (Hess, 1994), or a combination of both mechanisms, could have produced the melting. It has also been suggested (e.g. Ryder, 1976; James, 1980; Snyder et al., 1995a; 1995b; Shervais & McGee, 1998) that the Mg-suite and evolved plutonic rocks are part of a continuum of crystallisation products from a parental basaltic magma with a KREEP-like composition.

The diversity of the mare basalt sample collection indicates the complexity of their genesis. Their distinctive europium anomalies (Figure 1.6) suggest that they formed by the partial melting of cumulates which crystallised from the magma ocean after plagioclase had been removed. Experimental work has shown that the mare basalts are likely to have formed at a depth of 100 – 500 km from source rocks that were rich in olivine, orthopyroxene and some clinopyroxene (Shearer & Papike, 1993; Shearer et al., 2006). It is thought that the eruption of the mare basalts is a continuation of the early episodes of basaltic magmatism

represented by the plutonic suites, with the onset of mare volcanism occurring before 4.35 Ga (Terada et al., 2007) and continuing to at least ~2.9 Ga, based on absolute dating of lunar meteorite NWA 773 (Fernandes et al., 2003; Borg et al., 2004) or perhaps to as recently as ~1.0 Ga, based on crater counting studies (Hiesinger et al., 2003).

1.3.3. *Lunar stratigraphy*

Lunar geologic history has been dominated by impact cratering during and since the end of mare basalt eruption. Various chronologies (e.g. those in Figure 1.13) use the ejecta deposits of large basins and craters as global marker horizons; that of Wilhelms et al. (1987) is the most widely accepted (Stöffler et al., 2006). This chronostratigraphy subdivides lunar history into five time intervals: the Pre-Nectarian (oldest), Nectarian (both pre-mare basalt eruption), Imbrian, Eratosthenian and Copernican (youngest).

1.3.4. *Unresolved issues in lunar geology*

Although the Moon is the best studied extra-terrestrial planetary body, the understanding of it geology and history is still incomplete. The scientific rationale for the continued exploration of the Moon are outlined in various documents (e.g. National Research Council, 2007), but some of the most important remaining issues include: (i) the precise shape of the lunar crater frequency curve (the production function that relates the time a unit has been exposed to meteorite bombardment to the number of craters, with a given diameter, which can be seen on its surface), and therefore the absolute calibration of the relative timescale; (ii) the age of the South Pole-Aitken basin (the oldest impact basin); (iii) the nature of volatiles within the lunar interior; and (iv) the true nature of the Moon's volcanic history and therefore its thermal evolution. The work in this thesis addresses some of the issues relating to the third ("key planetary processes are manifested in the diversity of lunar crustal rocks") and fifth ("lunar volcanism provides a window into the thermal and compositional evolution of the moon") NRC science concepts.

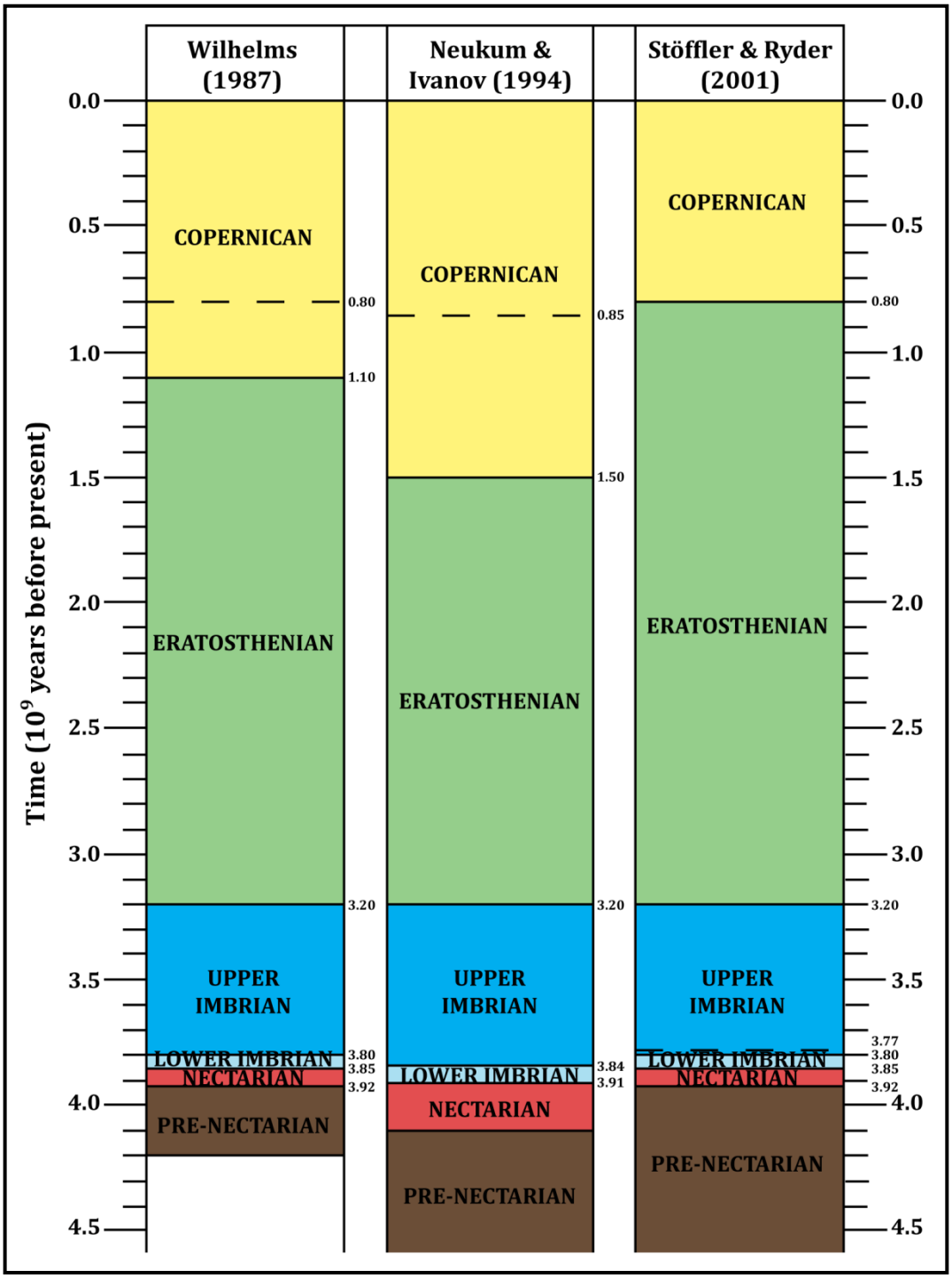

Figure 1.13. Comparison of three lunar stratigraphies (Wilhelms et al., 1987; Neukum & Ivanov, 1994; Stöffler & Ryder, 2001). Dashed lines in the stratigraphies of Wilhelms et al. (1987) and Neukum & Ivanov (1994) indicate radiometric ages, which the authors attribute to the formation of the crater Copernicus. In Stöffler & Ryder (2001) two formation ages for the Imbrium basin have been proposed: 3.85 Ga and 3.77 Ga (dashed line). The Pre-Nectarian and Nectarian periods were times of intense impact bombardment, when a number of the large impact basins visible on the Moon were formed (e.g. Nectaris, Serenitatis and Crisium). The Imbrium and the youngest impact basin, Orientale, formed in the Early Imbrian and the end of the intense bombardment allowed extruded mare basalts to be preserved. The Eratosthenian saw volcanic activity continue, along with smaller and less frequent impact events. Volcanic activity ceased completely during the Copernican (adapted from Figure 1.9 of Hiesinger & Head, 2006).

1.4. Methods of compositional planetary remote sensing

1.4.1. *X-ray fluorescence (XRF)*

X-rays are a part of the electromagnetic radiation spectrum, between the ultraviolet and gamma-rays, with wavelengths between ~0.003 nm and 3 nm. X-ray fluorescence (XRF) is the process whereby secondary (fluorescent) X-rays are emitted from an atom that has been energetically excited by incoming, primary X-rays (Figure 1.14). In XRF spectroscopy the energy of the fluorescent X-rays is analysed in order to study the nature of the irradiated atoms.

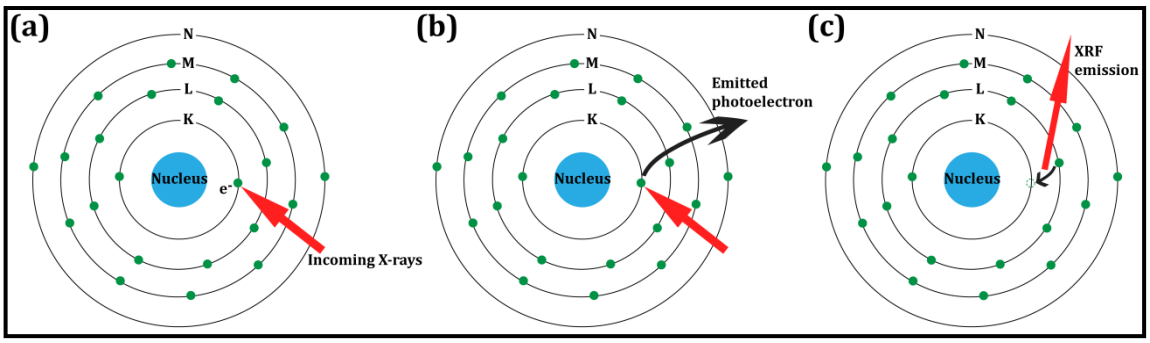

Figure 1.14. Cartoon of the XRF process. (a) An incident X-ray is absorbed by an atom within the target material. (b) When the energy of the absorbed X-ray photon is greater than the binding energy of a K-electron, the electron can be emitted from the atom. (c) The resulting vacancy in the K-shell leaves the atom in an unstable condition, so electrons from outer shells are transferred to fill the vacancy. An X-ray photon with energy equal to the difference in the binding energies of the two shells is emitted; this is the X-ray fluorescence. The same process can also occur in the other electron shells (adapted from http://www.amptek.com/xrf.html).

Two separate phenomena can result from interactions between the incoming, primary X-rays and the electrons in the target atoms and these are evident in XRF spectra (e.g. Figure 1.15):

(i) Production of *bremsstrahlung* (continuous) radiation due to the loss of kinetic energy of the liberated electrons caused by electronic repulsion (Röntgen, 1896).

(ii) Production of characteristic radiation lines after the direct ionisation of target atoms by the incoming X-rays. This ionisation occurs when the energy of the incident X-ray photon is greater than the binding energy (and is most efficient when the X-ray photon energy is only a little higher than the binding energy) of an inner-shell electron in the target atom (Fitton, 1997). The electronic configuration that results is

unstable and quickly reverts to its normal state via the transfer of an outer shell electron to the unfilled inner level, and therefore represents a loss in the potential energy of the atom (Fitton, 1997). In the case of XRF, the energy is manifest as an emitted X-ray photon whose energy is equal to the difference between the binding energies of the two electron shells involved, it is thus characteristic and unique to the element itself.

The de-excitation process can differ, if the energy originally released does not exit the atom, but is instead re-absorbed at another energy level; ionisation eventually occurs after the ejection of an electron from a separate outer shell. This process is known as the *Auger effect* (Burhop, 1952). The intensity of radiation depends on the relative efficiency of these two opposing de-excitation processes (direct ionisation and the Auger effect) and is expressed as the *fluorescent yield*. The fluorescent yield decreases markedly with decreasing atomic number (Bambynek et al., 1972) because the Auger effect is more pronounced for atoms with lower atomic number.

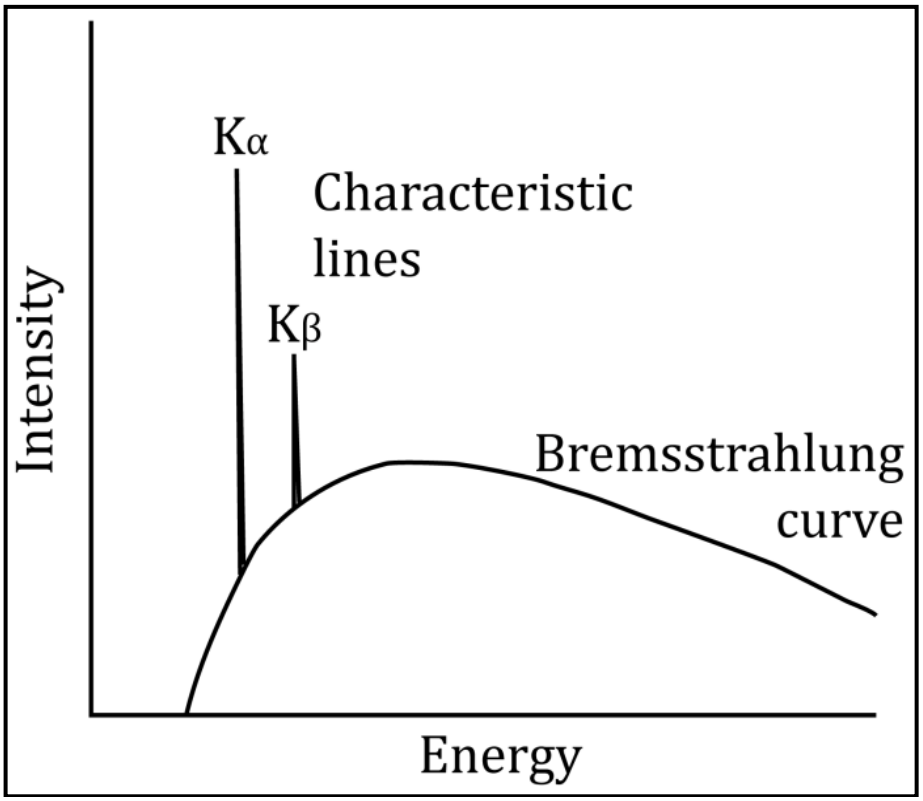

Figure 1.15. Theoretical XRF spectrum showing the shape of the bremsstrahlung (continuum) radiation and the superimposed characteristic K_α and K_β lines of a hypothetical element.

Some generalisations in the nomenclature for characteristic X-ray lines can be made (Jenkins, 1974):

(i) The final position of the transferred electron determines the series of radiation, e.g. ionisation from the K-shell followed by the filling of the K-vacancy produces K-series radiation. The subscripts α, β etc. refer to specific transitions to these shells.

(ii) The α line is always the strongest in a given series, followed by β, γ, etc.

(iii) A given transition can produce more than one line (due to quantum spin values of ½ or -½), e.g. $K_{\alpha 1}$ and $K_{\alpha 2}$.

As an incident X-ray photon interacts with a target electron, scattering can occur. If this collision is elastic, no energy is lost and the scattering is *coherent* (also known as *Raleigh* scattering). However, if some of the electron's energy is lost in the interaction, the wavelength of the energy will increase; this is known as *incoherent* or *Compton* scattering.

Laboratory XRF spectrometers use well characterised, primary X-ray beams to excite fluorescent X-ray emission from suitably prepared samples. The intensity of the characteristic line is proportional to the abundance of the specific element in the sample, thus the resulting spectrum can be used to quantitatively analyse the sample's elemental composition. The source of primary X-rays in laboratory XRF spectrometers is usually either an X-ray tube with a given anode (e.g. tungsten or molybdenum) or a suitable radioactive element (e.g. ^{55}Fe or ^{57}Co).

In XRF spectrometry detectors are required which can convert the quantum energy of an incident X-ray photon into an electrical pulse, two common examples are proportional counters and semi-conductor detectors (Fitton, 1997). In proportional counters a central anode wire runs through a metal shell filled with a gas (e.g. He, Ne, Ar, Kr, Xe) at low pressure. When an X-ray photon enters the chamber, the gas becomes ionised and the charge that collects on the anode is transformed into a voltage pulse which can be amplified and recorded by a connected computer system (Fitton, 1997). X-ray photons with higher energies cause an increase in the number of ionisations that occur and as such the output pulse is proportionally larger. Proportional counters are capable of handling very high counting rates without appreciable loss of information, i.e. they have a low dead time.

Proportional counters were employed for the Apollo XRF instrument (Adler et al., 1972a; 1972b) and in the XRF spectrometer payload on the (current) MESSENGER mission to Mercury (Schlemm et al., 2007).

Semiconductor detectors can measure X-rays with much better precision and at lower energies than traditional gas detectors (Strüder et al., 2004). They allow charge to be rapidly collected, and so can be used in high-rate environments (Strüder et al., 2004). The semiconductor properties of a material arise when a narrow energy 'gap' exists between a lower (valence) band of filled energy levels and an upper (conduction) band of empty energy levels, as illustrated in Figure 1.16 (Parry, 1997). The arrival of an X-ray photon is marked by a short period in which the material behaves as a conductor, lasting only until the promoted electrons fall back into the lower energy band; this process creates a potential difference across the semiconductor crystal and generates a pulse of current (Parry, 1997). The magnitude of each pulse is proportional to the number of electrons that have been promoted, which is in turn dependent on the energy of the incident photon which caused the excitation (Parry, 1997). Even at room temperature a number of electrons can be promoted to the conduction band, this creates a background current that can obscure low photon intensities and is why semiconductor detectors work best at low temperatures (Parry, 1997).

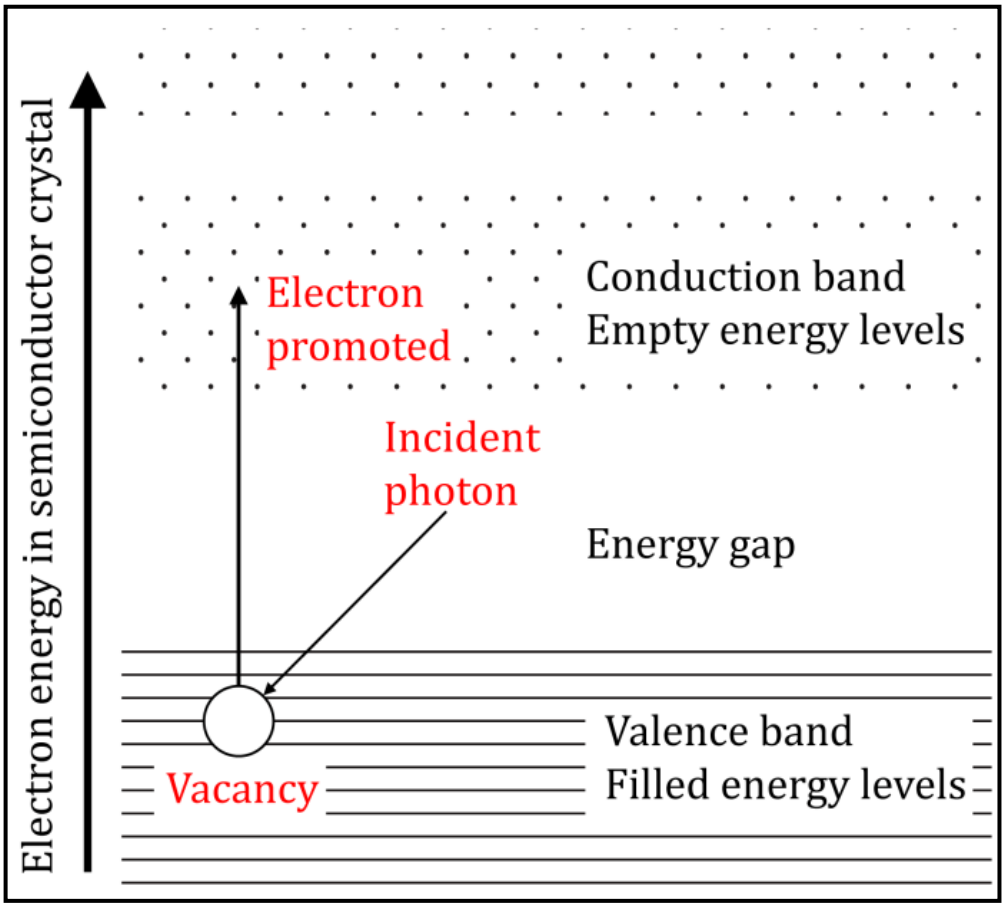

Figure 1.16. Cartoon illustrating the basic mechanics of semiconductor detectors. In the normal state, all electrons are in the valence band and are unable to migrate. When a high-energy incident photon enters the semiconductor crystal, the transfer of energy causes the promotion of a number of electrons across the energy gap into the conduction band where the electrons are free to migrate, leaving vacancies in the valance band to which further migration can occur (adapted from Parry, 1997).

Planetary XRF experiments

Planetary XRF experiments are miniature versions of their laboratory equivalents, where X-rays emitted from the solar corona act as the incident, exciting X-ray source (Korchak, 1971). These experiments are limited to bodies in the inner solar system where the X-ray flux is high enough to generate detectable levels of XRF, and those (e.g. the Moon, Mercury and asteroids) lacking atmospheres which would otherwise absorb the incident X-rays (Yin et al., 1993). The measured X-ray flux from the planetary surface is dependent on the intensity and shape of the incident spectrum. This means that the solar X-ray output spectrum, which is highly variable even on short timescales (e.g. Donnelly, 1976; Bouwer, 1983; Crosby et al., 1993), must be simultaneously measured by an accompanying solar X-ray monitor.

The low energy of both solar X-rays and planetary XRF radiation limit the mean penetration and escape depths of the X-rays in a surface to less than 100 µm (Adler et al., 1973; Yin et al., 1993; Clark & Trombka, 1997). Measurements of this surficial layer of the regolith are assumed to be representative of the underlying layers of regolith and bedrock, so long as the surface is sufficiently gardened / mature (Taylor, 1975; Clark et al., 1990).

The first planetary XRF spectrometer was flown onboard the Russian satellite Luna 12 in 1968 (Adler et al., 1973) and these instruments have since been included in the payloads of a number of missions to the Moon (Apollo 15 and Apollo 16, SMART-1, Kaguya, Chang'e-1, Chang'e-2 & Chandrayaan-1), asteroids (NEAR, Hayabusa) and Mercury (MESSENGER and the forthcoming BepiColombo); some of these are described below.

Apollo 15 & Apollo 16

XRF spectrometers were flown onboard the Command Service Module (CSM) of Apollo 15 and Apollo 16 as part of the Scientific Instrument Module (Yin et al., 1993). The instruments (Figure 1.17) consisted of three gas-filled (90% Ar, 9.5% CO_2, 0.5% He) large area (25 cm^2) proportional counters, mounted alongside one another. Each counter was covered by a 0.025 mm thick beryllium window that reduced the detection of X-rays scattered from the lunar surface which would have otherwise dominated the lunar flux at low energies (Clark, 1979; Tandberg-Hanssen & Emslie, 1988). The resolution of the individual detectors was insufficient to resolve the three low energy key rock-forming elements magnesium, aluminium and silicon. Filters were therefore required; one counter had no filter, one had a magnesium filter (absorbed Al and Si X-rays), and one had an aluminium filter (absorbed Si X-rays). An additional, smaller proportional counter with a pin-hole sized beryllium window was mounted on the opposite side of the spacecraft to the detectors and this monitored the incident solar X-ray flux. A single large area collimator assembly was fitted to the front of the instrument to ensure that the field of view for all three detectors was equal (Adler et al., 1972a; 1972b; 1972c; 1972d; 1973). The non-polar orbits and short duration of these two missions meant that the total area of the lunar surface mapped using XRF was only ~10%, all within ~25° of the equator (Clark & Adler, 1978;

Clark & Hawke, 1981) The data have usually been presented as intensity ratios of Al/Si and Mg/Si (e.g. Figure 1.18); silicon is a good normalising factor because it varies by <5% in the regolith across the lunar surface (Yin et al., 1993).

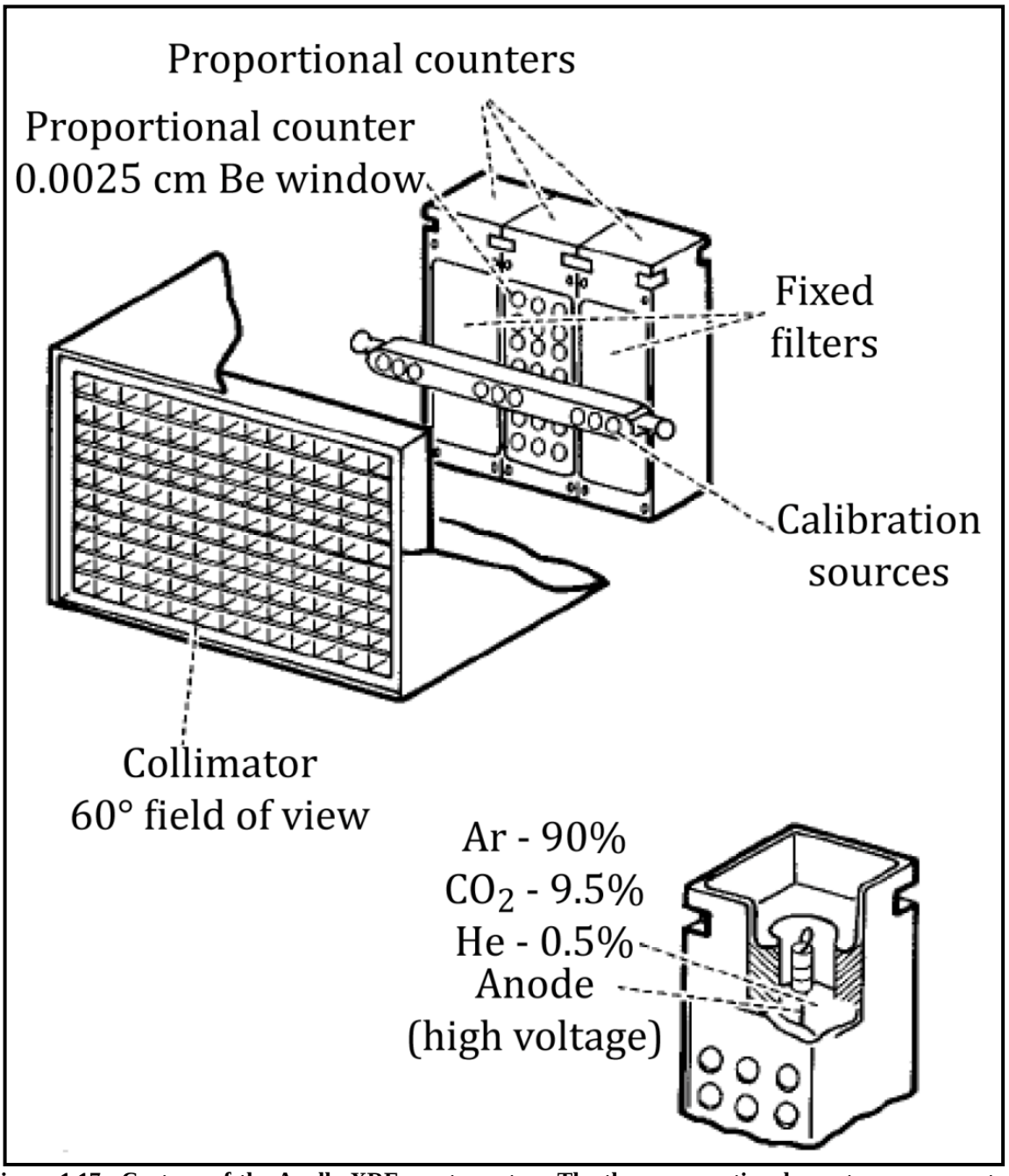

Figure 1.17. Cartoon of the Apollo XRF spectrometer. The three proportional counters are mounted side-by-side, two of which have filters (Mg & Al) in front of their beryllium windows. The holder for the in-flight calibration sources and the collimator are also shown (adapted from Adler et al., 1972b).

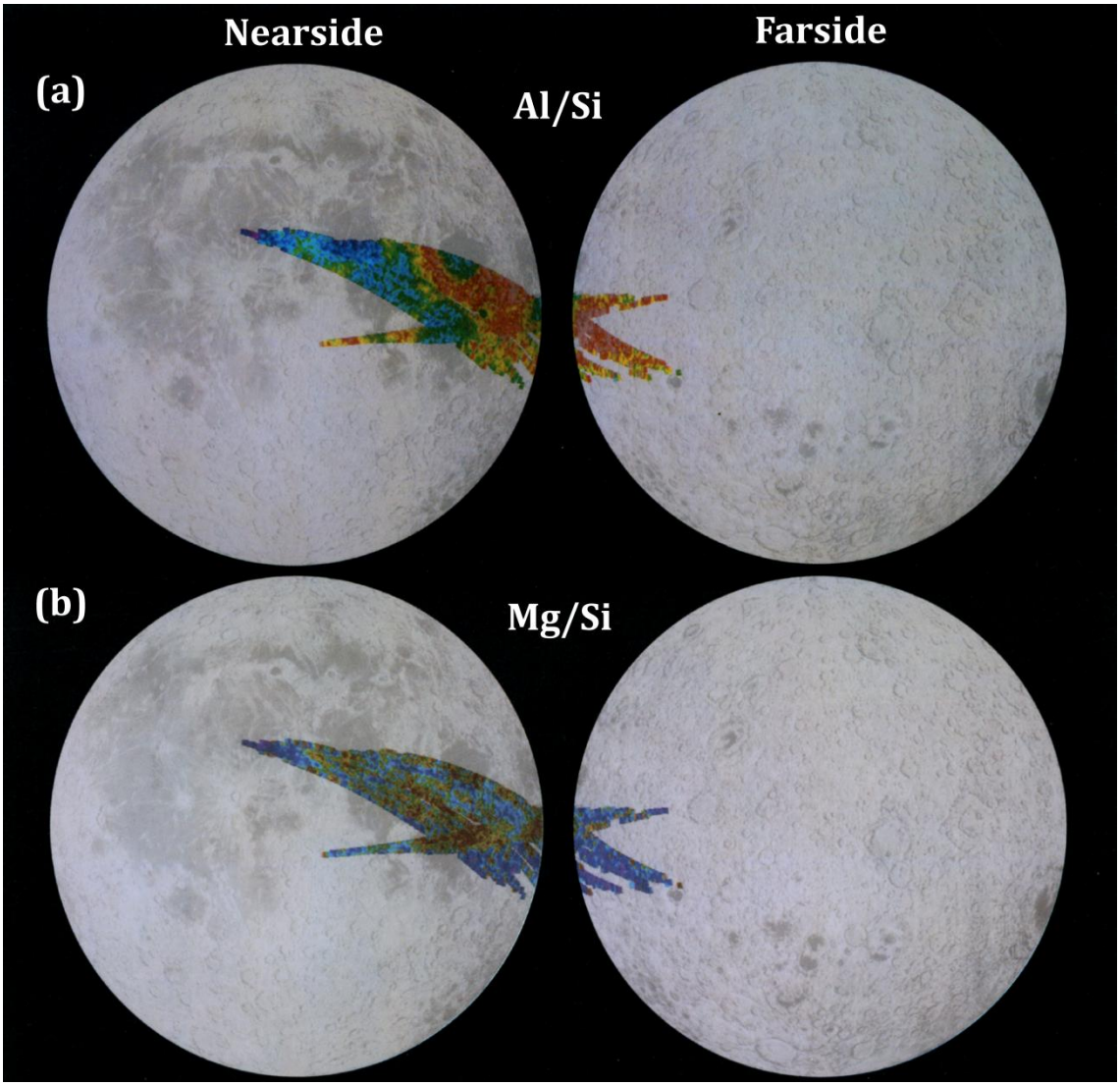

Figure 1.18. Maps of Apollo 15 and 16 orbital XRF data (Clark & Adler, 1978; Clark & Hawke, 1981). (a) Al/Si colours indicate the following concentration ratios: pink, >0.82; red, 0.77-0.82; yellow, 0.72-0.77; green, 0.66-0.72; cyan, 0.58-0.66; blue, 0.49-0.58; violet, <0.49. The highland regions of the Moon are revealed as more Al-rich than the maria. (b) Mg/Si colours indicate the following ratios: pink, >0.31; red, 0.21-0.31; yellow, 0.26-0.28; green, 0.25-0.26; cyan, 0.24-0.25; blue, 0.23-0.24; violet, <0.23. Anorthositic highland areas tend to have relatively low Mg/Si ratios (adapted from plates 10.4 and 10.5 of Spudis & Pieters, 1991).

D-CIXS & C1XS

D-CIXS (Demonstration of a Compact Imaging X-ray Spectrometer) was the XRF instrument payload on ESA's SMART-1 mission (Grande et al., 2003). The instrument demonstrated novel miniaturised X-ray spectrometer technology, based around the use of swept charge device (SCD) solid-state detectors (Holland et al., 2004) and was designed to map major rock-forming elements (e.g. Mg, Al, Si, Ca, Ti and Fe) by measuring the lunar

XRF between 1 and 10 keV (Dunkin et al., 2003; Grande et al., 2007). An accompanying payload, XSM (X-ray Solar Monitor) simultaneously measured the solar X-ray flux (Huovelin et al., 2002). Although D-CIXS successfully demonstrated technological innovations, the scientific results (including the first detection of Ti K_α from the lunar surface) were limited, for a number of reasons (Grande et al., 2007; Swinyard et al., 2009). These included: (i) radiation damage to the detectors during the long cruise phase before lunar orbit insertion and (ii) operation during a period of low solar activity (approach to solar minimum) which limited the X-ray signal and restricted the surface coverage to areas covered during flare events. Experience and lessons learnt with D-CIXS (Crawford et al., 2009; Swinyard et al., 2009) led to a significantly improved design for C1XS (Chandrayaan-1 X-ray Spectrometer) which is described in detail in chapter 2.

1.4.2. *UV-Vis & NIR spectroscopy*

Reflectance spectra from common rock-forming minerals are known to exhibit diagnostic absorption features in the ultraviolet (0.2 – 0.4 μm), visible (0.4 – 0.7 μm) and near-infrared (0.7 – 5 μm) wavelengths. The influence of the mineral's chemical and physical structure on the nature of the absorptions has been studied and is well-defined (Burns, 1993) and the absorption wavelengths are thus characteristic of the composition and mineralogy of the material measured. Rocks, as complex mixtures of minerals, have reflectance spectra which are non-linear combinations of superimposed spectra from the individual constituent minerals. The UV-Vis-NIR reflectance spectra of the most common lunar surface minerals are shown in Figure 1.19.

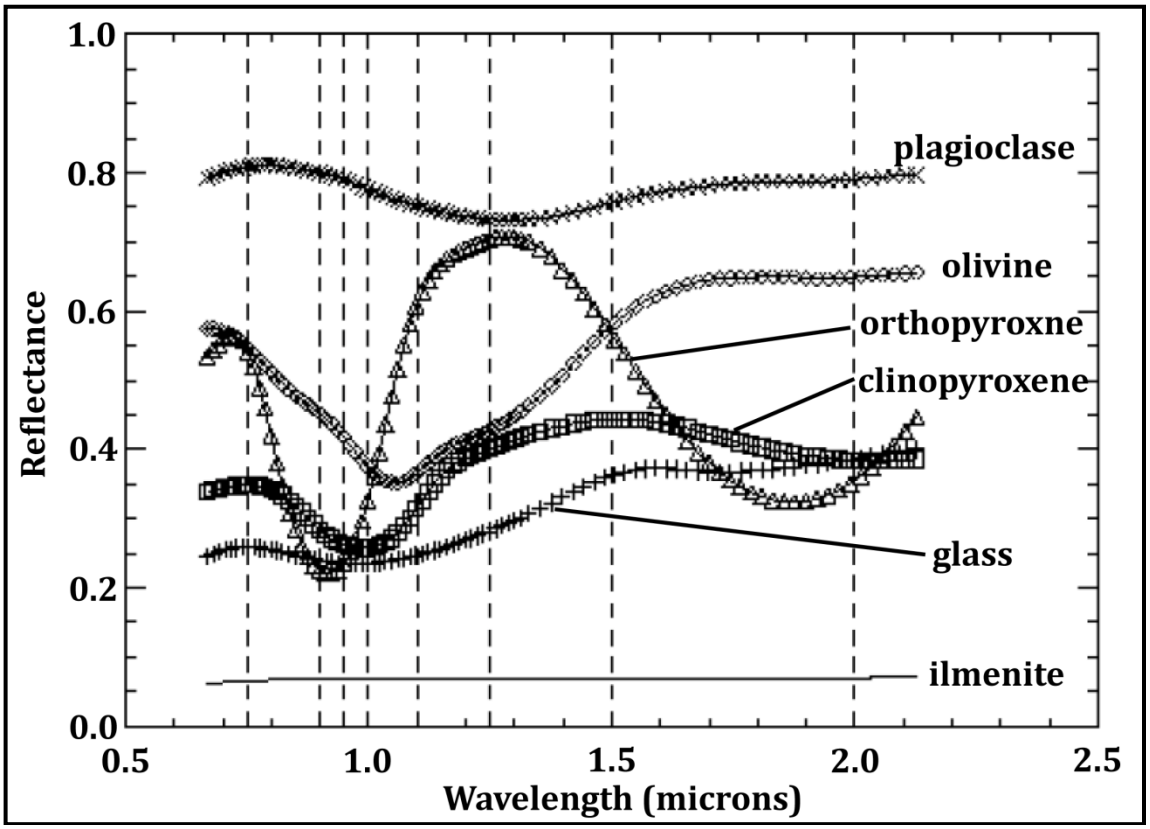

Figure 1.19. UV-Vis-NIR reflectance spectra of the most common lunar minerals. The mafic minerals olivine, orthopyroxene and clinopyroxene can be distinguished by the relative positions of their iron absorption band at ~1 µm and by the presence / lack of an absorption band at ~2 µm. Plagioclase has a higher albedo than the mafic minerals and lacks strong absorption features. Ilmenite has a flat, dark and featureless spectrum. Dashed lines indicate Clementine bandpass wavelengths (adapted from Lucey et al., 2006).

Clementine

Clementine spent 71 days in lunar orbit mapping the lunar surface with a variety of geochemical and geophysical instruments, including a UV-Vis and a separate NIR lightweight charge-coupled device (CCD) camera. Spectral bands were selected using filter wheels, these wavelengths (Table 1.3) were chosen to characterise the broad lunar continuum and to sample parts of the spectrum with absorption bands diagnostic of iron-bearing minerals and plagioclase (Nozette et al., 1994). Calibration of the NIR dataset was substantially delayed (Lucey et al., 1997; 1998; 2000a; Eliason et al., 2003; Cahill et al., 2004) and its release followed that of the UV-Vis dataset by several years. During this time a number of methods were developed that employed the five UV-Vis wavelengths to make qualitative and quantitative estimates of various chemical and mineralogical constituents of the lunar surface (Lucey et al., 2000b; Pieters et al., 2001; 2006; Gillis et al., 2003; 2004;

Lucey, 2004; 2006), these are described in chapter 5, where the Clementine multispectral data are used to characterise crater ejecta deposits in two mare regions.

Table 1.3. Bandpass filter wavelengths on the UV-Vis and NIR cameras onboard the Clementine mission (Nozette et al., 1994).

UV-Vis Bandpass filters (μm)	NIR Bandpass filters (μm)
0.415 ± 0.020	1.100 ± 0.030
0.750 ± 0.005	1.250 ± 0.030
0.900 ± 0.015	1.500 ± 0.030
0.950 ± 0.015	2.000 ± 0.030
1.000 ± 0.015	2.600 ± 0.030
	2.780 ± 0.060

SELENE Spectral Profiler (SP) & Chandrayaan-1 Moon Mineralogy Mapper (M^3)

Despite the success of the first global mapping of the Moon by Clementine, high-resolution mineralogical information was still lacking. Two more recent instruments: Spectral Profiler (SP) on Kaguya and M^3 (Moon Mineralogy Mapper) on Chandrayaan-1 have somewhat fulfilled this goal. SP was a Vis-NIR (0.5 – 2.6 μm) spectrometer, with 296 spectral channels and a small (500 m) field of view (Matsunaga et al., 2001). Among its early scientific highlights is the most conclusive detection of crystalline, iron-bearing plagioclase on the lunar surface made to-date (Matsunaga et al., 2008).

The M^3 imaging spectrometer also operated in the Vis-NIR wavelengths (0.42 – 3.0 μm) and aimed to provide low-resolution spectral (140 m/pixel; 86 spectral channels) data for the entire lunar surface, as well as high-spectral resolution science data (80 m/pixel; 260 spectral channels) for 25 – 50% of the surface (Pieters et al., 2009b). With its expanded spectral range, reaching further into the near-infrared it was able to detect an absorption feature at ~3 μm. This feature was found to be associated with soils at moderate to high latitudes and at small, fresh impact craters in the anorthositic highlands. The feature is consistent with adsorbed H_2O or OH molecules in the soil, and suggests that there is a minor hydrate phase or hydration process occurring on the surface, of which there is little evidence in the returned or meteorite collections. The lack of correlation with Lunar Prospector Neutron Spectrometer hydrogen data (which sample about the top metre of the lunar surface) indicates that these phases are likely to be limited to the top few mm of the

surface and are created by its interaction with solar wind protons (Pieters et al., 2009c). These findings have been confirmed with results obtained from spectrometers onboard the Cassini (Clark, 2009) and Deep Impact missions (Sunshine et al., 2009), which used the Moon as a calibration target during their lunar flyby phases. These instruments had extended spectral ranges, further into the near-infrared wavelengths and were therefore able to characterise this 3 μm absorption feature better and confirm a surficial OH or H_2O signature.

1.4.3. *Gamma-ray spectroscopy*

Planetary gamma-ray spectroscopy allows the quantitative measurement of various major, minor and trace elements in the surfaces of bodies that do not possess a thick atmosphere. Gamma-rays are produced in the planet's surface by the decay of long-lived radioactive elements, as well as by interactions of cosmic rays with surface atoms (Figure 1.20). The intensity of the radiation is proportional to the concentration of the elements from which it originates, along with the flux of neutrons which cause the nuclear reactions and the emission of gamma-rays. This means that both the resulting gamma-ray intensity and the incident neutron flux must be measured in a planetary experiment in order to make accurate quantitative estimates of the surface composition.

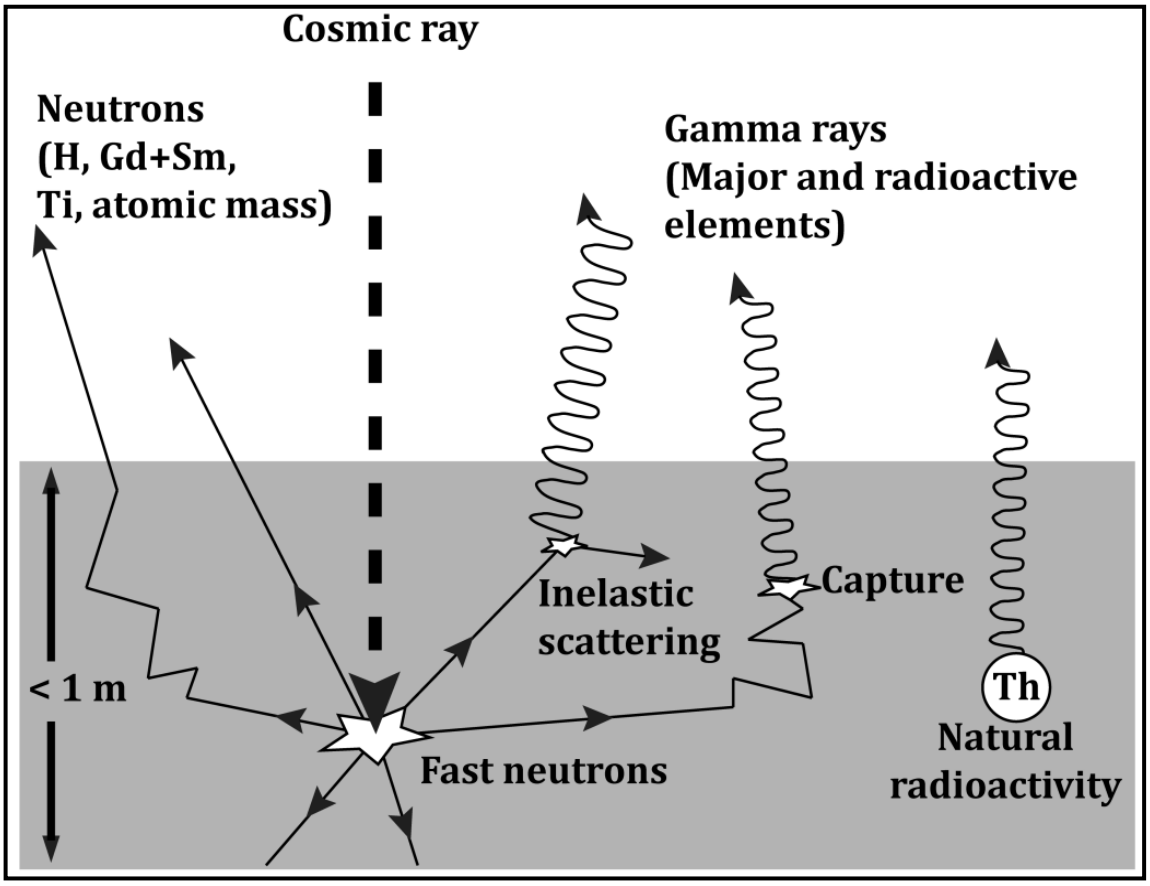

Figure 1.20. Schematic diagram of a cosmic ray interaction with the lunar (or other planetary) surface (from Prettyman et al., 2006).

Apollo 15 & Apollo 16

Wide-scale orbital gamma-ray spectroscopy from the Moon was first conducted during the Apollo 15 and 16 missions (Spudis & Pieters, 1991). These spectrometers had an analytical energy range of 0.2 – 10 MeV (including nearly all useful characteristic gamma-ray lines of common rock-forming elements), and a spatial resolution of ~75 km on the lunar surface (Metzger, 1993). The total combined surface coverage from both missions was ~23%, with none at latitudes greater than 30° (Spudis & Pieters, 1991). Although the poor energy resolution of the instruments and the short duration of the missions limited the quality of the data, the final data (for Th, Fe, Ti, K and Mg) products provided many important insights into the geochemical nature of the Moon's surface (Figure 1.21).

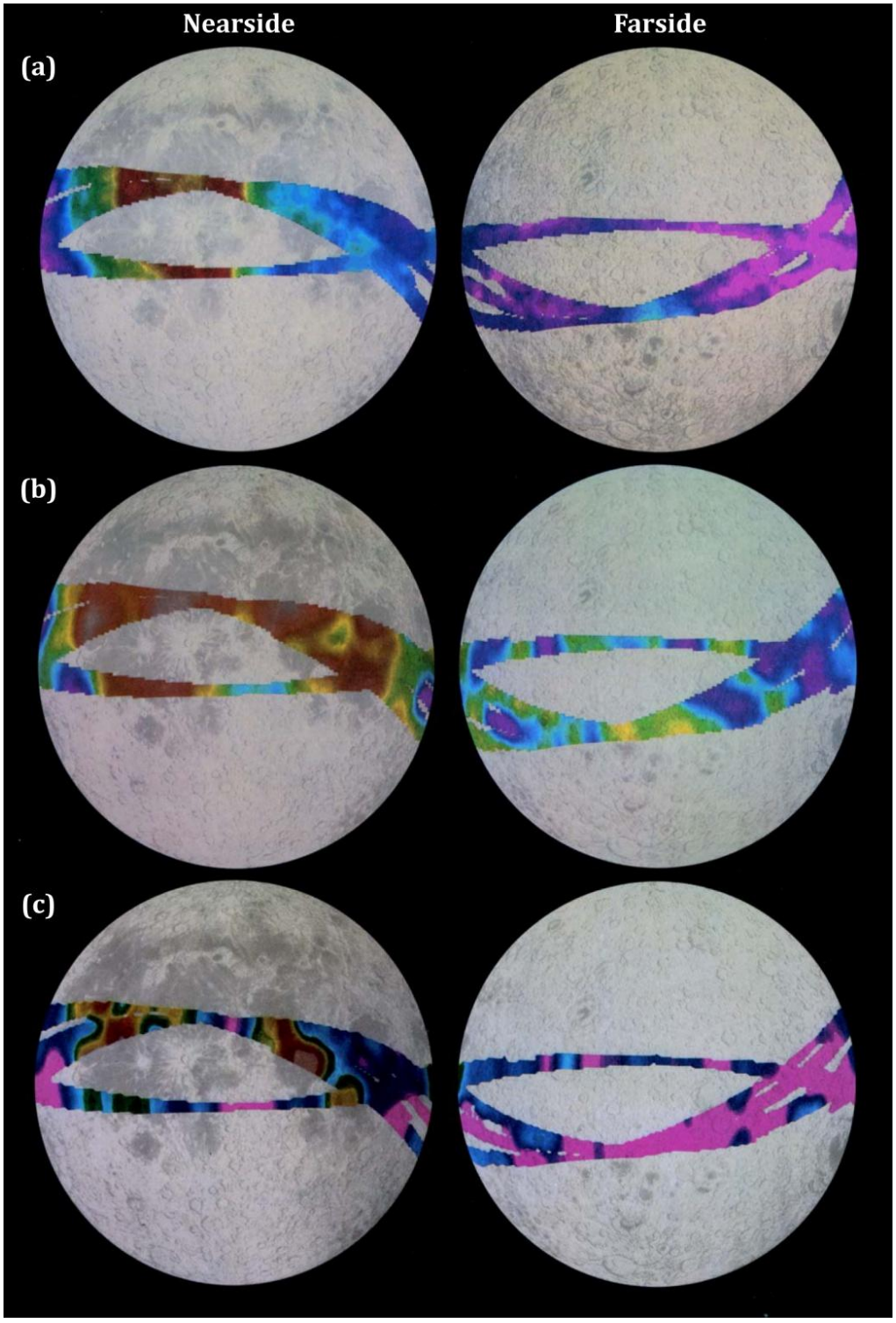

Figure 1.21. Results from Apollo 15 and 16 orbital gamma-ray measurements. (a) Concentration of Th (μg/g), where: red, >5.7; orange, 4.6-5.7; yellow, 3.8-4.7; green, 2.8-3.8; cyan, 1.9-2.8; blue, 0.9-1.9; violet, <0.9 (BVSP, 1981). The brighter colours (higher Th content) tend to indicate those regions with abundant KREEP. (b) Concentration of Fe (wt. %), where: pink, >11.4; red, 8.5-11.4; yellow, 6.5-8.5; green, 5.0-6.5; cyan, 3.7-5.0; blue, 2.2-3.7; violet, <2.2 (Davis, 1980). The highest Fe concentrations correlate with the mare basalts. (c) Concentration of Ti (wt. %), where: pink, >4.51; red, 3.61-4.51; yellow, 2.81-3.61; green, 2.00-2.81; cyan, 1.30-2.00; blue, 0.60-1.30; violet, <0.60 (Metzger & Parker, 1979). Ti concentrations vary greatly within the maria (adapted from Plates 10.1-10.3 of Spudis & Pieters, 1991).

Lunar Prospector

One of the main goals of the 1998 Lunar Prospector mission was to map the global abundance of major (Mg, Al, Si, Ca, Ti, Fe, O) and radioactive (U, Th, K) elements in the top few tens of centimetres of the lunar surface using gamma-ray and neutron spectroscopy (Binder, 1998; Feldman et al., 2004). The first results (for Fe and Th) were associated with intense, well-resolved spectral features; finding the abundance of other elements required a spectral un-mixing algorithm (Prettyman et al., 2006). An algorithm (Prettyman et al., 2006) has been developed in order to calibrate the Lunar Prospector elemental data with the compositions of the lunar meteorites (Korotev et al., 2003; Warren, 2005), allowing the absolute abundances to be estimated from Lunar Prospector gamma-ray data. The algorithm has been applied to spectra binned into 20°, 5° and 2° equal-area pixels, and some of the corresponding global abundance maps for various elements are shown in Figure 1.22. One of the major findings from these data is that K and Th are concentrated on the nearside and occur in close association with the Imbrian and Procellarum basins, a region now known as the Procellarum KREEP terrane (PKT).

1.5. Aims of this project

In this thesis a three-pronged approach to remote sensing of the Moon is employed: (i) the calibration of the C1XS flight instrument (chapter 2) and laboratory XRF experiments (chapter 3) are described, whose results are used to provide the new, scientifically robust C1XS XRF dataset; (ii) two sections of the C1XS dataset, for a regions over the two major lunar maria (Mare Serenitatis and Oceanus Procellarum) are analysed and the results are discussed in the context of existing sample and remote sensing datasets; and (iii) an in-depth study of the lava flow stratigraphy of the two mare regions studied in chapter 4, is conducted using Clementine multispectral data (chapter 5). Chapter 6 summarises the findings and conclusions of this thesis and makes recommendations for future work.

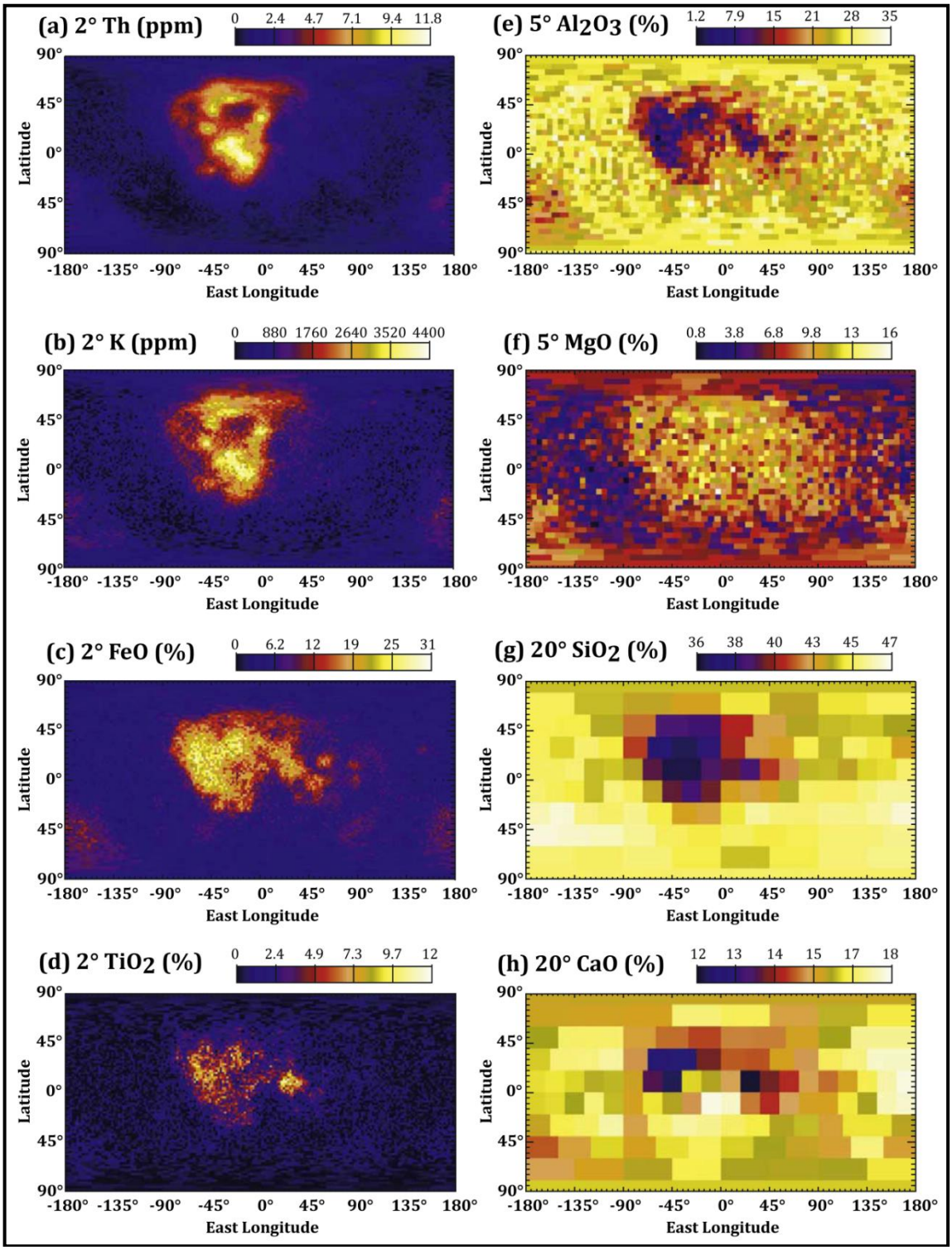

Figure 1.22. Lunar Prospector elemental abundance maps, determined by spectral un-mixing, binned into (i) 2° equal-area pixels, for (a) Th, (b) K, (c) Fe and (d) Ti; (ii) 5° equal-area pixels, for (e) Al and (f) Mg; and (iii) 20° equal-area pixels, for (g) Si and (h) Ca (adapted from Prettyman et al., 2006).

Chapter 2: Chandrayaan-1 X-ray Spectrometer (C1XS): instrument overview, calibration and data processing

2.1. Chandrayaan-1 mission & C1XS scientific objectives

C1XS (Chandrayaan-1 X-ray Spectrometer) was an ESA (European Space Agency) payload instrument onboard the Indian Space Research Organisation's (ISRO) first lunar mission, Chandrayaan-1 (Goswami & Annadurai, 2009). It was a compact X-ray spectrometer (energy dispersive) designed to detect X-ray fluorescence from the lunar surface, in order to map the abundance of major rock-forming elements (Grande et al., 2009). The C1XS hardware was designed and built at the Rutherford Appleton Laboratory, along with contributions from the ISRO satellite centre and CESR (Centre d'Etude Spatiale des Rayonnements), Toulouse. A team at the e2v Centre for Electronic Imaging (CEI) at Brunel University carried out work in characterising the detectors (Smith & Gow, 2009), and an accompanying solar monitor payload (XSM) was provided by the University of Helsinki Observatory. Photographs of both the C1XS and XSM flight instruments are shown in Figure 2.1. The Chandrayaan-1 mission was launched on 22nd October 2008 and reached its nominal lunar orbit (100 km) on 12th November 2008. On 19th May 2009 the orbit was raised to 200 km in attempt to deal with temperature problems experienced by the satellite. The planned two-year mission ended prematurely on 29th August 2009 when communications with the satellite were lost.

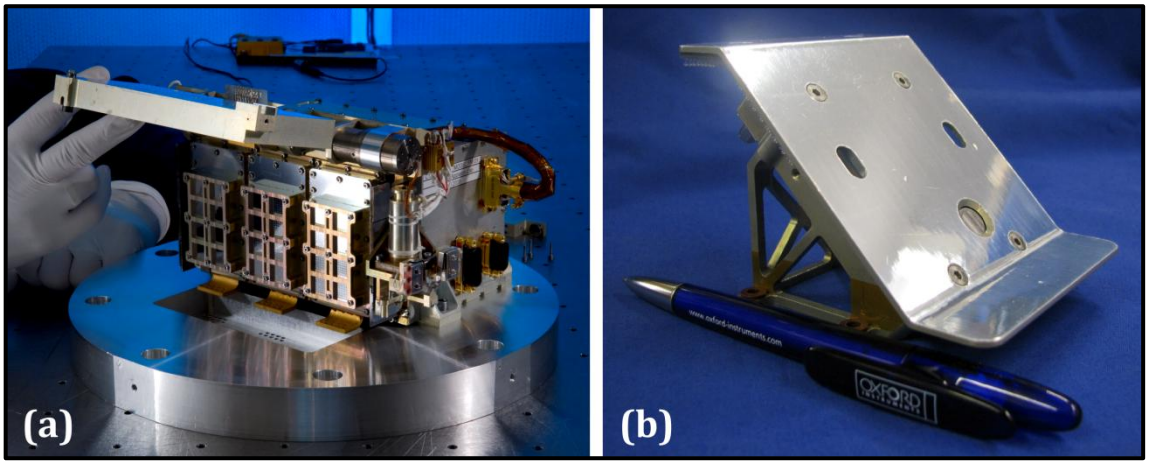

Figure 2.1. Photographs of (a) the C1XS flight instrument on a fixture for vibration testing (courtesy of RAL) and (b) the XSM flight instrument (from Howe et al., 2009).

C1XS was designed to meet a number of scientific objectives that relate to lunar geology on regional and local scales, as laid out in Crawford et al. (2009). In summary, the aim of C1XS was orbital determination of the major element geochemistry in the lunar surface, to permit mapping of variations between lunar terranes and lithologies. Determination of major element abundances also allows a number of parameters, such as the magnesium number (Mg# = atomic Mg/(Mg + Fe)) and refractory element budget to be established and thus further characterise the large and small scale stratigraphy of the crust, mare basalt evolution, and possible identification of new lunar lithologies. Although the C1XS instrument itself performed to a higher level than had been stipulated, the curtailed mission coupled with low solar activity which produced only a small number of low-energy flares meant that the dataset obtained was limited in size and the scientific results will be fewer than originally envisaged.

2.2. Instrument design

C1XS was developed using heritage from the technology demonstrator instrument D-CIXS which flew on ESA's SMART-1 mission to the Moon (Grande, 2001; Grande et al., 2003; 2007). Although many of the instrument features remained unchanged, e.g. the use of swept charge device (SCD) detectors (see section 2.2.2), several hardware and software alterations were made and resulted in an improved instrument. This increased capability is illustrated in Figure 2.2, which compares an actual D-CIXS spectrum with a predicted C1XS spectrum for the same flare event. The design of the C1XS instrument is described fully in Howe et al. (2009).

The C1XS instrument had a mass of 5.56 kg and dimensions: 250 mm (wide) × 150 mm (tall) × 190 mm (deep). It was divided into two sections: (i) the larger electronics module contained within a 4 mm thick aluminium wall which provided the main instrument structure; and (ii) the front detector module that housed the 24 SCD detectors and their associated drive electronics, radiation shielding and a cooling interface (copper cooling straps). A schematic diagram of the C1XS instrument is shown in Figure 2.3. A collimator stack (see section 2.2.1) containing aluminium filters was fixed in front of the detectors in order to define the instrument's 28° FOV (field of view) and block low energy photons and

electrons from reaching the detectors. The entire detector module was protected by a 5 mm thick aluminium door that also contained a radioactive ^{55}Fe calibration source for each detector.

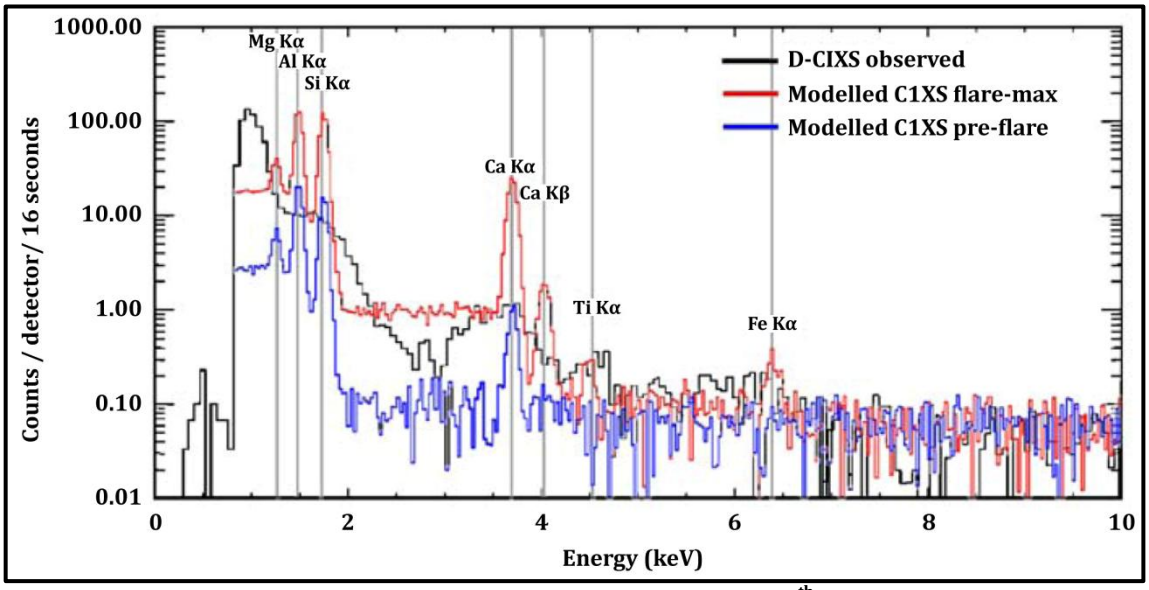

Figure 2.2. Comparison between a D-CIXS spectrum (obtained on 18th November 2005 over a mixed mare/highland region near Mare Cognitum) and the predicted C1XS performance for the same flare event. The C1XS energy resolution (FWHM = 110 eV) adopted was that obtained from the pre-flight calibration campaign (see section 2.3). The red spectrum shows the C1XS response at the peak of the M1 flare event; the blue spectrum is the response from the quiescent period before the flare. Even at the pre-flare level, the improved performance of C1XS means that the three low-energy lines of Mg, Al and Si are clearly resolvable, and at the M1 flare level both Ti and Fe are also detectable (from Crawford et al., 2009).

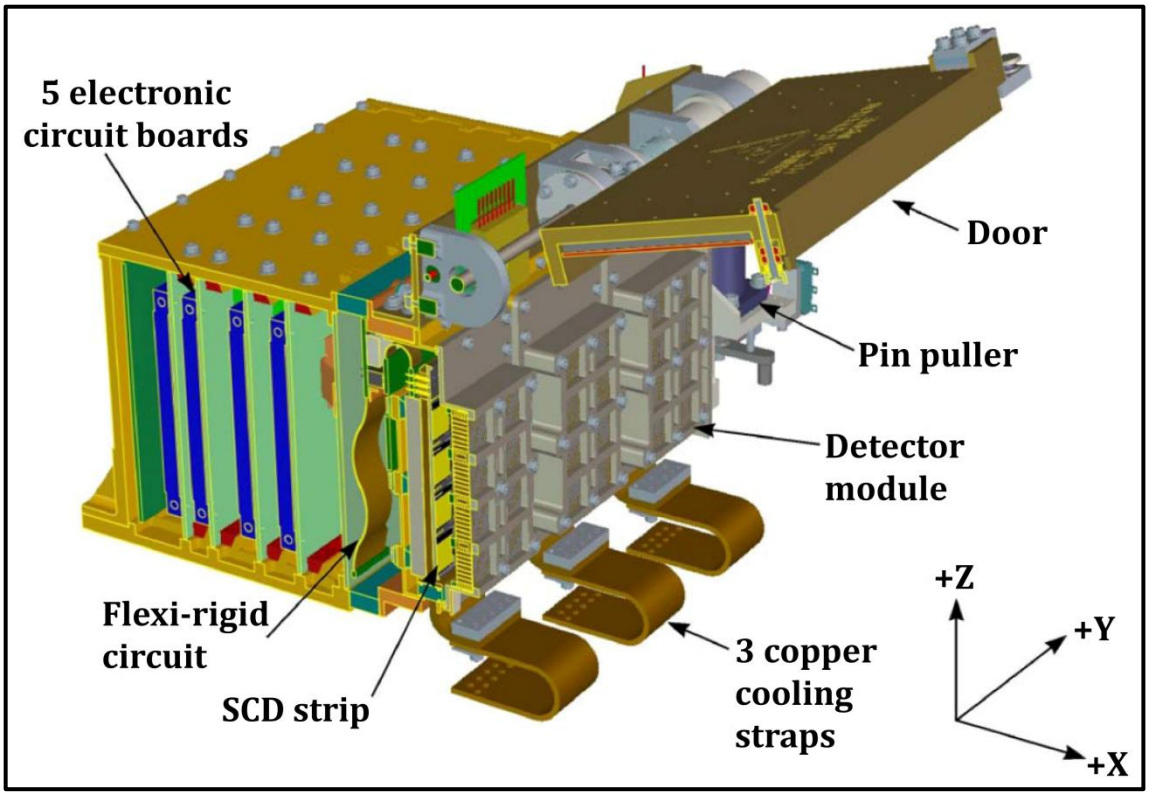

Figure 2.3. Schematic view of the C1XS instrument with one side cut away and major components labelled (from Howe et al., 2009).

2.2.1. *Collimators*

The collimator stack (Figure 2.4) consisted of six individual computerised numeric control (CNC) machined copper sheets with 1.5 mm^2 holes and a wall thickness of 0.15 mm. In order to limit the light and low-energy electrons that could potentially reach the SCDs and mimic X-ray signals, 0.2 µm thick aluminium foil sheets were mounted at the top and bottom of the collimator stack (two were used to lessen the likelihood of problems arising from micro-defects in one foil).

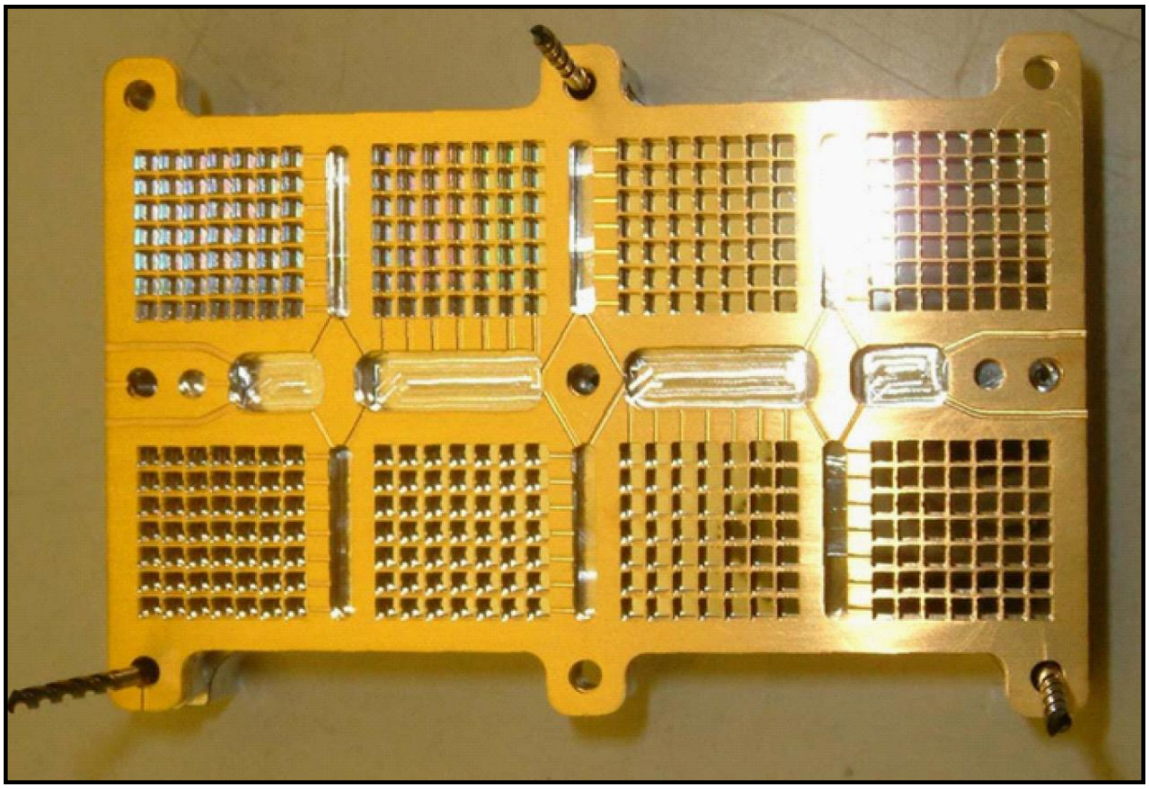

Figure 2.4. Photograph of a partially built gold-coated copper collimator stack for one module of detectors (from Howe et al., 2009).

2.2.2. *Swept charge devices (SCDs)*

C1XS employed an array of 24 swept charge device (SCD) detectors. These are a specific type of traditional CCD (charge coupled device) developed by e2v to allow rapid X-ray detection at elevated temperatures (Lowe et al., 2001). The devices (Figure 2.5) work by continuously 'sweeping' charge along three charge transport channels (clock lines) that run across the active detector area (~1 cm^2) to an output amplifier located at one corner (Lowe et al., 2001). The circuit following the amplifier uses correlated double sampling (CDS) to create a voltage that is fed to an analogue-to-digital converter (ADC), which in turn produces a 14-bit number equivalent to the energy of the X-ray event (Howe et al., 2009). Twelve detectors are read out using one 3D-Plus unit which houses the ADC and CDS circuits. The two 3D-Plus units are controlled using a field-programmable-gate-array (FPGA) that sequences the detector readout and digitisation so that valid X-ray events can be selected according to predetermined criteria involving two thresholds (Howe et al., 2009). The two event selection modes are as follows:

(i) ***multi-pixel mode***: up to five pixels are selected when the second one of them exceeds threshold 1 (see Figure 2.6).

(ii) ***single-pixel mode***: one pixel is selected when it is greater than threshold 1 and when the pixels immediately before and after it are both below threshold 2 (see Figure 2.6).

The FPGA thresholds could be adjusted when temperature fluctuations caused the detector offsets to change, so that the zero energy position would stay on the energy scale (Howe et al., 2009).

All the validated (selected) X-ray events were stored in a FIFO (first in, first out) system which was read by the C1XS microcontroller 32 times a second. This microprocessor unit time-stamped the data and converted it into readable output science and housekeeping (containing information concerning instrument temperatures, operation mode etc.) packets. The C1XS telemetry data format was dependent on the total instrument count rate; there were three possible formats:

(i) ***time-tagged three-pixel mode (type 10)***: when the rate was <320 events/sec the FPGA chose the multi-pixel data selection mode. This telemetry packet contained the event time and three energy values (for the event itself and the one immediately before and after).

(ii) ***time-tagged single pixel mode (type 11)***: when the rate was >320 events/sec the FPGA chose the single-pixel selection mode. This telemetry packet contained the event time and energy value.

(iii) ***high-resolution low-count spectral mode (type 12)***: when the rate was >800 events/sec the FPGA chose the single-pixel mode. This format was a 512-channel spectrum with variable bin widths (i.e. the 4096 detector readout channels were binned into 512 spectral channels) to maximise scientific return by giving more channels at low energies where the resolution is best, but still producing the maximum energy range; these spectra were generated every 8 seconds. Due to the low solar activity during the mission the count rate never reached the required level for this data type to be obtained.

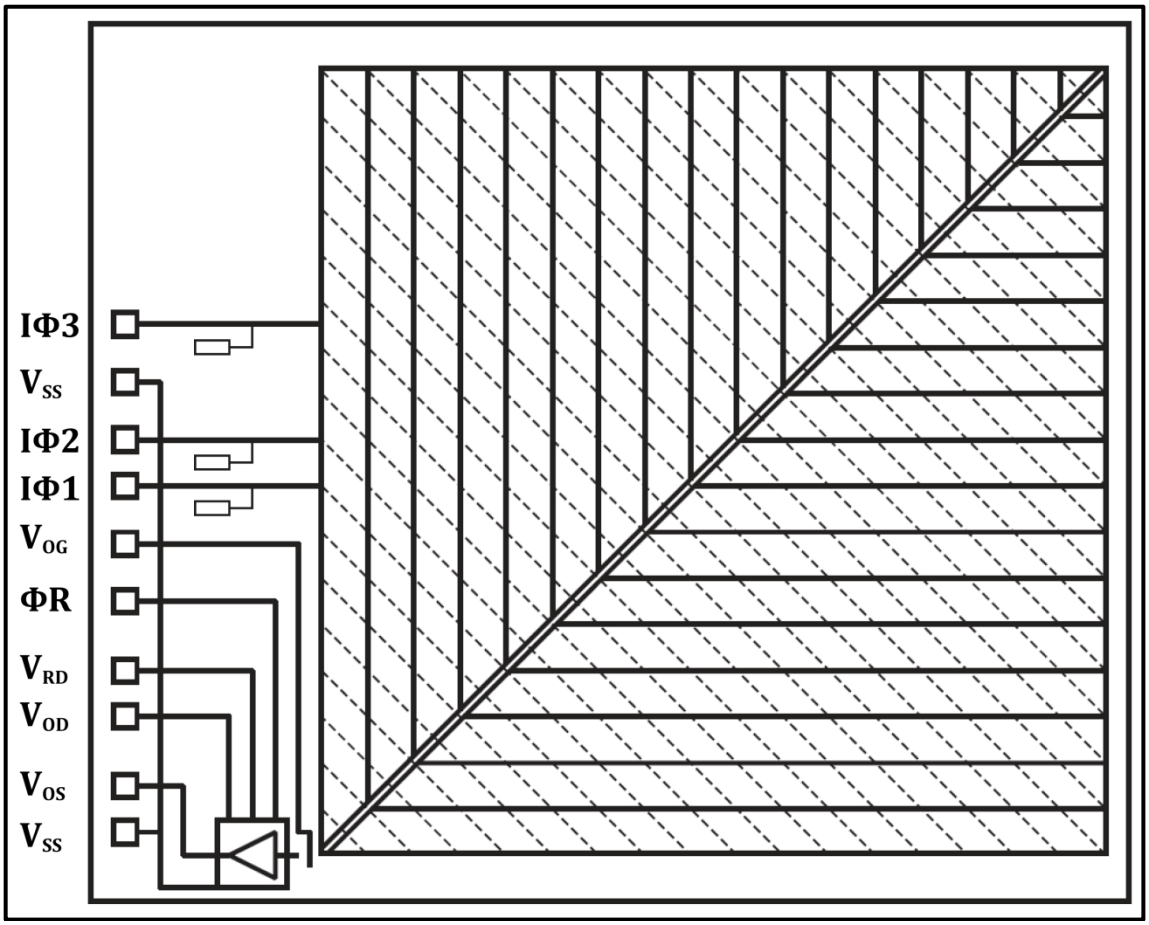

Figure 2.5. A schematic diagram of the internal structure of an SCD. Dashed lines represent the electrodes and solid lines indicate the charge transport channels. Charge on the detector is swept towards the central channels and towards the output amplifier at the bottom left corner by the action of the clock signals (adapted from Smith et al., 2007).

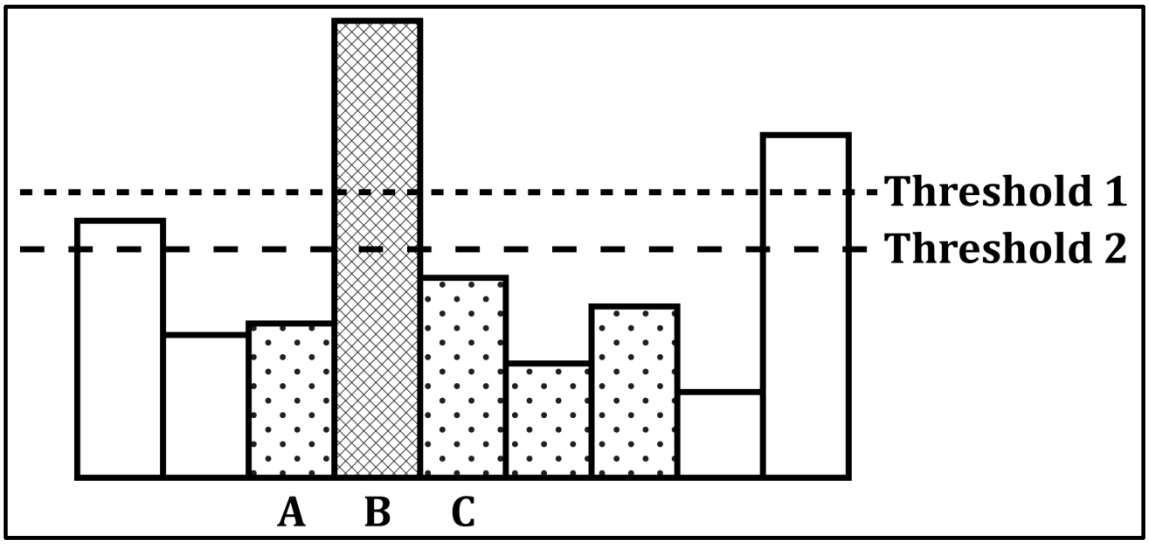

Figure 2.6. Cartoon illustrating the selection of C1XS pixel events. In 'single-pixel' mode an X-ray event is selected when a pixel (B) is greater than threshold 1, but the pixels immediately before (A) and after (C) it are both lower than threshold 2. In 'multi-pixel' mode, up to five pixels (dotted and hatched pixels) are selected when a pixel (B) is greater than threshold 1.

2.3. Instrument calibration

A full pre-mission flight-instrument calibration was conducted in the RESIK X-ray calibration facility (Figure 2.7 and Figure 2.8) at the Rutherford Appleton Laboratory (Narendranath et al., 2010). This facility was originally built to calibrate the ReSIK (Rentgenovsky Spektrometrs Izognutymi Kristalami) soft X-ray Bragg crystal spectrometer that flew onboard the Russian Koronas-F satellite (Lang et al., 1993). The facility provides a controlled X-ray beam, which is generated using a high-voltage electron gun with a choice of anode (e.g. Al, Mg, Mo, Ti, Cr, Co, Cu). The resultant spectrum consists of a bremsstrahlung continuum curve and superimposed characteristic lines between 1 and 10 keV. The X-rays pass through an evacuated beam line with a number of motorised control points (where various slits, pin-holes and a crystal monochromator can be employed to alter the shape and size of the X-ray beam as well as to isolate a specific X-ray line of interest in the 2 – 8 keV energy range) to the main (~1 m diameter) vacuum chamber (Figure 2.7 and Figure 2.8). Primary (i.e. C1XS) and secondary (i.e. Si-PIN diodes) detectors are placed on computer-controlled translation and rotation stages within the main vacuum chamber. The chamber also has remote temperature monitoring and control capabilities.

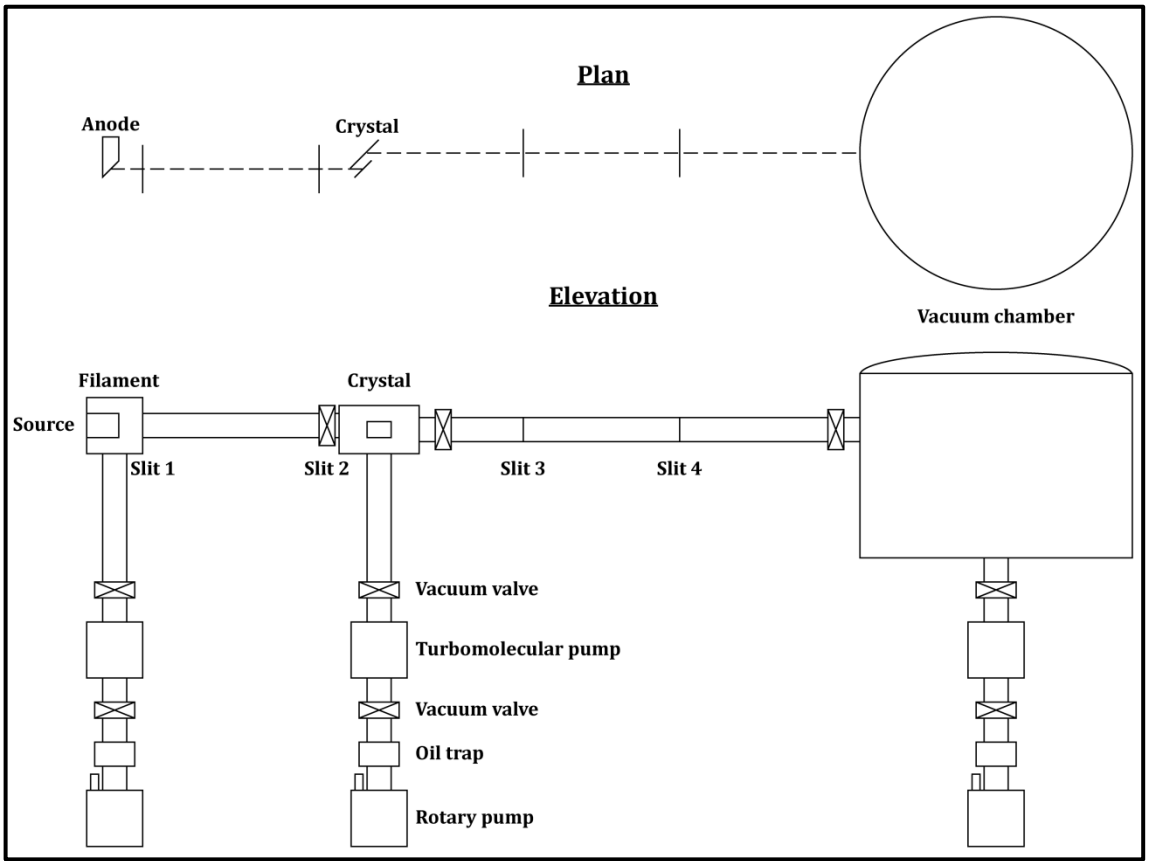

Figure 2.7. Schematic diagram of the RESIK X-ray facility beam line, showing the positions of key features (adapted from Lang et al., 1993).

The main purpose of the calibration campaign was to establish the detector characteristics and efficiencies, as well as the variation of these parameters with temperature. In order to calibrate the detectors and obtain their absolute efficiencies, a standard reference Si-PIN diode (Amptek XR100-CR) that had previously been calibrated at the beam-lines of the PTB/BESSY II synchrotron was employed. The efficiency of this Si-PIN diode has been calculated to better than 3% accuracy for energies between 1 and 10 keV (Narendranath et al., 2010).

Most of the RESIK calibration measurements were made in the *high-resolution low-count spectral mode* in anticipation of the mission's science data being obtained in this format; some measurements were also obtained in the other two *time-tagged* formats (see section 2.2.2). The calibration involved a number of separate procedures, including the determination of (for each detector):

(i) SCD energy resolution as a function of incident X-ray energy and temperature;

(ii) zero energy position and FWHM as functions of temperature; and

(iii) absolute detection efficiency.

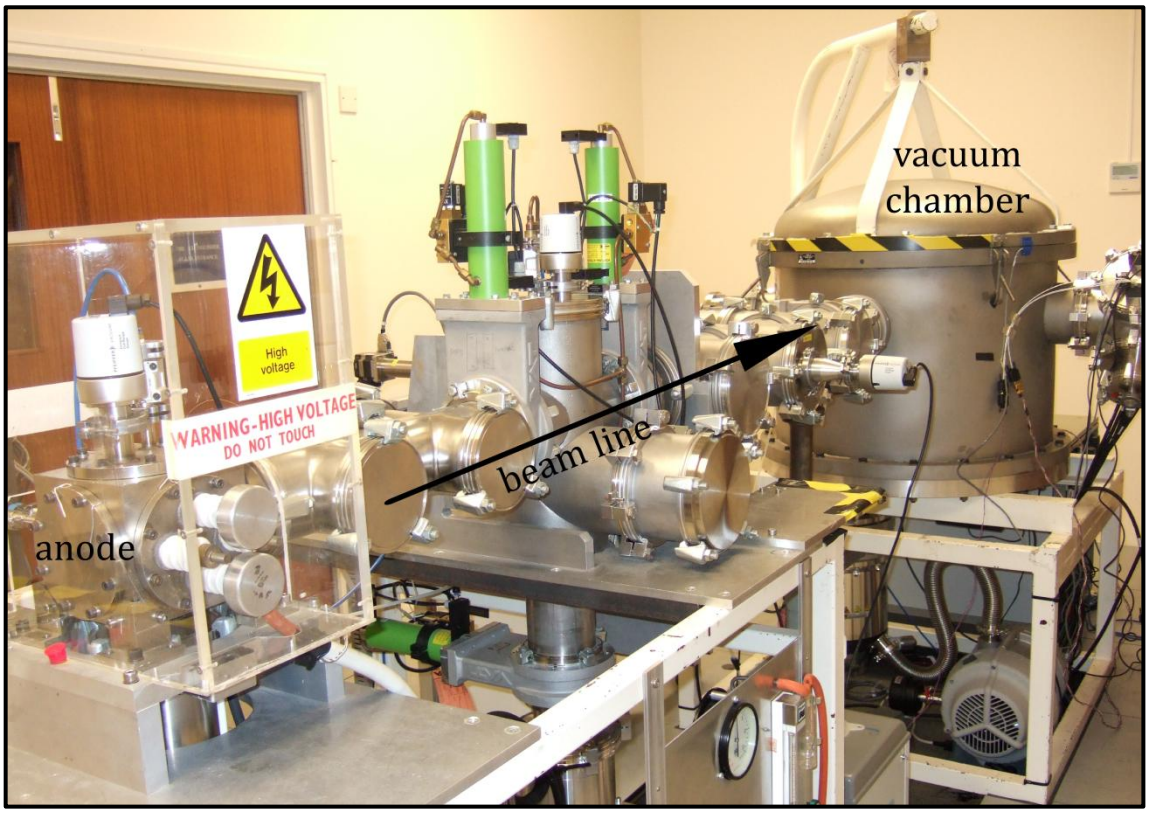

Figure 2.8. Photograph of the RESIK X-ray calibration facility at the Rutherford Appleton Laboratory, taken from close to the HV anode looking towards the main vacuum chamber (RAL).

The gain of each detector was determined from data obtained using the copper anode and the crystal monochromator in order to isolate the highest available calibration line (Cu K_α: 8.04 keV). Gain is calculated by first measuring the positions (channel number) of the Cu K_α line and the zero energy peak (zero voltage signal, whose position is temperature dependent), and then dividing the energy difference which separates them (i.e. 8.04 keV) by the equivalent number of channels. Figure 2.9a shows how the gain of each detector varies with temperature between about -30°C and about -5°C. All the detectors have a very small positive gradient except for detector 20, which has a very small negative gradient.

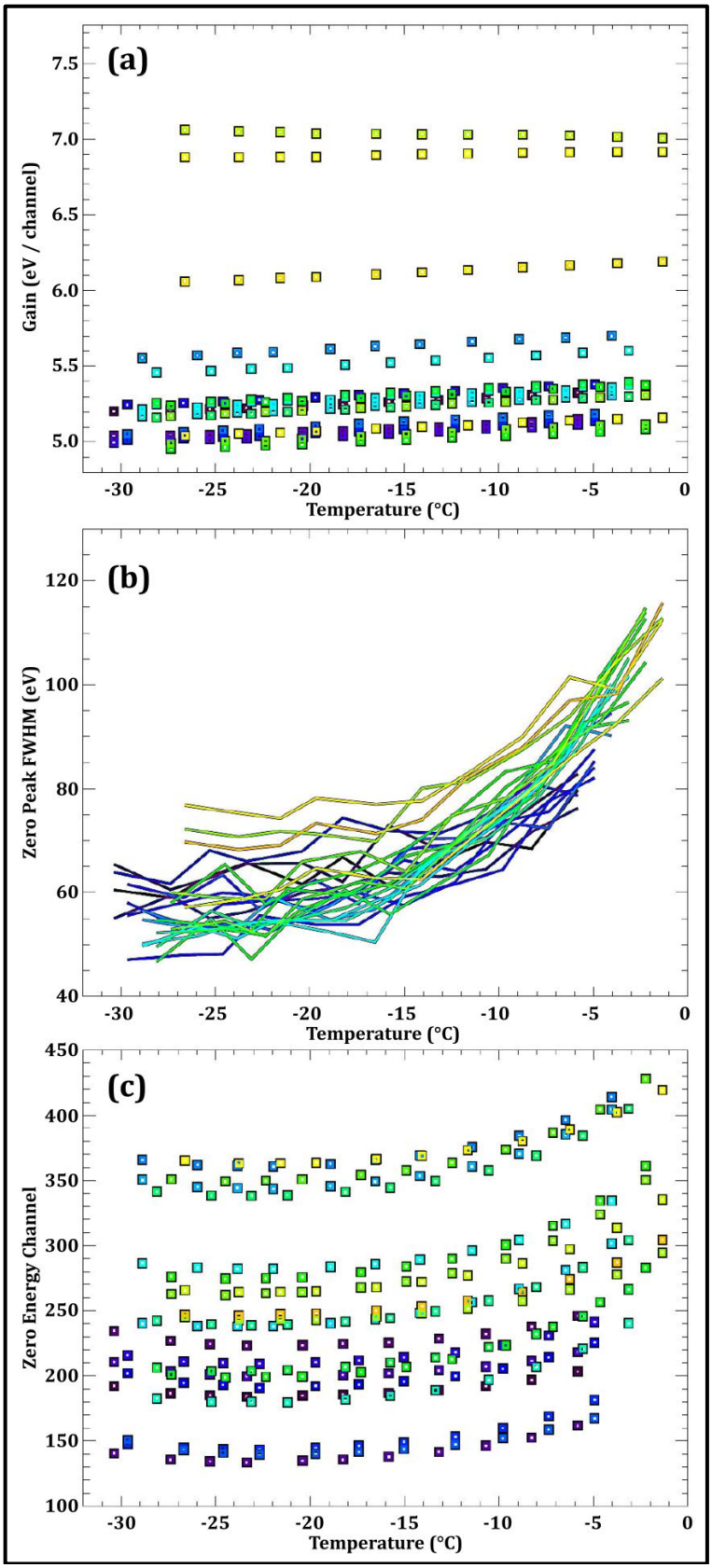

Figure 2.9. Graphs illustrating the (a) detector gain; (b) zero energy peak FWHM; and (c) zero energy peak centre channel position, as a function of temperature for all 24 SCD detectors on the C1XS flight instrument (adapted from Kellett, 2008).

Although the FWHM of each detector's zero energy peak varies as a function of temperature, the behaviour exhibited by all 24 SCDs is remarkably similar. Figure 2.9b illustrates that for all the detectors the FWHM increases with temperature, with a large increase in gradient at temperatures warmer than about -15°C. Based on this evidence, a nominal operating temperature for the C1XS instrument during flight was specified as -17.5°C. The position (channel) of the zero energy peak centre for each detector is shown in Figure 2.9c as a function of temperature. A specific offset was required to bring the zero energy peak onto the channel scale and this was applied to each detector individually. The data in Figure 2.9c were used to ensure that the zero energy peak did not subsequently drift off the scale as the gain increased with temperature.

The detector response to a beam of mono-energetic photons is characterised by the spectral redistribution function (SRF) which varies with temperature fluctuations. The detection efficiency of each SCD is required in order to accurately determine absolute X-ray line fluxes. The spectral response of each detector can be represented as a two-dimensional matrix where each element is the probability that a photon with a certain energy is registered in a specific channel (Narendranath et al., 2010). The absolute detection efficiency of each SCD was calculated and derived with a nominal uncertainty of 4.6% (Narendranath et al., 2010).

2.3.1. *In-flight calibration*

Additional in-flight calibrations of the detectors were conducted when the instrument door was closed and the spectrum from the radioactive ^{55}Fe sources (one for each detector) contained within it could be measured. The radiation sources were covered by a thin Ti foil and thus the resultant spectrum provided four calibration lines: Ti K_α (4.5 keV), Ti K_β (4.9 keV), Mn K_α (5.9 keV) and Mn K_β (6.5 keV). It had also been planned for an observation of a well-known and calibrated astronomical X-ray source, such as the Crab nebula, to be conducted. However, the premature end of the mission meant that this was never achieved, although a long integration of the X-ray background was obtained. Crab observations made by D-CIXS (Grande et al., 2007; Swinyard et al., 2009) were compared to the laboratory-derived C1XS detector efficiencies as a method of verification.

2.4. Dataset

C1XS commissioning was completed on November 23rd 2008; from this point until the mission end, data from a total of thirty-one solar flare events were obtained. This number was smaller than predicted because of the unusually quiet solar conditions (e.g. Russell et al., 2010) of the prolonged solar minimum. Of these, only two were at, or above, the intensity which the instrument was designed to detect (i.e. C-class flares: $10^{-6} – 10^{-5}$ Wm^{-2}). However, due to the excellent performance of the instrument, data from lower magnitude A- ($10^{-8} – 10^{-7}$ Wm^{-2}) and B- ($10^{-7} – 10^{-6}$ Wm^{-2}) class flares were also obtained. The footprint on the lunar surface of the data from these flares is elongated from the nominal 25 km (or 50 km from the raised 200 km orbit) because longer integration times are required to obtain significant and scientifically useful signal to noise ratios. Many background (of quiet sky, no X-ray events) spectra were obtained throughout the mission and the shape of the background spectrum has been found to be generally stable, except at certain times of the month when the Moon is inside of the Earth's magnetotail. The background therefore needs to be subtracted from the lunar spectrum for each flare individually. All the flare events are listed in Table 2.1 and their ground tracks (boresight position) are shown in Figure 2.10. In chapter 4 the analysis of an A-class flare (no. 1 in Table 2.1) and a B-class flare (no. 4 in Table 2.1), whose footprints run through Mare Serenitatis and Oceanus Procellarum respectively, is conducted and discussed.

Table 2.1. List of solar X-ray flare events from which C1XS observed lunar XRF, with their dates, times, lunar boresight reference point and the phase angle.

		Start				End			
Flare No.	Date	UT (hh:mm:ss)	Boresight latitude (°)	Boresight longitude (°)	Phase angle (°)	UT (hh:mm:ss)	Boresight latitude (°)	Boresight longitude (°)	Phase angle (°)
1	12/12/2008	02:27:00	44.2	14.0	45.2	02:39:00	8.1	12.9	9.6
2	10/01/2009	15:55:30	8.4	-17.3	26.3	16:09:00	-32.8	-18.2	40.0
3	11/01/2009	01:45:00	10.7	-22.7	27.5	01:59:00	-32.1	-23.6	39.8
4	10/02/2009	23:06:00	71.1	-69.2	79.1	23:27:00	7.4	-69.6	56.6
5	12/02/2009	16:21:00	84.5	-92.7	86.2	16:48:00	3.1	-92.3	58.1
6	03/07/2009	23:07:54	-59.1	27.2	58.6	23:12:00	-47.3	26.9	47.6
7	04/07/2009	01:10:18	-74.4	27.0	73.1	01:26:58	-26.5	25.4	29.1
8	04/07/2009	03:25:56	-51.6	24.7	51.4	03:34:36	-26.8	23.6	29.3
9	04/07/2009	05:32:56	-53.7	22.9	53.2	05:42:04	-27.5	23.1	29.7
10	04/07/2009	07:42:32	-48.3	22.3	48.0	07:50:10	-26.4	21.9	28.8
11	04/07/2009	09:43:48	-66.8	21.9	65.2	09:57:40	-27.1	20.8	29.2
12	04/07/2009	11:51:36	-66.6	20.7	64.9	12:06:00	-25.3	19.6	27.7
13	04/07/2009	13:53:32	-82.8	23.4	83.7	14:12:32	-28.4	18.5	33.1
14	04/07/2009	16:14:24	-45.1	17.9	48.0	16:20:48	-26.8	17.3	31.8
15	04/07/2009	20:20:24	-72.1	16.8	73.4	20:35:36	-28.6	15.0	33.4
16	04/07/2009	22:28:54	-69.8	15.3	71.2	22:43:52	-27.0	13.8	32.1
17	05/07/2009	02:44:36	-69.0	13.4	70.5	02:58:40	-28.8	11.6	33.6
18	05/07/2009	04:51:06	-72.5	12.7	73.7	05:07:38	-25.3	10.4	30.7
19	05/07/2009	07:00:28	-67.8	11.0	69.3	07:15:28	-24.9	9.2	30.5
20	05/07/2009	09:15:04	-48.2	8.6	50.9	09:23:02	-25.4	8.1	30.9
21	05/07/2009	11:10:36	-83.0	13.4	83.6	11:31:08	-24.4	6.9	29.9
22	05/07/2009	13:24:40	-64.9	7.2	66.6	13:39:12	-23.4	5.7	29.5
23	05/07/2009	15:41:04	-40.1	4.9	43.7	15:47:16	-22.4	4.5	28.7
24	06/07/2009	00:03:24	-64.6	1.7	66.3	00:17:42	-23.8	0.0	29.9
25	06/07/2009	02:15:50	-51.2	-0.3	53.8	02:25:30	-23.6	-1.1	29.8

		Start				End			
Flare No.	**Date**	**UT (hh:mm:ss)**	**Boresight latitude (°)**	**Boresight longitude (°)**	**Phase angle (°)**	**UT (hh:mm:ss)**	**Boresight latitude (°)**	**Boresight longitude (°)**	**Phase angle (°)**
26	06/07/2009	04:23:30	-51.4	-1.5	54.0	04:32:12	-26.6	-2.2	32.1
27	06/07/2009	06:32:16	-48.5	-2.7	51.2	06:40:26	-25.2	-3.4	31.0
28	06/07/2009	08:37:18	-56.2	-3.5	58.3	08:47:12	-28.0	-4.5	33.3
29	06/07/2009	12:57:08	-43.8	-6.4	46.9	13:03:54	-24.5	-6.9	30.5
30	06/07/2009	15:00:24	-56.5	-7.0	58.6	15:10:04	-28.9	-7.9	34.1
31	06/07/2009	17:04:00	-68.3	-7.1	69.6	17:19:40	-23.6	-9.2	29.9

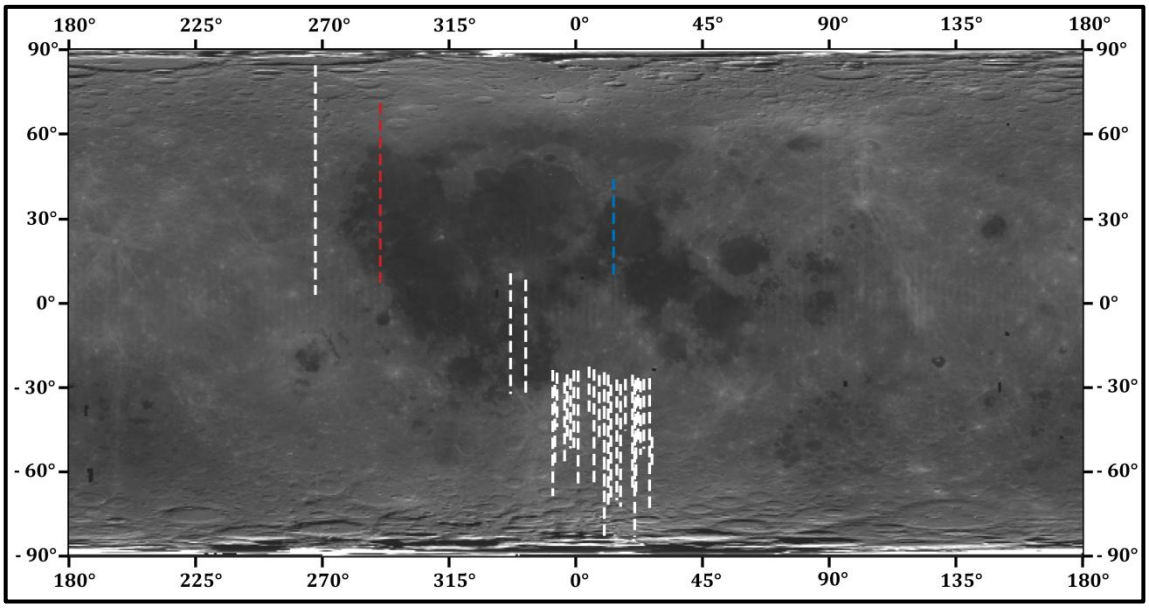

Figure 2.10. Clementine 750 nm basemap of the Moon with the C1XS flare event ground tracks (boresight position) shown. The blue and red tracks show the two flares running through Mare Serenitatis and Oceanus Procellarum respectively, which are analysed in chapter 4.

2.5. Data processing

C1XS data processing in this thesis is achieved via a set of IDL (Interactive Data Language) routines (written by B. Kellett at RAL) which (i) read the original data files and create separate files pertaining to detector parameters, housekeeping information and the spectral data, (ii) use calibration data to produce energy calibrated files and (iii) subtract a time-specific, modelled X-ray background in order to produce a final spectrum to be used in a fitting algorithm that gives elemental abundance estimates (see section 2.5.1). These routines are described fully in section 4.2.1.

2.5.1. *RAL abundance algorithm*

The scientific analysis of all planetary XRF datasets requires an algorithm that converts X-ray fluxes to elemental abundances and ratios, in order to make geological interpretations about the target body. One such code, used for the analysis of C1XS data has been developed at RAL by Bruce Swinyard and is known as the *RAL abundance algorithm* (Swinyard et al., 2009; 2010; Weider et al., in review). This model analyses XRF spectra in order to obtain elemental abundances following the fundamental parameters approach

(e.g. He & Van Espen, 1991) and particularly the formulation given in Clark and Trombka (1997), as this is the most relevant approach for the analysis of unknown materials using broad band illuminating X-ray sources rather than the monochromatic sources commonly used in laboratory XRF studies. The algorithm methodology is described fully in Swinyard et al. (2010) and Weider et al. (in review) and is outlined here:

(i) A model input spectrum is generated, based on that which has been measured (e.g. by XSM).
(ii) The efficiency of the X-ray spectrometer as a function of energy is required.
(iii) A primary model spectrum is generated using an arbitrary initial target (rock) composition.
(iv) The modelled spectrum created in step (iii) is normalised to the XRF data using the total counts within the Si K_α peak. This step utilises the fact that for most lunar soils and regolith breccias (e.g. consolidated soils), the Si concentration lies within a narrow range of 18 – 23 elemental wt. % (e.g. Rhodes & Blanchard, 1981; Fruland, 1983; Morris et al., 1983; Simon et al., 1985; McKay et al., 1986; 1989; Jerde et al., 1987; 1990); the Si concentration in the model can therefore be fixed and all other elemental abundances are assessed against it.
(v) For each elemental line observed in the XRF spectrum, the spectrum is regenerated so that the abundance of the specific element is varied, while keeping all others fixed. Each new spectrum is normalised to the Si K_α peak.
(vi) The best fit abundance for the element under test is chosen when the χ^2 value between the data and the model in a region around the line is at a minimum.
(vii) Each elemental line is tested in turn, starting with the highest energy lines. The fixed compositions are updated with the best fit abundances each time.
(viii) When all lines have been tested, the new values are used as the fixed test composition (i.e. initial starting composition) and the procedure is repeated until the abundances show no significant variation between runs; this usually takes two complete iterations.

Chapter 3 describes laboratory experiments on planetary analogue samples which are used to test the accuracy of this algorithm; in chapter 4 the algorithm is employed to analyse an

A-class and a B-class flare, whose footprints run through Mare Serenitatis and Oceanus Procellarum respectively (see Figure 2.10).

2.6. Summary

C1XS was a compact XRF spectrometer payload on Chandrayaan-1, which orbited the Moon for 10 months. Although limited in size by the lack of solar activity during the mission, the C1XS dataset, which includes flare intervals of a lower intensity than from which the instrument was designed to obtain data, proves the high capability of the instrument and the success of its design. Experiments to support the development of the modelling code which is used to convert X-ray line fluxes to elemental abundance ratios are described in chapter 3 and data from two flare periods are analysed in chapter 4.

Chapter 3: Planetary XRF analogue laboratory experiments[2]

3.1. Introduction

The RAL abundance algorithm (Swinyard et al., 2009; 2010; Weider et al., in review), described in section 2.5.1, is designed to convert C1XS (or other planetary) X-ray flux data into elemental ratios and abundances, for use in making geological interpretations about the target body. The model adopts the fundamental parameters approach (He & Van Espen, 1991; Clark & Trombka, 1997) that was informed by the results from materials science studies (e.g. Claisse & Samson, 1962; Berry et al., 1969; Hawthorne & Gardner, 1978) that focused on characterising the XRF emission from a homogeneous surface, using an energetic, monochromatic X-ray illuminating source. The reality for planetary XRF experiments however, differs strongly from such an ideal situation; for example:

(i) regoliths (layers of broken, melted, altered and compositionally heterogeneous debris; McKay et al., 1991) typically cover the surface of airless bodies such as the Moon and Mercury.

(ii) the solar X-ray source is highly variable and polychromatic.

(iii) the viewing geometry constantly changes as the satellite orbits the planet and the planet orbits the Sun.

It is therefore necessary to characterise how the XRF flux from a planetary regolith varies with factors such as solar incidence angle, spacecraft viewing geometry, surface roughness and porosity, as well as rapid changes in the incident solar X-ray spectrum, in order to obtain accurate absolute abundance estimates (Joy et al., 2010).

Recently, a number of planetary XRF analogue laboratory studies have been conducted in order to constrain how the XRF emission from geological samples, using a soft polychromatic source of X-rays varies with viewing geometry and target surface characteristics (e.g. Maruyama et al., 2008; Näränen et al., 2008; 2009; Owens et al., 2008). In the past, the geologically meaningful end-product of planetary XRF data has been abundance ratios of the measured elements, rather than absolute elemental abundances (e.g.

[2] This chapter has been submitted as a paper to *Planetary and Space Science* (October 2010).

Andre et al., 1977), and it was believed that such normalisations negated inaccuracies caused by the so called *regolith effects*. However, with the improvements in both spatial and spectral resolution of the new generation of solid-state detector planetary XRF instruments, this issue has been revisited based on recent findings. It has been reported that XRF line intensities increase with (i) decreasing grain-size and that this trend is greater at lower energy (Maruyama et al., 2008) and (ii) with increasing incidence angle and that this trend is greater at higher energy (Näränen et al., 2008; 2009).

3.1.1. *Aim of the experiments*

The aim of the experimental campaigns described in this chapter was to build upon the previous studies by creating a simple laboratory simulation of a planetary XRF mission. The main objective was to measure how the XRF intensity from a number of lunar regolith analogue samples varies with grain-size and phase angle (and the dependence on energy). Grain-size variation of the samples simulates the variable physical characteristics of the lunar (or other planetary) regolith. Changing the phase angle replicates the variation in the viewing geometry of an XRF instrument as it orbits a planetary body. The data obtained are primarily used to provide accurate laboratory test data for verifying the RAL abundance algorithm (Weider et al., in review; section 3.5), but can also be used to inform other XRF modelling codes.

3.1.2. *Experimental campaigns: Brunel & RESIK*

For the study described in this chapter, two sets of experiments were conducted using separate laboratories, apparatus and samples. In the Brunel University (preliminary) experiments (section 3.2.1) a module of SCD detectors was employed as the X-ray detection device. These detectors provide better spectral resolution than the Si-PIN diode used in the later, more extensive RESIK campaign conducted at RAL (section 3.2.2). Employment of the SCDS provided a more faithful laboratory test of the C1XS detectors and electronics. However, the inability to vary incidence and emergence angles independently in the Brunel configuration meant that the dependence of XRF on phase

angle could only be investigated in the RESIK experiments[3]. In this chapter, first the methods of both campaigns are discussed before the results and a synthesised discussion and comparison with results from previous studies are given. Results from modelling of lunar regolith simulant data with the RAL abundance algorithm are also presented (section 3.5).

3.2. Methods

3.2.1. *Brunel experiments*

Apparatus

The first set of experiments were conducted at Brunel University in the Centre for Sensors and Instrumentation, in the School of Engineering and Design (and the e2v centre for electronic imaging, which has since relocated to the Open University), using the same equipment as employed in the radiation study that assessed the effectiveness of the C1XS flight detectors (Smith & Gow, 2009). The Brunel apparatus consisted of a desktop vacuum chamber (Figure 3.1) attached to an Oxford Instruments X-ray tube with a tungsten source, which provided the incident X-ray beam for the measurements. The incident X-rays were collimated through a steel tube, with an 8 mm diameter aperture. This collimator extended to a distance 11.5 mm away from the octagonal target wheel, upon which the samples were placed. The module of four e2v CCD54 SCD detectors was mounted on a shapal (aluminium nitride ceramic) cold finger attached to a thermo-electric cooler. This allowed the detectors to be operated at low temperatures (-10°C to -50°C). The module was housed in a camera-head attached to the front flange of the vacuum chamber with just one (central) detector used for the measurements. The XRF measurements were conducted with a current of 0.2 mA (and a 10 kV voltage) applied to the tungsten X-ray tube, for a standard integration time of 50 seconds (although many measurements were made with longer integration times of 5, 10 or 15 minutes). A standard

[3] Incidence angle is defined as the angle between the normal to the sample's surface and the incoming X-ray beam; emergence angle is defined as the angle between the normal to the sample's surface and the XRF measured by the detector; phase angle is defined as the angle between the incident and emergent X-ray beams.

90° phase angle geometry (incidence and emergence angles both 45°) was used for all the measurements.

Samples

The samples used in the Brunel experiments were made from four different terrestrial rocks and were chosen to represent possible lunar lithologies:

(i) **Icelandite**: a fine-grained iron-rich, aluminium-poor andesite

(ii) **Etna basalt**: a basalt consisting of a fine-grained matrix and small (~1 mm) pyroxene and plagioclase phenocrysts.

(iii) **Peridotite**: a mantle xenolith rich in olivine and with accessory spinel and pyroxene; thus rich in magnesium and iron, but silica-poor.

(iv) **Lunar regolith simulant (JSC-1A)**: a powdered basaltic mare regolith simulant developed by NASA (McKay et al., 1994; Rickman, 2007).

Although pressed pellets are the standard sample preparation method for laboratory XRF experiments, preparing samples in this way does not accurately preserve the surface roughness and loose powder characteristics of planetary regoliths (Näränen et al. 2008). Thus, a novel approach to sample preparation was employed in this study in an attempt to preserve the surface roughness and porosity of samples. The three hand specimens (icelandite, Etna basalt and peridotite) were crushed and then sieved into different grain-size fractions. Four 'glass-slide' samples (layers of glue mixed with rock powder on a standard thin section glass-slide) were then made for each of these rocks, from powders with the following grain-size fractions: (i) 250 μm to 500 μm, (ii) 125 μm to 250 μm, (iii) 75 μm to 125 μm and (iv) <75 μm (e.g. those shown in Figure 3.2). In addition, smooth, polished thick section samples (~2 cm × 4 cm with a thickness of ≥0.5 mm) of icelandite, Etna basalt and peridotite were made (Figure 3.3). JSC-1A was prepared as an unsieved pressed pellet shown in Figure 3.2f (a thick section of this cannot be made because it exists only as a powder). The bulk composition of these samples (Table 3.1) was measured (by K.H. Joy and S. James) at the Natural History Museum, London using ICP-AES (inductively coupled plasma atomic emission spectroscopy) following the techniques described by Joy et al. (2008).

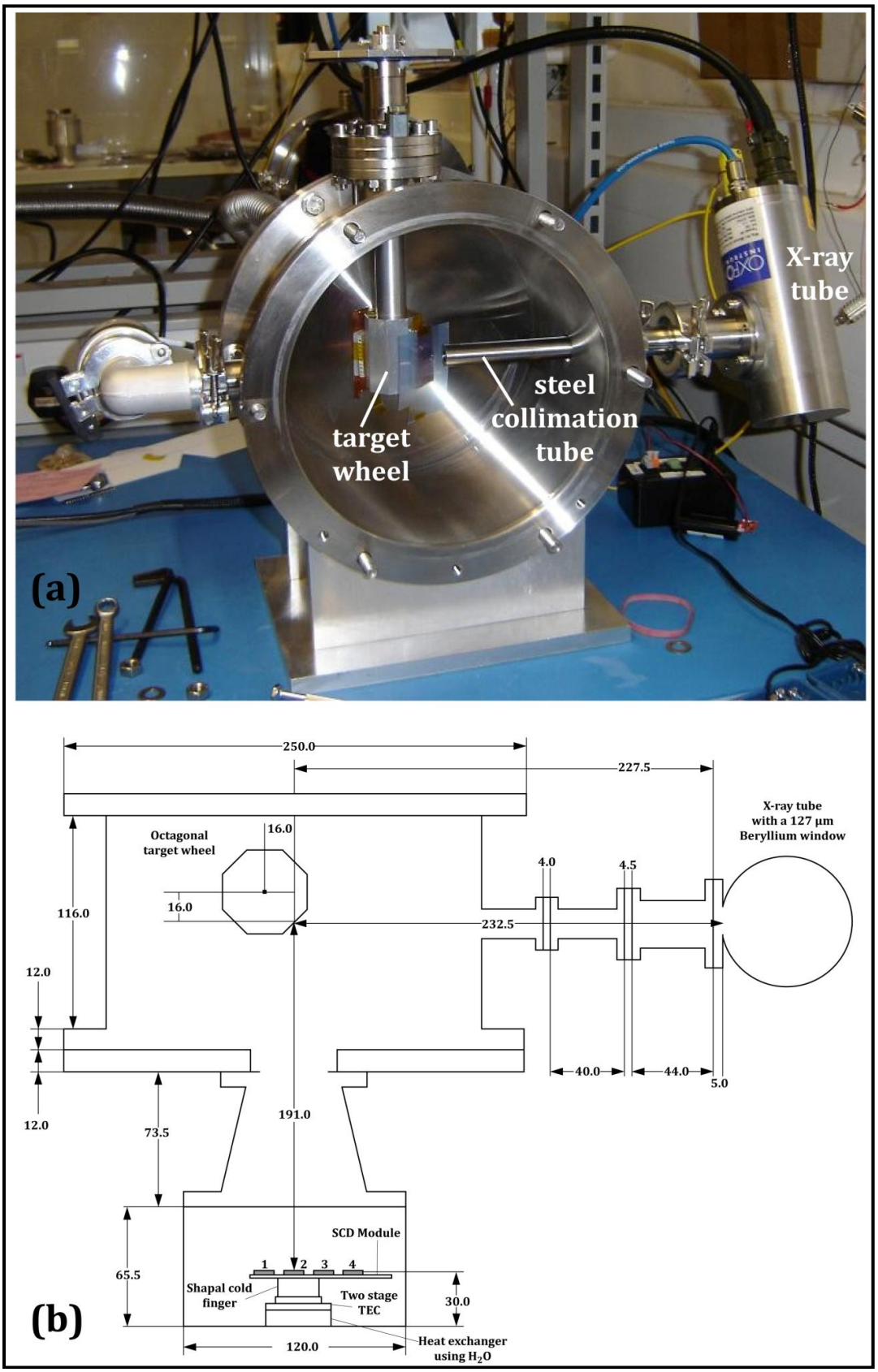

Figure 3.1. The desktop vacuum chamber used in the Brunel experiments: (a) shows the chamber with the open face missing the detector-holding camera-head (courtesy of J. Gow); (b) shows the dimensions (in mm) involved in the apparatus.

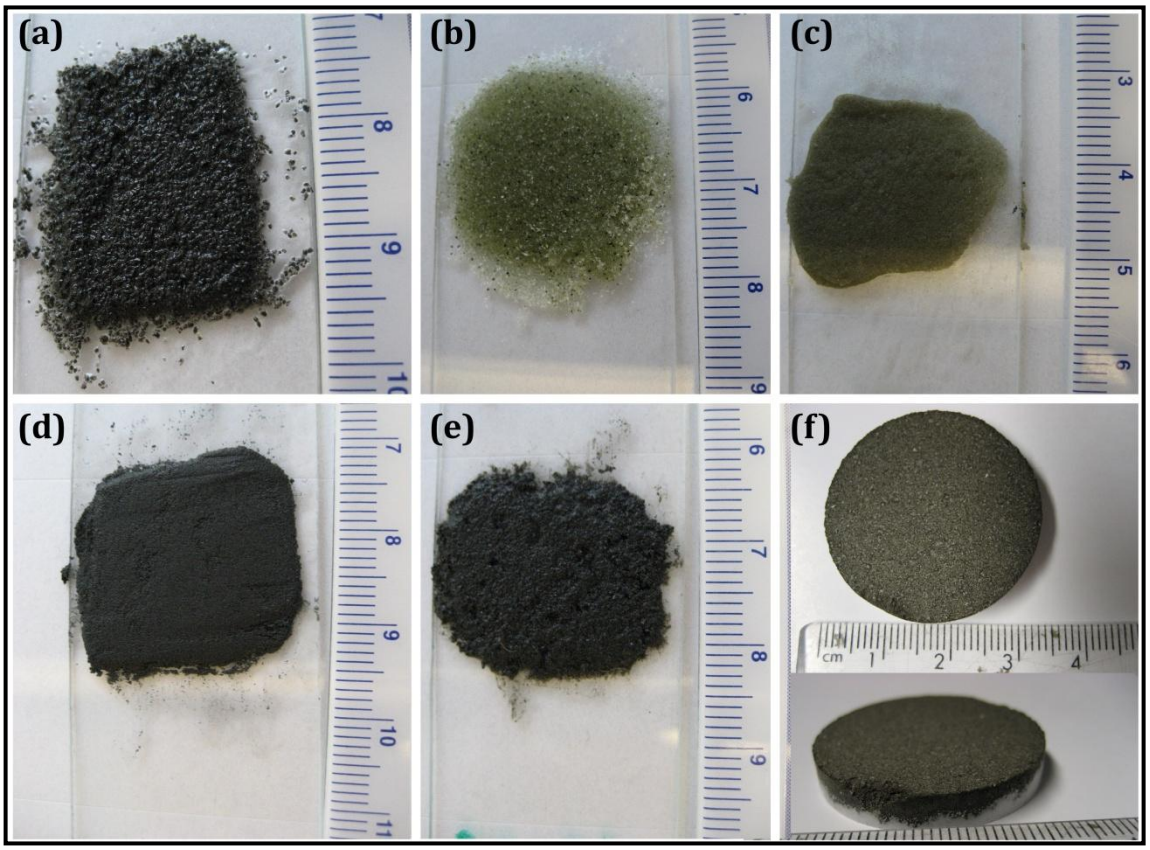

Figure 3.2. Photographs of a selection of the Brunel glass-slide samples: (a) Etna basalt, 250 – 500 µm; (b) peridotite, 125 – 500 µm; (c) peridotite, <75 µm; (d) Icelandite, 75 – 125 µm; (e) JSC-1A, unsieved; and (f) the JSC-1A pressed pellet sample.

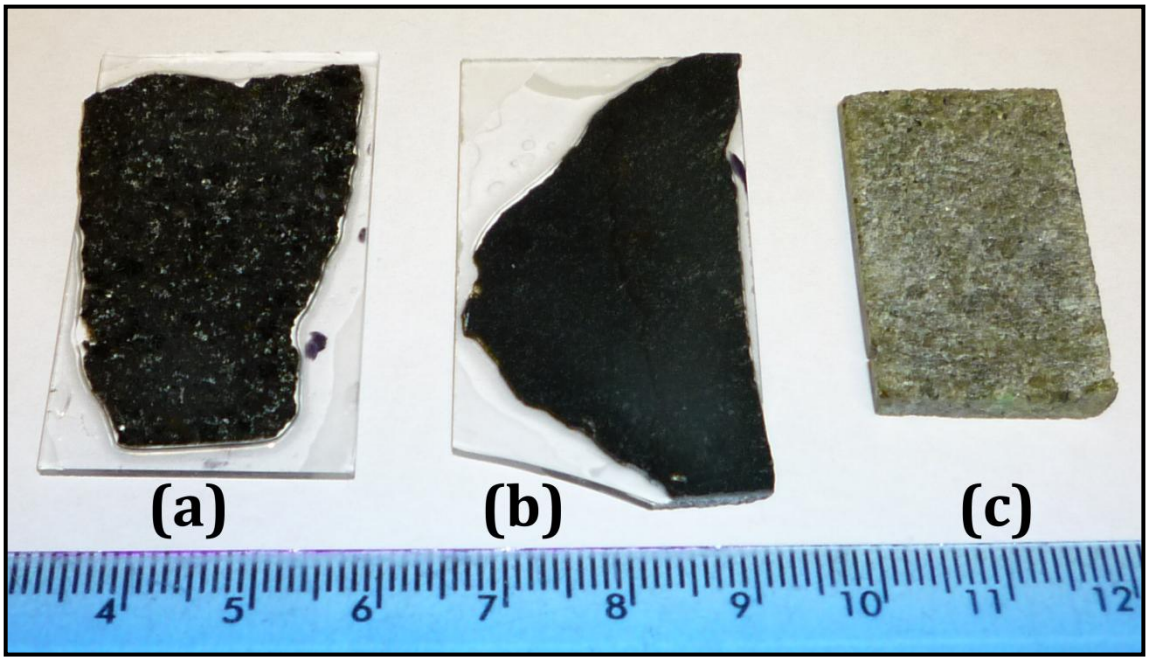

Figure 3.3. Photograph of the Brunel thick section samples: (a) Etna basalt, (b) icelandite and (c) peridotite.

Table 3.1. ICP-AES (inductively coupled atomic emission spectrometry) bulk composition data (oxide wt. %) for the four lithologies used as samples in the Brunel experiments (data obtained at the Natural History Museum, London following the techniques described by Joy et al., 2008). Errors are 1 σ based on repeat analyses.

Major & minor components (%)	Rock sample			
	Etna Basalt	**Icelandite**	**Peridotite**	**JSC-1A**
SiO_2	48.4 ± 0.36	50.00 ± 0.14	44.40 ± 0.13	46.00 ± 0.45
TiO_2	1.68 ± 0.01	2.79 ± 0.02	0.017 ± 0.001	1.76 ± 0.02
Al_2O_3	17.4 ± 0.10	13.70 ± 0.09	1.05 ± 0.01	16.30 ± 0.09
Cr_2O_3	0.005 ± 0.001	0.005 ± 0.001	0.542 ± 0.001	0.018 ± 0.001
Fe_2O_3	10.70 ± 0.09	16.20 ± 0.14	8.13 ± 0.06	12.20 ± 0.11
MnO	0.177 ± 0.001	0.252 0.001	0.121 ± 0.001	0.183 ± 0.001
MgO	5.30 ± 0.03	5.13 ± 0.08	44.70 ± 0.21	8.45 ± 0.03
CaO	10.30 ± 0.05	9.66 ± 0.05	0.634 ± 0.001	9.67 ± 0.05
Na_2O	4.07 ± 0.01	2.82 ± 0.01	0.10 ± 0.01	3.24± 0.03
K_2O	2.06 ± 0.02	0.603 ± 0.001	0.023 ± 0.001	0.81 ± 0.01
P_2O_5	0.697 ± 0.001	0.358 ± 0.001	0.023 ± 0.001	0.728 ± 0.001
Total	100.70	101.48	99.72	99.40

3.2.2. *RESIK experiments*

RESIK facility

The second experimental XRF campaign was conducted in the RESIK X-ray calibration facility (Lang et al., 1993) at RAL (described in section 2.3) that was also used for the pre-flight calibration of C1XS (Narendranath et al., 2010). In these experiments, a copper anode was used to create the incident X-ray beam with a current of 5 mA and a voltage of 20 kV (alternative current and voltage settings were used for a specific, long integration measurement whose results were used to test the RAL abundance algorithm; see section 3.5)

Detectors

Figure 3.4 shows a schematic diagram and photograph of the interior of the main vacuum chamber and the apparatus employed in the RESIK experiments. Two Si-PIN diode detectors were used: PIN 1 (previously calibrated at the PTB/BESSY II synchrotron, see section 2.3) as the XRF detector located on the DUT (device under test) stage and PIN 3 (PIN 2 was not utilised in the experiments), on the PIN stage, faced down the incoming beam and measured the incident X-ray spectrum at regular intervals during the

experiments. PIN 1 was placed on a 15° wedge (Figure 3.5) so that it did not impede the incident X-ray beam from illuminating the sample at small incidence angles. Both PIN diodes have an opening angle of ±71°, however so that only a small solid angle of XRF from the sample was detected, PIN 1 was fitted with a copper collimator (Figure 3.6a) which limited its opening angle to ±9°, translating to a field of view (FOV) of 1150 mm^2 on the face of the sample. In addition, PIN 3 was fitted with a 1.020 ± 0.005 mm diameter pin hole, with an opening angle of ±20° (Figure 3.6b), in order to limit its detection area, and allow the incident X-ray beam to be measured directly when a current of 5 mA (used for the measurements and required to ensure reasonably high count rates and short integration times) was employed, without saturation of the detector.

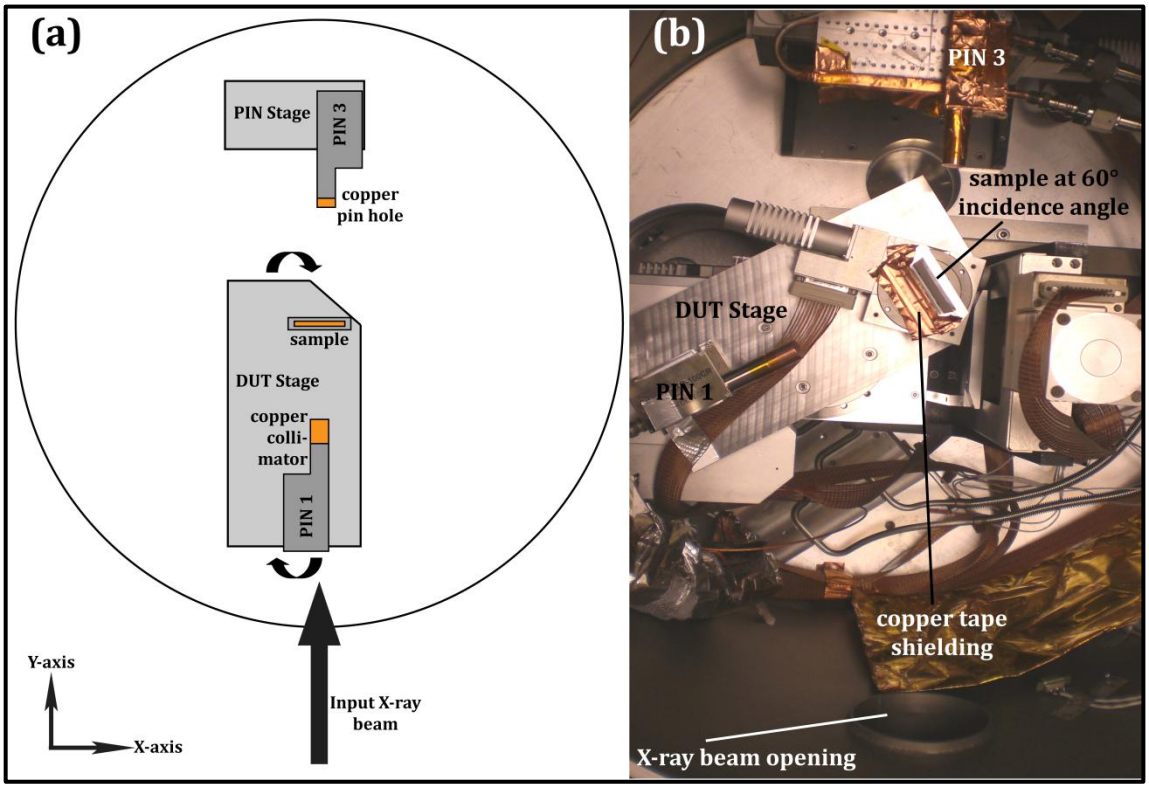

Figure 3.4. (a) Simplified diagram of the major components within the main RESIK vacuum chamber. Both the PIN stage and the rotatable DUT stage are shown, as well as the positions of the two X-ray detectors and the vertically mounted sample. (b) Photograph of the chamber, with the DUT stage rotated so that the sample is at an incidence angle of 60°.

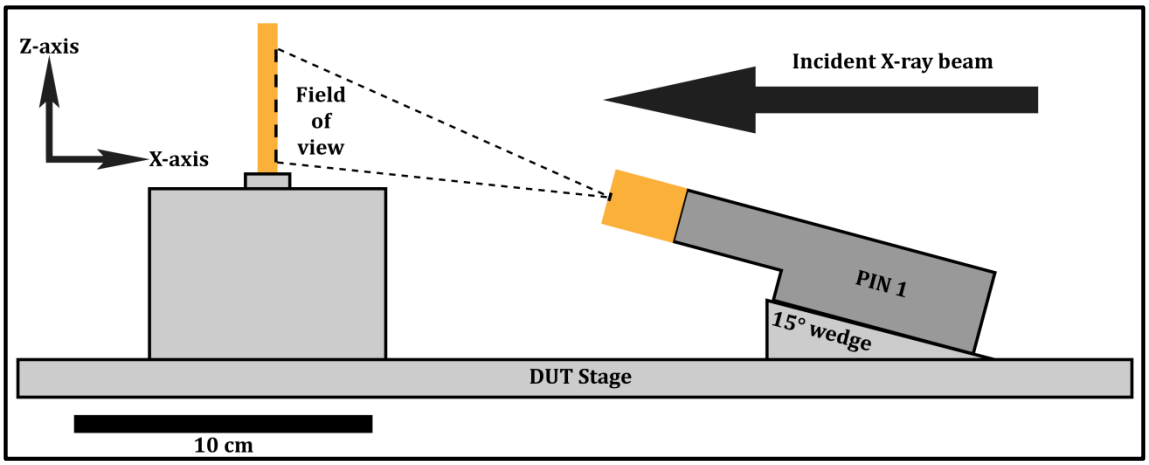

Figure 3.5. Side-on view of equipment within the vacuum chamber, showing PIN 1 on the 15° wedge that allowed it to be placed beneath the level of the sample and thus not block the incident X-rays at small incidence angles.

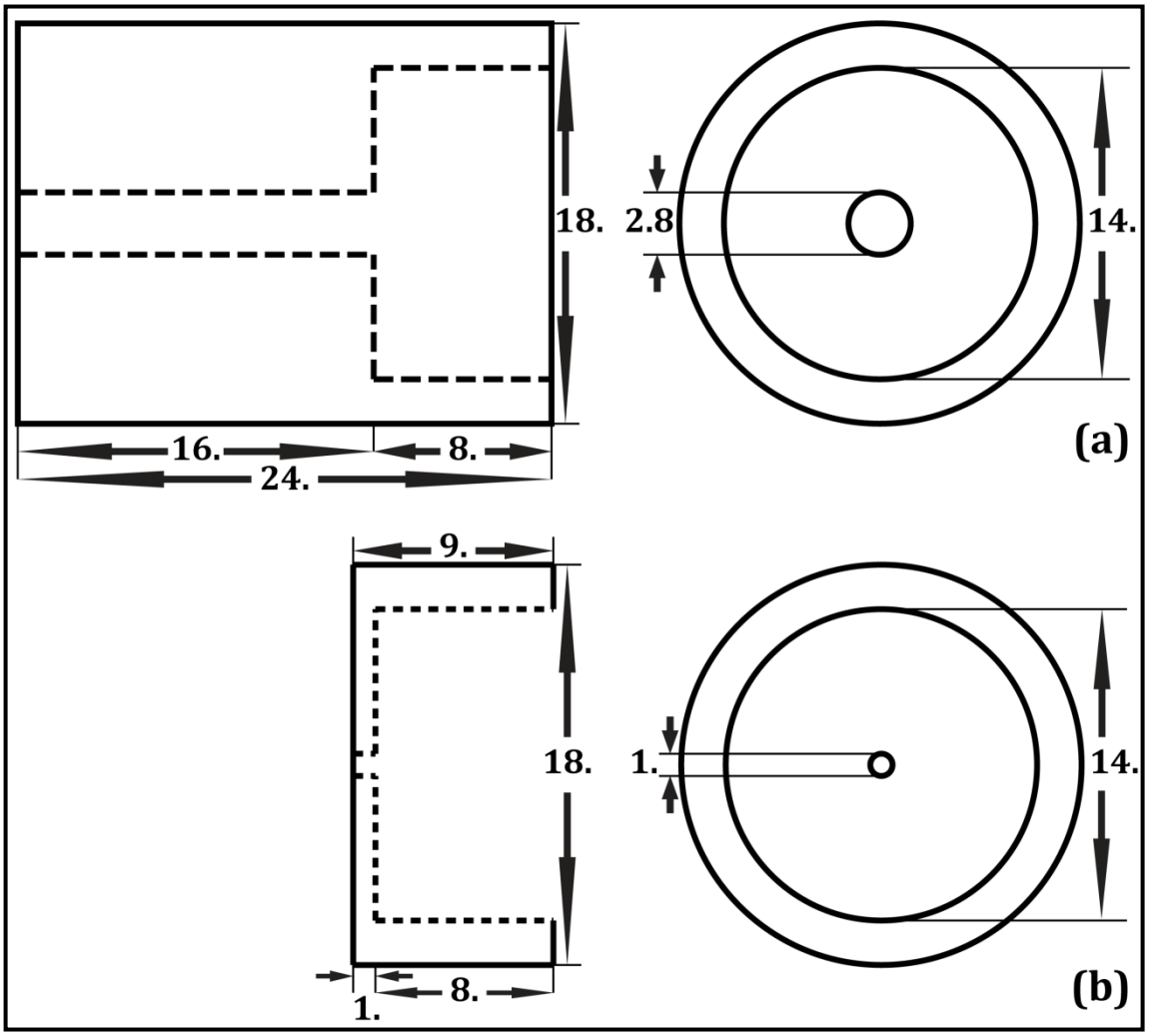

Figure 3.6. Drawings for (a) the collimator used to limit the opening angle of PIN 1 to ±9° and (b) the pin hole used to limit the detection area of PIN 3 (dimensions are in mm) and allow the input X-ray beam to be directly measured.

The DUT stage could be moved along the X-axis (left-right in Figure 3.4) and Z-axis (in-out of page in Figure 3.4); in order to alter the incidence angle (between 0° and 80°) of the X-ray beam onto the sample, the DUT stage was rotated around the Z-axis. All the measurements were conducted with an emergence angle of 0°. This was due in part to time constraints, but also to simulate a nadir-pointing planetary XRF instrument such as C1XS. The constant 0° emergence angle means that the phase angle varied with the incidence angle, to which it was always equal. It was also possible to move the PIN stage along the X- and Z-axes. PIN 3 was located directly behind the sample, so that when the sample was moved out of the beam PIN 3 was no longer obstructed and the input spectrum could be measured.

Samples

A separate set of regolith-analogue samples from those used in the Brunel experiments were measured in the RESIK campaign. High purity oxides (≥97%) of four major rock-forming elements (Mg, Al, Si and Fe) were obtained in powder form as well as smooth, homogeneous slabs. The aim of the sample preparation (as for the Brunel samples) was to preserve the surface roughness and porosity of the powders in a vacuum-suitable form. The Brunel sample preparation method was considered to be insufficiently consistent and standardised (e.g. the glue to powder ratio was not constant and creating an overall flat surface was difficult), therefore the RESIK powders were prepared by sieving the powders into two grain-size fractions, which were then pressed by hand onto a 5 × 5 cm square of double-sided carbon adhesive tape attached to a copper plate (see Figure 3.7). Two grain-size fractions were used in an attempt to create surfaces with different surface roughness. In addition to these 'mono-oxide' samples, three samples consisting of mixtures of the pure oxides were also made. The lunar regolith simulant, JSC-1A that was used in the Brunel experiments, was also sieved and made into two separate grain-size fraction samples. The JSC-1A pressed pellet used at Brunel was also measured in RESIK, and acted as a substitute for a smooth homogeneous slab of this material. The different RESIK samples and their grain-size fractions are listed in Table 3.2.

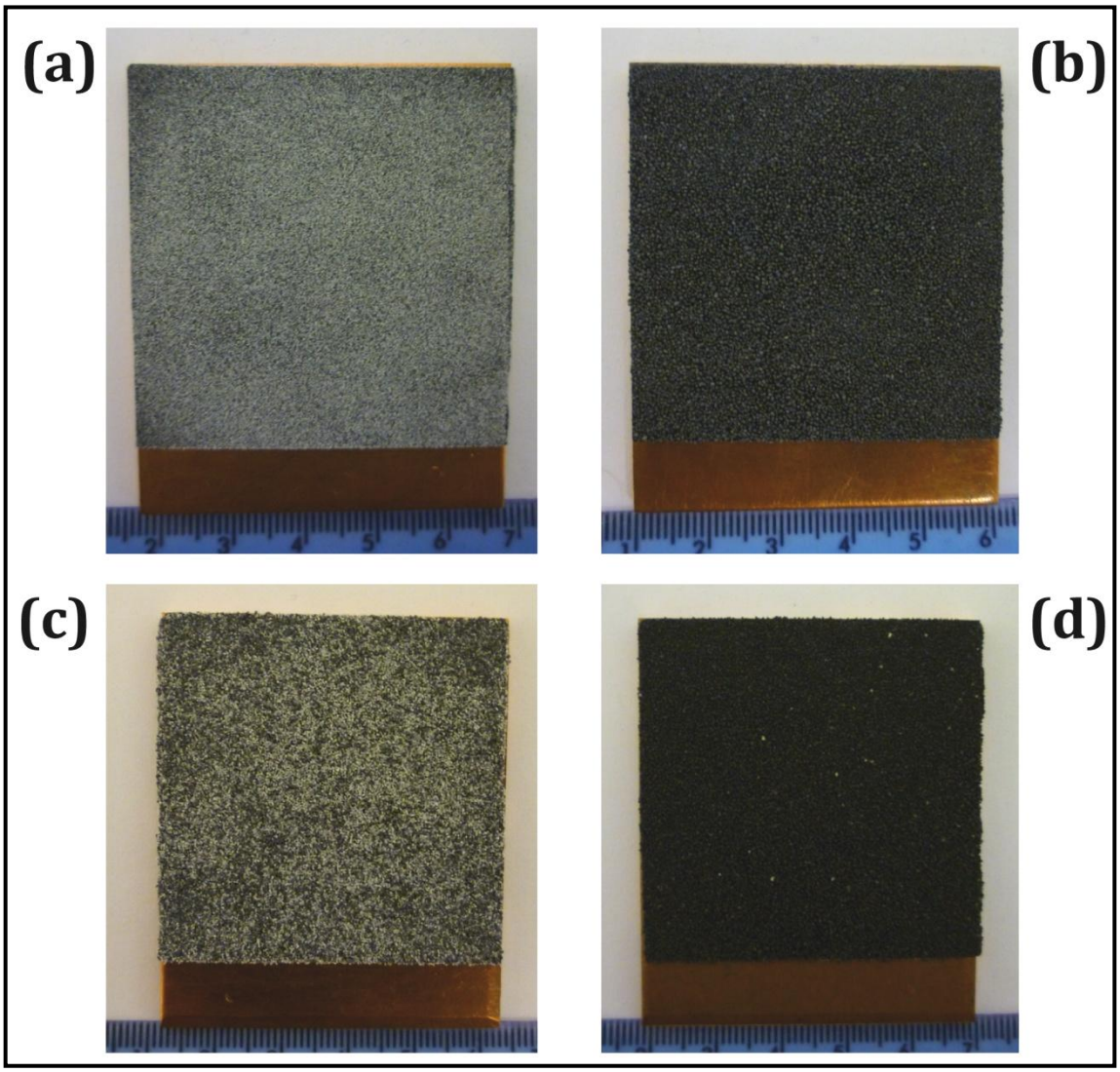

Figure 3.7. Photographs of a selection of the samples used in the RESIK experiments: (a) SiO_2 fine, (b) FeO coarse, (c) mixture 1 (SiO_2 + FeO coarse), (d) JSC coarse. The 5 cm × 5 cm area of the actual sample can be seen, with the bottom of the underlying copper plate also visible, this section of copper fits into the aluminium sample holder and keeps the sample upright.

Table 3.2. List of samples used in the RESIK XRF experiments, showing their composition, grain-size fraction, surface roughness (the root mean square of the heights measured using the laser profiler described in section 3.2.3) and the estimated sample coverage (area of samples covered by material, estimated by tracing the outlines of grains in the SEM images and finding their total area in Adobe Illustrator). The height measurements that give surface roughness have a standard error of ±0.1%.

Sample	Grain-size (μm)	Surface roughness (μm)	Estimated sample coverage (%)
MgO flat	-	-	100
MgO fine	38 – 75	81.4	98
MgO coarse	250 – 500	97.1	85 – 90
Al_2O_3 flat	-	-	100
Al_2O_3 fine	38 – 75	113.3	65
Al_2O_3 coarse	75 – 250	79.6	75
SiO_2 flat	-	-	100
SiO_2 fine	38 – 75	67.2	76
SiO_2 coarse	250 – 500	71.4	76
Fe_3O_4 flat	-	-	100
FeO fine	38 – 75	74.2	97
FeO coarse	250 – 500	65.4	79
JSC-1A pellet	Mixed	43.9	100
JSC-1A fine	38 – 75	93.1	97
JSC-1A coarse	250 – 500	68.3	75
Mixture 1 (SiO_2 + FeO)	250 – 500	4.6	77 (64% SiO_2, 36% FeO)
Mixture 2 (SiO_2 + FeO)	38 – 75	23.2	86 (48% SiO_2, 52% FeO)
Mixture 3 (Al_2O_3 + SiO_2)	75 – 500	21.1	73 (50% Al_2O_3, 50% SiO_2)

3.2.3. *Physical characterisation of samples*

In order to characterise the physical nature of the samples, a series of SEM (scanning electron microscope) images (e.g. those in Figure 3.8 to Figure 3.11) were obtained on two machines (JEOL JXA-8100 and JEOL-6408LV) at UCL/Birkbeck. These backscatter and secondary electron images reveal the mineralogical heterogeneity of the Brunel samples (Figure 3.8), as well as their grain-size and grain-shape distributions, surface textures and porosities, and the glue content of the glass-slide samples. Images of the RESIK samples (such as those in Figure 3.9 to Figure 3.11) highlight the differences in the size, shape and texture of the individual grains in each of the powders, as well as allowing the surface area of the samples covered by grains to be estimated (using grain-tracing and area calculation techniques in Adobe Illustrator). The MgO powder is somewhat cohesive and larger clumps of several single grains form various shapes (Figure 3.9a and Figure 3.9b). The Al_2O_3 grains are generally equant and sub-rounded ('popcorn-like'), although some more oblate and angular grains are also present (Figure 3.9c and Figure 3.9d); these grains have a

'platy' texture. The SiO_2 grains differ in being more angular and elongate/bladed (Figure 3.9e and Figure 3.9f), and the FeO grains are somewhat intermediate in shape (sub-angular) between the Al_2O_3 and SiO_2 grains, with a 'knobbly' texture (Figure 3.9g and Figure 3.9h).

The surface roughness of each of the RESIK samples (except the smooth slabs) was calculated as the root mean square (equation 1) of the heights measured using a Scantron Proscan 2000 laser profiler at UCL. A 2×2 mm area of each sample (assumed to be representative of the whole sample) was scanned using a step size of 1 µm (i.e. a total of 4×10^6 measurements) and having a standard error of ±0.1%. The results are given in Table 3.2 and reveal that the grain-size fraction of the powder used is not always a direct proxy for the roughness of the resulting surface (i.e. coarser grains do not always give rougher surfaces).

$$h_{rms} = \sqrt{\frac{1}{n}\sum_{i=1}^{n}(z_i - \bar{z})^2} \quad (1)$$

where n is the number of height measurements, z_i is a single height measurement, and $\bar{z}$ is the mean of the measurements (Bryant et al., 2007).

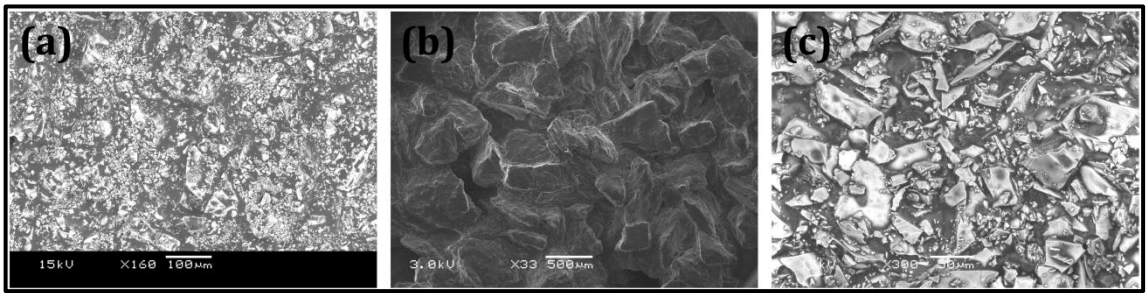

Figure 3.8. Example SEM images of the Brunel samples. (a) Etna basalt, 75 – 125 µm glass slide (low-voltage secondary electron mode); (b) icelandite, 250 - 500 µm glass-slide (high-voltage secondary electron mode); (c) peridotite, <75 µm glass-slide (low-voltage secondary electron mode). The images show surface textures, grain shapes and sizes, sample porosity and glue content.

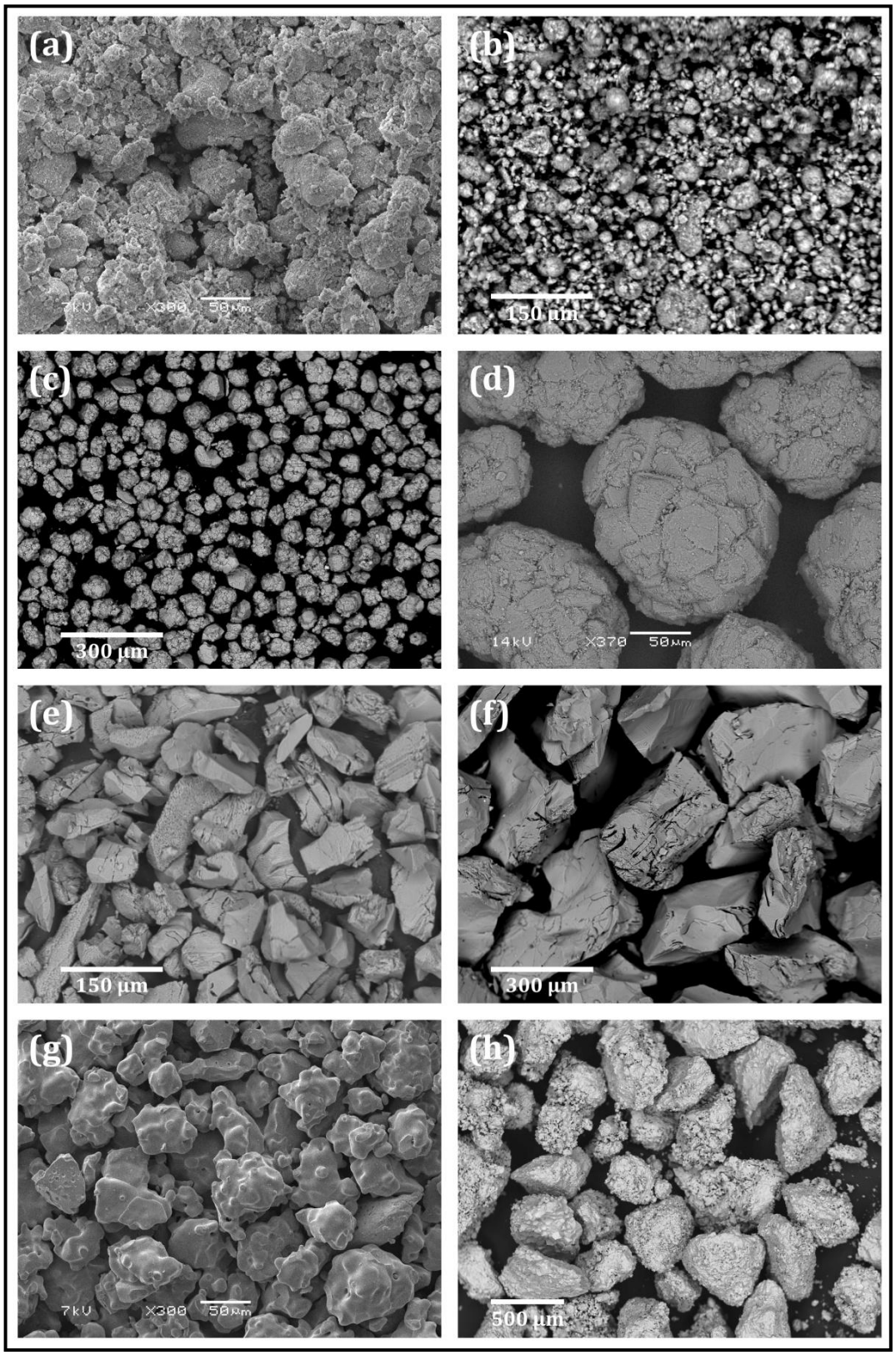

Figure 3.9. SEM images for the mono-oxide samples at various magnifications: (a) MgO fine (secondary electron mode); (b) MgO coarse (back scatter electron mode); (c) Al_2O_3 fine (back scatter electron mode); (d) Al_2O_3 coarse (back scatter electron mode); (e) SiO_2 fine (secondary electron mode); (f) SiO_2 coarse (secondary electron mode); (g) FeO fine (secondary electron mode); and (h) FeO coarse (backscatter electron mode).

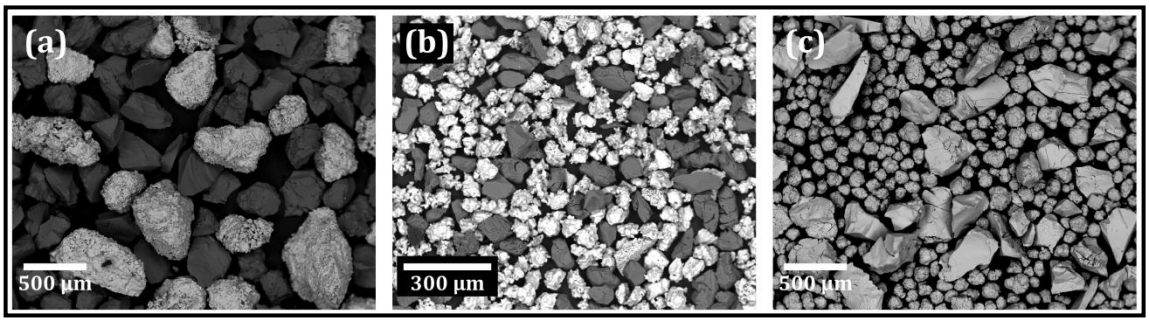

Figure 3.10. SEM images (back scatter electron mode) of the three simple oxide mixture samples: (a) mixture 1 (SiO_2 + FeO coarse), (b) mixture 2 (SiO_2 + FeO fine) and (c) mixture 3 (Al_2O_3 + SiO_2 coarse). The dark grains in (a) and (b) are SiO_2 and the lighter grains are FeO; in (c) the Al_2O_3 grains are smaller and rounder.

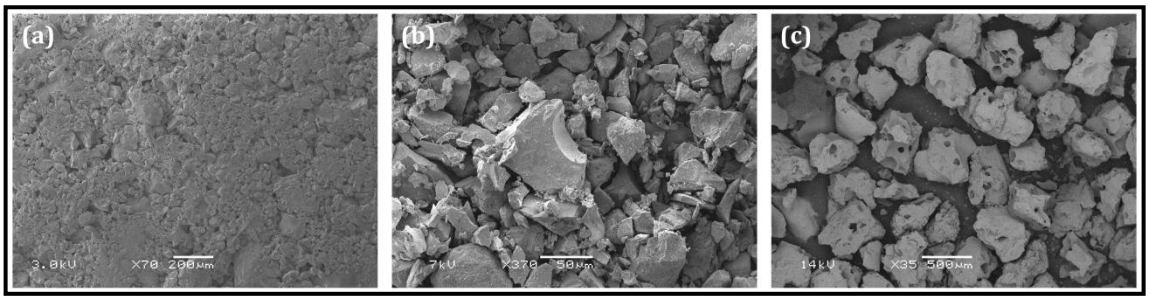

Figure 3.11. SEM images of the JSC-1A samples: (a) the pressed pellet (high-voltage secondary electron mode); (b) the fine-grained sample (high-voltage secondary electron mode); and (c) the coarse-grained sample (back scatter electron mode).

3.3. Results

3.3.1. *Brunel*

Incident X-ray beam

The incident X-ray beam, generated using a current of 4×10^{-3} mA (and a voltage of 10 kV), was measured using a Si-Li detector with an effective area of 3.0×10^{-5} m^2, placed in a direct line with the X-ray source for an integration period of two hours. To prevent saturation of the detector, a pin hole (4.91×10^{-8} m^2) was placed in front of the detector to reduce its effective area. The resulting spectrum is shown in Figure 3.12a and consists of a broad bremsstrahlung curve with a tungsten M_α line (from the tungsten X-ray tube source) at ~1.8 keV, as well as two smaller elemental lines (P K_α from the doping of the Si-Li detector and S K_α from the stainless steel collimator) superimposed.

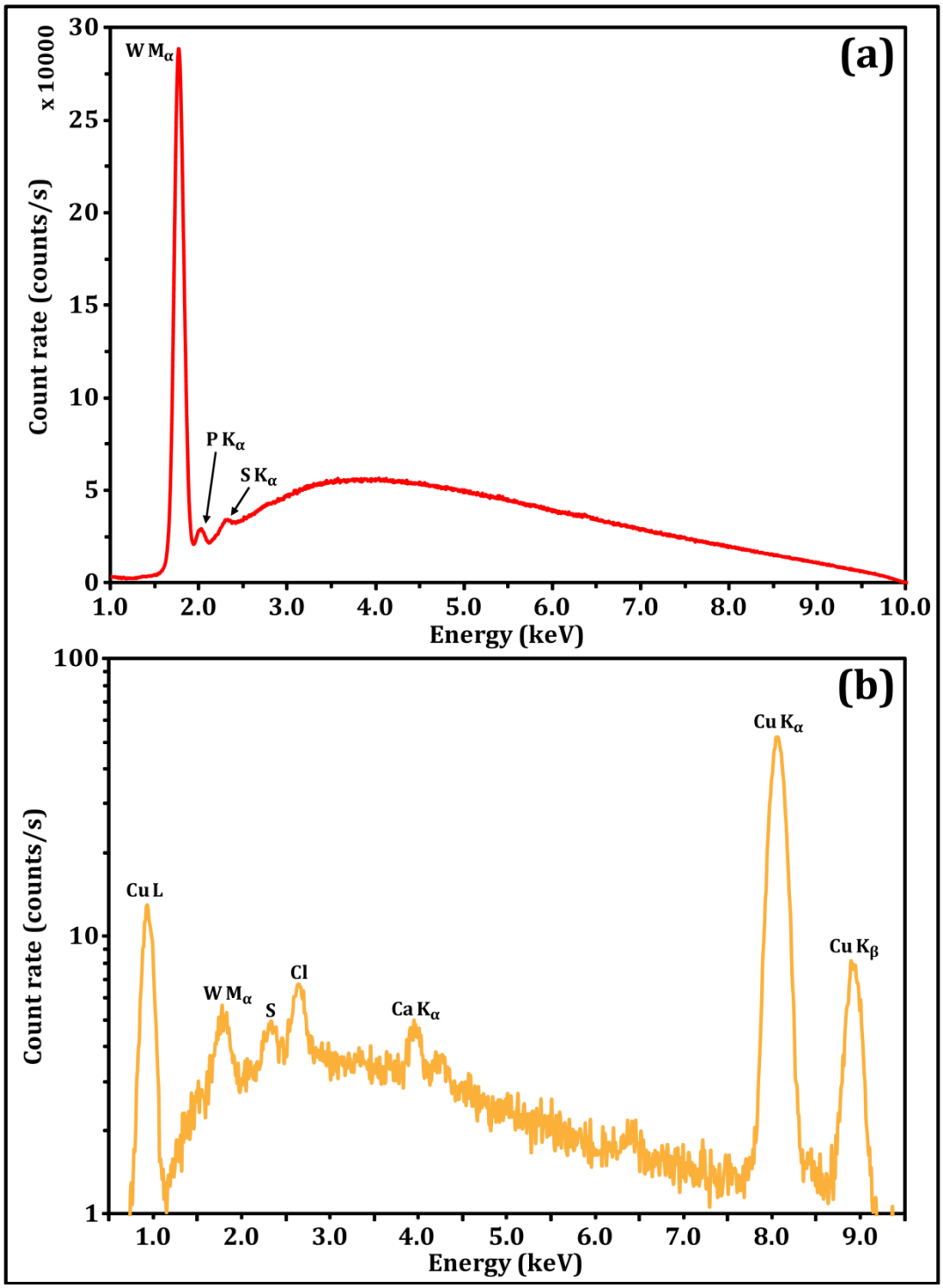

Figure 3.12. Typical input spectra for (a) the Brunel and (b) the RESIK XRF experiments. The spectrum in (a) is generated from a tungsten X-ray tube using a current of 0.004 mA and a pin hole (4.91×10^{-8} m^2) to reduce the effective area of the Si-Li detector with which it is measured (2 hour integration). The W M_α line is the strongest peak, with two smaller lines (from phosphorus in the Si-Li detector and sulphur in the steel collimator) superimposed on the broad bremsstrahlung curve. (b) Spectrum measured using PIN 3 fitted with a 1 mm diameter pin hole (see Figure 3.6b) to limit its detection area, for an integration period of 1 minute. The beam was generated by a voltage of 20 kV and a current of 5 mA applied to a copper anode. The spectrum shows the broad bremsstrahlung curve with various characteristic lines superimposed (the Cu L_α and K lines originate from the copper anode; the other lines are due to contaminants on the anode which increase with time).

Sample XRF measurements

Each of the four glass-slides of icelandite, Etna basalt and peridotite samples (as well as the thick section samples) were measured for 15 minutes in the standard geometry in order to test whether XRF line intensity varies with grain-size. Figure 3.13 shows the count rates (derived by fitting Gaussian distributions to the individual spectral peaks using OriginPro 8.1 software) of the elemental lines with the highest signal to noise ratios in the spectra for each lithology. These values have been normalised to those from the relevant thick section sample. Two main trends are observed: (i) XRF line intensity decreases with increasing grain-size, and (ii) XRF count rates are greater at higher energy (i.e. for higher mass elements). This energy trend is primarily a function of their fluorescent yield (Bambynek et al., 1972), however the relative abundance of the different elements within these mineralogically and compositionally heterogeneous samples may also be a factor.

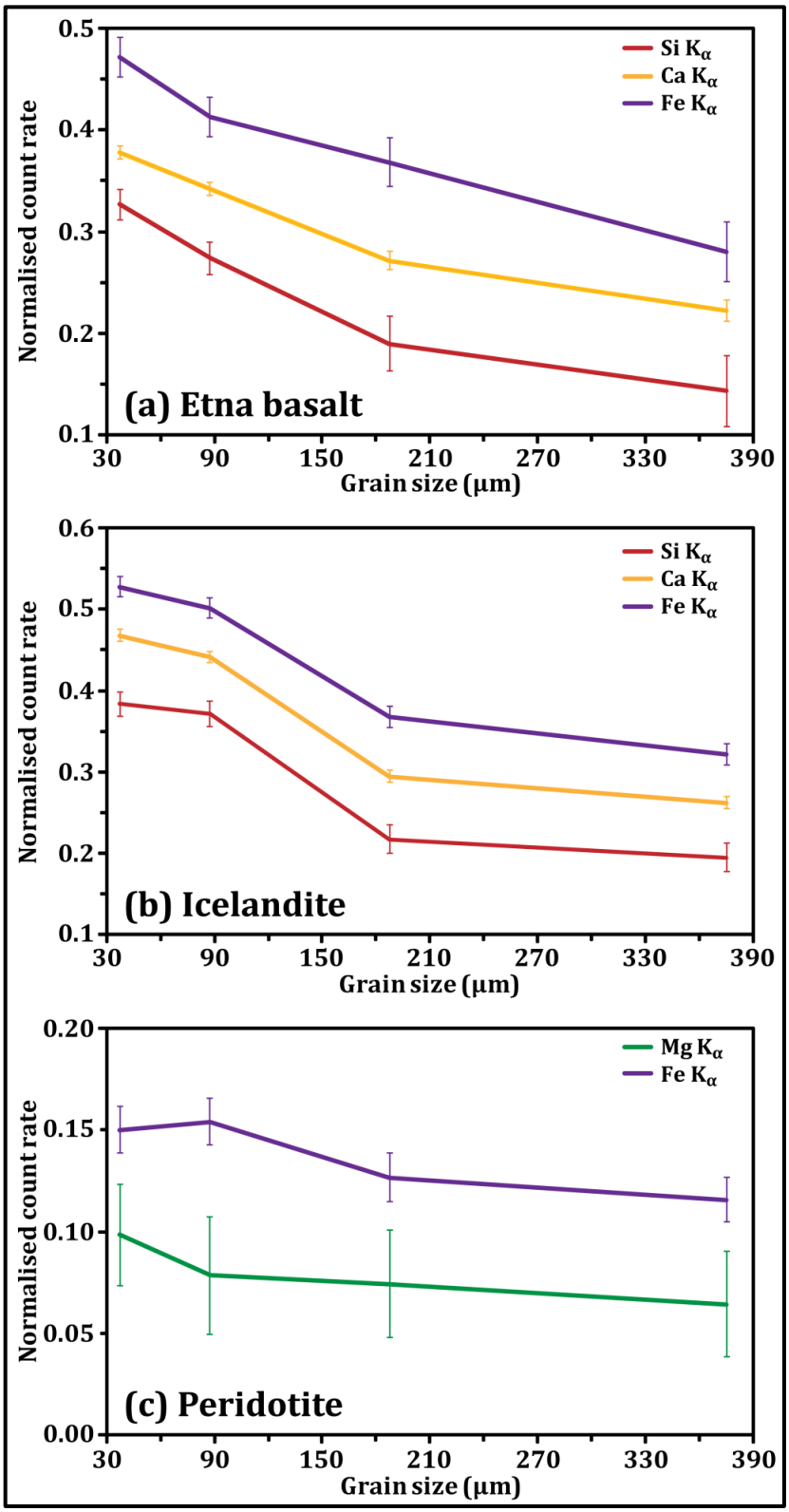

Figure 3.13. Normalised count rates (relative to the rate from the equivalent thick section sample) of the elemental lines with the highest signal to noise ratios in the spectra of the (a) Etna basalt, (b) icelandite and (c) peridotite glass-slide samples. Generally, there is a decrease in XRF intensity with increasing grain-size (this is not the case for Mg in peridotite within the errors shown). Data points are plotted at the median of each grain-size bin. The error bars represent 1 σ confidence limits of the Gaussian fits to the data.

3.3.2. *RESIK*

Incident X-ray beam

The incident X-ray beam was monitored and measured at regular intervals throughout the experiments, using PIN 3 fitted with a 1 mm diameter pin hole (see Figure 3.6b). An example, 1 minute integration incident spectrum is shown in Figure 3.12b. Although there is some temporal variation in the intensity of the incident X-ray beam, the total number of counts within any single 1 minute spectrum never varies by more than 5%, and by <1% during a single day's (~7 hours) measurements.

Mono-oxide samples

Figure 3.14 displays the elemental line count rate (derived by fitting the XRF spectra with a first-order polynomial background and Gaussian peaks) for each of the mono-oxide samples, as a function of incidence (phase) angle. These data have been corrected numerically for two separate phenomena: (i) the changing cross-section of the incident X-ray beam that the sample intersects as incidence angle varies (this is a cosine function and is illustrated in Figure 3.15); and (ii) the relative area of the samples covered by grains (see Table 3.2). A number of first-order observations are made from these data: (i) XRF line intensity increases with atomic number (i.e. count rates for Fe > Si > Al > Mg), because elements with greater mass possess greater fluorescence yields (Bambynek et al., 1972); (ii) XRF line intensity varies little, if at all, between the different grain-size samples with a particular composition (contrary to the Brunel findings, see Figure 3.13); and (iii) XRF line intensity increases at the highest incidence (phase) angles, reaching a level that is ~30% greater than the intensity at 0°. This increase generally occurs above an incidence angle of ~50° to 60°. The SiO_2 powder samples do not follow this trend; their XRF line intensity does not significantly increase at the highest phase angles.

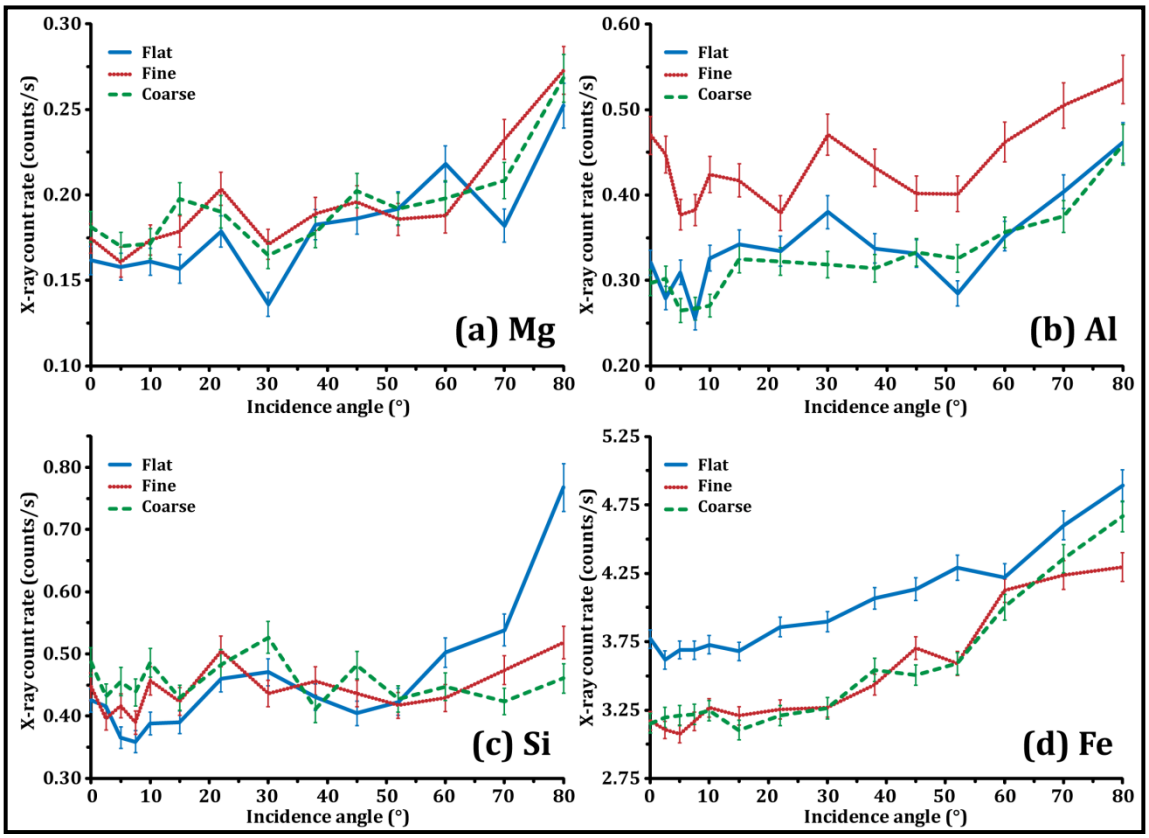

Figure 3.14. The XRF line count rate (corrected for beam cross-section and grain-coverage differences) for each of the mono-oxide samples: (a) MgO, (b) Al_2O_3, (c) SiO_2 and (d) FeO (Fe_3O_4 for the flat sample) and the variation with incidence angle. A small increase in count rate is observed (above ~50 - 60°) for all the samples other than the two SiO_2 powder samples. Error bars are at the 1 σ confidence level of the Gaussian fits to the data.

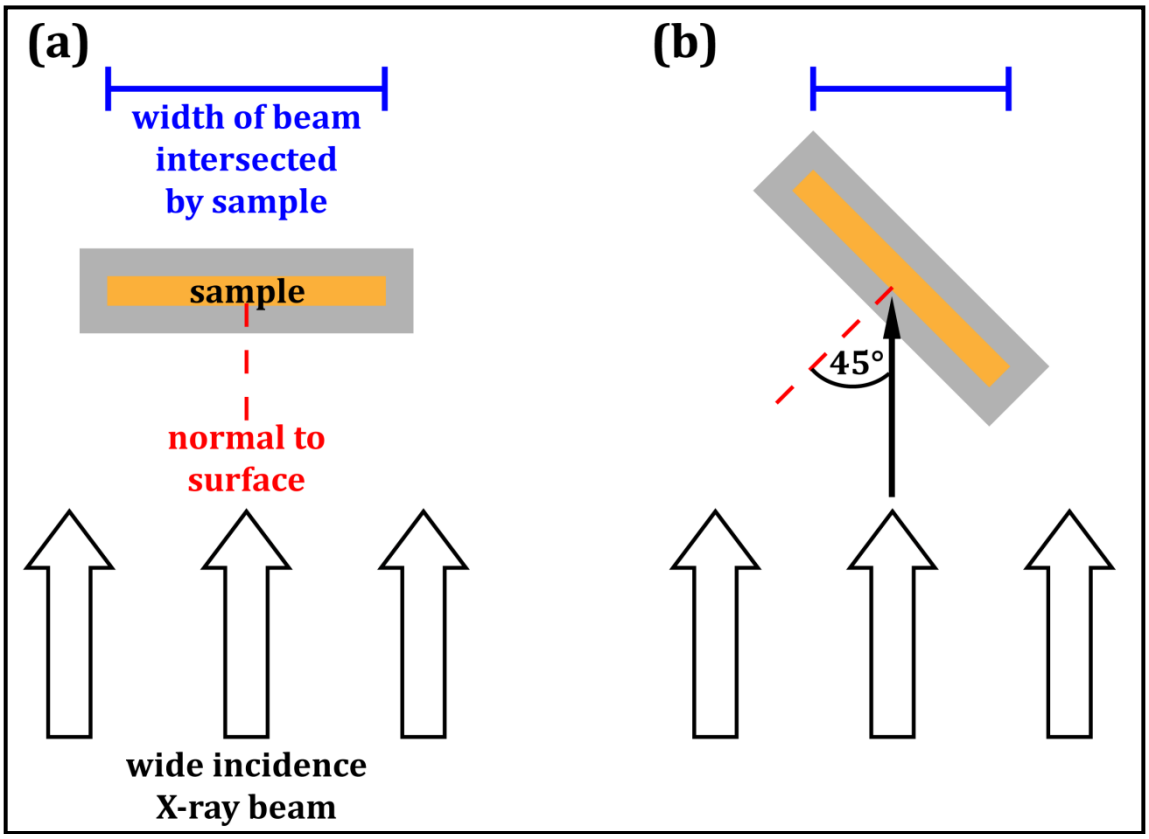

Figure 3.15. Diagram illustrating how the width of the incident X-ray beam intersected by the sample (in RESIK) decreases (as a cosine function) with increasing incidence angle; (a) shows the sample at an incidence angle of 0° and (b) at 45°.

Simple oxide mixture samples

The XRF count rates (normalised at 15°) of the elemental lines in the simple oxide mixture samples are shown in Figure 3.16a as a function of incidence angle. The relative increase in XRF line intensity, at incidence angles of more than ~50°, is higher for iron, than for the lower energy elements silicon and aluminium. In addition, the Fe K_α and K_β line intensities from mixture 1 (SiO_2 + FeO; 250 – 500 μm) are significantly greater than from mixture 2 (SiO_2 + FeO; 38 – 75 μm) at the highest incidence angles. Figure 3.16b compares the absolute XRF count rates (corrected for beam cross-section and sample-coverage differences) for the iron and silicon lines from mixtures 1 and 2; those for iron are greater than for silicon, however the intensity of iron from mixture 2 is greater than from mixture 1, whereas for silicon the opposite is true.

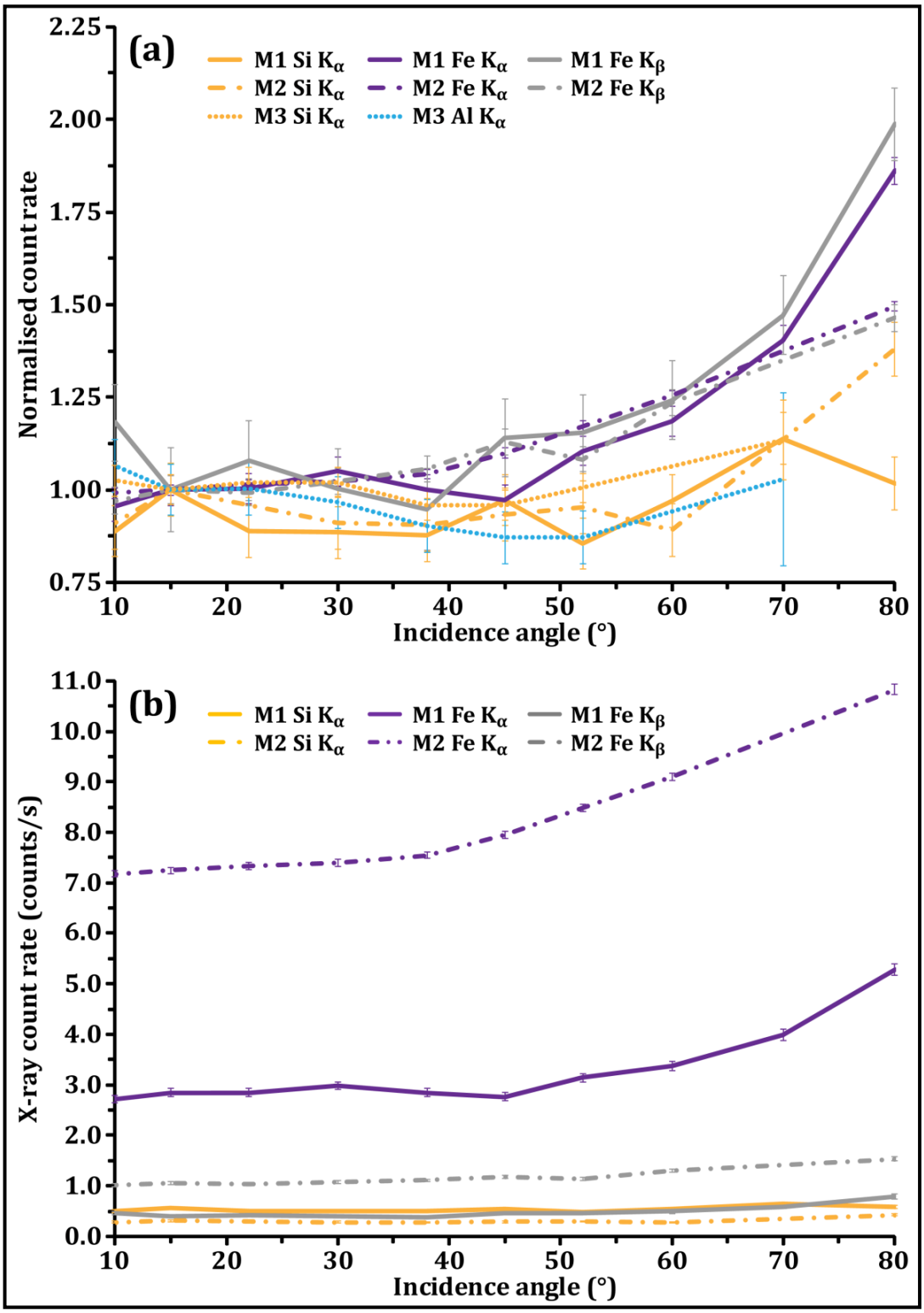

Figure 3.16. (a) Normalised XRF count rates (to 15°) for the elemental peaks in the spectra from the three simple oxide mixture (M) samples (mixture 1: SiO_2 + FeO, 250 – 500 µm; mixture 2: SiO_2 + FeO, 38 – 75 µm; mixture 3: Al_2O_3 + SiO_2, 75 – 500 µm) as a function of incidence angle. (b) XRF count rates as a function of incidence angle (corrected for beam cross-section, grain-coverage differences and the relative abundance of the mixture of the mixture components) for the iron and silicon elemental lines from mixtures 1 and 2. Error bars are at the 1 σ confidence level of the Gaussian fits to the data.

Lunar regolith simulant (JSC-1A) samples

Figure 3.17 illustrates the variation in XRF count rate with incidence angle for the Si K_α, Ca K_α and Fe K_α lines (those characteristic lines with the highest signal to noise ratios) in the JSC-1A sample spectra. These data have been normalised at 15° (in Figure 3.17a, Figure 3.17b and Figure 3.17c) so that the magnitude of the relative XRF increase with incidence angle can be directly compared between different elements and samples. The increase is negligible or very small for these data. Figure 3.17d, Figure 3.17e and Figure 3.17f display the same data as absolute values corrected for beam cross-section and sample coverage differences, as well as the relative oxide contents (see Table 3.1). These show that the XRF intensity from the three samples is most different for iron and least for silicon, suggesting that a possible grain-size effect is energy dependent.

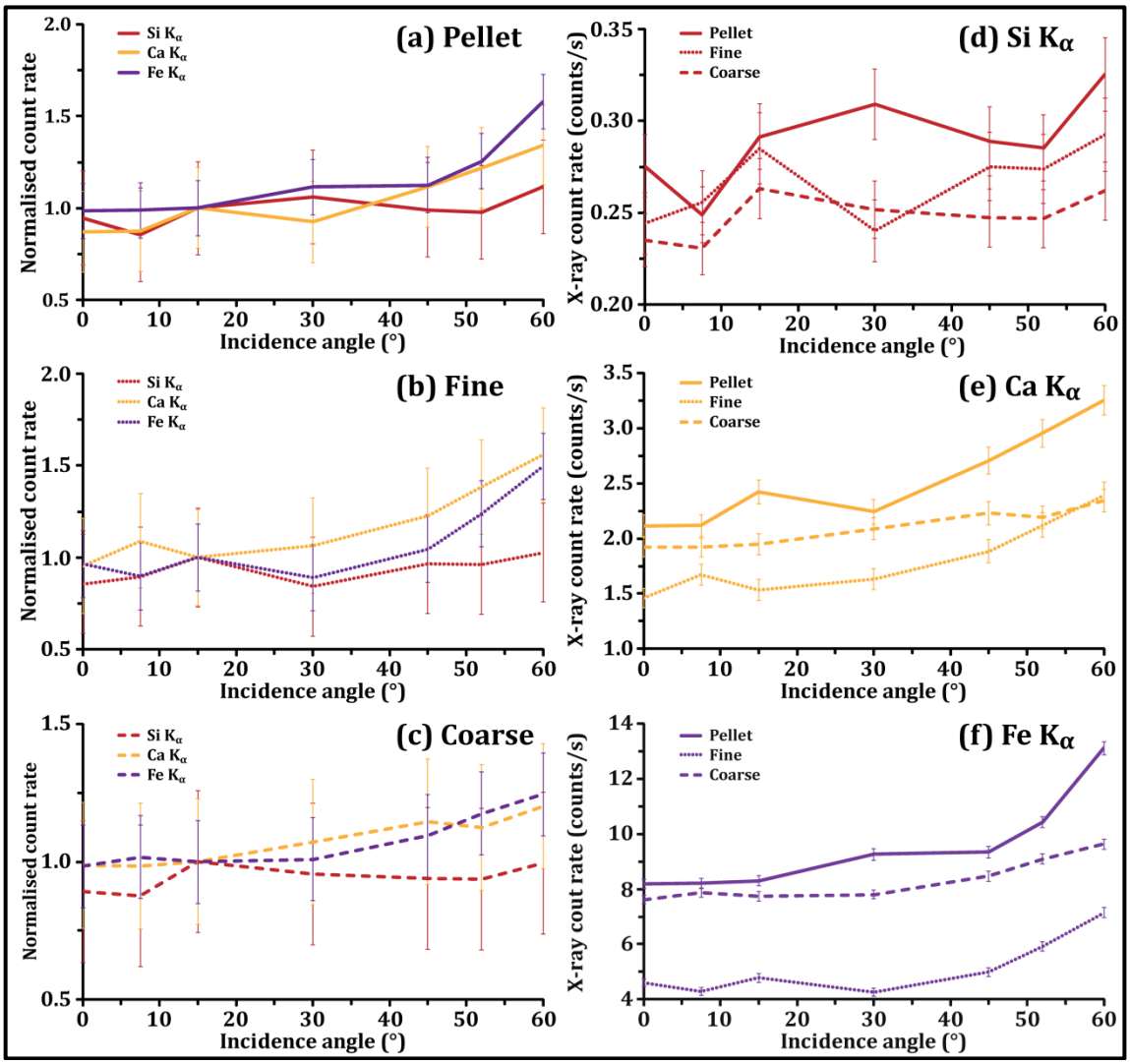

Figure 3.17. XRF data for the JSC-1A samples. The elemental count rates for the three lines of interest are shown as a function of incidence angle and are normalised at 15°, for (a) the pressed pellet, (b) the fine-grained and (c) the coarse-grained samples. The absolute count rates (corrected for beam cross-section and grain-coverage differences, as well as the relative compositional proportions) for (d) Si K_α, (e) Ca K_α and (f) Fe K_α, are compared between the three samples as a function of incidence angle. Error bars are at the 1 σ confidence level of the Gaussian fits to the data.

3.4. Discussion

3.4.1. *Grain-size effect*

A grain-size effect has previously been reported (e.g. Maruyama et al., 2008; Näränen et al., 2008) where the XRF intensity from samples of the same rock decrease with increasing grain-size, and that this effect is greater at lower energies. Although these findings can only really be compared directly with our Brunel and RESIK JSC-1A results (Figure 3.13

and Figure 3.17) because these are the only measurements of heterogeneous rock samples, it is also possible that a grain-size effect may be apparent in the mono-oxide and simple oxide mixture data.

No obvious trend with increasing grain-size (or indeed, surface roughness) is evident from the mono-oxide data (Figure 3.14), however there are some differences in the XRF line intensity from the different samples of aluminium and iron oxides (Figure 3.14b and d). The intensity of Fe K_α from the Fe flat samples is greater than for the two powder samples (Figure 3.14d) and this may be due, at least in part, to the slightly different compositions (Fe_3O_4 for the flat sample and FeO for the powder) causing a difference in the total amount of iron present in the samples. The greater XRF line intensity from the Al fine sample, compared with the other two aluminium samples (Figure 3.14b), may be caused by its surface roughness, which is greater than for the coarse sample (Table 3.2). The rougher surface provides a larger sample area from which fluorescence can occur. The surface roughness of the two powder samples for each of the other oxides is about equal and this is reflected in the fact that no other grain-size (or surface roughness) effect is observed.

Figure 3.16b illustrates that although the Fe intensity (Fe K_α and K_β) from mixture 2 (38 – 75 μm) is higher than from mixture 1 (250 – 500 μm), whereas for silicon the opposite is true. It is proposed that this is due to enhanced fluorescence of Si due to excitement by Fe XRF from the neighbouring grains. The Si XRF produced in this way is greater for mixture 1 than mixture 2 because of its larger grain-size and thus greater Si surface area. Fe XRF line flux decreases with increasing grain-size; this follows the effect which has previously been reported (Maruyama et al., 2008; Näränen et al., 2008) and which is observed in the Brunel data (Figure 3.13).

Maruyama et al. (2008) and Näränen et al. (2008) note that the magnitude of the grain-size effect (XRF intensity decreases with increasing grain-size) is greater at lower energies. The Brunel data (Figure 3.13) tend to agree with this finding, however the JSC-1A data (Figure 3.17d, e and f) show the opposite, i.e. the grain-size effect *increases* with energy. If the heavier elements in the samples cause enhanced XRF of lower energy lines (as seen with the simple mixture samples), one would expect this to be most effective for (i) the

lowest energy lines (i.e. Si) when the number of heavier elements is greatest, than for the higher energy lines and (ii) for the larger grain-sizes. This phenomenon will be dependent on the relative abundance of the different elements with the rock or mixture sample and this has been accounted for in the data shown in Figure 3.17. The disagreement between the results presented here and those from the earlier studies (Maruyama et al., 2008; Näränen et al., 2008) can thus be explained if the relative elemental abundances of the samples have not been considered. The Brunel glass-slide data (Figure 3.13) provide further support for this idea; the XRF intensity decreases with increasing grain-size and whilst the shape of the slope for each elemental line is consistent for a particular lithology, it varies for different rock types. This, however, could also be due to unrepresentative plotting of grain-size information, where the midpoint (median) of the grain-size fraction for each sample is plotted, but where a mean or modal value may perhaps be more representative.

It has already been suggested that the rough surface of the fine-grained Al_2O_3 sample (Table 3.2) causes its XRF line intensity to be greater than that of the other two samples with the same composition. If this is indeed the case, it should be expected that the XRF line intensity from the JSC-1A samples would be greatest for the fine sample and least for the pressed pellet (refer to Table 3.2). However, the reverse is actually observed (Figure 3.17a, Figure 3.17b and Figure 3.17c). This discrepancy is probably evidence of an additional physical sample characteristic, such as porosity or packing efficiency having an effect on XRF intensity, and these are things that should thus be measured and quantified in future experiments.

Whilst the mono-oxide data do not provide evidence of a grain-size effect on XRF line intensity, those from the simple-mixture and rock samples indicate that in general, XRF line intensity decreases with increasing grain-size (e.g. by between ~30% and ~55% in the Brunel samples). The interaction between elements within heterogeneous samples, and the physical characteristics of the samples, means that the nature of the grain-size effect is not always clear.

The ancient space-weathered lunar surface is covered by a regolith that is mostly fine-grained and consistent at the large spatial and small depth scales relevant to planetary XRF.

However, asteroid surfaces are more likely be irregular in nature, e.g. 25143 Itokawa imaged by Hayabusa (Saito et al., 2006), which is thought to exhibit both rough and smooth terrains whose regoliths are likely to vary in grain-size. Apparent chemical heterogeneities across the surfaces of such asteroids as determined with XRF measurements (e.g. Nittler et al., 2001; Okada et al., 2006) are therefore likely to be caused, at least in part, by the grain-size effect if this is not accounted for.

3.4.2. *Phase angle effect*

There is an almost ubiquitous increase in XRF line intensity with incidence angle for all the elemental lines and samples presented here, and this is called the *phase angle effect*. The magnitude of this rise is neither consistently affected by energy nor surface roughness, at least for the mono-oxide samples. However, the two powder SiO_2 samples display a negligible phase angle effect. This anomalous behaviour may be caused by the more angular shaped grains which make up this powder, compared to the other mono-oxide samples (see section 3.2.3 and Figure 3.9). For the simple mixture samples (Figure 3.16a) there is an increase in the size of the phase angle effect at higher energy (i.e. greater for iron than silicon and aluminium). This agrees with the findings of Näränen et al. (2008), however the size of the effect for a particular element is inconsistent between different samples. This could be an example of a matrix effect, where the relative proportion of the two components is influential. The JSC-1A data (Figure 3.17a, b and c) show insignificant or very small phase angle effects over the incidence angle range (0° - 60°), however its magnitude is about consistent with that reported by Näränen et al. (2008) for other heterogeneous rock samples. Näränen et al. (2008) also report that the phase angle effect is greater for rougher samples, but this is not observed in the RESIK data.

The phase angle effect is caused by fluorescence occurring closer to the surface of a sample at higher incidence angles, thus providing a greater chance for the XRF to escape and be detected (Figure 3.18). This relationship approximates a cosine law and explains why the intensity increase becomes significant only above an incidence angle of ~50° or 60°. It is thus important to consider this effect at high phase angles when dealing with real planetary XRF data obtained at these angles (i.e. at high latitudes). The actual response however, is

not a pure cosine relationship because at larger incidence angles less of the grain area (or volume) produces XRF. The precise relationship depends on the grain shape, with the XRF response from spherical grains reducing at a slower rate with increasing incidence angle than cubic grains (Hawthorne & Gardner, 1978).

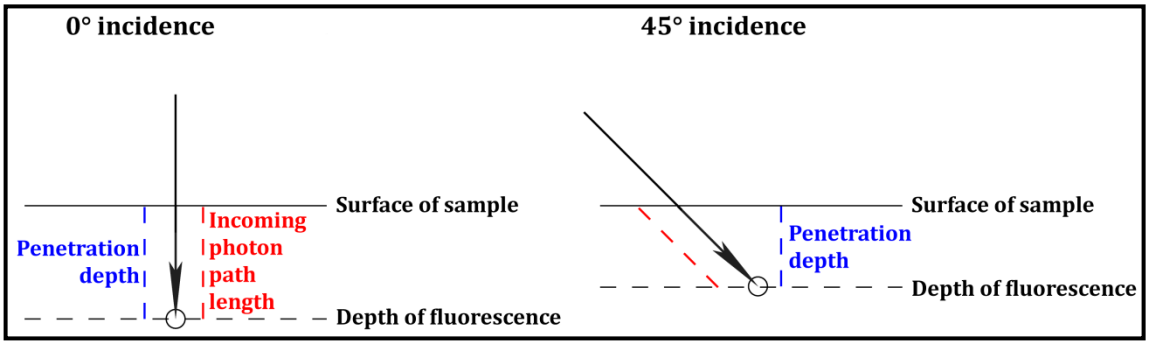

Figure 3.18. Diagram illustrating the cause of the phase angle effect. The length of the path that an incoming X-ray photon will travel before fluorescence occurs is constant within a specific material, but as the incidence angle increases, the depth (normal to the sample surface) from which the fluorescent X-ray must escape in order to be detected will decrease (as a cosine of the angle) and the count rate will correspondingly increase.

The penetration depth of specific energy X-rays within the same material (i.e. Fe X-rays in iron or Al X-rays in Al) is about equal (Henke et al., 1993). This means that the size of the phase angle effect should be about the same for all the compositionally distinct mono-oxide samples, and this is indeed the case. The situation becomes more complicated for the heterogeneous samples because fluorescent X-rays may have to travel through material that is not the same as that from which it originated (e.g. a fluorescent iron X-ray may have to travel through an aluminium atom in order to escape the sample). The relative proportions of the two or more sample components will therefore become significant. This may explain the apparent energy trend observed for the simple mixture data. It is easier for higher energy X-rays (i.e. Fe) to penetrate through a low density material (i.e. Al) rather than vice versa. The same energy trend is not apparent in the JSC-1A data, but this may be due to the smaller incidence angle range.

The data from the RESIK and Brunel experiments consistently show the presence of a phase angle effect, where the XRF intensity increases with incidence (and phase angle) in a manner approximating a cosine law. In the mono-oxide samples, there is no evidence for energy dependence; however the heterogeneous sample data do suggest that the phase angle

effect is greater at higher energy (i.e. between 0° and 60° the XRF count rate for Si K_α in JSC-1A increases by ~15%; Ca K_α increases by ~30% and Fe K_α by ~40%).

These kind of experiments are relevant in a wider planetary XRF context, especially for instruments, such as NEAR that operate at high phase angles. Okada (2002; 2004) predicted that the XRF observations made by the X-ray spectrometer (XRS) on NEAR would provide erroneously high Fe/Si ratios due to the large phase angle it operated at (~100°) and that this might explain the discrepancy between the XRS and the NEAR gamma-ray spectroscopy results. The magnitude of the phase angle effect is thought to increase as the difference in energy of the two lines being compared increases (Okada, 2002). Indeed, Lim & Nittler (2009) find that the Fe/Si ratios from NEAR XRS data increase with path length (function of incidence and emission angles), but the Ca/Si ratio shows no consistent trend.

3.5. Laboratory testing of the RAL abundance algorithm

3.5.1. *Laboratory data*

The methodology of the RAL abundance algorithm has already been described (Swinyard et al., 2010; Weider et al., in review and section 2.5.1), but in this section it is tested with two sets of laboratory XRF data for the JSC-1A lunar regolith simulant. These were as follows:

(i) **Brunel**. These results were obtained using an SCD as the X-ray detector, a tungsten anode (with a current of 0.2 mA applied), incidence and emergence angles both 45° and a total integration time of 10 minutes. For full details of the experimental setup refer to section 3.2.1.

(ii) **RESIK.** These results were obtained during an additional, long-integration (total 1215 minutes) measurement, using a Si-PIN diode as the X-ray detector, a copper anode, and incidence and emergence angles both equal to 0°. The experimental setup was the same as that described in section 3.2.2 other than the current and voltage applied to the copper anode. In the original RESIK experiments a current of 5 mA and a voltage of 20 kV were used and produced the input spectrum shown in

Figure 3.12b, with strong Cu L_α and K lines. The Cu K_α line at ~8.04 keV significantly enhanced the XRF response of the Fe K_α and reduced the ability for meaningful elemental abundances for the higher energy lines to be obtained because the strength of the anode line could not be simultaneously measured. In order to accurately test the abundance algorithm, an input spectrum without these lines was therefore required. This was obtained by reducing the copper anode voltage to 8 kV, and applying an increased current of 10 mA in order to achieve reasonable fluorescence rates. This increased beam current caused sputtering of the tungsten filament and the W M_α line to appear in the input spectrum in addition to the strong Cu L_α line (see Figure 3.19c).

3.5.2. *Modelling results*

The actual verification of the RAL abundance algorithm with these data was conducted by B. Swinyard (author of the RAL abundance algorithm), according the following procedures. The input X-ray spectra from both laboratory campaigns were fitted with a polynomial with all characteristic lines removed. It is only the W M_α lines (and the Cu L_α line in the RESIK spectrum) in both input spectra that contain significant flux and so these were fitted with a Gaussian curve to establish the total line counts in relation to the continuum. This flux was then assigned to a single bin in the input spectrum at the known energy of the line. The two input spectra along with their corresponding measured XRF spectra are shown in Figure 3.19, along with their fitted models. The modelled elemental wt. % values for both cases are given in Table 3.3. The errors given are estimated by testing for the variation in elemental abundance where the variance between the model and the data increases by a factor of two. This provides a robust estimate of the variation in the abundance that is consistent with a 1 σ uncertainty in the fit. Figure 3.19 clearly illustrates how important it is to measure the incident solar X-ray spectrum in planetary XRF; two different incident spectra give two very different XRF spectra of the same material. The effect of using different temperature flare models on real C1XS data is explored in section 4.2.3.

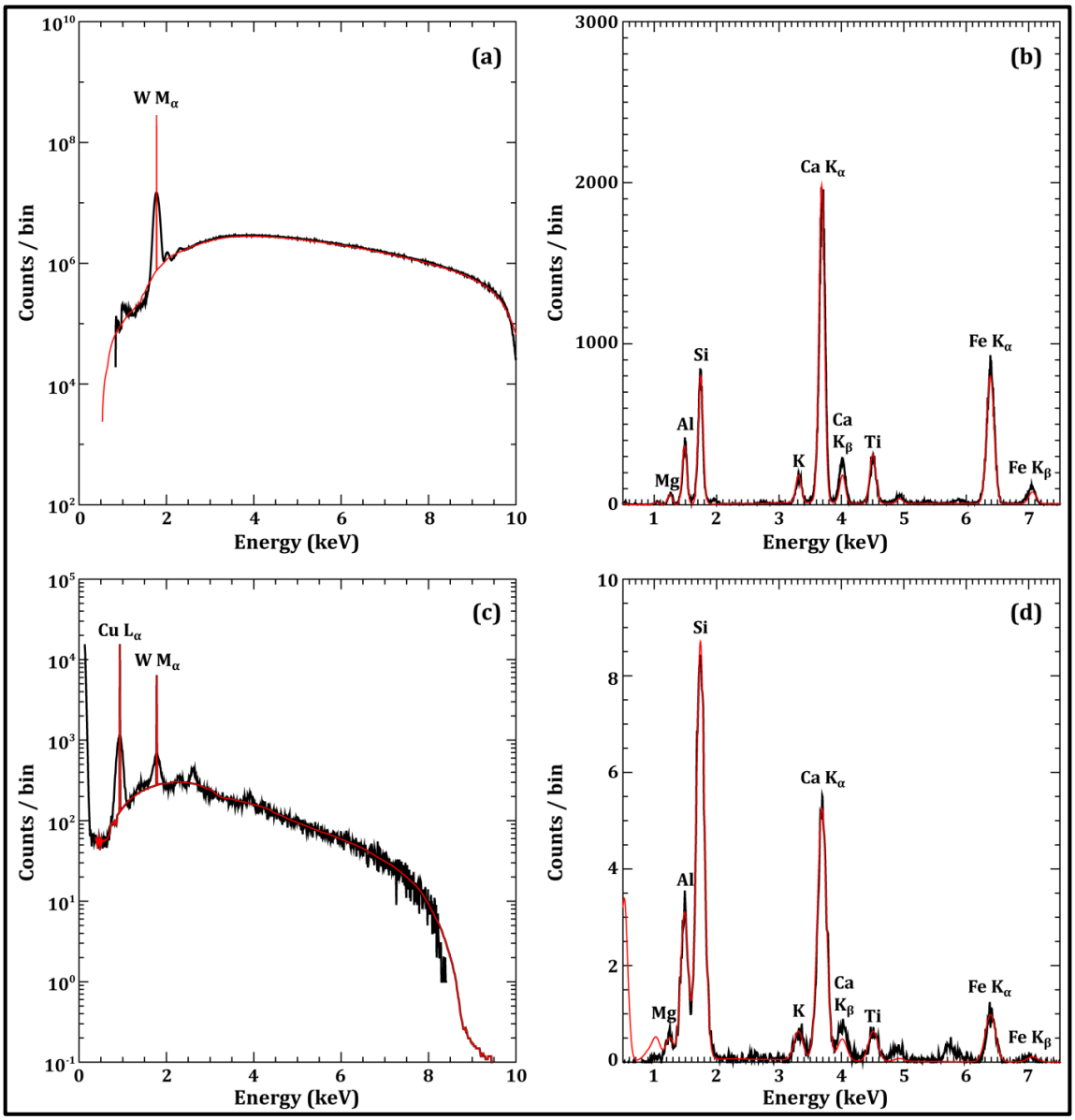

Figure 3.19. Illustrating the RAL abundance algorithm fitting procedure; raw data are shown in black and the fitted spectra in red. (a) and (c) show the input spectra for the Brunel and RESIK measurements of JSC-1A respectively; the corresponding resultant XRF spectra are shown in (b) and (d). In both cases only the strongest lines in the input spectra are fitted (W M_α for Brunel; Cu L_α and W M_α for RESIK), the other chamber or contamination lines are ignored. In (d) the poor fitting of Na (at ~1 keV) is caused not by a problem in the model, but is due to the poor efficiency of the detector at this low energy; the V and Mn lines (at ~4.9 keV and ~5.9 keV respectively) are not fitted in the model because their presence is due to contaminations from chamber lines, as seen from (b). Note the difference in total counts contained in the two sets of spectra. The quantitative results are given in Table 3.3.

Table 3.3. The elemental wt. % abundance values for JSC-1A as measured using ICP-AES, and as derived using the RAL abundance algorithm on data obtained during the Brunel and the RESIK experimental campaigns. The numbers in bold are fixed during the modelling and are taken from the ICP-AES results (the ICP-AES oxygen value is derived from the calculated difference of all the reported oxides, as shown in Table 3.1, rather than just of the elements shown here). Generally, within the errors provided (1 σ uncertainty in the fit), the derived abundances from both the Brunel and RESIK data fall within 1.0 elemental wt. % of the measured ICP-AES abundances. Two exceptions are: (i) the underestimation of Mg from the RESIK data; this is due to the poor response and calibration of the Si-PIN detector, as well as the inefficient excitation from the input spectrum at this low energy; and (ii) the overestimation of Ca from the Brunel data; this reflects a probable difference between the continuum and photo-peak efficiency in the SCD detectors using the particular electronics and readout scheme employed. It is these two issues (as well as the slightly low estimation of Fe in the RESIK results) that produce totals which vary somewhat from 100 wt. %.

Element	ICP-AES (wt. %)	Brunel (wt. %)	RESIK (wt. %)
O	44.71	**44.70**	**44.70**
Na	2.40 ± 0.02	2.80 ± 0.80	**2.40**
Mg	5.10 ± 0.02	4.30 ± 0.60	2.00 ± 0.60
Al	8.63 ± 0.05	9.50 ± 1.20	8.80 ± 0.50
Si	21.52 ± 0.21	**21.50**	**21.50**
K	0.67 ± 0.01	1.00 ± 0.10	0.80 ± 0.90
Ca	6.91 ± 0.04	9.50 ± 0.70	6.80 ± 0.50
Ti	1.05 ± 0.01	2.00 ± 0.50	1.30 ± 0.5
Fe	8.53 ± 0.08	8.50 ± 0.80	6.50 ± 1.0
Total	99.52	103.80	94.80

The effect of the strong W M_α line at ~1.8 keV on the resultant model spectrum was tested, and it was found that varying the line to continuum ratio over a range of two had little effect on the results of the fitting procedure. The Cu L_α line at ~0.9 keV is too low in energy to excite any lines of interest in the sample and so it can safely be ignored. However, as indicated above, the Cu K_α line had a strong effect on the results and it is clear that significant line emission in solar spectra will restrict the efficacy of the fluorescence method for planetary experiments if the solar spectrum is not measured with high enough spectral resolution.

3.5.3. *Accuracy of the algorithm*

Within the errors provided, the derived abundances from both the Brunel and the RESIK data fall within 1.0 element wt. % of the measured ICP-AES abundances (Table 3.3). The Mg abundance derived from the RESIK data is one exception (Ca in the Brunel results is another), and is caused by the poor response and calibration of the Si-PIN detector and inefficient excitation from the input beam at low energies (i.e. below the energy of aluminium). Although the modelling of the RESIK results (using the Si-PIN diode

detector) at higher energies allows accurate elemental abundances to be derived, the Brunel results (using an SCD and therefore more applicable to C1XS) are used to discuss the accuracy of the methodology.

The median of the absolute deviations between the measured (ICP-AES) and modelled abundances is 0.6%; the weighted mean of these deviations is 0.3%. The exception to this overall result is the over estimation of the Ca concentration in the analysis of the Brunel data. This value clearly lies outside the experimental and systematic error estimates. However, the RESIK results (using the Si-PIN) agrees well with the expected value and it is thought that this overestimation is not due to the modelling approach adopted. Rather, this result reflects a probable misunderstanding in the efficiency of the SCD detectors in this particular electronics readout system.

The effect of changing the fixed silicon abundance within the range quoted for lunar soils (i.e. between 18 and 23 elemental wt. %; Rhodes & Blanchard, 1981; Fruland, 1983; Morris et al., 1983; Simon et al,. 1985; McKay et al., 1986; 1989; Jerde et al., 1987; 1990) was investigated, and the following are noted:

(i) the total abundance (sum of all elemental wt. % values for the elements in the derived spectrum) varies between 94.5% and 107.5%; the total abundance which is nearest to 100% occurs when the Si elemental abundance is fixed at 20 wt. %. However, the Si abundance continues to be fixed at 21.5 wt. % for the modelling because this is its concentration in JSC-1A, as indicated by the ICP-AES results (Table 3.3).

(ii) when the Si elemental abundance is fixed at 20 wt. %, the absolute deviation between the measured and the modelled values is at a minimum (median deviation is 0.11%).

In a situation where a well resolved input spectrum measured using a well calibrated detector is available, and where the analysis of the measured XRF spectrum is not dominated by noise (and including the fact that the Si abundance is fixed as a calibration point), the RAL abundance algorithm and reduction technique achieves an overall accuracy (1 σ) of 1.0 elemental wt. % across the energy range that encompasses Na and Fe. It is therefore possible for the method to be used to determine lunar surface compositions with good accuracy and allow significant geological conclusions to be drawn. As part of the

calibration of future planetary XRF instruments, the direct measurements of rock samples, as described in this chapter, should be conducted in order to obtain a full picture of the system response.

3.6. Conclusions & future work

Laboratory experiments have been conducted in an attempt to simulate results from planetary XRF missions using simple, characterised planetary regolith analogue samples and a polychromatic source of X-rays. This provides data with which to test XRF modelling codes and explore the nature of previously reported regolith effects. There is evidence for a grain-size effect (XRF line intensity generally decreases with increasing sample grain-size) in these data, and that this effect is dependent on the relative abundance of elemental components, as well as physical sample characteristics. An almost ubiquitous phase angle effect (XRF line intensity increases with incidence angle) is observed, and this is in agreement with previous studies conducted on heterogeneous rock samples (e.g. Maruyama et al., 2008; Näränen et al., 2008). The phase angle effect need only be accounted for above phase angles of >60° (i.e. near the terminator or poles for a nadir pointing instrument orbiting a spherical planet) and the relative size of the effect for different elements should be considered when expressing XRF results as elemental ratios at these phase angles.

Characterisation of the materials used to make the samples revealed several important findings. SEM imaging of the samples highlighted that the grains in the separate powders did not all have the same shape or surface texture. Laser profiling illustrated that the assumption of larger grain-size fractions providing rougher surfaces is not always correct. As such, in any future experiments of this kind, these factors should be considered and a set of more homogeneous samples which differ only in composition, and not in grain-size, shape or surface texture, should be employed. Further work, on additional samples, including extra mono-oxides (e.g. Ti and Ca), simple-oxide mixtures and relevant lithologies, and with a larger range of grain-sizes (and surface roughness) applicable to planetary regoliths would be beneficial and help complete the understanding of the issues at hand. Future experimental campaigns could also be improved by using (i) an SCD module

(as in the Brunel experiments) rather than a Si-PIN diode (as in the RESIK experiments) as the XRF detector (specifically to support instruments such as C1XS which employ SCDs); (ii) longer integration times, to provide higher signal to noise ratios and reduced errors; and (iii) an incident X-ray source that better resembles a solar X-ray spectrum.

XRF spectra of a lunar regolith simulant, JSC-1A, were obtained during both the experimental campaigns outlined here and the results were used to test the accuracy of the RAL abundance algorithm which will be used to estimate the major element abundance of the lunar surface from C1XS data (e.g. chapter 4). When the input spectrum is well defined and the XRF spectrum has a sufficient signal to noise ratio, the algorithm can recover a known rock composition to within 1.0 elemental wt. % (1 σ).

Chapter 4: C1XS flare analyses – Mare Serenitatis and Oceanus Procellarum

4.1. Introduction

C1XS obtained lunar XRF spectra from thirty-one separate solar flare events during the mission (see Table 2.1). In this chapter, data from two of these flares, with predominantly basaltic ground tracks, are analysed. The first data were obtained from an A-class (10^{-8} – 10^{-7} Wm^{-2}) flare on 12th December 2008 (between 02:27:00 U.T. and 02:39:00 U.T.) with a track (~1150 km in length) that runs through Mare Serenitatis (at a longitude of ~13°). The second flare reached B-class magnitude (10^{-7} – 10^{-6} Wm^{-2}) on 10th February 2009 (between 23:07:54 U.T. and 23:25:09 U.T.). This flare has a ~1800 km ground track through western Oceanus Procellarum at a longitude of ~290°. Both flares have a footprint width of 50 km (full-width). The boresight tracks of both these flares are shown in Figure 2.10. The broad location on the Moon for both flares is shown in Figure 4.1 and the regions within the two boxes are shown in more detail in Figure 4.2 through Figure 4.11.

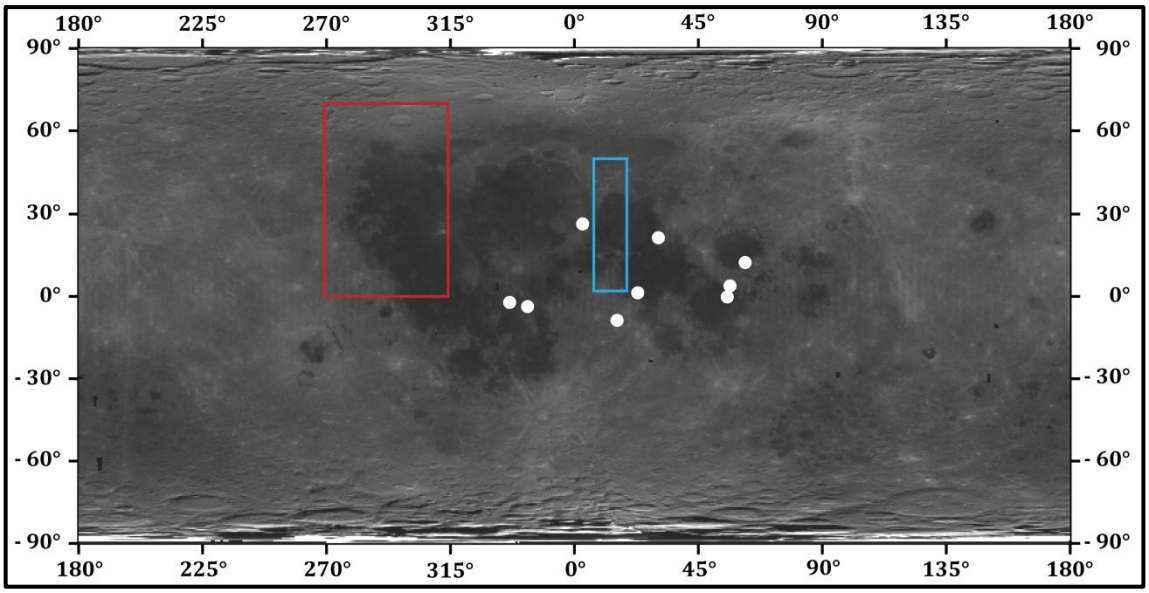

Figure 4.1. Clementine albedo (750 nm) image of the Moon (simple cylindrical projection) showing (i) the broad areas on the lunar surface that contain the footprints of both the Mare Serenitatis (blue box) and the Oceanus Procellarum (red box) flares. These areas are shown in more detail in Figure 4.2 to Figure 4.11. The white dots indicate the Apollo and Luna landing sites from which samples have been returned (see also Figure 1.1).

The mostly basaltic nature of these flare footprints provides an opportunity to meet one of the major C1XS science objectives: to study the composition and evolution of mare basalts

over a number of lava flows (Crawford et al., 2009), and this can be achieved both on an inter- and intra-mare scale. Oceanus Procellarum amongst the lunar maria consists of lava flows with especially variable compositions and eruption ages (e.g. Pieters, 1978; Wilhelms et al., 1987; Hiesinger et al., 2003), as illustrated in Figure 4.8 to Figure 4.11. However, the C1XS flare ground track only samples a subset of these deposits. Likewise, Mare Serenitatis is made up of distinct lava flows (e.g. Hiesinger et al., 2000, map 29 individual deposits), although their temporal range is smaller than for Oceanus Procellarum (see Figure 4.3 and Figure 4.8).

4.1.1. Mare Serenitatis: geological setting

Wilhelms et al. (1987) assign a Nectarian age to the Serenitatis basin and an absolute radiometric age of ~3.89 Ga is given by Dalrymple and Ryder (1996), which also falls in the Nectarian, as defined by Stöffler and Ryder (2001). Basalt samples collected from the south east of the basin during Apollo 17 indicate that KREEP volcanism was occurring in the region prior to the basin-forming impact (Ryder et al., 1977; Ryder, 1987). The oldest (~3.8 Ga) mare basalt units (with unusually low albedo) are often exposed at the edge of the basin, where they contact highlands material; the youngest (~2.5 Ga) basalts tend to occur in the centre of the basin (Hiesinger et al., 2000). The C1XS flare ground track travels through the length of western Mare Serenitatis, sampling the highland areas to its north and south (e.g. Figure 4.2). It passes through lava flows which range in age from ~3.8 Ga to ~2.8 Ga (Figure 4.3), which appear (Figure 4.5 and Figure 4.6) to be low-Ti basalts (~3 – 4 wt. % TiO_2) with relatively high FeO contents (~16 – 20 wt. %)[4].

[4] The maps of TiO_2 (Figure 4.5 and Figure 4.10) and FeO (Figure 4.6 and Figure 4.11) content are generated using Clementine multispectral reflectance data and the algorithms of Gillis et al. (2003) and Gillis et al. (2004) respectively. These, along with other abundance algorithms, are described in section 5.1.2.

Figure 4.2. Clementine albedo image of the area included within the blue box in Figure 4.1, showing the ground track (~1150 km long, 50 km wide) of the Mare Serenitatis flare (the area contained within the dotted lines is a subsection entirely within Mare Serenitatis). Major features are labelled.

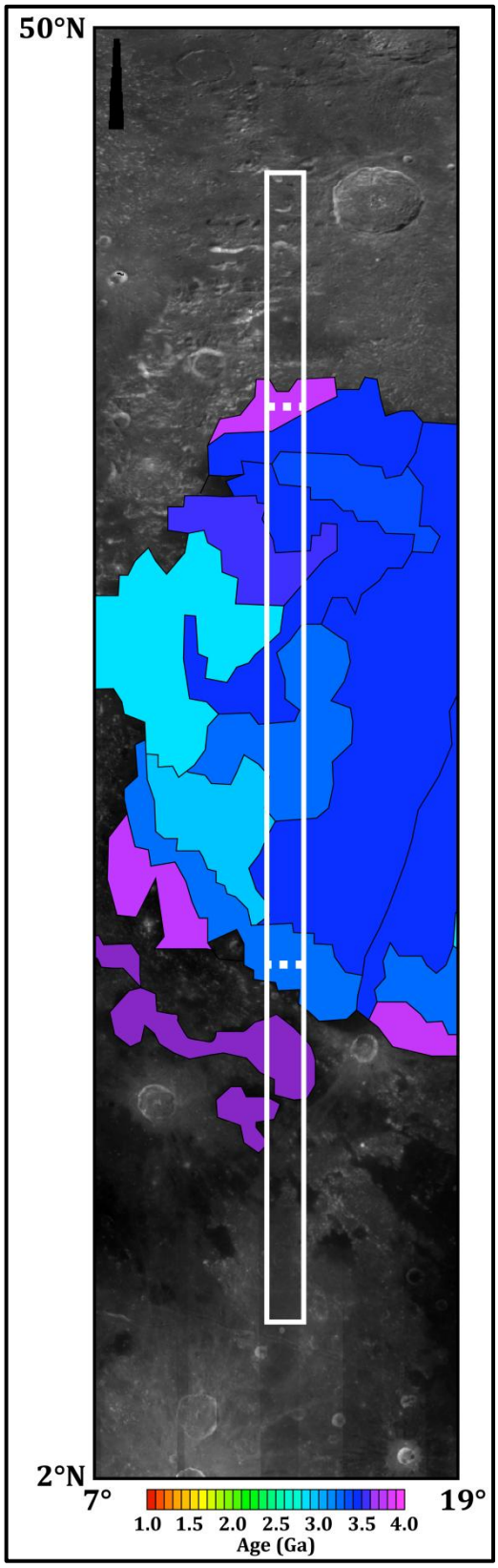

Figure 4.3. Albedo image of the Mare Serenitatis flare region with the lava flow boundaries, as mapped by Hiesinger et al. (2000) superimposed, as well as the C1XS flare ground track (and its mare subsection). The basaltic units are coloured according to their estimated, crater counting age. The lava flow map is taken from Hiesinger et al. (2008).

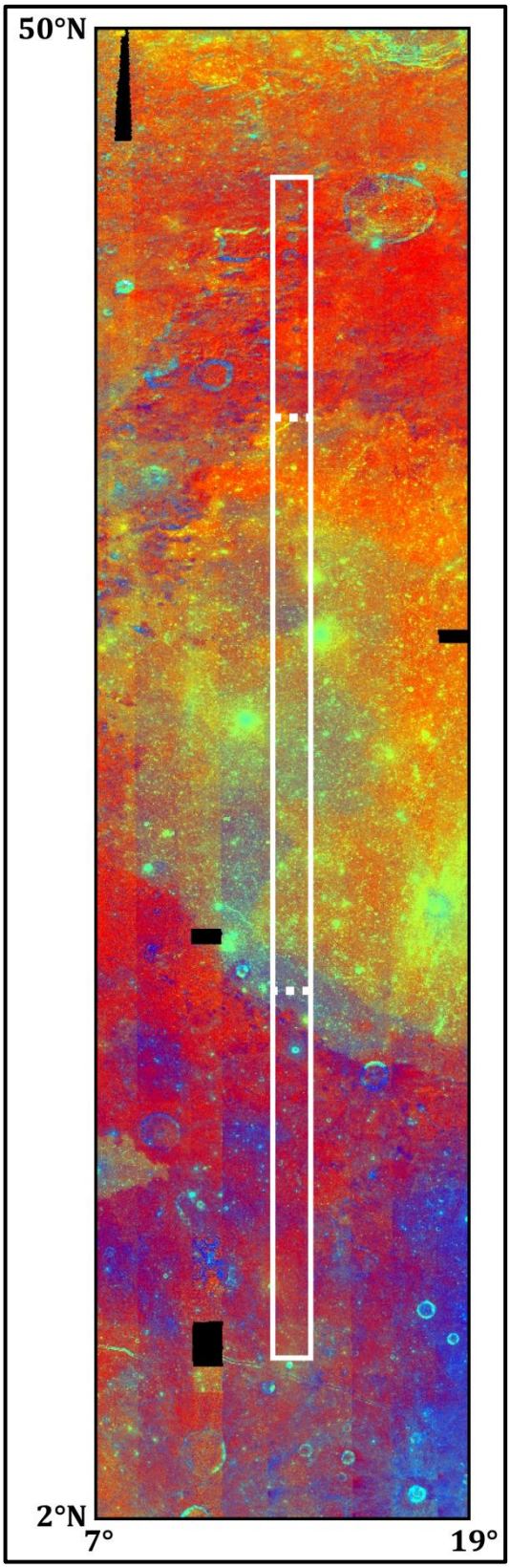

Figure 4.4. Clementine false colour (RGB image, where red = 750/415 nm; green = 750/950 nm; blue = 415/750 nm) image showing the Mare Serenitatis flare ground track (and the mare subsection). A dark red colour indicates mature highlands material, orange and blue represent mature low- and high-Ti basalts respectively, and cyan indicates either fresh highlands or fresh basaltic material.

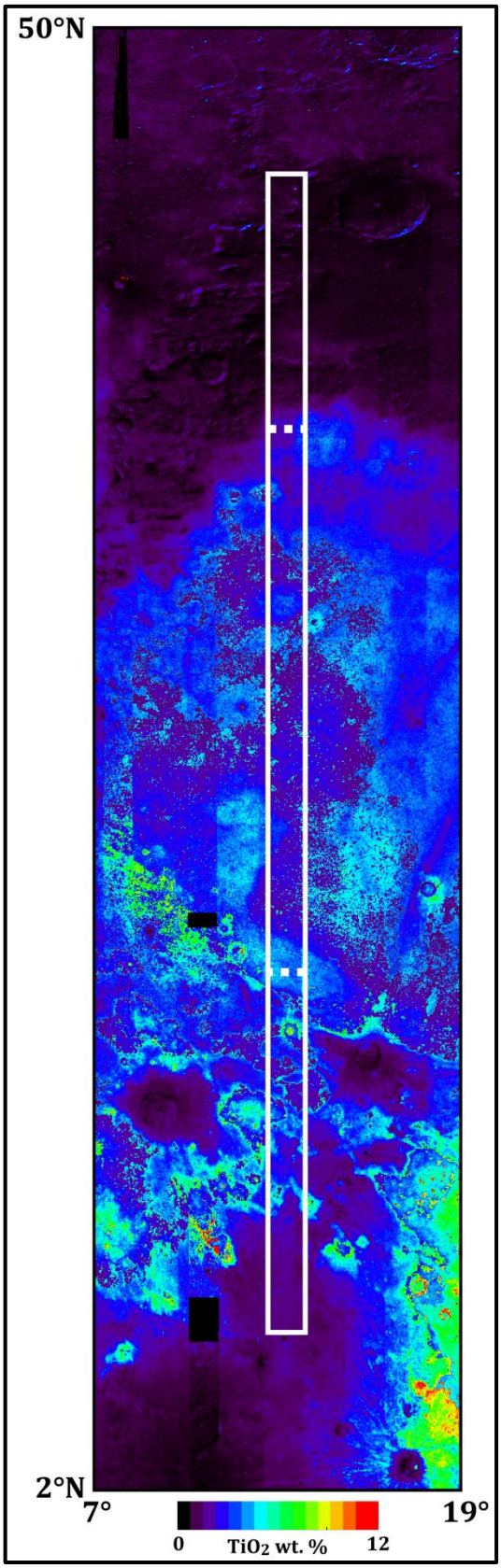

Figure 4.5. Map of TiO_2 wt. % content for the Mare Serenitatis flare region, derived from Clementine multispectral reflectance data according to the algorithm of Gillis et al. (2003), with the flare ground track and the mare subsection shown.

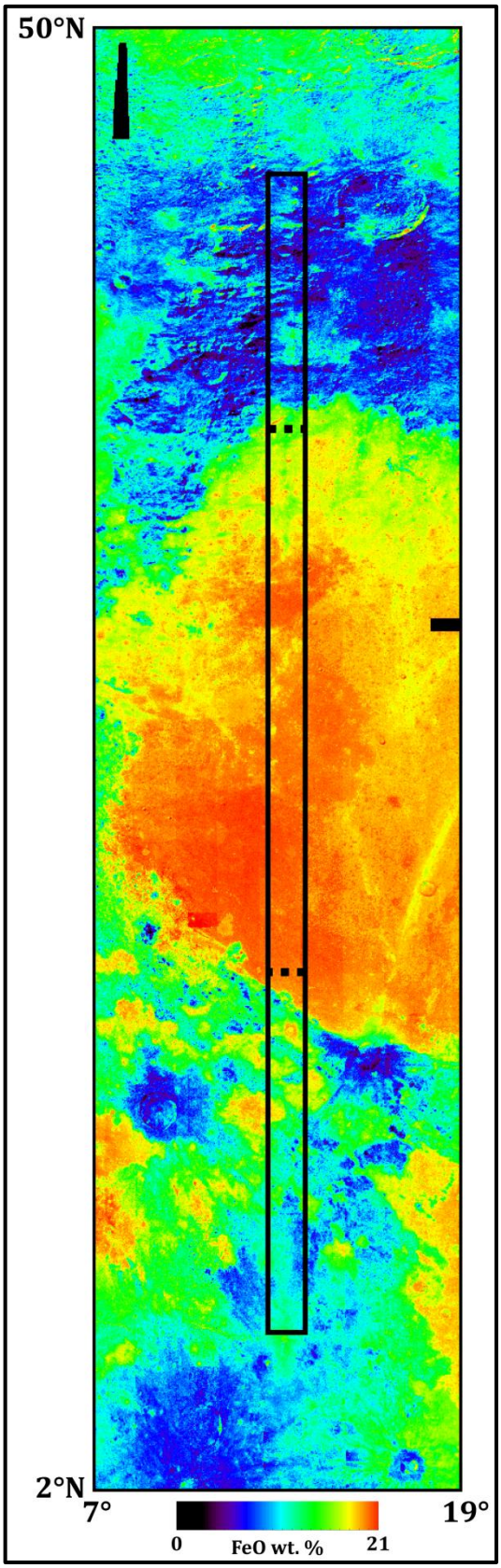

Figure 4.6. Map of FeO wt. % content for the Mare Serenitatis flare region, derived from Clementine multispectral reflectance data according to the algorithm of Gillis et al. (2004), with the flare ground track and the mare subsection shown.

4.1.2. Oceanus Procellarum: geological setting

Wilhelms et al. (1987) note the concentric nature of the deposits within the Oceanus Procellarum, and this is clearly visible in the false colour image of the second flare region (Figure 4.9). The Oceanus Procellarum flare ground track falls mainly within the outer band of the Procellarum deposits, consisting of mostly low-Ti (~3 wt. %) basalts that are of Upper Imbrian age (~3.5 Ga). This ground track is more variable in terms of FeO content (Figure 4.11) than TiO_2 (Figure 4.10). The FeO contents of the seven individual regions of interest for this flare (see section 4.2.2) vary from ~6 wt. % in the highlands of region 1, to between ~15 wt. % and ~18 wt. % in the different basaltic deposits. The diversity of the whole of Oceanus Procellarum is much better represented by this range of FeO contents, than by the relatively constant TiO_2 abundances.

The inner parts of the Procellarum basin contain younger (up to ~1 Ga; Hiesinger et al., 2003, therefore some of the youngest basaltic lunar deposits) and more Ti-rich basalts, as well as other large scale, volcanic, non-mare deposits, such as the Aristarchus Plateau and Marius Hills (Wilhelms et al., 1987). The superposition of numerous impact basins and craters on top of the (postulated) original Procellarum basin, through its long history, is likely to have created a complex lithospheric and mantle structure that probably influenced the pattern of extruded materials now observed at the surface (Wilhelms et al., 1987).

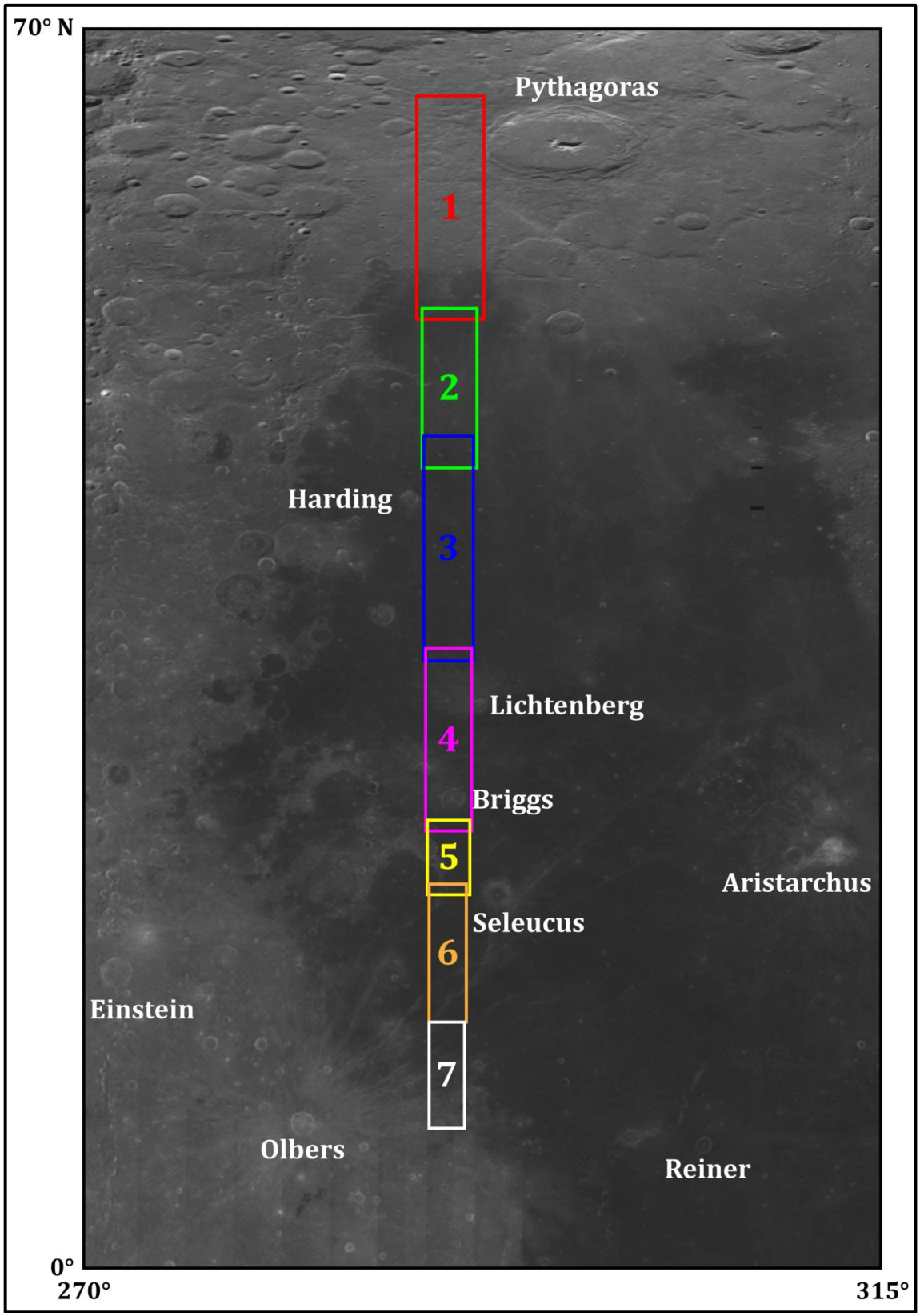

Figure 4.7. Clementine albedo image of the area included within the red box in Figure 4.1 showing the ground track (~1800 km long, 50 km wide) of the Oceanus Procellarum flare. This flare has been split into seven regions of interest (see section 4.2.2) which have been assigned a colour and number. The major craters are labelled.

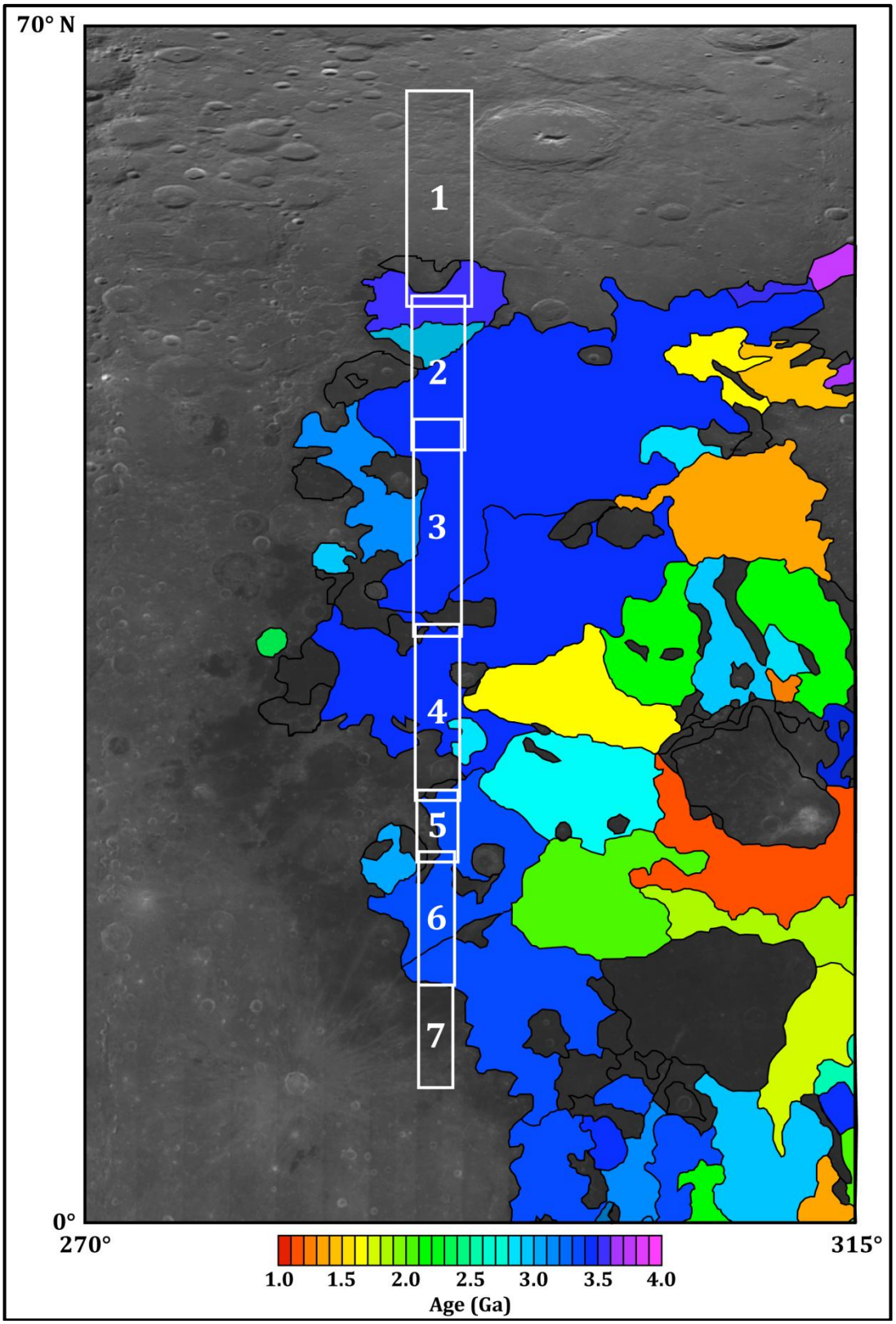

Figure 4.8. Albedo image of the Oceanus Procellarum flare region with the basaltic mapping of Hiesinger et al. (2003) superimposed, as well as the seven regions of interest into which the flare has been split. As in Figure 4.3, the basaltic units are coloured according to their estimated, crater counting age. Those units without a colour either have not been dated through crater counting, or are not basaltic in nature. The lava flow map is taken from Hiesinger et al. (2008).

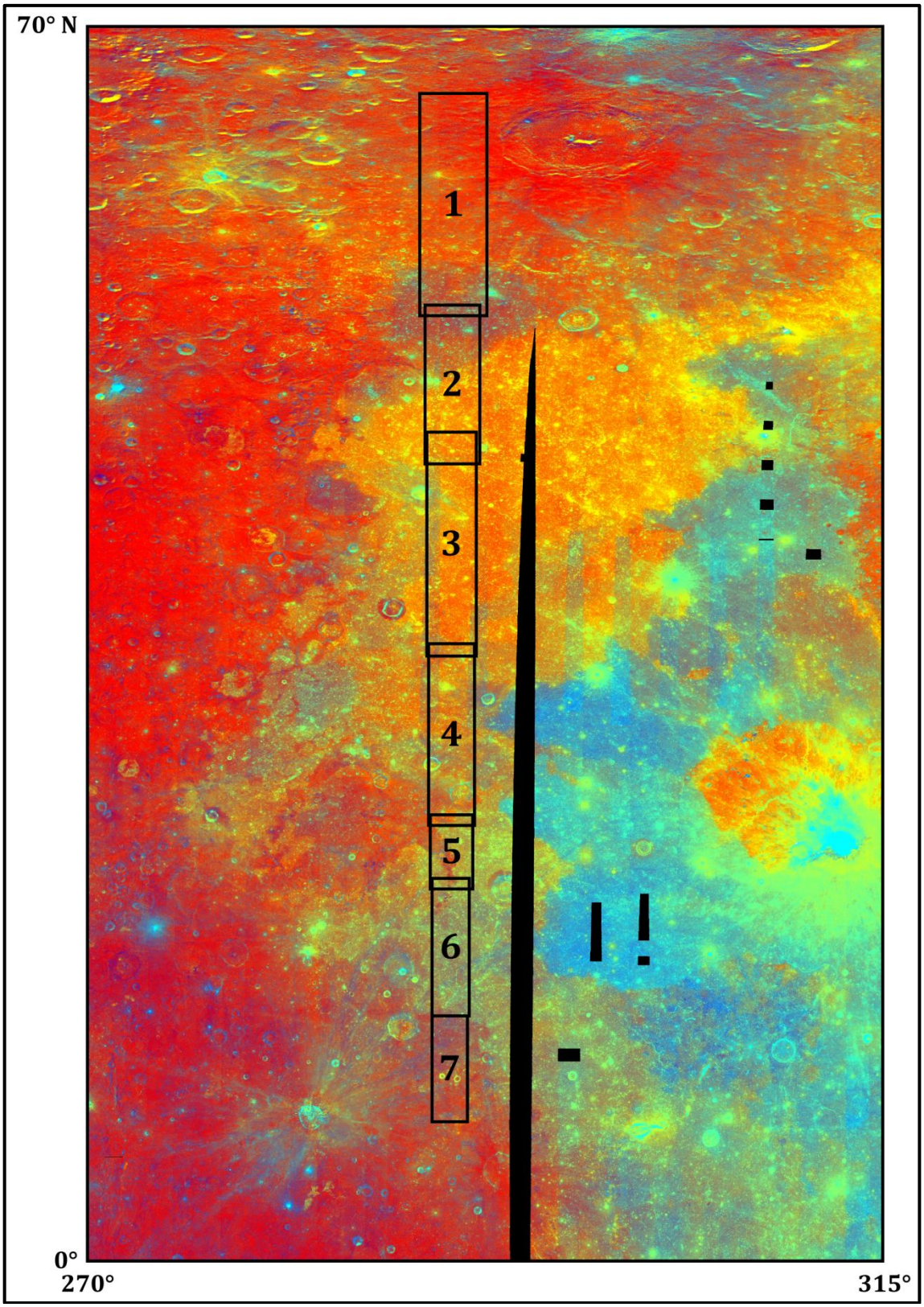

Figure 4.9. Clementine false colour image showing the footprints of the seven regions of interest in the Oceanus Procellarum flare. The colour scheme is the same as that in Figure 4.4.

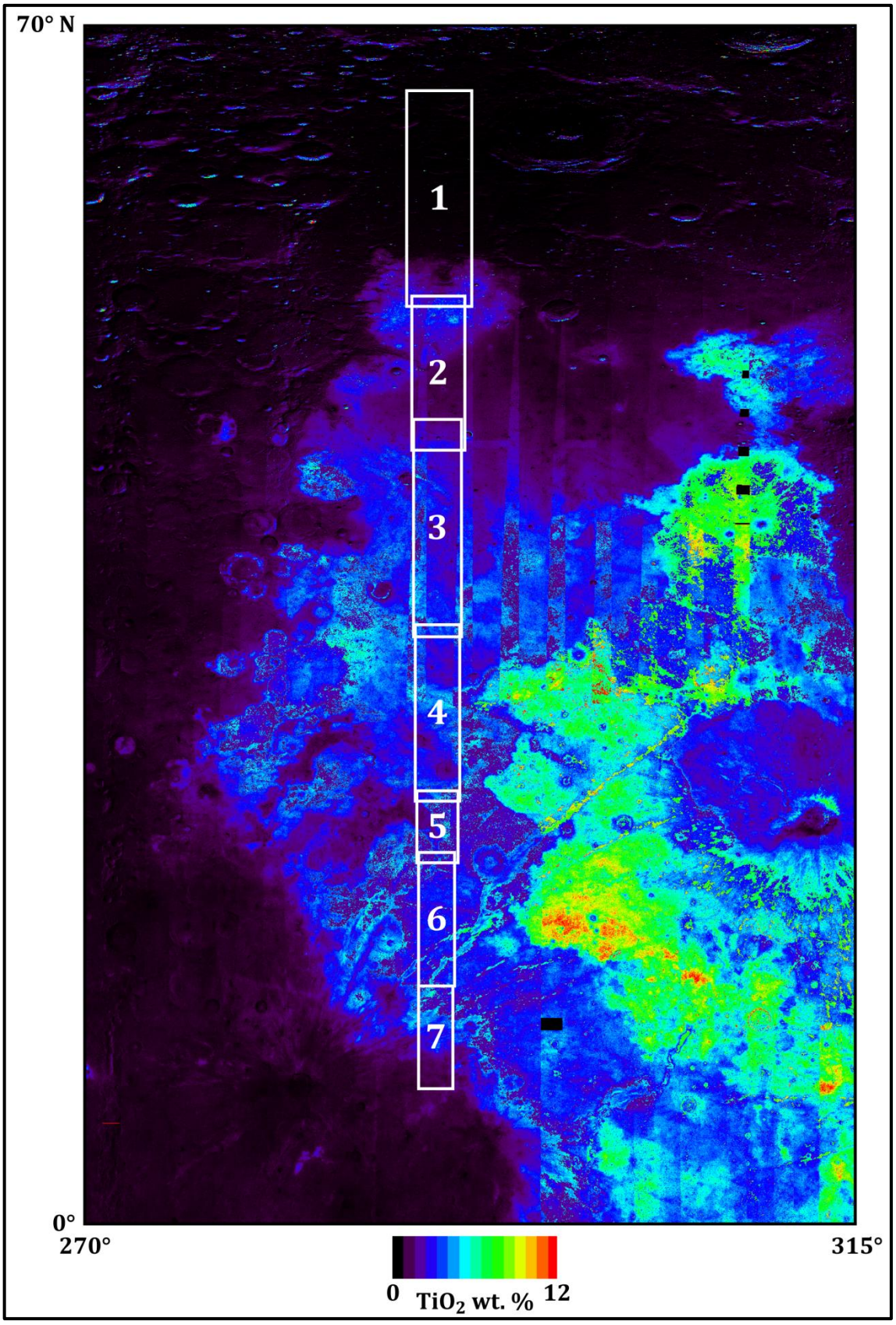

Figure 4.10. Map of TiO_2 wt. % content for the Oceanus Procellarum flare region, according to the algorithm of Gillis et al. (2003), with the footprint of the seven individual regions of interest shown.

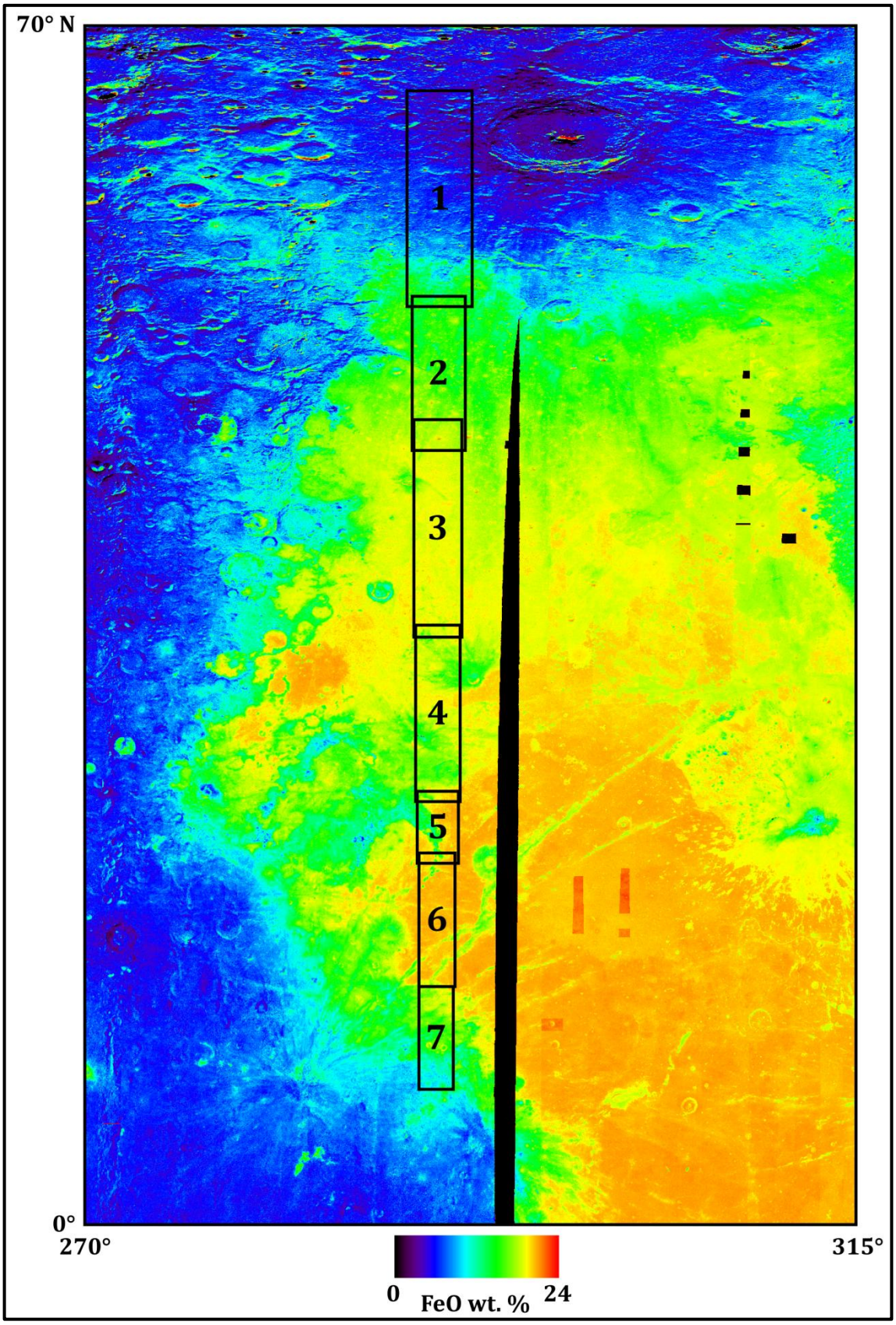

Figure 4.11. Map of FeO wt. % content for the Oceanus Procellarum flare region, according to the algorithm of Gillis et al. (2004), with the footprint of the seven individual regions of interest shown.

4.2. Methods

4.2.1. *Data processing*

As outlined in section 2.5, the processing of raw C1XS data, into calibrated, X-ray background-subtracted spectra, is conducted with a set of IDL routines (written by B. Kellett) that:

(i) rename the original data files with a form (Level 0 data) that includes the time at which they were obtained;

(ii) read the Level 0 data and creates three separate *.dat* files: (a) type 9 data which contain detector parameter information, relating to the detector zero noise peaks (see section 2.3), (b) type 0 data which are the house keeping information, and (c) the actual X-ray event data as type 10, 11 or 12 (spectral type) packets (depending on the count rate, see section 2.2.2), for the two flares analysed in this chapter, type 11 packets were generated;

(iii) collate the data for the period of interest, fit the zero peaks for each detector, and use the RESIK calibration gain values (which are temperature dependent; see section 2.3) to produce an energy calibrated spectrum; and

(iv) plot intensity as it varies with time and energy (e.g. Figure 4.13) for specific (time interval) files. For these analyses, the data from all twenty-four detectors have been coadded to obtain the maximum signal. The input from each detector is independently corrected for temperature dependent gain changes, using instrument housekeeping temperature information (see Figure 4.12). At this stage, the X-ray background (see below) level is subtracted from the measured signal. The resultant spectra are then summed in time, in order to ensure that the signal to noise ratio is sufficient for geological interpretation. The spectral data are then written into *ascii* files which can be fitted using the RAL abundance algorithm (described in section 2.5.1), or other suitable modelling code, to produce quantitative elemental abundance estimates.

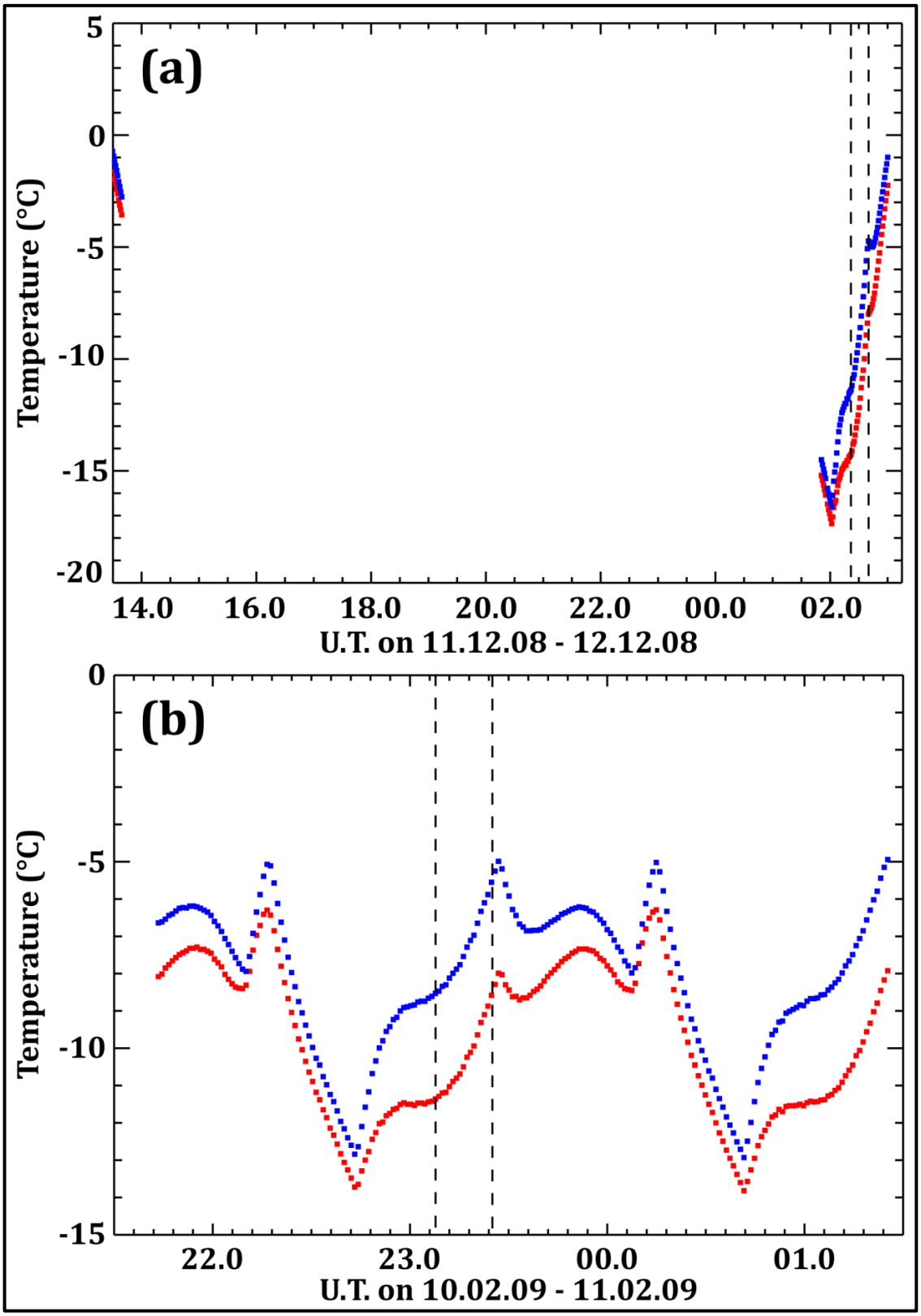

Figure 4.12. Detector temperature variation during the (a) Mare Serenitatis and (b) Oceanus Procellarum flares. The black dashed lines indicate the start and end of the analysis periods. The two coloured lines represent data from the two temperature sensors on the instrument. The temperature varies from about -15°C to about -5°C during the Mare Serenitatis flare and from about -11.5°C to -5°C during the Oceanus Procellarum flare.

X-ray background subtraction

X-ray background signals in X-ray detectors can have both an internal and an external source. The internal source arises from the dark current and signal processing noise of the detector; this is temperature dependent and increases with radiation damage (Gow et al., 2008). Pre-flight calibration results showed that the internal background was negligible at temperatures lower than -5°C (Kellett, 2008). The external contribution is caused by the interaction of protons and electrons (e.g. solar cosmic rays and galactic cosmic rays) in lunar orbit with the detectors. Those particles with low energies can interact directly with the detectors, deposit energy and thus mimic an X-ray event; interactions involving higher energy particles can create secondary particles that will also be indistinguishable from an X-ray event. During the mission, C1XS collected many spectra of the quiet X-ray background, observing a featureless continuum that is independent of temperature and which varies little with time, i.e. within an orbit, between orbits, or between 'day-side' and 'night-side' observations (B. Kellett, personal communication). However, during crossings of the Earth's geotail by the Moon, the background significantly increased, with a harder continuum (i.e. flux is increased at higher energies). Observations made close to the terminator reveal a strong Al line in the background spectra and this signal is thought to be caused by PIXE (Particle Induced X-ray Emission) from the Al-filters in front of the detectors (see section 2.2.1) because there is no concomitant rise in the Mg and Si lines.

The 'average' C1XS X-ray background, with a quiet, featureless continuum is applicable to the Mare Serenitatis flare in December 2008, however, the Oceanus Procellarum flare occurred during one of the geotail crossings and its X-ray background has a greater intensity than the average C1XS spectrum (the observations did not occur close to the terminator and therefore a strong Al-line contribution due to PIXE is not an issue). However, the slope of the average background spectrum (between the spectrum above and below 10 keV) and that during the Oceanus Procellarum flare is constant. The high energy section is therefore fitted and the constant spectral slope is used to determine the low-energy background flux (this background subtraction was conducted by B. Kellett).

4.2.2. *Flare track regions of interest*

The weak, A-class, Mare Serenitatis flare cannot be split into a large number of regions of interest (ROI) due to lack of signal. However, one subsection with a footprint entirely within the mare deposit has been defined (as shown in Figure 4.3 to Figure 4.6). The spectrograms in Figure 4.13 show the flux detected by C1XS for the two flares. The solid red lines in Figure 4.13a indicate the period of analysis for the Mare Serenitatis flare; the dotted lines indicate the mare subsection. For the Oceanus Procellarum flare (Figure 4.13b), the period of intense flux is divided into seven ROI, as indicated by the red lines and numbers. The start and end times of the flare sections are used to determine their individual footprints on the lunar surface from the SPICE[5] data. The approximate footprint boundary coordinates of the regions of interest, are given in Table 4.1.

The seven ROI into which the Oceanus Procellarum flare ground track has been split, allow the analysis to be conducted at the finest spatial resolution possible, by coadding several individual spectra (given the relatively poor counting statistics) to generate sufficient signal to noise ratios. This approach means that geologically distinct units may be incorporated into a single region. An alternative method could be to split the data according to previously determined unit boundaries (i.e. those in Figure 4.8).

[5] This loosely stands for Spacecraft ephemeris, Planet ephemeris, Instrument description, C-matrix (pointing information), Events, but this is not a simply explained acronym. SPICE is a system which provides instrument information during acquisition of planetary data. For the period of data acquisition, the data relate to: (i) the time, (ii) the instrument mode, (iii) the location of the spacecraft, (iv) the orientation of the spacecraft and instrument, (v) location, size, shape and orientation of the target body, and (vi) other relevant events occurring on the spacecraft or the ground data system. For full details see: http://naif.jpl.nasa.gov/naif/spiceconcept.html.

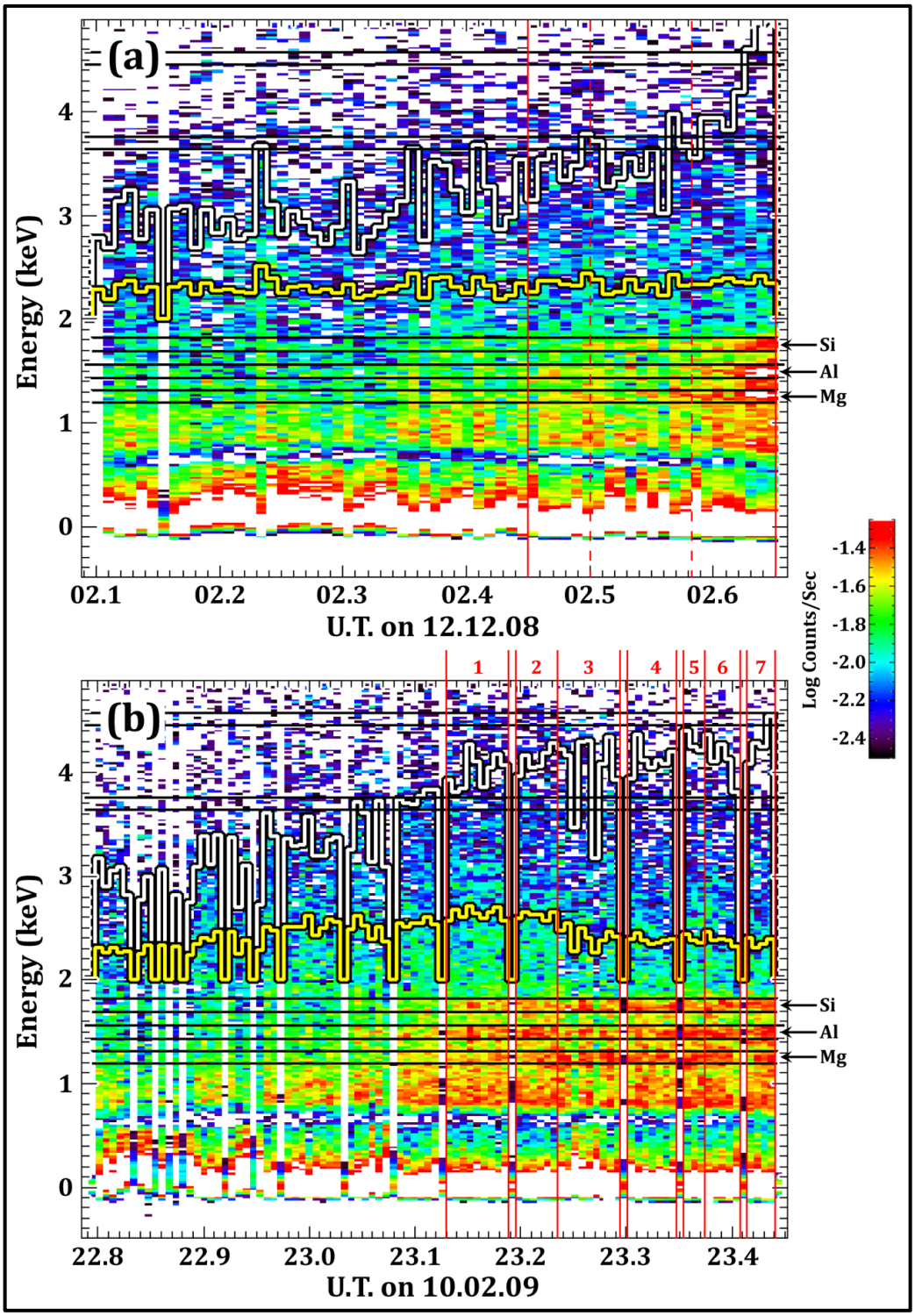

Figure 4.13. Spectrograms for the (a) Mare Serenitatis and (b) Oceanus Procellarum flares. The Mare Serenitatis flare includes one subsection (within the dotted lines) whose footprint falls entirely within the mare deposit. The Oceanus Procellarum flare is been split into seven ROI, of unequal length; these are indicated by the solid red lines and numbers. The periods of data acquisition end when the instrument reverts to 'stand-by' mode because of its rising temperature (see Figure 4.12). The yellow and white lines show the integrated counts in the energy ranges of 1 – 2 keV and 4 – 17 keV respectively; i.e. the rising white line indicates an A- or B-class flare that excites Mg, Al and Si, whereas the yellow line will only rise when the flare state is stronger and elements such as Ca and above are excited.

Table 4.1. Start and end times, approximate footprint boundary coordinates, mean phase angle and the length of the footprint, for the whole of the Mare Serenitatis flare (M.S. all) and its mare subsection (M.S. mare), as well as the Oceanus Procellarum (O.P.) regions of interest. The Mare Serenitatis flare occurred on 12th December 2008; the Oceanus Procellarum flare occurred on 10th February 2009.

ROI	Start U.T. (h:m:s)	End U.T. (h:m:s)	North (° N)	South (° N)	West (°)	East (°)	Mean phase angle (°)	Footprint length (km)
M.S. all	02:27:00	02:39:00	45.2	7.2	12.7	13.9	27.4	1153
M.S. mare	02:30:00	02:35:00	36.1	19.2	12.7	13.9	28.8	512
O.P. 1	23:07:54	23:11:29	66.2	53.6	-71.2	-67.4	73.4	382
O.P. 2	23:11:52	23:14:15	54.2	45.2	-70.9	-67.8	70.5	273
O.P. 3	23:14:15	23:17:50	47.0	34.3	-70.8	-68.0	68.6	385
O.P. 4	23:18:13	23:21:00	35.0	24.7	-70.7	-68.1	67.0	312
O.P. 5	23:21:24	23:22:12	25.3	21.1	-70.6	-68.2	64.8	127
O.P. 6	23:22:35	23:24:34	21.7	13.9	-70.5	-68.4	62.5	237
O.P. 7	23:25:09	23:26:33	13.9	7.9	-70.5	-68.5	61.0	182

4.2.3. *Elemental abundance modelling*

The RAL abundance algorithm (see section 2.5.1) has been used to model the calibrated, X-ray background-subtracted flare spectra in order to obtain quantitative elemental abundance estimates for the fluorescent lines they contain. The algorithm contains a number of parameters which can be changed in order to obtain the best modelled fit to the spectrum in question. The effect of these parameters on the modelling results is investigated (mostly using the Oceanus Procellarum flare spectra) in the following sections.

Incident solar X-ray spectrum

An incident solar X-ray spectrum (or spectra) for the flare period is required as an input for the algorithm; this must contain both the bremsstrahlung continuum *and* characteristic elemental lines. Although XSM was flown onboard Chandrayann-1 in order to measure the solar X-ray spectra for this purpose, both the A-class Mare Serenitatis and the B-class Oceanus Procellarum flares were below its detection capabilities (Huovelin et al., 2002) and no XSM spectra are available for this period. An alternative means of acquiring solar X-ray spectra for these flares is therefore required, and in this work the *atomdb* (version 2.0.0) database and modelling software (Harvard Chandra X-ray Center: http://cxc.harvard.edu/atomdb/features_idl.html) has been employed. This software generates a high resolution modelled solar spectrum with both the bremsstrahlung continuum and superimposed characteristic lines at given (quantised) temperatures. Three

example spectra, derived at temperatures of 3.1, 4.0 and 5.0 MK, are shown in Figure 4.14 at an energy bin resolution of 1 eV. The position and relative strength of the solar elemental lines are fundamental to the modelling of lunar XRF and it is therefore important that the spectral resolution of the modelled solar spectra[6] is as good as possible in order to produce the most accurate and robust results.

A temperature estimate for both flares is required to generate the most accurate modelled solar spectra for these analyses. Ordinarily, the 1 minute averages of the solar X-ray flux as measured by the GOES-10 (Geostationary Operational Environmental Satellite) Space Environment Monitor can be used to estimate solar flare temperature and brightness (Grande et al., 2007; Swinyard et al., 2009). These data are normally obtained in short (0.5 – 3.0 Å) and long (1.0 – 8.0 Å) wavelength bandpasses, however during these flares, GOES data were only acquired in the long bandpass (see Figure 4.15) and the temperature cannot be derived from the GOES data.

A maximum flare temperature for the Oceanus Procellarum (B-class) flare can be estimated, based on the fact that no Ca K_α line flux is detected by C1XS during this flare. The Ca lines in the modelled solar spectra (at ~3.6 keV) appear at a temperature of 4.0 MK with an intensity strong enough to excite a small amount of fluorescence; this is used as a maximum estimated temperature for the flare. This finding is in agreement with Kay et al. (2003), who show that solar flares (with coronal mass ejections) with a peak intensity equal to this flare have peak temperatures of 3.0 – 4.0 MK. Figure 4.15b illustrates that the Oceanus Procellarum flare was relatively constant in its intensity during the period of C1XS XRF data acquisition and therefore a larger range of flare temperatures do not need to be derived. The lower limit for the Oceanus Procellarum flare (i.e. 3.1 MK) is used as an upper limit for the A-class Mare Serenitatis flare; a lower limit of 2.5 MK for this flare was assumed (B. Kellett, personal communication). The abundance algorithm was therefore run using solar models generated for flare temperatures of both 2.5 MK and 3.1 MK for the Mare Serenitatis flare and for 3.1 MK and 4.0 MK for the Oceanus Procellarum flare, in

[6] Even in a case where XSM spectra are available, the spectral resolution (250 eV at 6 keV; Huovelin et al., 2002) is not good enough to resolve the individual elemental lines. An XSM spectrum should not be used directly for XRF modelling, rather its relative shape should be used to estimate the flare temperature so that a modelled spectrum can be generated with a database such as *atomdb*.

order to obtain estimates of elemental abundance ratios. The Oceanus Procellarum flare data were also fitted with a solar model for a flare temperature of 5 MK in order to more clearly investigate the effect of employing different flare temperatures on the modelling results (see Figure 4.16).

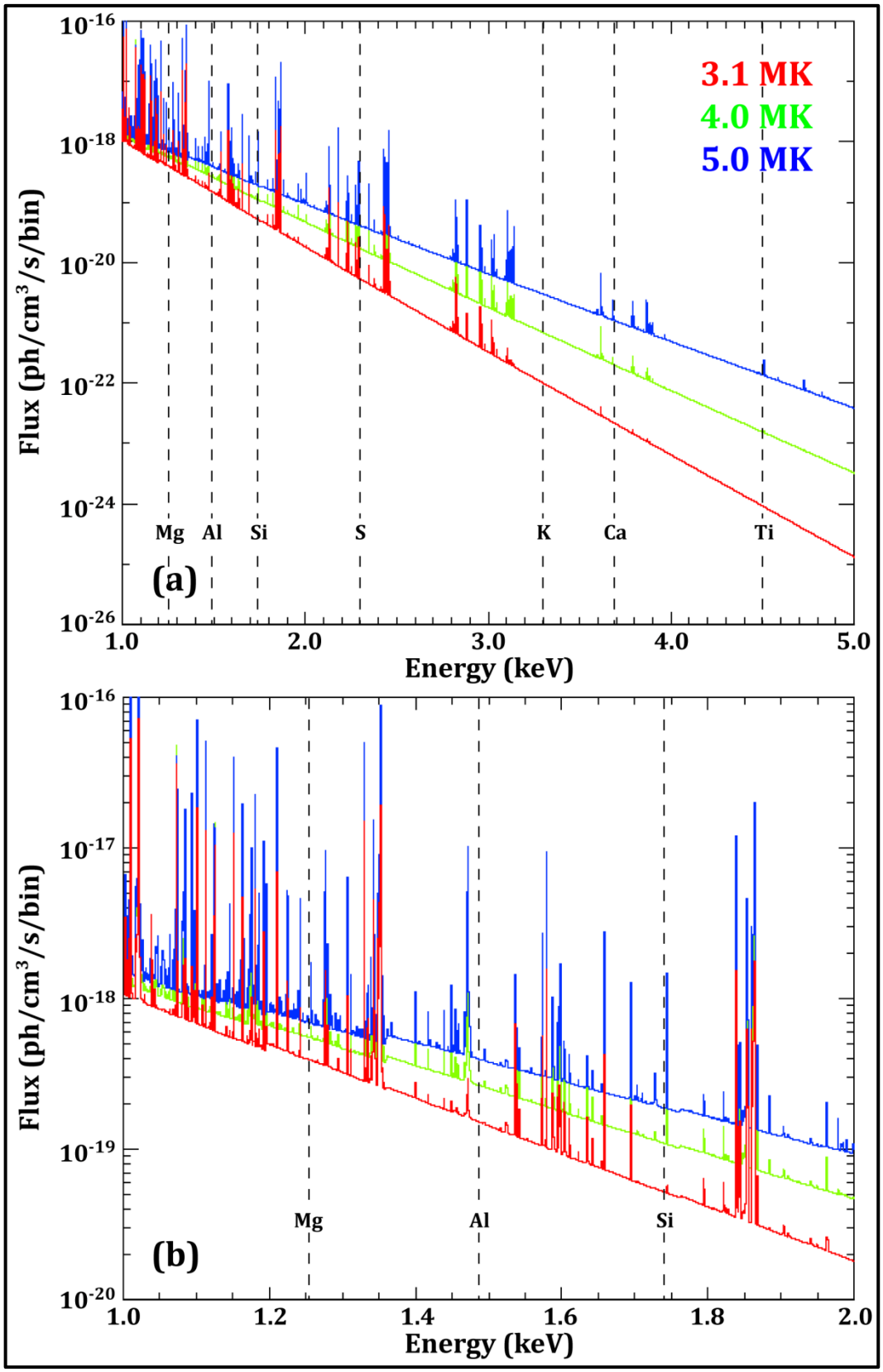

Figure 4.14. ***atomdb*** **generated modelled solar spectra at flare temperatures of 3.1 MK, 4.0 MK and 5.0 MK in the (a) 1.0 – 5.0 keV energy range. The large cluster of characteristic lines around the energies of Mg, Al and Si are shown in detail in (b) for the 1.0 – 2.0 keV energy range. Dashed lines indicate the K_α characteristic energies of major rock forming elements.**

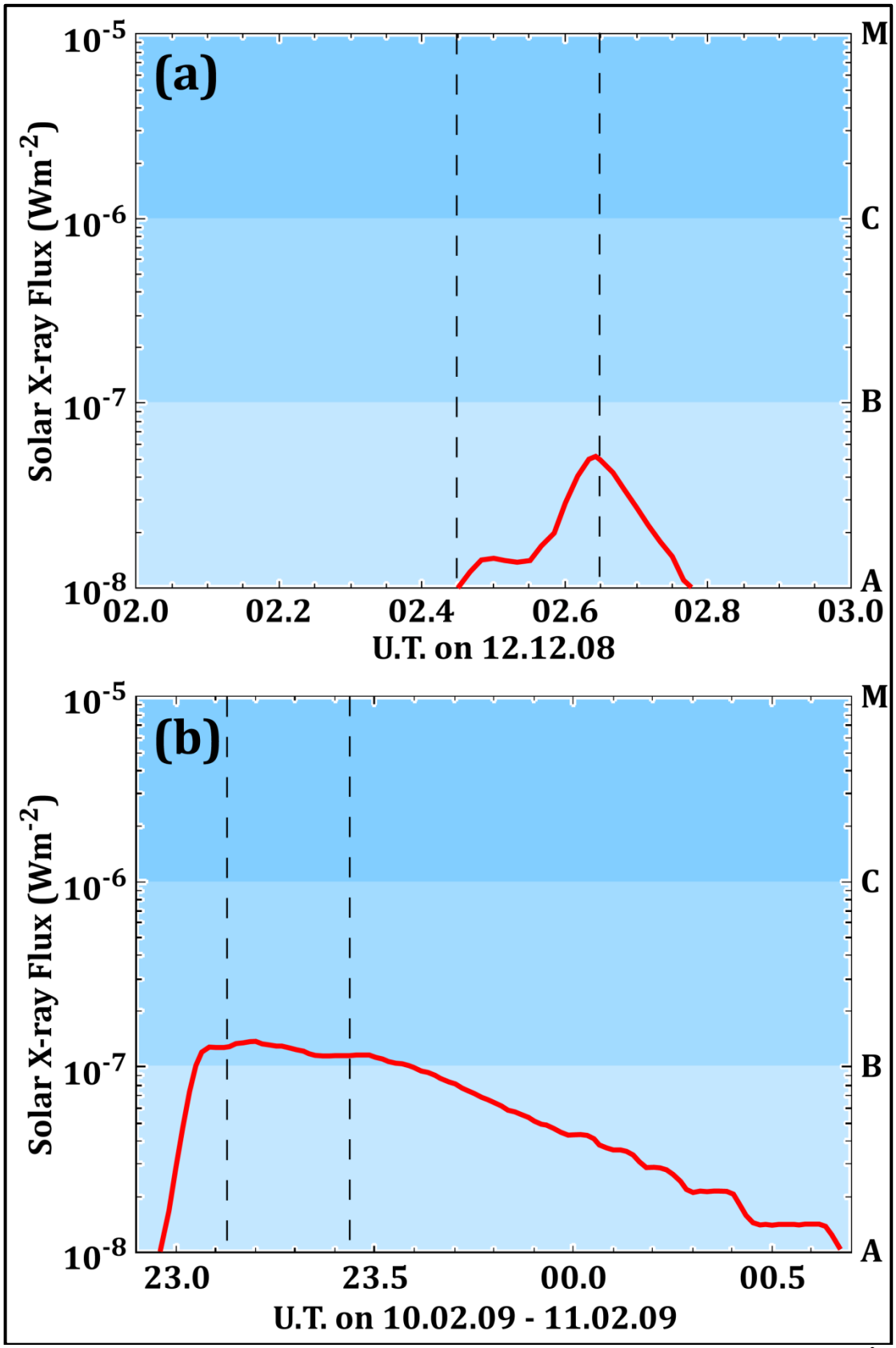

Figure 4.15. Solar X-ray flux data as measured in the GOES-10 long wavelength bandpass (1 – 8 Å) for (a) the Mare Serenitatis and (b) the Oceanus Procellarum flares. Dashed lines indicate the period of analysis of both flares. No short bandpass GOES data is available. Letters refer to the flare class.

C1XS spectral resolution

The spectral resolution of C1XS varies with temperature (Kellett, 2008; see Figure 2.9), as well as with other issues such as long term radiation damage (Gow et al., 2008; Smith & Gow, 2009). A parameter within the abundance algorithm can be set in order to produce modelled spectral fits which have elemental peaks with widths (resolution) that match the data. To find the optimum value for the Oceanus Procellarum flare, all of the seven ROI spectra were coadded to give a spectrum with the highest possible signal to noise ratio. The code was run until the best fit was realised (for each flare) and this value (i.e. the FWHM of element peaks) was kept constant for analyses of any of the shorter spectra.

Initial rock composition

The abundance algorithm operates by comparing and iteratively fitting the XRF (C1XS) spectra to an initial rock (major element) composition, which is specified prior to running the code. The effect on the resulting MgO/SiO_2 and Al_2O_3/SiO_2 ratios of using three different starting compositions for this input parameter was investigated, and is illustrated in Figure 4.16. The three rock compositions (given in Table 4.2) were: (i) typical lunar highlands crust (from Table 8.2 of Taylor, 1982), (ii) lunar regolith simulant JSC-1A (see section 3.2.1) which was used as a typical lunar mare basalt, and (iii) the average lunar surface as derived from Lunar Prospector gamma-ray data (Prettyman et al., 2006). Figure 4.16 illustrates that the difference in the MgO/SiO_2 and Al_2O_3/SiO_2 ratios that result from the modelling when using these different initial rock compositions is very small or negligible (i.e. the points overlie each other for any given ROI and flare temperature) and thus the modelling results are independent of the initial rock composition assumed. These results were generated using (i) solar models for flare temperatures of 3.1, 4.0 and 5.0 MK; (ii) a scattering coefficient (see below) of 1.0; and (iii) a phase angle of 0°. For the remaining analysis in this chapter the average lunar surface composition (Prettyman et al., 2006) is employed as the initial rock composition because it is relevant for the whole lunar surface and makes no assumptions about the lithologies observed by C1XS.

Table 4.2. The major element compositions used as initial conditions in the modelling code. The typical lunar highlands composition is taken from Table 8.2 of Taylor (1982); the lunar regolith simulant, JSC-1A is taken to have a typical lunar mare basalt composition (as measured using ICP-AES, see section 3.2.1); and the average lunar surface composition is that derived from Lunar Prospector gamma-ray data (Prettyman et al., 2006). Abundances are expressed as elemental wt. % values.

	Lunar highland crust (wt. %)	JSC-1A (wt. %)	Average lunar surface (wt. %)
C	0.00	0.00	0.00
O	44.77	44.71	43.55
Na	0.00	2.40	0.00
Mg	4.10	5.10	4.35
Al	13.0	8.63	12.35
Si	21.0	21.52	20.30
S	0.00	0.00	0.00
K	0.00	0.67	0.07
Ca	11.30	6.91	11.29
Ti	0.34	1.05	0.56
Fe	5.10	8.53	5.93
Total	**99.61**	**99.52**	**98.40**

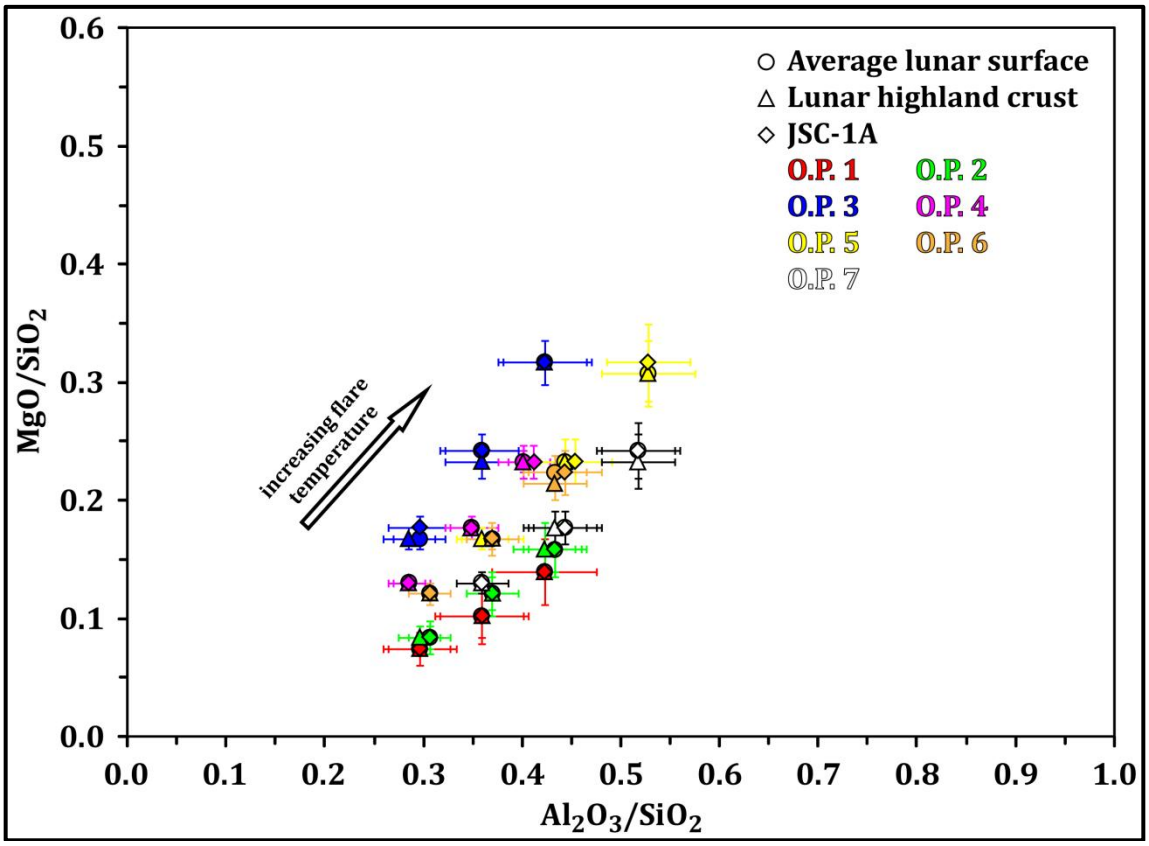

Figure 4.16. MgO/SiO_2 vs. Al_2O_3/SiO_2 oxide wt. % ratios for the seven Oceanus Procellarum ROI. These oxide ratios were converted from the Mg and Al elemental wt. % values generated by the RAL abundance algorithm which was run using three different modelled solar X-ray spectra with flare temperatures of 3.1 MK, 4.0 MK and 5.0 MK. For each ROI the result at 3.1 MK has the lowest ratios and at 5.0 MK, the highest (the arrow indicates the approximate trend of the modelled ratios at increasing flare temperature). For each ROI and each flare temperature, the model is run using three different initial rock compositions (an average lunar surface value from Lunar Prospector results: Prettyman et al., 2006; an average lunar highlands crust value: Taylor, 1982; and the composition of the lunar regolith simulant, JSC-1A, taken as a typical lunar basalt composition), which are given in Table 4.2 and are designated by the three different symbols. The results are seen to be essentially independent of the assumed initial rock composition. Error bars indicate 1 σ fitting errors.

Scattering coefficient

A coefficient is included in the algorithm that deals with the amount of Thomson scattering (elastic scattering of electromagnetic radiation) of X-rays from the lunar surface (Clark & Trombka, 1997), which will vary depending on the viewing geometry during the observation and the physical characteristics of the lunar surface being observed. It is important that this contribution to the spectrum is properly determined, so that the true level of XRF, and therefore elemental abundances, can be established. Both the modelled MgO/SiO_2 and Al_2O_3/SiO_2 ratios increase with the level of scattering (having a larger value for this coefficient), as illustrated in Figure 4.17 for two example Oceanus Procellarum

regions (O.P 1 and O.P. 5) whose spectra are modelled using solar spectra for flare temperatures of 3.1 MK and 4.0 MK. Changing the scattering coefficient mostly affects the fitting of the data at low energies (i.e. below ~1 keV where the greatest concentration of solar lines occur), and causes a larger change in the MgO/SiO_2 ratios than the Al_2O_3/SiO_2 ratios. For these data (from both flares), very small amounts of solar flux scattering need to be invoked in order to fit the measured spectra (see Table 4.3).

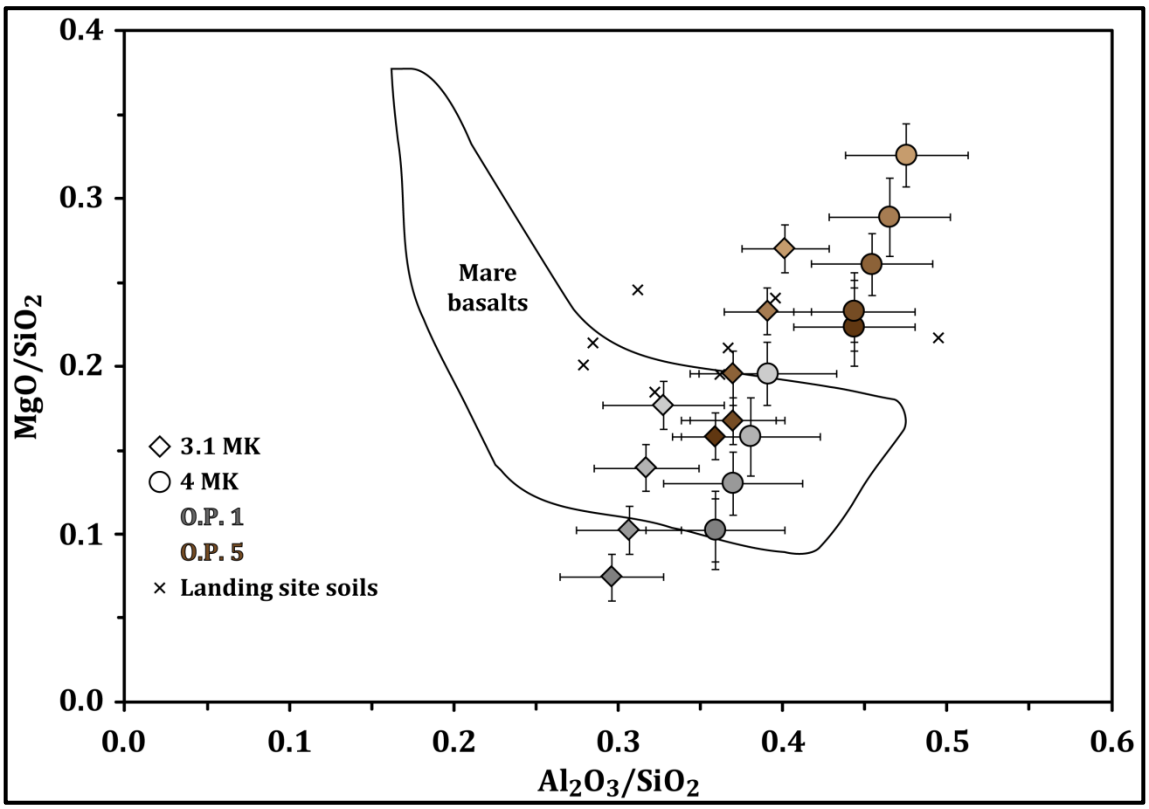

Figure 4.17. MgO/SiO_2 vs. Al_2O_3/SiO_2 graph for two example Oceanus Procellarum regions (ROI 1 and ROI 5), illustrating the effect on the ratios derived when different scattering coefficients are used in the fitting algorithm. For both ROI the algorithm is run using solar models for two flare temperatures (3.1 MK and 4.0 MK) and six different scattering coefficients (0.05, 0.5, 1.0, 5.0, 10.0 and 15.0; darker shaded symbols represent lower coefficients). The composition of mare basalts and average soils from the Apollo and Luna landing sites are shown for comparison. For both flares, very small coefficients (0.05 or less; see Table 4.3) are required in order to fit the spectra around 1 keV (see Figure 4.19 to Figure 4.21), indicating that very little scattering of the solar flux was occurring during the data acquisition. Varying the scattering coefficient below ~1.0 has no effect on these ratios (i.e. the data points overlie one another). Error bars indicate 1 σ fitting errors.

Phase angle

The phase angle is the final algorithm variable whose effect on modelling results has been investigated. The results presented so far, in Figure 4.16 and Figure 4.17, have been generated using a phase angle of 0° (for a nadir pointing instrument such as C1XS, this represents a situation where the Sun is directly behind the instrument). However, the phase angle varies from ~10° to ~45° for the Mare Serenitatis flare and from ~60° to ~75° for the Oceanus Procellarum flare. The code was therefore rerun to incorporate the mean phase angle of the flare or individual ROI, given in Table 4.1. This parameter accounts for the phase angle effect measured in chapter 3, treating it as a cosine of the incidence angle (equal to the phase angle for nadir-pointing instruments), as per the formulation of Clark & Trombka (1997).

The results presented in this chapter are given as ratios of two oxides (whose elements have similar K_α line energies), as such, two possible sources of error due to the phase angle effect are eliminated: (i) the small deviation of this effect from a cosine law, and (ii) the phase angles of observation for the Oceanus Procellarum flare are greater than 60°, which is the point at which the phase angle effect becomes important (see section 3.4.2). The Mare Serenitatis observations occurred at phase angles between ~10° and ~45°, which is within the range of negligible phase angle effect. The mid-point of the modelling results (in terms of MgO/SiO_2 and Al_2O_3/SiO_2 ratios) given by the algorithm for each Oceanus Procellarum ROI, using solar flare models at temperatures of 3.1 MK and 4.0 MK, are shown in Figure 4.18. Two separate cases are illustrated: (i) an arbitrary phase angle of 0° is used, and (ii) the mean phase angle for each ROI is used. There is only a small difference (mean phase angles give lower ratios) in the abundance ratios between these two situations.

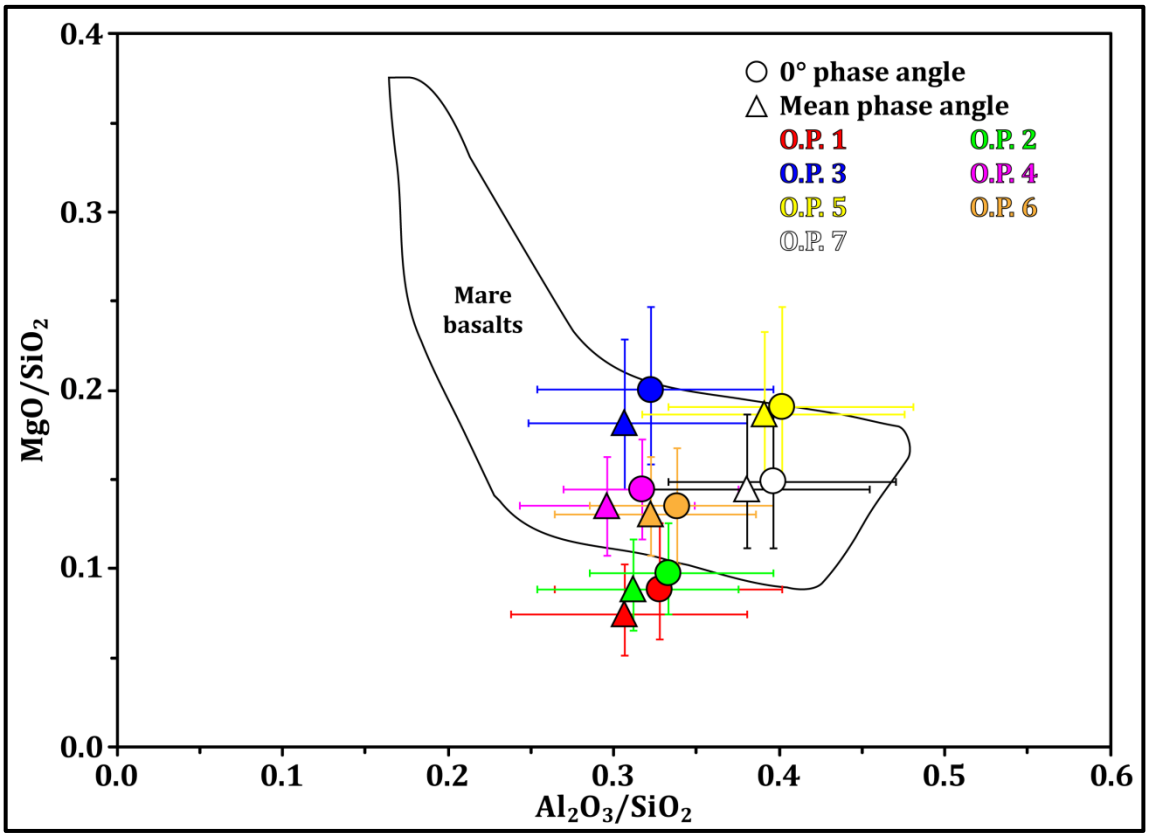

Figure 4.18. MgO/SiO_2 vs. Al_2O_3/SiO_2 for each of the seven Oceanus Procellarum ROI, with the abundances derived from running the code using (i) a fixed phase angle of 0° (circles) and (ii) the mean phase angle value for each region, given in Table 4.1 (triangles). Each data point represents the mean of the abundance ratios derived using solar models for flare temperatures of 3.1 MK and 4.0 MK; the error bars incorporate the range represented by these two temperatures and the 1 σ fitting errors. The approximate region occupied by mare basalt samples in terms of these oxide ratios is also shown to provide geological context.

4.3. Results

The final results presented here, for both the Mare Serenitatis and the Oceanus Procellarum flares, have been generated using the RAL abundance algorithm with optimum parameters given in Table 4.3. The C1XS instrument efficiency is derived from a modelled curve (Swinyard et al., 2010) which has been normalised to measurements made of (i) monochromated characteristic X-ray lines conducted during C1XS flight calibration at RESIK (see section 2.3), and (ii) the Crab nebula made by D-CIXS (Grande et al., 2007; Swinyard et al., 2009).

Table 4.3. RAL abundance algorithm parameter values used in deriving elemental wt. % values for the Mare Serenitatis (M.S.) and Oceanus Procellarum (O.P.) flares. The average lunar surface composition (Prettyman et al., 2006), given in Table 4.2 is used as the assumed initial rock composition.

ROI	Solar flare temperature (MK)	Spectral resolution factor	Solar flux scattering factor	Mean phase angle (°)
M.S. all	2.5 & 3.1	2.2	0.01	27.4
M.S. mare	2.5 & 3.1	2.2	0.05	28.8
O.P. 1	3.1 & 4.0	1.8	0.01	73.4
O.P. 2	3.1 & 4.0	1.8	0.01	70.5
O.P. 3	3.1 & 4.0	1.8	0.04	68.6
O.P. 4	3.1 & 4.0	1.8	0.05	67.0
O.P. 5	3.1 & 4.0	1.8	0.05	64.8
O.P. 6	3.1 & 4.0	1.8	0.05	62.5
O.P. 7	3.1 & 4.0	1.8	0.05	61.0

The fitted spectra (in the 0.5 – 2.5 keV energy range) for the Mare Serenitatis flare (and its mare subsection) are shown in Figure 4.19, and for the each Oceanus Procellarum ROI these are shown in Figure 4.20 and Figure 4.21. These spectra show the three energy peaks for Mg K_α (1.25 keV), Al K_α (1.49 keV) and Si K_α (1.74 keV). The resultant modelled elemental abundances are given in Table 4.4 for Mare Serenitatis and Table 4.5 for Oceanus Procellarum. The analytical totals of these results are not always close to 100 wt. % and this issue is investigated in the discussion (section 4.4.1). The mean MgO/SiO_2 and Al_2O_3/SiO_2 ratios for each ROI (from both solar flare temperature models) are calculated and shown in Table 4.6 along with errors which combine the 1 σ fitting errors and range in values provided by the two temperatures. The Lunar Prospector values which most closely match the C1XS ROI are also shown for comparison. These results are also plotted in Figure 4.22, where the C1XS results are compared with lunar sample lithologies and Lunar Prospector gamma-ray data from the area around the flare ground tracks. The C1XS results lie in the region of mare basalt compositions, however their agreement with Lunar Prospector results is poor. These results will be discussed in depth in the next section.

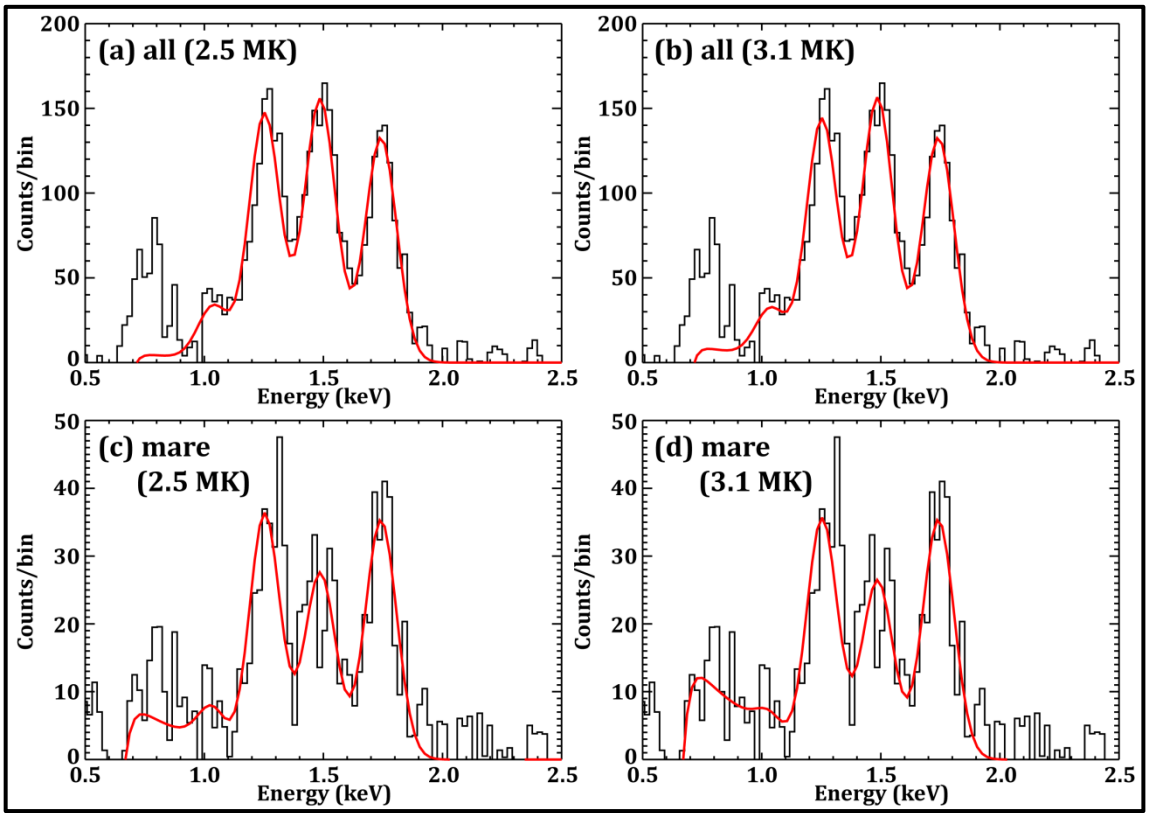

Figure 4.19. The background subtracted C1XS spectra for the whole Mare Serenitatis flare (a and b) and the mare subsection (c and d), with the RAL abundance algorithm fitted model generated using solar models for flare temperatures of 2.5 MK and 3.1 MK. The Mg K_α (1.25 keV), Al K_α (1.49 keV) and Si K_α (1.74 keV) peaks can be seen in each case. There is a clear difference between the relative strength of the Mg and Al lines in the two separate areas; the mare subsection has a much lower Al contribution, which is reflected in the oxide ratios presented in Figure 4.22a. The group of lines at ~0.8 keV is a scattered solar line contribution and is disregarded in the fitting routine. The Na peak (~1.0 keV) is also attributable to scattered solar lines rather than XRF.

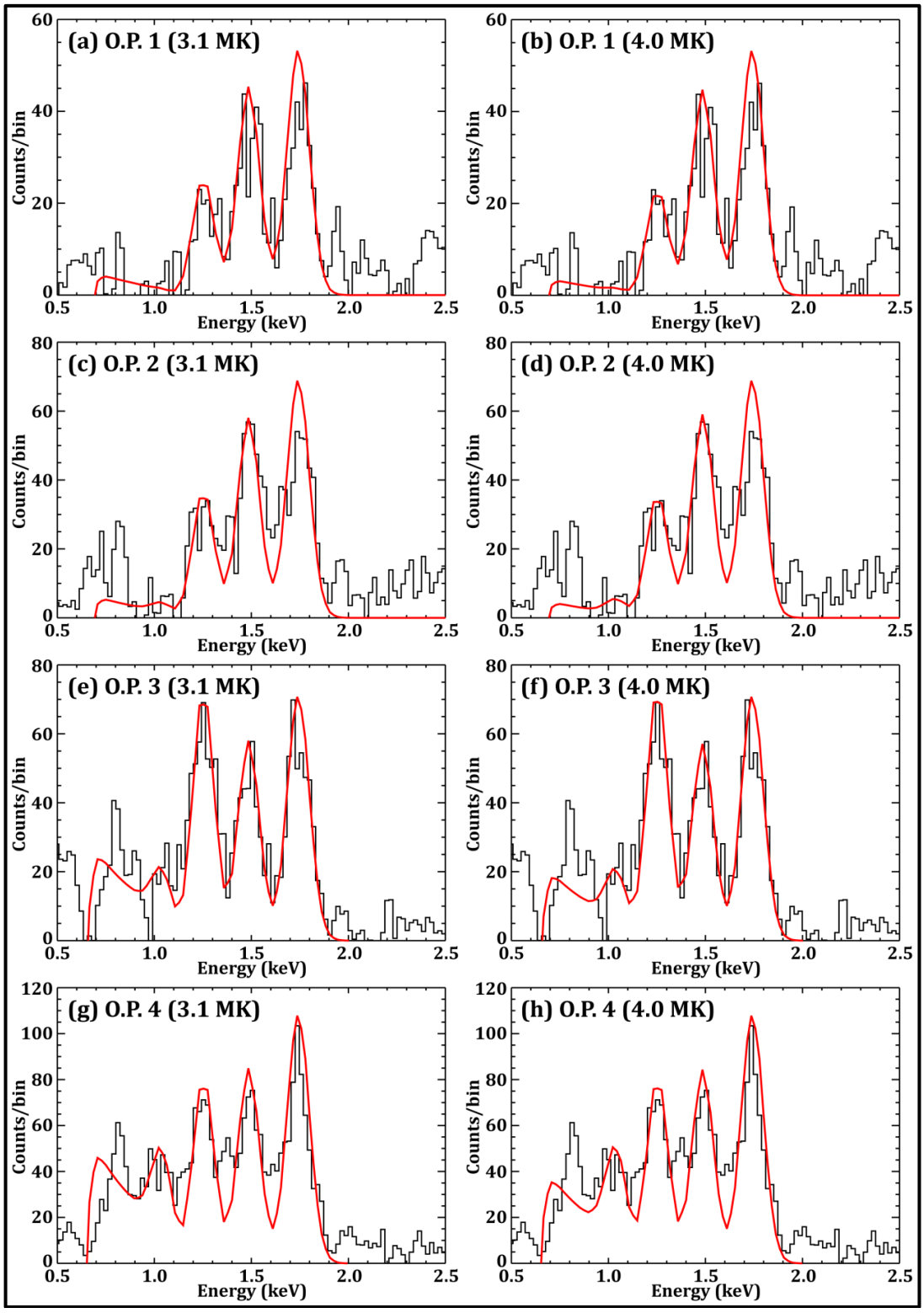

Figure 4.20. The background-subtracted C1XS spectra for ROI 1 – 4 of the Oceanus Procellarum flare, with the RAL abundance algorithm fitted models generated using solar models for flare temperatures of 3.1 MK and 4.0 MK. The Mg K_α (1.25 keV), Al K_α (1.49 keV) and Si K_α (1.74 keV) peaks can be seen in each case. The spectral lines of ROI 4 exhibit a slightly odd shape, this may be due to a small calibration error. The group of lines at ~0.8 keV (and indeed the Na peak at ~1.0 keV) is a scattered solar line contribution and is disregarded in the fitting routine. The Na peak (~1.0 keV) is also attributable to scattered solar lines rather than XRF.

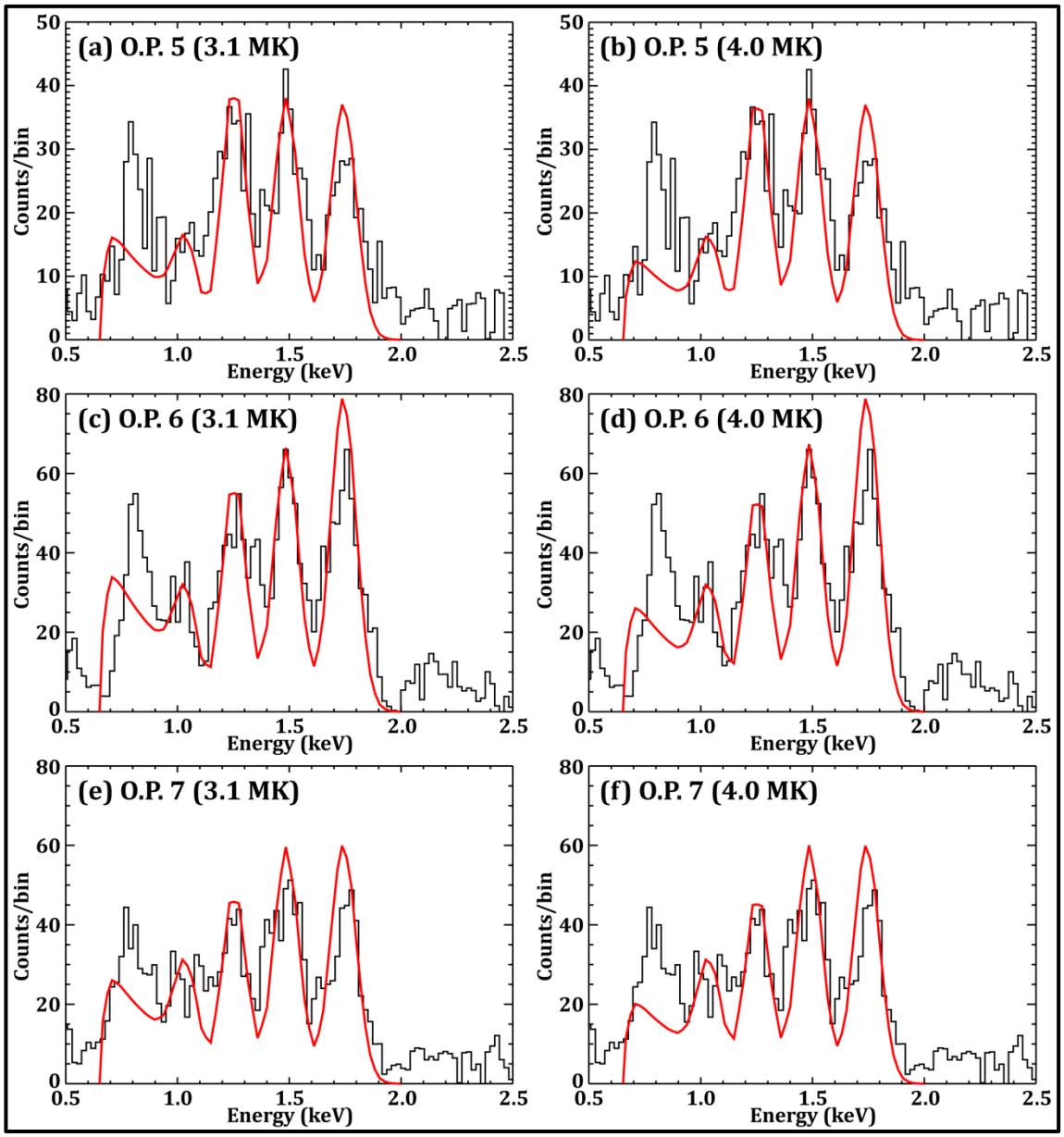

Figure 4.21. The background-subtracted C1XS spectra for ROI 5 – 7 of the Oceanus Procellarum flare, with the RAL abundance algorithm fitted models generated using solar models for flare temperatures of 3.1 MK and 4.0 MK. The Mg K_α (1.25 keV), Al K_α (1.49 keV) and Si K_α (1.74 keV) peaks can be seen in each case. The group of lines at ~0.8 keV is a scattered solar line contribution and is disregarded in the fitting routine. The Na peak (~1.0 keV) is also attributable to scattered solar lines rather than XRF.

Table 4.4. Elemental wt. % values for the whole of the Mare Serenitatis flare and its mare subsection, modelled using solar models for flare temperatures of 2.5 MK and 3.1 MK and other algorithm parameters set according to Table 4.3. The issue of the analytical totals not being equal to ~100% is discussed in section 4.4.1. Only the low energy lines of Mg, Al and Si are excited (Na is attributed to a scattered solar line contribution) in these spectra, and therefore only these lines are fitted in the model (Si is kept constant at 21 elemental wt. %, which is the median of the range of lunar soil values; see section 3.5.3 and references therein). All other elements are fixed at their abundance in the initial rock composition (fixed elements are denoted with *). Fitting errors, where applicable are given at the 1 σ confidence level.

	All		Mare	
	2.5 MK	**3.1 MK**	**2.5 MK**	**3.1 MK**
C*	0.00	0.00	0.00	0.00
O*	44.00	44.00	44.00	44.00
Na	0.45 ± 0.10	0.70 ± 0.18	0.55 ± 0.20	0.70 ± 0.35
Mg	3.00 ± 0.13	4.50 ± 0.13	3.00 ± 0.13	4.50 ± 0.38
Al	7.75 ± 0.38	10.00 ± 0.38	5.25 ± 0.88	6.50 ± 1.13
Si*	21.00	21.00	21.00	21.00
S*	0.00	0.00	0.00	0.00
K*	0.00	0.00	0.00	0.00
Ca*	11.29	11.29	11.29	11.29
Ti*	0.56	0.56	0.56	0.56
Fe*	5.93	5.93	5.93	5.93
Total	**93.98**	**97.98**	**91.58**	**94.48**

Table 4.5. Elemental wt. % values for each of the Oceanus Procellarum ROI, modelled using solar models for flare temperatures of 3.1 MK and 4.0 MK and other algorithm parameters set according to Table 4.3. The issue of the analytical totals not always being equal to ~100% is discussed in section 4.4.1. Only the low energy lines of Mg, Al and Si are excited (Na is likely to be a scattered solar line contribution) in these spectra, and therefore only these lines are fitted in the model (Si is kept constant at 21 elemental wt. %, which is the median of the range of lunar soil values; see section 3.5.3 and references therein). All other elements are fixed at their abundance in the initial rock composition (fixed elements are denoted with *). Fitting errors, where applicable, are given at the 1 σ confidence level.

	O.P. 1		O.P. 2		O.P. 3		O.P. 4		O.P. 5		O.P. 6		O.P. 7	
	3.1 MK	4.0 MK	3.1 MK	4.0 MK	3.1 MK	4.0 MK	3.1 MK	4.0 MK	3.1 MK	4.0 MK	3.1 MK	4.0 MK	3.1 MK	4.0 MK
C*	0.00	0.00	0.00	0.00	0.00	0.00	0.00	0.00	0.00	0.00	0.00	0.00	0.00	0.00
O*	44.00	44.00	44.00	44.00	44.00	44.00	44.00	44.00	44.00	44.00	44.00	44.00	44.00	44.00
Na	0.10 ± 0.18	0.15 ± 0.28	0.20 ± 0.23	0.35 ± 0.35	0.90 ± 0.28	1.30 ± 0.43	1.40 ± 0.15	2.10 ± 0.25	1.30 ± 0.33	1.90 ± 0.50	1.25 ± 0.20	1.85 ± 0.35	1.55± 0.18	2.30 ± 0.30
Mg	1.75 ± 0.38	2.25 ± 0.50	2.00 ± 0.25	2.75 ± 0.38	4.00 ± 0.13	5.75 ± 0.38	3.00 ± 0.13	4.25 ± 0.13	4.25 ± 0.38	5.75 ± 0.50	3.00 ± 0.13	4.00 ± 0.38	3.25 ± 0.25	4.50 ± 0.50
Al	6.50 ± 0.88	8.00 ± 1.00	6.50 ± 0.50	8.25 ± 0.63	6.50 ± 0.63	8.00 ± 1.00	6.25 ± 0.50	7.75 ± 0.50	8.25 ± 0.75	10.25 ± 1.00	6.75 ± 0.50	8.50 ± 0.63	8.00 ± 0.63	10.00 ± 0.75
Si*	21.00	21.00	21.00	21.00	21.00	21.00	21.00	21.00	21.00	21.00	21.00	21.00	21.00	21.00
S*	0.00	0.00	0.00	0.00	0.00	0.00	0.00	0.00	0.00	0.00	0.00	0.00	0.00	0.00
K*	0.00	0.00	0.00	0.00	0.00	0.00	0.00	0.00	0.00	0.00	0.00	0.00	0.00	0.00
Ca*	11.29	11.29	11.29	11.29	11.29	11.29	11.29	11.29	11.29	11.29	11.29	11.29	11.29	11.29
Ti*	0.56	0.56	0.56	0.56	0.56	0.56	0.56	0.56	0.56	0.56	0.56	0.56	0.56	0.56
Fe*	5.93	5.93	5.93	5.93	5.93	5.93	5.93	5.93	5.93	5.93	5.93	5.93	5.93	5.93
Total	**91.13**	**93.18**	**91.48**	**94.13**	**94.18**	**97.83**	**93.43**	**96.88**	**96.58**	**100.68**	**93.78**	**97.13**	**95.58**	**99.58**

Table 4.6. Mean MgO/SiO_2 and Al_2O_3/SiO_2 ratios for the Mare Serenitatis flare (M.S. all) and its mare subsection (M.S. mare), and for each ROI of the Oceanus Procellarum (O.P.) flare. These mean values are calculated from the individual results for each flare temperature given in Table 4.4 and Table 4.5. The errors combine the fitting errors and the range in values incorporated due to the two temperature models. The C1XS values are compared with the Lunar Prospector gamma-ray results (Prettyman et al., 2006) for the pixels which coincide with the C1XS regions. The C1XS results generally agree well with the Lunar Prospector results in terms of Al_2O_3/SiO_2, but they are systematically lower in terms of MgO/SiO_2 (also shown in Figure 4.22).

		MgO/SiO_2			Al_2O_3/SiO_2		
ROI	**Lunar Prospector Index**	**C1XS**	**Lunar Prospector Values**	**Mean**	**C1XS**	**Lunar Prospector Values**	**Mean**
M.S. all	1046	0.14 ± 0.03	0.27	0.28	0.37 ± 0.06	0.45	0.40
	1118		0.25			0.36	
	1190		0.25			0.29	
	1262		0.29			0.29	
	1334		0.31			0.25	
	1400		0.27			0.34	
	1460		0.28			0.43	
	1520		0.34			0.76	
M.S. mare	1190	0.14 ± 0.04	0.25	0.28	0.25 ± 0.07	0.29	0.29
	1262		0.29			0.29	
	1334		0.31			0.25	
	1400		0.27			0.34	
O.P. 1	1609	0.07 ± 0.03	0.23	0.21	0.31 ± 0.07	0.52	0.56
	1653		0.20			0.51	
	1692		0.20			0.67	
O.P. 2	1506	0.09 ± 0.03	0.24	0.23	0.31 ± 0.06	0.39	0.42
	1562		0.22			0.35	
	1609		0.23			0.52	
O.P. 3	1386	0.18 ± 0.05	0.27	0.27	0.31 ± 0.07	0.38	0.40
	1446		0.29			0.44	
	1506		0.24			0.39	
O.P. 4	1245	0.14 ± 0.03	0.21	0.25	0.30 ± 0.05	0.36	0.34
	1246		0.23			0.27	
	1317		0.23			0.34	
	1318		0.30			0.37	
	1306		0.27			0.38	
O.P. 5	1173	0.19 ± 0.05	0.23	0.22	0.39 ± 0.08	0.30	0.30
	1174		0.21			0.27	
	1245		0.21			0.36	
	1246		0.23			0.27	
O.P. 6	1101	0.13 ± 0.03	0.29	0.24	0.32 ± 0.06	0.31	0.32
	1102		0.21			0.40	
	1173		0.23			0.30	
	1174		0.21			0.27	
O.P. 7	1029	0.14 ± 0.04	0.20	0.24	0.38 ± 0.07	0.56	0.44
	1030		0.28			0.48	
	1101		0.29			0.31	
	1102		0.21			0.40	

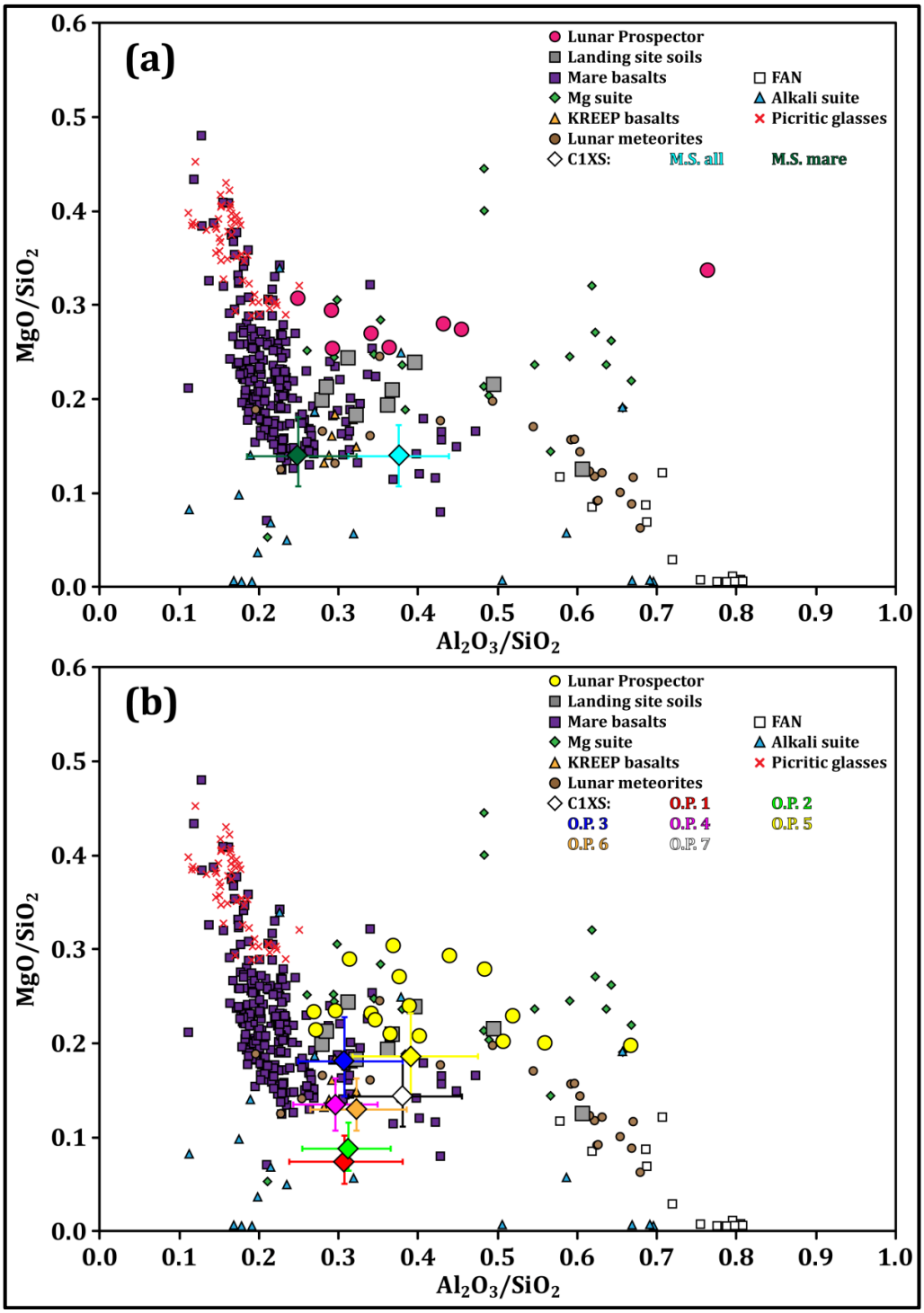

Figure 4.22. MgO/SiO_2 vs. Al_2O_3/SiO_2 plots showing the abundance ratios (given in Table 4.6) derived for (a) the Mare Serenitatis flare (M.S. all) and its mare subsection (M.S. mare) and (b) each of the Oceanus Procellarum (O.P) ROI. The error bars incorporate the 1 σ fitting errors as well as the range in values given by the two flare temperatures. Also shown are: (i) the Lunar Prospector gamma-ray data (Prettyman et al., 2006) for pixels whose coordinates overlap with the flare ground tracks; (ii) the average returned soil compositions (from Table 7.15 of McKay et al., 1991) from each of the Apollo and Luna landing sites; and (iii) sample compositions of various lunar lithologies: the mare basalts, ferroan anorthosites (FAN), Mg-suite, alkali suite, KREEP basalts, picritic glasses and lunar meteorites (from Papike et al., 1998; Righter 2010 and references therein).

4.4. Discussion

4.4.1. *Oxide totals*

The generally low analytical totals in Table 4.4 and Table 4.5 may be indicative that the Mg and Al modelling results are somehow inaccurate. However, if the fixed Ca, Ti and Fe abundances, which derive from the average lunar surface values given in Table 4.2 and that are used as the initial rock composition in the modelling, are replaced with mean values for the Lunar Prospector indices whose area overlap with the flare ground tracks, the results in Table 4.7 and Table 4.8 are produced. These analytical totals are closer to 100 wt. % and reflect the fact that more relevant Ca, Ti and Fe values are being used for this predominantly basaltic region. The mare basalts cover only 17% of the lunar surface (Head, 1976) and thus the average lunar composition employed originally will have elemental abundances that do not accurately reflect the basaltic nature of the areas observed by C1XS during these flares.

Oxide totals that do not total to 100% are also an inherent problem of the Lunar Prospector dataset (Prettyman et al., 2006). The average oxide sum for all pixels in the 20° dataset is 98%, with a population standard deviation of 2% (Prettyman et al., 2006). Figure 4.23 illustrates this information and shows that the patterns are not random. In Mare Serenitatis and Oceanus Procellarum the oxide sums are on the order of 94%, indicating that the abundances of some of the elements in this region have been underestimated. Prettyman et al. (2006) are unable to discern if this "missing" 6% is distributed uniformly across all the measured oxides (thus giving small errors for each one), or if only one of the oxides is underestimated by 6%. This problem with the Lunar Prospector dataset could explain the mainly low oxide totals shown in Table 4.4 and Table 4.5, as long as the low Lunar Prospector abundances are not attributed to MgO and Al_2O_3.

Table 4.7. Elemental wt. % values for the whole Mare Serenitatis flare (all) and its mare subsection (mare), where the fixed values (indicated by *) of Ca, Ti, and Fe (highlighted in red) have been changed (from those in Table 4.4) to the mean values provided by the Lunar Prospector index points that overlap with the flare footprint. The fitted C1XS results for Na, Mg and Al (highlighted in blue) are the only non-fixed abundances. The use of more appropriate Lunar Prospector values gives analytical totals which are closer to 100% than the average lunar crust values used in Table 4.4 because this flare footprint is a predominantly basaltic region.

	All		Mare	
	2.5 MK	**3.1 MK**	**2.5 MK**	**3.1 MK**
C*	0.00	0.00	0.00	0.00
O*	44.00	44.00	44.00	44.00
Na	0.45 ± 0.10	0.70 ± 0.18	0.55 ± 0.20	0.70 ± 0.35
Mg	3.00 ± 0.13	4.50 ± 0.13	3.00 ± 0.13	4.50 ± 0.38
Al	7.75 ± 0.38	10.00 ± 0.38	5.25 ± 0.88	6.50 ± 1.13
Si*	21.00	21.00	21.00	21.00
S*	0.00	0.00	0.00	0.00
K*	0.00	0.00	0.00	0.00
Ca*	9.85	9.85	8.70	8.70
Ti*	1.3	1.3	1.46	1.46
Fe*	10.73	10.73	13.09	13.09
Total	**98.08**	**102.08**	**97.05**	**99.95**

Table 4.8. Elemental wt. % values for each of the seven Oceanus Procellarum ROI, where the fixed values (indicated by *) of Ca, Ti, and Fe (highlighted in red) have been changed (from those in Table 4.5) to the mean values provided by the Lunar Prospector index points that overlap with the flare footprint. The fitted C1XS results for Na, Mg and Al (highlighted in blue) are the only non-fixed abundances. The use of more appropriate Lunar Prospector values (see text above) gives analytical totals which are closer to 100% than the average lunar crust values used in Table 4.5 because this flare footprint is a predominantly basaltic region.

	O.P. 1		O.P. 2		O.P. 3		O.P. 4		O.P. 5		O.P. 6		O.P. 7	
	3.1 MK	4.0 MK	3.1 MK	4.0 MK	3.1 MK	4.0 MK	3.1 MK	4.0 MK	3.1 MK	4.0 MK	3.1 MK	4.0 MK	3.1 MK	4.0 MK
C*	0.00	0.00	0.00	0.00	0.00	0.00	0.00	0.00	0.00	0.00	0.00	0.00	0.00	0.00
O*	44.00	44.00	44.00	44.00	44.00	44.00	44.00	44.00	44.00	44.00	44.00	44.00	44.00	44.00
Na	0.10 ± 0.18	0.15 ± 0.28	0.20 ± 0.23	0.35 ± 0.35	0.90 ± 0.28	1.30 ± 0.43	1.40 ± 0.15	2.10 ± 0.25	1.30 ± 0.33	1.90 ± 0.50	1.25 ± 0.20	1.85 ± 0.35	1.55± 0.18	2.30 ± 0.30
Mg	1.75 ± 0.38	2.25 ± 0.50	2.00 ± 0.25	2.75 ± 0.38	4.00 ± 0.13	5.75 ± 0.38	3.00 ± 0.13	4.25 ± 0.13	4.25 ± 0.38	5.75 ± 0.50	3.00 ± 0.13	4.00 ± 0.38	3.25 ± 0.25	4.50 ± 0.50
Al	6.50 ± 0.88	8.00 ± 1.00	6.50 ± 0.50	8.25 ± 0.63	6.50 ± 0.63	8.00 ± 1.00	6.25 ± 0.50	7.75 ± 0.50	8.25 ± 0.75	10.25 ± 1.00	6.75 ± 0.50	8.50 ± 0.63	8.00 ± 0.63	10.00 ± 0.75
Si*	21.00	21.00	21.00	21.00	21.00	21.00	21.00	21.00	21.00	21.00	21.00	21.00	21.00	21.00
S*	0.00	0.00	0.00	0.00	0.00	0.00	0.00	0.00	0.00	0.00	0.00	0.00	0.00	0.00
K*	0.00	0.00	0.00	0.00	0.00	0.00	0.00	0.00	0.00	0.00	0.00	0.00	0.00	0.00
Ca*	10.14	10.14	10.14	10.14	10.14	10.14	10.14	10.14	10.14	10.14	10.14	10.14	10.14	10.14
Ti*	1.32	1.32	1.32	1.32	1.32	1.32	1.32	1.32	1.32	1.32	1.32	1.32	1.32	1.32
Fe*	11.34	11.34	11.34	11.34	11.34	11.34	11.34	11.34	11.34	11.34	11.34	11.34	11.34	11.34
Total	**96.15**	**98.20**	**96.50**	**99.15**	**99.20**	**102.85**	**98.45**	**101.90**	**101.60**	**105.70**	**98.80**	**102.15**	**100.60**	**104.60**

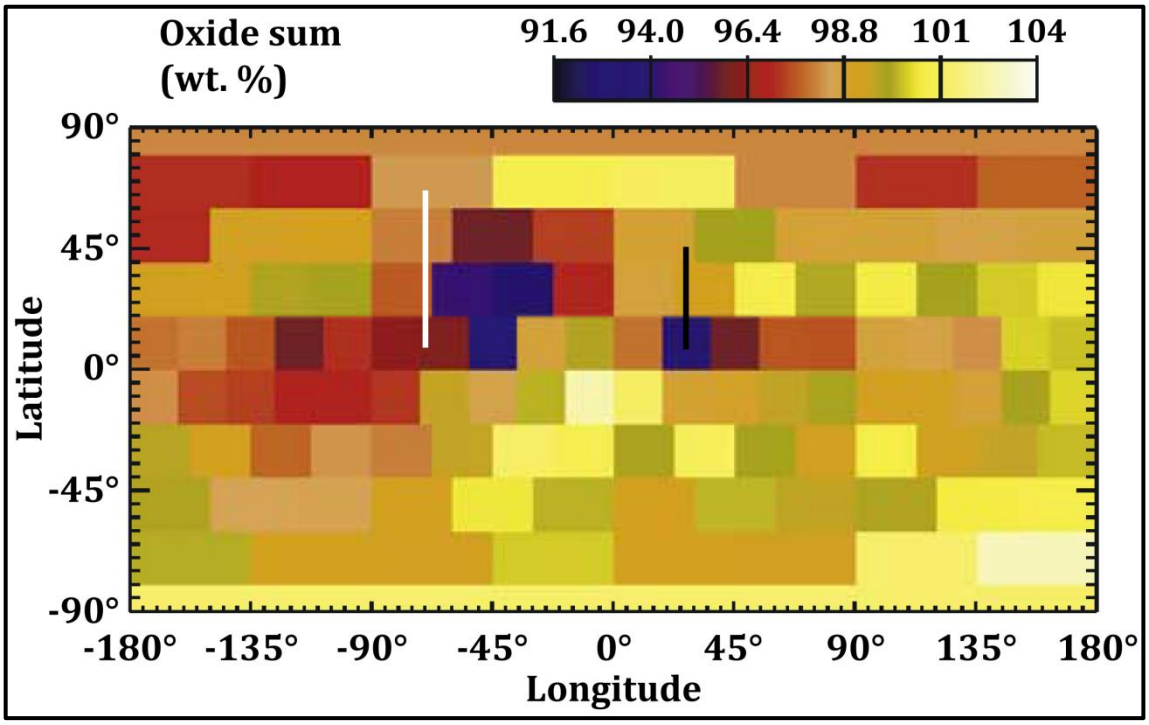

Figure 4.23. Map of the sum of the weight fractions of major oxides for the Lunar Prospector gamma-ray 20° equal-area pixel dataset, with the Mare Serenitatis (black) and Oceanus Procellarum (white) flare ground tracks shown (adapted from Prettyman et al., 2006).

4.4.2. *Diversity between the ROI*

Figure 4.3 to Figure 4.6 for Mare Serenitatis and Figure 4.8 to Figure 4.11 for Oceanus Procellarum illustrate the chemical and temporal diversity of the lava flows covered by the two flare ground tracks. In terms of age (Figure 4.3 and Figure 4.8) and TiO_2 content (Figure 4.5 and Figure 4.10), both flare footprints show little variation along their length. The Mare Serenitatis lava flows have an age range of ~1.0 Ga (between ~2.8 Ga and ~3.8 Ga); the range the for Oceanus Procellarum deposits is narrower (<0.5 Ga, between ~3.0 Ga and ~3.5 Ga). The TiO_2 content of the mare deposits in both maria is about equal at around 3 wt. %. The FeO content maps (Figure 4.6 and Figure 4.11), however, do indicate that the flare tracks pass through regions which are more variable in this regard. It is therefore expected that the C1XS regions of interest will display at least some variation in their MgO/SiO_2 and Al_2O_3/SiO_2 ratios, especially between highlands and mare areas.

Figure 4.22b does indeed show that O.P. 1 (predominantly highlands) and O.P. 2 have a lower MgO content than the other regions (both in Mare Serenitatis and Oceanus

Procellarum), and that regions M.S.-all, O.P. 5 and O.P. 7 have slightly higher Al_2O_3 contents than the remaining areas. However, the diversity between the different regions is better illustrated in terms of their FeO and TiO_2 contents (derived from Clementine multispectral reflectance data for the ROI areas) as given in Table 4.9 and shown in Figure 4.24 where they are plotted (as ratios to SiO_2) against the MgO/SiO_2 and Al_2O_3/SiO_2 C1XS results. These data are also compared with the compositions of high-Ti, low-Ti and VLT mare basalt, KREEP basalt and ferroan anorthosite samples in terms of these oxide ratios.

Table 4.9. FeO and TiO_2 content estimates (and their ratios to SiO_2) for each flare ROI. These values have been derived from Clementine multispectral reflectance data using the Gillis et al. (2004) and Gillis et al. (2003) algorithms respectively (see section 5.1.2). The Si abundance is fixed at 21 wt. % (the value used in the C1XS modelling; see Table 4.4 and Table 4.5).

ROI	FeO (wt. %)	FeO/SiO_2	TiO_2 (wt. %)	TiO_2/SiO_2
M.S. all	15.15	0.34	2.17	0.05
M.S. mare	19.40	0.43	2.54	0.06
O.P. 1	7.69	0.17	0.41	0.01
O.P. 2	16.14	0.36	1.68	0.04
O.P. 3	18.73	0.42	2.55	0.06
O.P. 4	17.77	0.40	2.91	0.07
O.P. 5	18.63	0.42	2.42	0.05
O.P. 6	20.03	0.45	2.79	0.06
O.P. 7	14.80	0.33	2.21	0.05

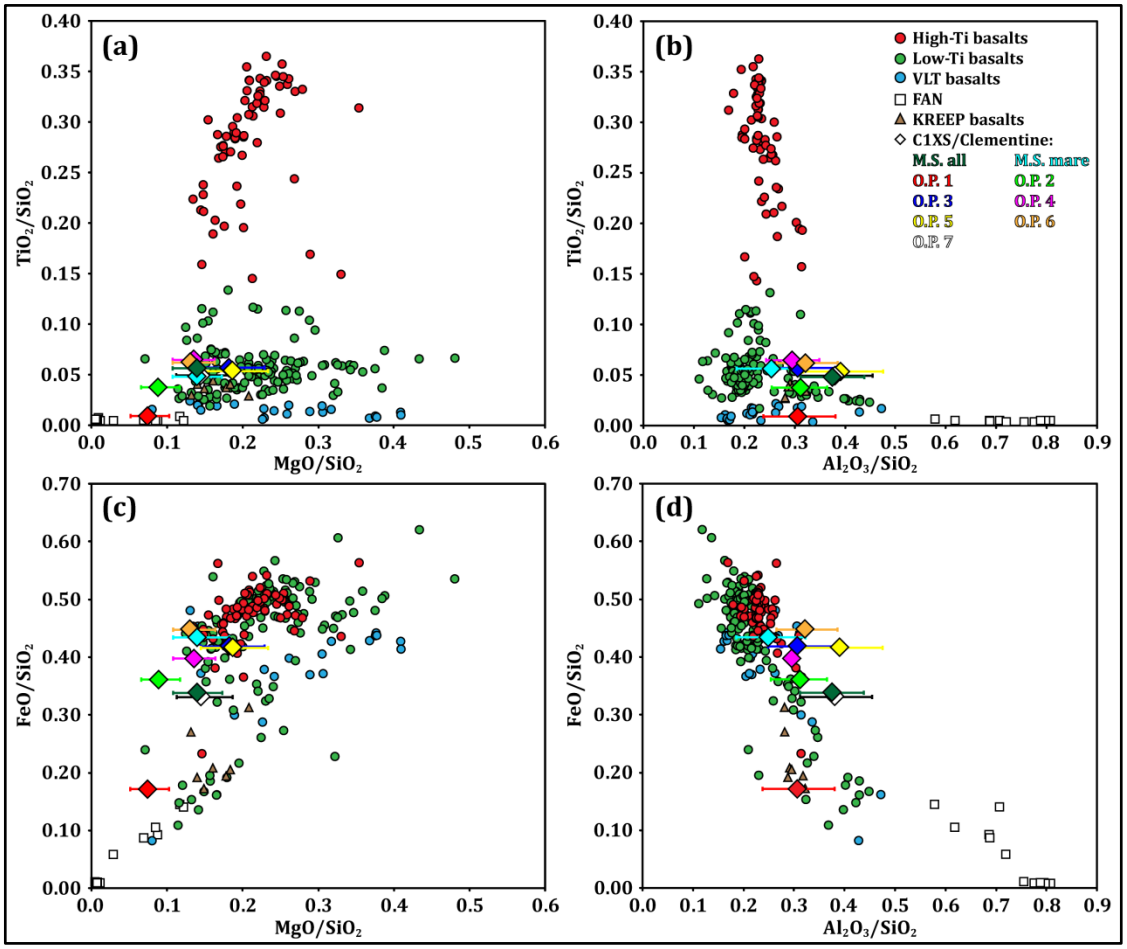

Figure 4.24. Plots of the MgO/SiO_2, Al_2O_3/SiO_2, TiO_2/SiO_2 and FeO/SiO_2 ratios of mare basalt (split into categories according to their Ti-content, following the classification scheme of Neal & Taylor, 1992), KREEP basalt, and ferroan anorthosite (FAN) samples from the Apollo and Luna collections, as well as for the C1XS ROI in Mare Serenitatis and Oceanus Procellarum. For these regions, the MgO/SiO_2 and Al_2O_3/SiO_2 ratios are derived from the C1XS results presented in this chapter; the TiO_2/SiO_2 and FeO/SiO_2 ratios are derived from Clementine multispectral reflectance data according to the algorithms of Gillis et al. (2003) and Gillis et al. (2004) respectively (see Table 4.9). These graphs suggest that the C1XS regions generally consist of low-Ti basalts and that they are more diverse in terms of their FeO content than their TiO_2 content. One exception is the region O.P. 1 that does not represent a low-Ti mare basalt, but instead appears to be some kind of mixture of FAN and mare basalt material. The same legend applies to all four plots.

A number of points are illustrated in the graphs of Figure 4.24:

(i) the classification of mare basalt samples into high-Ti, low-Ti and VLT categories does not make them distinguishable in terms of their MgO and Al_2O_3 content;

(ii) the ROI are more diverse in terms of their FeO content (Figure 4.24c and Figure 4.24d) than their TiO_2 content (Figure 4.24a and Figure 4.24b);

(iii) the majority of the ROI consist of low-Ti basalts, with relatively high Al_2O_3 contents (with Al_2O_3/SiO_2 greater than ~0.3).

It is possible that the lithologies detected by C1XS may include a KREEP basalt component, especially due to the fact that the ground tracks of both flares pass through the outer regions of the PKT (see Figure 4.25). The FeO contents illustrated in Figure 4.24c and Figure 4.24d, however, do not indicate that this is the case, and any KREEP component must be minor (indeed not all the basalt samples collected from within the PKT are KREEP basalts).

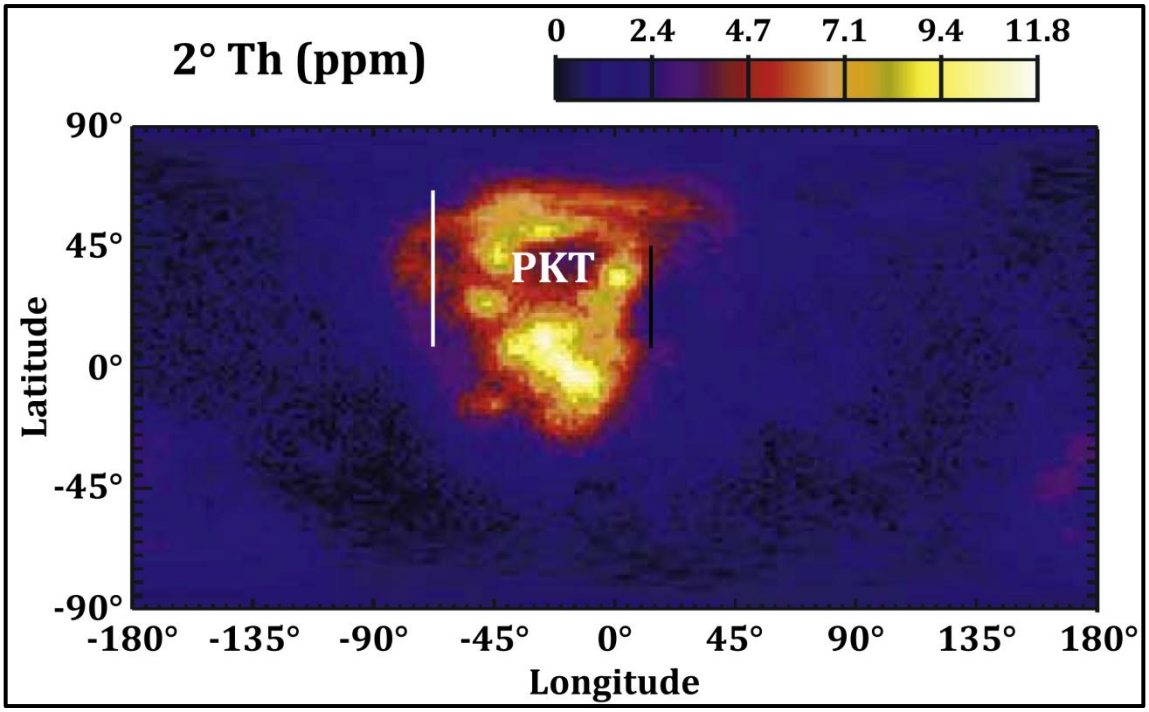

Figure 4.25. Map of Lunar Prospector thorium abundance (in ppm) showing the Mare Serenitatis (black) and Oceanus Procellarum (white) flare ground tracks through outer eastern and western parts of the PKT (adapted from Prettyman et al., 2006).

The region O.P. 1 is the only one that is clearly distinct from the other low-Ti basalt regions, in terms of the ratios plotted in Figure 4.24. It has lower ratios of TiO_2/SiO_2, FeO/SiO_2 and MgO/SiO_2 and therefore appears to be more representative of the ferroan anorthosite suite. This region encompasses a mostly highlands area, but also the northern most part of Oceanus Procellarum within the flare ground track in its southern section (see for example Figure 4.7 and Figure 4.8). Therefore, the C1XS (and Clementine) data should reflect a mixture of the two lithologies. Figure 4.26 illustrates the simple mixing trends between a mean FAN composition and a mean high-Ti (red line), low-Ti (green line) or VLT (blue line) mare basalt composition (data are taken from Papike et al., 1998), at 10%

increments in terms of MgO/SiO_2, Al_2O_3/SiO_2, TiO_2/SiO_2 and FeO/SiO_2 ratios. Also plotted on these graphs are the C1XS/Clementine values, as shown in Figure 4.24.

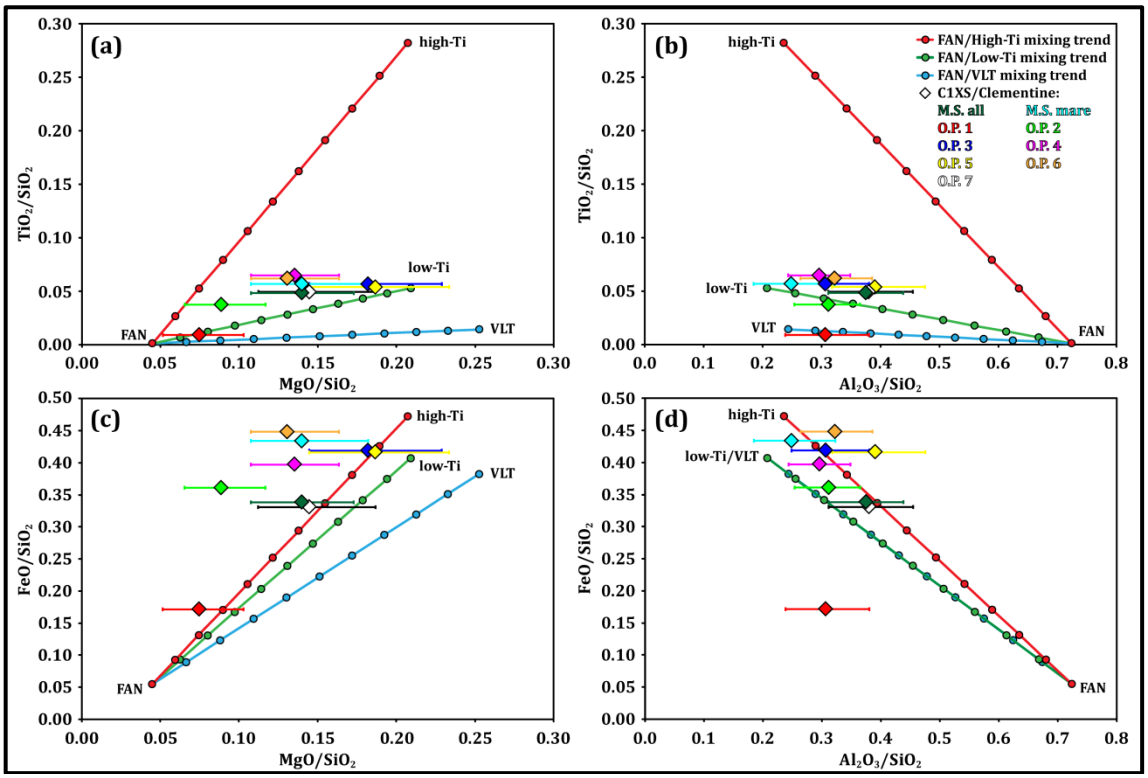

Figure 4.26. Simple mixing trends, in terms of MgO/SiO_2, Al_2O_3/SiO_2, TiO_2/SiO_2 and FeO/SiO_2 ratios, between a mean FAN composition and mean high-Ti, low-Ti or VLT mare basalt composition (data from Papike et al., 1998), at 10% increments. Also plotted are the C1XS/Clementine values, as shown in Figure 4.24.

The O.P. 1 and M.S.-all C1XS regions are the two ROI which incorporate both highlands areas and mare basalt and therefore their data points may lie on one of the mixing trends. O.P. 1 consists of ~80% highlands and ~20% (low-Ti) mare basalt (see Figure 4.27); in terms of MgO/SiO_2, TiO_2/SiO_2 and FeO/SiO_2 (Figure 4.26a and Figure 4.26c) its data point does sit in approximately the expected position of an 80:20 FAN-mare basalt mixture. However in terms of Al_2O_3/SiO_2 this mixing ratio does not account for the C1XS result for this ROI, and is in keeping with it plotting away from the FAN field in Figure 4.22b and Figure 4.24. This low Al_2O_3/SiO_2 ratio may represent a surficial enhancement (C1XS is most sensitive to the top few hundred microns of the surface) of mare material over the highlands region, due to transfer in crater ejecta. However, it seems unlikely that this would occur on such a large scale, and it is not suggested in the Clementine FeO wt. % content value.

Possible explanations for this apparently low Al abundance for region O.P. 1 include:

(i) the C1XS Al estimate has been underestimated; this seems unlikely as this is the only ROI for which this problem is evident and does not appear to have any distinguishing feature in terms of the data acquisition;

(ii) the simple mixing trend between a mean FAN and a mean low-Ti basalt composition employed in Figure 4.26 is not good enough to explain the composition of O.P. 1. Invoking other highlands lithologies such a troctolite or a norite instead of FAN in such mixtures also cannot explain its composition, although a norite/low-Ti basalt composition of about the correct proportions does provide approximately the correct Al_2O_3/SiO_2, FeO/SiO_2 and TiO_2/SiO_2 ratios, but not MgO/SiO_2 (it is too high). Perhaps, therefore, a more complex mixture with at least three end-members needs to be employed to explain this result.

(iii) a highlands lithology with the particular major element concentrations represented by O.P. 1 is not present within the sample collection.

In Figure 4.22b the compositions of regions O.P. 1 and O.P. 2 are similar, which is surprising because O.P. 2 is an entirely basaltic region. However, in Figure 4.24, when the MgO/SiO_2 and Al_2O_3/SiO_2 ratios are plotted in conjunction with the Clementine TiO_2/SiO_2 and FeO/SiO_2 ratios, their compositions are much less alike and O.P. 2 appears to represent a less-Mg rich basalt than the other regions in the Oceanus Procellarum flare. This may be indicative of the lower olivine concentrations (if the olivine is forsteritic) at the edge of Oceanus Procellarum than its interior (Lucey, 2004). This probably also represents the inclusion of the youngest lava flow (see Figure 4.8) that falls within this flare's footprint, and therefore is likely to have a slightly different composition than the older, surrounding lava flows that make up of the other ROI. The similarity in terms of Al_2O_3/SiO_2 between regions O.P. 1 and O.P. 2 is only an issue because of the low Al_2O_3/SiO_2 ratio provided for O.P. 1.

The Mare Serenitatis footprint (M.S. all) appears to be ~60% (low-Ti) mare basalt and ~40% highlands (see Figure 4.2) and Figure 4.26 suggests that the C1XS/Clementine results can be explained with approximately that mixture. In terms of all the oxides, region O.P. 7 is very similar to M.S. all and this is because it does include some highlands material

in its southernmost part (see Figure 4.27). For all the remaining regions, an almost entirely mare basalt composition should be expected, with any highlands contribution (from crater ejecta) being most apparent in terms of Al_2O_3/SiO_2. These regions do indeed seem to indicate mixtures of mare basalt material and a small (<30%) highlands contribution, which is likely to originate from the high albedo, ejecta contamination that can be seen in all the regions (see Figure 4.27). Figure 4.26a and Figure 4.26c suggest that many of the C1XS data points have MgO/SiO_2 ratios that are slightly lower than what the mixing trends would suggest. This could be for a number of reasons, e.g. (i) the C1XS MgO abundances have been underestimated, (ii) the MgO/SiO_2 ratios of the different categories of mare basalts are not well represented by the mean values used, or (iii) the MgO/SiO_2 ratio values for the areas observed by C1XS are not represented in the sample collection.

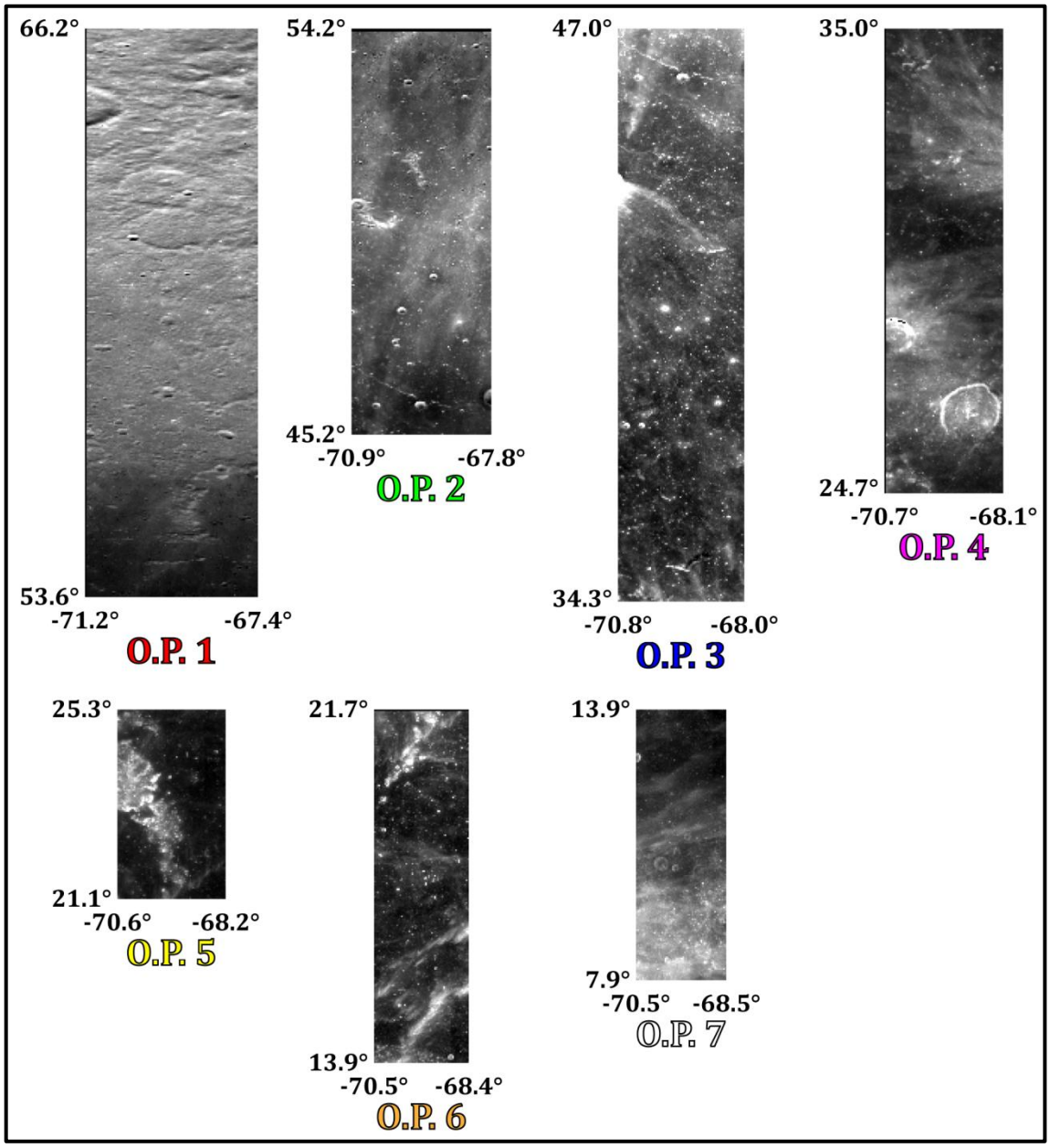

Figure 4.27. Clementine 750 nm (albedo) images for each of the Oceanus Procellarum flare ROI, with their coordinates shown.

4.4.3. *Comparison with Lunar Prospector results*

In addition to the sample compositions plotted in Figure 4.22, the Lunar Prospector gamma-ray values for the pixels which overlap the C1XS flare ground tracks are shown (see also Table 4.6). The C1XS results for both flares are in better agreement with the range of mare basalt compositions in the Apollo and Luna collection than the Lunar Prospector results (although no samples have been returned from the regions encompassed

by either flare ground track), or indeed than between the sample and Lunar Prospector data. Table 4.6 and Figure 4.22 show that in terms of Al_2O_3/SiO_2 the two remote sensing datasets agree well within the C1XS errors, but less so in terms of MgO/SiO_2, where the C1XS results are systematically lower. There could be three reasons for this discrepancy: (i) the C1XS results presented here are inaccurate; (ii) the Lunar Prospector results presented by Prettyman et al. (2006) are inaccurate; or (iii) there is an intrinsic problem with comparing planetary XRF and gamma-ray spectroscopy data.

Given that the RAL abundance algorithm methodology has been proven using laboratory test data from a lunar regolith simulant (see section 3.5), and that the errors associated with the uncertain solar flare temperatures are much larger than the algorithm's fitting errors (see section 4.2.3), it is thought that the lack of agreement between the C1XS and Lunar Prospector results are not due to the inaccuracy of the C1XS abundances presented because the C1XS errors are most likely overestimated.

The better agreement between the sample and C1XS data than the C1XS and Lunar Prospector data, or indeed the sample and Lunar Prospector data, further suggest that the inaccuracy lies with the Lunar Prospector results (although it must be stressed that samples have not been returned from the areas in question). It has been noted (e.g. Wöhler et al., 2011) that the correlation between major element sample compositions and the Lunar Prospector gamma-ray data for the respective landing sites (as presented by Elphic et al., 2000) is not always good. This is especially true for Mg and Al, but particularly the former which is systematically overestimated (by up to ~5 elemental wt. %) by Lunar Prospector. If these inaccuracies are true for other parts of the lunar surface (including the areas of Mare Serenitatis and Oceanus Procellarum observed during the two C1XS flares), then this could, at least partly, explain the C1XS-Lunar Prospector discrepancy and also why they seem to be more different in terms of Mg than Al.

It is also important to discuss the third possibility; the discrepancy arises due to intrinsic differences between the two techniques, rather than because of either dataset being inaccurate. The difference in energy of the radiation measured in the two techniques means that XRF only samples the very top few 100 microns of the lunar regolith (Yin et al., 1993),

whereas gamma-rays can penetrate to a depth of ~1 m (Prettyman et al., 2006), and also that XRF spectroscopy is subject to matrix effects (as discussed in chapter 3) which gamma-rays are not, as they can escape from the surface unimpeded. The different sampling depths of the techniques may mean that compositionally distinct parts of the regolith are measured, with XRF "seeing" only the finest fraction of the soil at the very surface, and gamma-rays "seeing" a greater mixture, down to a depth of ~1 m. Regolith grain sorting processes (e.g. seismic shaking) may be able to stratify the regolith and produce compositional layering. This has been proposed (Riner et al., 2008) to explain the significantly higher Fe/Si ratios determined from the XRS on NEAR for the asteroid Eros (Lim & Nittler, 2009), than those determined from the GRS. An alternative explanation for possible compositional stratification, may be the presence of impact-formed, amorphous and inclusion-rich rims (60 – 200 nm) on the surface of individual soil grains (e.g. Keller & McKay, 1997). These are thought (Pieters et al., 1993b; Allen et al., 1996; Keller & McKay, 1997) to be one of main causes of spectral darkening due to space weathering in reflectance spectroscopy (see section 5.1.2). However, any compositional anomalies in these very thin rims (even in terms of the micron scale XRF occurs on) are unlikely to play a significant role in affecting the C1XS results.

This issue of comparing planetary XRF and gamma-ray spectroscopy results is an important one that warrants further investigation. Further comparisons with C1XS data and new gamma-ray results from Kaguya (e.g. Gasnault et al., 2009) will be required in the future to help determine the nature of this problem. It is also important for other planetary bodies, such as Eros which has already been studied and Mercury, with the forthcoming XRF and GRS datasets from MESSENGER (Goldsten et al., 2007; Schlemm et al., 2007), for which it is especially important because there is no ground truth sample data available.

4.5. Summary

In this chapter, two solar flares from which C1XS XRF data were obtained have been analysed. These are the only two within the C1XS dataset that sampled basaltic areas of the Moon. On 12th December 2008, an A-class solar flare led to data acquisition for a ground track through Mare Serenitatis and a B-class solar flare on 10th February 2009 for

which C1XS had a footprint over the western part of Oceanus Procellarum. The calibrated, gain-corrected and background subtracted X-ray spectra for these flares have been fitted using the RAL abundance algorithm, and new estimates of the MgO/SiO_2 and Al_2O_3/SiO_2 ratios for the different regions have been provided. These results are in better agreement with existing lunar sample compositions than Lunar Prospector gamma-ray data for the same regions. The results have also been used in combination with TiO_2 and FeO wt. % content values derived from Clementine multispectral data to allow the geochemistry of the different regions to be understood in more detail.

The C1XS results generally confirm the geochemical similarity of the different lava flows that have been observed (e.g. Hiesinger et al., 2000; 2003) and the compositions can be mostly explained in terms of simple mixing between typical highlands (FAN) and mare materials. However, for at least one region (the most northern part of the Oceanus Procellarum flare ground track) the Al_2O_3/SiO_2 is lower than can be invoked with these models. The poor agreement between the C1XS results presented in this chapter and the gamma-ray compositions derived from Lunar Prospector (more so in terms of MgO/SiO_2 than Al_2O_3/SiO_2) may be explained through a combination of inaccurate gamma-ray results and the difference in sampling depths for the two techniques. The sampling depth variations mean that XRF is subject to regolith matrix effects that gamma-ray spectroscopy is not, and may cause compositionally distinct layers in a grain-sorted regolith to be measured.

Although Oceanus Procellarum is noted for the temporal and compositional heterogeneity of its lava flows, the subset sampled during the C1XS flare is limited in its diversity and indeed is remarkably similar to the section of Mare Serenitatis observed during the other solar flare. The small size of the C1XS dataset therefore limits the extent to which the goal of studying lava flow diversity on the Moon with C1XS can be met. However, with greater coverage of the lunar surface from XRF spectrometers on future missions, the techniques employed in this chapter should make it possible to achieve this aim.

Chapter 5: Lava flow stratigraphy in Oceanus Procellarum and Mare Serenitatis[7]

5.1. Introduction

Mapping studies of the nearside lunar mare basalts have demonstrated that they are mosaics of temporally distinct lava flows (e.g. Wilhelms & McCauley, 1971; Scott et al., 1977; Pieters, 1978; Heather & Dunkin, 2002; Hiesinger et al., 2003). These areas therefore potentially contain scientifically valuable localities for future human and/or robotic exploration (e.g. Spudis, 1996; Crawford et al., 2007; Fagents et al., 2010). The analysis of lunar rock samples, collected *in-situ* from distinct lava flows would help solve some of the outstanding issues in lunar science, e.g.: (i) the temporal volcanic history and evolution of the lunar mantle would be elucidated in greater detail by the study of samples from numerous, temporally distinct lava flows (e.g. Shearer et al., 2006); (ii) the calibration of the absolute lunar chronology and crater-counting curves would be improved by obtaining absolute radiometric ages for these lava flows (e.g. Stöffler et al., 2006) and; (iii) the study of the ancient Sun and solar system conditions could be achieved by obtaining palaeoregolith material trapped between consecutive lava flows (e.g. Wieler et al., 1996; Crawford et al., 2007; Fagents et al., 2010). The scientific output from any future exploration within the mare basins should be maximised by choosing a landing site where a diverse array of geological units occurs within an accessible radius. Such sites may include contacts between two or more individual lava flow deposits, or material around impact craters that has been excavated during the impact event, and therefore negates the need for sub-surface drilling. In this chapter impact craters within regions (distinct from those studied using C1XS data in chapter 4) of two of the major nearside maria, Oceanus Procellarum and Mare Serenitatis (Figure 5.1), are studied with a view to identifying ejecta deposits that have excavated sub-surface lithologies.

[7] The majority of this chapter has been published in Weider et al. (2010).

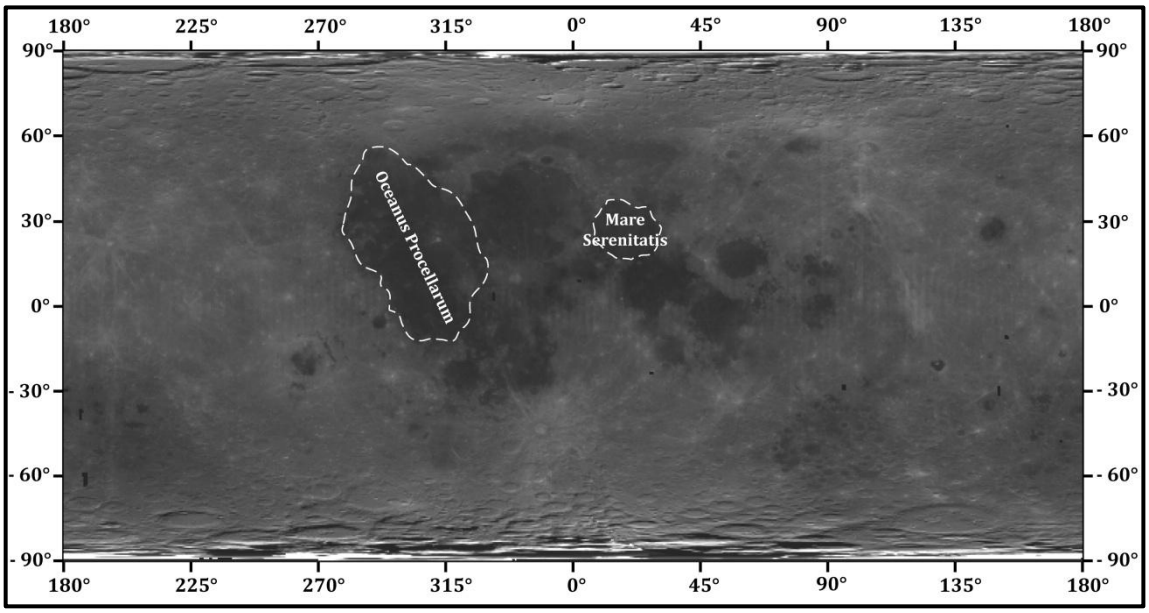

Figure 5.1. Clementine albedo (750 nm) image of the Moon showing the location and approximate outlines of Oceanus Procellarum and Mare Serenitatis.

5.1.1. *Impact craters: windows through lava flows*

During the formation of an impact crater, material from different vertical horizons within the original target surface is displaced or excavated (Figure 5.2). Material closest to the original surface acquires the most energy during the impact; it therefore has the greatest displacement and is deposited in the continuous ejecta blanket that extends for about one crater radius beyond the crater rim (Moore et al., 1974; Oberbeck et al., 1974). Originally deeper material is re-deposited around the rim and interior of the resultant craters. Situations occur in the maria where feldspathic basement material (e.g. the primary lunar crust) is overlain by a stack of temporally and compositionally distinct lava flows (Figure 5.2). Small impact craters within this region may excavate through to underlying lava flows, which, providing the effects of space weathering can be accounted for, may remain identifiable in the ejecta surrounding the craters from orbital remote sensing measurements.

The NASA Clementine mission (Nozette et al., 1994) produced a global, high-spatial resolution (100 m/pixel) multispectral dataset suitable for studying local geological and compositional variations of this kind. Indeed, in an earlier study Heather & Dunkin (2002) used Clementine UV-Vis data to investigate impact craters in Oceanus Procellarum, and

were able to distinguish anorthositic and basaltic material in a small proportion of the craters studied and from which they derived the total basalt thickness in this area. The aim of the work described in this chapter is to extend this approach to the identification of individual sub-surface lava flows with different compositions, as has been achieved previously by Rajmon & Spudis (2004) in Mare Tranquillitatis and Mare Fecunditatis.

The reflectance spectra of both olivine and pyroxene exhibit absorption features, due to the presence of ferrous iron, centred around 1 µm (Figure 1.19), but whose exact shape and position is dependent on chemical composition (Adams, 1974). The two minerals can be more definitively differentiated on the basis of a second absorption feature at ~2 µm that pyroxenes exhibit, but which olivines lack. This process of mineral determination is not fully realised with the Clementine UV-Vis dataset alone because it does not include wavelengths longer than 1 µm, and thus fails to reveal the precise shape of the 1 µm absorption feature and the presence/absence of the 2 µm absorption. As such, the incorporation of the Clementine NIR dataset with the UV-Vis allows the nature of mafic mineral phases to better defined, and can help distinguish between pyroxene-rich and olivine-rich lithologies. For instance, if lava flow 1 and 2 in Figure 5.2 were olivine-rich and pyroxene-rich respectively, it is possible that the ejecta of the impact crater would have spectral properties matching lava flow 2 (or the underlying basement material) rather than lava flow 1 in which it lies. The diameter of the impact crater could be used to make an estimate of its excavation depth (Melosh, 1989) and therefore provide constraints for the maximum thickness of the surface lava flow.

It has previously been reported that Oceanus Procellarum contains olivine-rich lava flows (Staid & Pieters, 2001; Staid et al., 2010). The first study area was therefore selected in a region with numerous lava flow units within this mare basalt. Similar techniques are employed in the second area, to evaluate the work of Ono et al. (2009) who used Kaguya radar data to infer the depth of a buried lava flow in Mare Serenitatis.

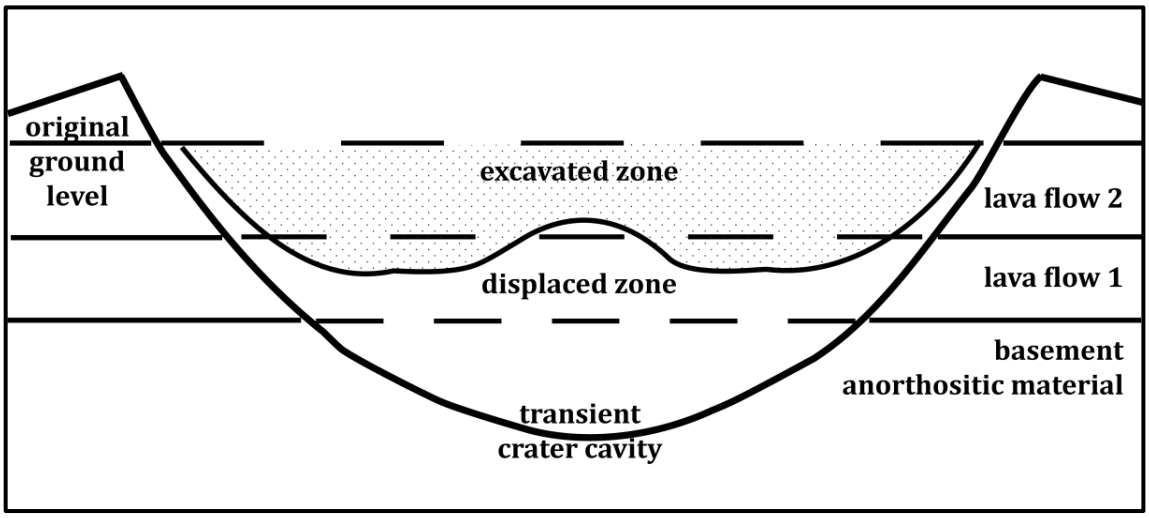

Figure 5.2. Simplified cross-section through an impact crater showing the hypothetical original target stratigraphy and the zones of excavated and displaced material. Excavated material is deposited in the crater's proximal ejecta blanket; displaced material is deposited on the rim and within the interior of the crater cavity.

5.1.2. *Multispectral reflectance spectroscopy*

Space weathering

Space weathering is the process by which the lunar surface is physically and chemically altered (*matured*) due to its continual bombardment by cosmic rays, solar wind particles and micrometeorites, as well as the subsequent formation of new phases including single-domain nanophase iron, agglutinates (see section 1.2.4) and amorphous coatings on individual grains (McKay et al., 1974; 1991; Hapke et al., 1975; Morris, 1976; Borg et al., 1980; Keller & McKay, 1993; Fischer & Pieters, 1994; 1996). The optical effects of the space weathering process complicate the interpretation of multispectral reflectance spectra from the lunar regolith. Lunar regolith maturation causes three main changes to reflectance spectra (illustrated in Figure 5.3): (i) reduction in the overall reflectivity (albedo); (ii) reduction in the intensity of absorption features and; (iii) an overall reddening of the continuum. The precise shape of each reflectance spectrum is therefore controlled by the opposing effects of composition and space weathering; these need to be decoupled in order to accurately assess the mineralogy and composition of the measured surface.

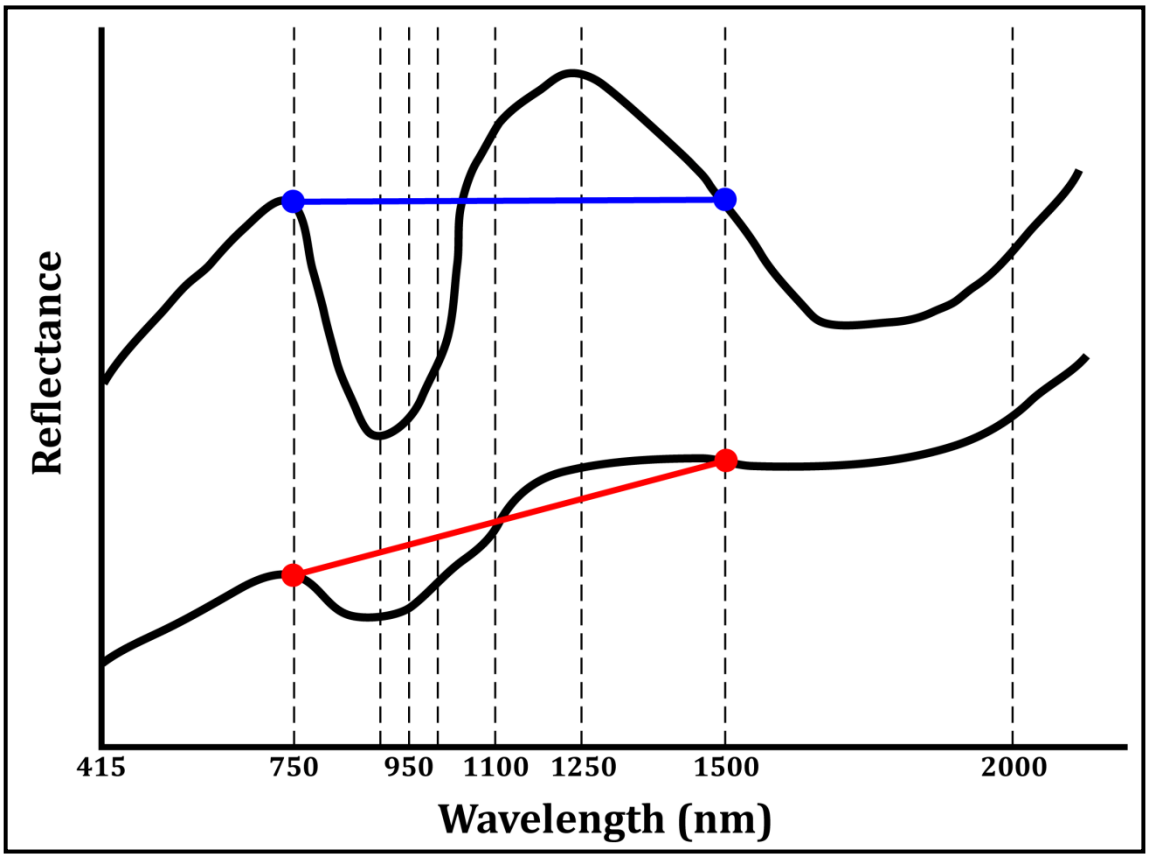

Figure 5.3. Two hypothetical pyroxene UV-Vis-NIR spectra, illustrating both the effects of maturation and the calculation of the continuum slope. The top 'immature' spectrum has a higher albedo, more intense absorption features and a less 'red' slope than the lower 'mature' spectrum. The continuum slope is the gradient of the straight line (blue/red) which fits the spectrum at 750 and 1500 nm. Dashed lines indicate the Clementine wavebands.

Mineralogical identification

Le Mouélic et al. (2000) incorporate both the UV-Vis and NIR Clementine wavebands to evaluate the level of space weathering with the magnitude of the spectral continuum slope. They use this measure to adjust absorption band depths in order to deal with the effects of space weathering. The slope of the continuum is defined as the gradient of the straight line which fits the spectrum at 750 nm and 1500 nm (points which lie outside the main absorption bands of lunar soils; Pieters, 1986), and normalised at 0.75 µm (illustrated in Figure 5.3):

$$continuum\ slope = \left(\frac{1}{R_{750}}\right)\frac{R_{1500} - R_{750}}{(1500 - 750)} \qquad (\text{nm}^{-1}) \qquad (2)$$

where R_{750} and R_{1500} are the Clementine reflectance values at 750 nm and 1500 nm. This parameter has a high value when the spectrum is mature and the slope is steep.

The continuum slope becomes increasingly steep ('red') as the exposure time of the material at the lunar surface and therefore the level of space weathering increase. The formation of agglutinates in the regolith does not solely explain this reddening (Pieters et al., 1993b) and is better attributed to the increasing amount of nanophase iron in the soil that can be evaluated by its intensity of ferromagnetic remanence (Hapke et al., 1975; Hapke, 1977; Allen et al., 1993; 1996; Pieters et al., 1993b). The correlation between the continuum slope (equation 2) and ferromagnetic remanence has been tested (Le Mouélic et al., 2000), with the continuum slope being found to reliably evaluate the level of spectral alteration caused by space weathering.

An increase in the amount of iron contained within mafic silicate minerals causes a decrease in their albedo and a strengthening of their 1 μm and 2 μm absorption bands (e.g. Pieters et al., 1993b). There is also a corresponding decrease in the ratio between the near infra-red and visible wavelengths (NIR/Vis) (Burns, 1993). The depth of the 1 μm and 2 μm absorption bands (defined in equations 3 and 4 respectively) in reflectance spectra are therefore diagnostic of composition. However, as demonstrated in Figure 5.3, they are also susceptible to weakening due to space weathering. The increase of nanophase iron within lunar soils as they mature, causes a decrease in reflectance and a concomitant increase in the NIR/Vis reflectance ratio (Fischer & Pieters, 1994). The 1 μm and 2 μm absorption depths correlate strongly with the continuum slope (equation 2) and thus corrected values (equations 5 and 6), calibrated for maturation effects, can be defined using the coefficients of these relationships (Le Mouélic et al., 2000).

$$1\ \mu m\ depth = 1 - \frac{R_{950}}{(2.2/3)R_{750} + (0.8/3)R_{1500}} \quad (3)$$

where R_{750}, R_{950}, and R_{1500} are the Clementine reflectance values at 750 nm, 950 nm, and 1500 nm. The denominator in this equation gives the interpolated level of the continuum slope at 950 nm. This parameter has a high value when the 1 μm absorption feature is deep, i.e. when there is abundant ferrous iron and/or little space weathering.

$$2\ \mu m\ depth = \frac{R_{2000}}{R_{1500}} \quad (4)$$

where R_{2000} and R_{1500} are the Clementine reflectance values at 2000 nm and 1500 nm. This parameter has a high value when the 2 μm absorption feature is weak, or absent, as is the case for olivine. It has a low value when the absorption is strong, i.e. for pyroxenes.

The maturity corrected versions of these equations are as follows:

$$corrected\ 1\ \mu m\ depth = 1\ \mu m\ depth + 0.286 \times (continuum\ slope) \quad (5)$$

where 1 μm depth and continuum slope are defined in equations 3 and 2 respectively, and 0.286 is the slope of the linear relationship between these two parameters.

$$corrected\ 2\ \mu m\ depth = 2\ \mu m\ depth + 0.32 \times (continuum\ slope) \quad (6)$$

where 2 μm depth and continuum slope are defined in equations 4 and 2 respectively, and 0.32 is the slope of the linear relationship between the these two parameters.

FeO & TiO_2 abundance algorithms

Mare basalt hand specimens are usually classified primarily by their bulk rock TiO_2 contents (Neal & Taylor, 1992) which can vary from <1 wt. % to ~13 wt. % (e.g. BVSP, 1981; Taylor et al., 1991). As such, lateral and vertical compositional variations of lava flows in the mare regions can also be classified on this basis from remote sensing data sensitive to TiO_2 concentration. The relationships between lunar surface reflectance spectra and sample FeO and TiO_2 contents have led to the development of several quantitative methods for estimating the composition of the lunar surface from suitable remote sensing datasets.

Lucey FeO & TiO_2

Lucey et al. (1995) first introduced a method for determining the FeO content of lunar soils from remote spectral reflectance data. It exploits the radial trends of samples with equal FeO content, but varying maturities away from a hypothetical mature end-member on a plot of reflectance at 750 nm versus the 950/750 nm (NIR/Vis) ratio (Figure 5.4). These trends are used to define an angular, iron-sensitive parameter (θ_{Fe}, equation 7). The linear polynomial relationship between it and laboratory obtained FeO wt. % abundances for lunar samples is then used to calculate FeO wt. % contents from the remotely sensed spectral information (equation 8). This approach has been updated and improved (Lucey et al., 1998; 2000b), with the most recent calibration aiming to provide the best correlation between θ_{Fe} and the FeO content of soils *and* minimise the effects of maturity. This version gives a position for the mature end-member (see Figure 5.4) of: $x_0 = 0.08$, $y_0 = 1.19$ (Lucey et al., 2000b).

$$\theta_{Fe} = -arctan\left(\frac{\left(\left(\frac{R_{950}}{R_{750}}\right) - y_{0Fe}\right)}{R_{750} - x_{0Fe}}\right) \quad (7)$$

This is used to calculate the FeO abundance:

$$wt.\%\, FeO_{Lucey} = (17.427 \times \theta_{Fe}) - 7.565 \quad (8)$$

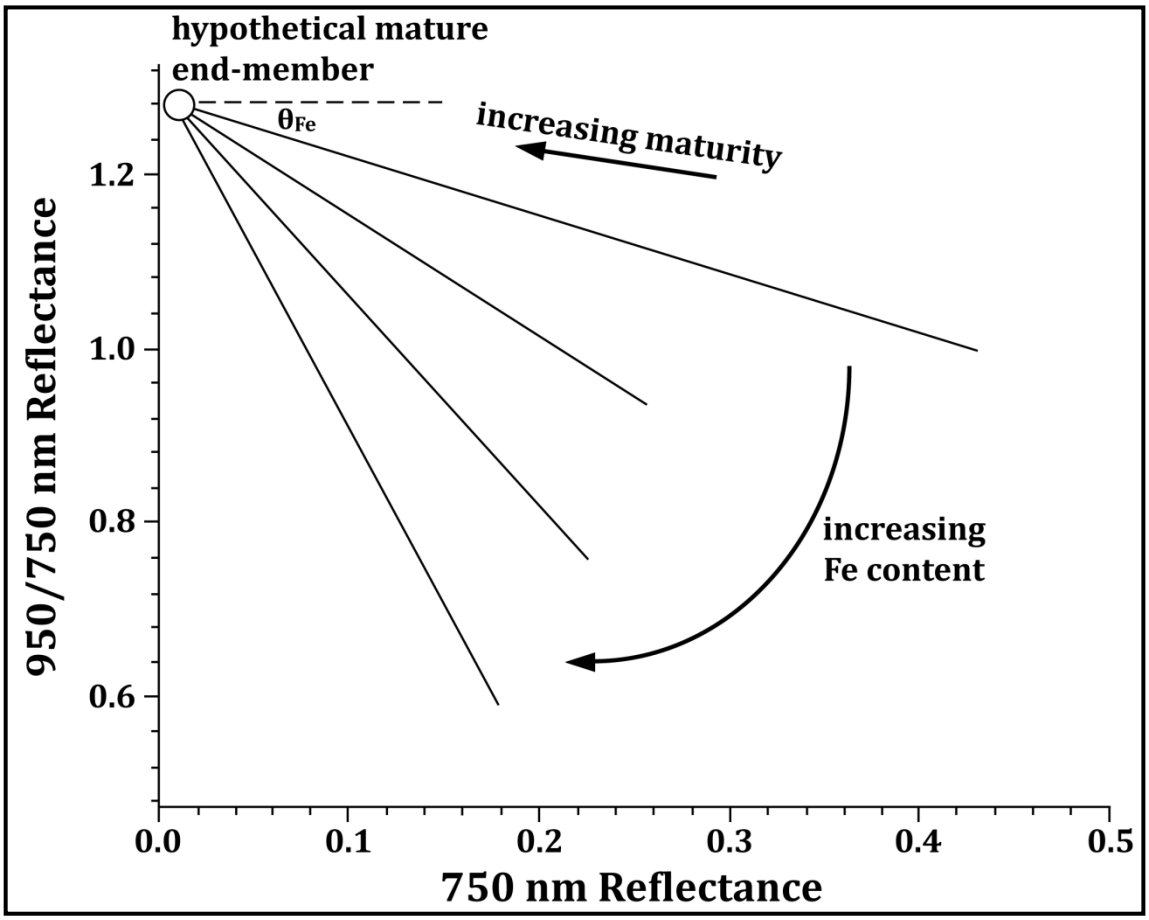

Figure 5.4. Diagram illustrating the Lucey et al. (1995; 1998; 2000b) method for separating iron and maturity trends and for calculating the iron-sensitive parameter (θ_{Fe}). Materials with equal FeO content and varying levels of maturity trend radially away from a theoretical mature end-member; iron-content increases with increasing angular distance (adapted from Wilcox et al., 2005).

Lucey et al. (1996) introduced a technique for estimating the TiO_2 content of lunar soils using the 415 nm and 750 nm Clementine reflectance values. This is based on a correlation between the TiO_2 wt. % content and the UV-Vis ratio of mature lunar soils, known as the *Charette relation* (Charette et al., 1974; Johnson et al., 1991; Melendrez et al., 1994). Lucey et al., (1996) define a titanium-sensitive parameter (θ_{Ti}, equation 9) in a similar way to that for iron (equation 7) and is based on a plot of the 415/750 nm ratio versus reflectance at 750 nm (Figure 5.5). An optimised location for the mature end-member, with coordinates: $x_0 = 0.0$, $y_0 = 0.42$ (Lucey et al., 2000b), allows the TiO_2 abundance to be estimated from remote measurements, using the power law that relates θ_{Ti} and sample TiO_2 content (equation 10).

$$\theta_{Ti} = arctan\left(\frac{\left(\left(\frac{R_{415}}{R_{750}}\right) - y_{0Ti}\right)}{(R_{750} - x_{0Ti})}\right) \quad (9)$$

$$wt.\%\, TiO_{2_{Lucey}} = 3.708 \times (\theta_{Ti})^{5.979} \quad (10)$$

Both Lucey algorithms have estimated 1 σ errors of 1 wt. % (Lucey et al., 2000b).

Gillis FeO & TiO_2

Gillis et al. (2003; 2004) review and find various problems with the Lucey et al. (2000b) algorithms and propose modifications to improve the accuracy of the compositional estimates they provide. A dichotomy between the unimodal distribution of the mare basalts in remote sensing data (Giguere et al., 2000) and the bimodal distribution of the sample data in terms of TiO_2 wt. % content has been noted (Lucey et al., 2006); although the sample data distribution may be an artefact of sampling and more closely match the remote sensing data with new random sampling provided by the lunar meteorites (Shearer et al., 2006). The Lucey TiO_2 algorithm (Lucey et al., 2000b) uses a single regression to calibrate all the returned samples, whereas Gillis et al. (2003) also use a second regression to provide a better fit for the compositions Apollo 11, Luna 16 and Luna 24 samples. Together, the two regressions yield results that more closely match the measured soil samples for each site. Their technique also produces a more bimodal TiO_2 distribution than the Lucey method. The Gillis TiO_2 algorithm continues to define the titanium-sensitive parameter as in equation 9, but uses a slightly altered end-member coordinate location (x_0 = -0.012, y_0 = 0.36) chosen to maximise the correlation between θ_{Ti} and the sample TiO_2 data. In order to account for the two trends the TiO_2 abundance is then estimated using equation 11, or when reflectance at 415 nm is <0.065 *and* the 415/750 nm ratio is >0.59, the second regression is employed (equation 12).

$$wt.\%\, TiO_{2_{Gillis,a}} = 1.7159 \times (\theta_{Ti})^{9.8817} \quad (11)$$

$$wt.\%\, TiO_{2_{Gillis,b}} = 0.14 + 0.24 \times (\theta_{Ti})^{15.5} \quad (12)$$

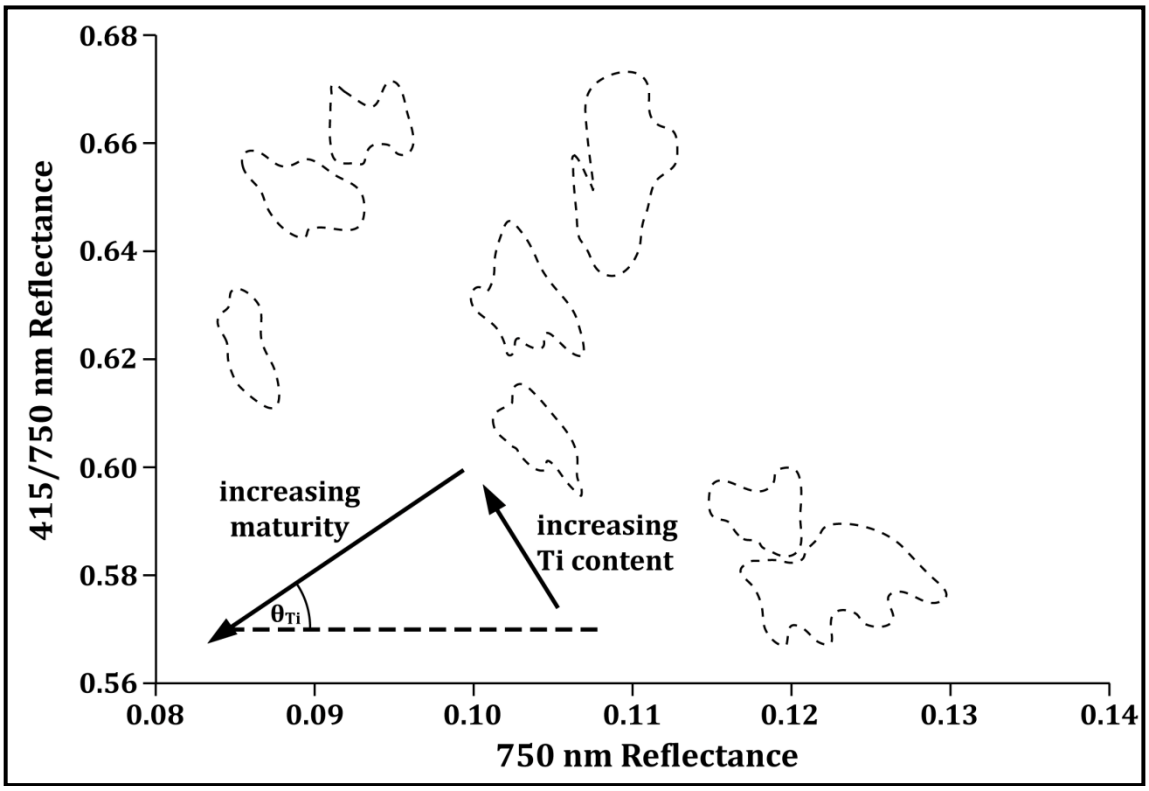

Figure 5.5. Diagram illustrating the Lucey et al. (1996; 2000b) method for separating titanium and maturity trends and for calculating the titanium-sensitive parameter (θ_{Ti}). The spectral properties of various Apollo and Lunar landing sites are enclosed by the dashed lines. The trends of increasing maturity and TiO_2 wt. % content are roughly orthogonal (adapted from Gillis et al., 2003).

Likewise, Gillis et al. (2004) raise issues with the Lucey et al. (2000b) FeO algorithm, claiming that it under predicts FeO wt. % values for low-Ti mare soils and that it is biased towards the large number of Apollo 15 and Apollo 17 samples, which lie on two parallel, but separate lines and whose main chemical difference is the TiO_2 wt. % content. The Gillis et al. (2003) FeO algorithm therefore incorporates a term to deal with the TiO_2 content. The iron-sensitive parameter, θ_{Fe}, is calculated as in equation 7, but with a different end-member position (x_0 = 0.07, y_0 = 1.155) which optimises the fit between the values of θ_{Fe} and sample FeO content as well as suppressing maturity effects. The FeO content is then calculated using equation 13, or equation 14 when the reflectance at 415 nm is <0.065 *and* the 415/750 nm ratio is >0.59.

$$wt.\%\ FeO_{Gillis,a} = (17.427 \times \theta_{Fe}) - 7.565 \quad (13)$$

$$wt.\%\ FeO_{Gillis,b} = (-0.2208 \times TiO_2 + 17.634)\theta_{Fe} + (0.0712 \times TiO_2 - 3.288) \quad (14)$$

Wilcox FeO

Staid & Pieters (2000) suggest that the trends of mare samples on the plot of NIR/Vis versus Vis reflectance are actually more parallel than they are radial (Figure 5.6). This being the case, the Lucey et al. (2000b) and Gillis et al. (2004) algorithms do not optimally decouple the effects of maturity and FeO content. Having evaluated several thousand small mare craters, Wilcox et al. (2005) agree that a parallel model more accurately describes the trends than the radial model, and thus define a new iron-sensitive parameter, ρ:

$$\rho = (R_{750} \sin\theta) + \left(\frac{R_{950}}{R_{750}} \cos\theta\right) \quad (15)$$

where θ is the average slope of the mare maturity trends, and has a value of 1.3885 radians (the average slope of the trends).

The correlation between ρ and the FeO content of Apollo and Luna samples allows the FeO content to be estimated from Clementine reflectance data using equation 16. The linear fit of this correlation is weaker for highland samples, and an alternative method for estimating such information should still be used. This algorithm better separates the effects of iron and maturity than the previous methods. Variations of >0.5 wt. % in the deduced FeO concentration are thought to be due to true iron variations, rather than incomplete suppression of maturity effects (Wilcox et al., 2005).

$$wt.\%\ FeO_{Wilcox} = (-137.97\rho) + 57.46 \quad (16)$$

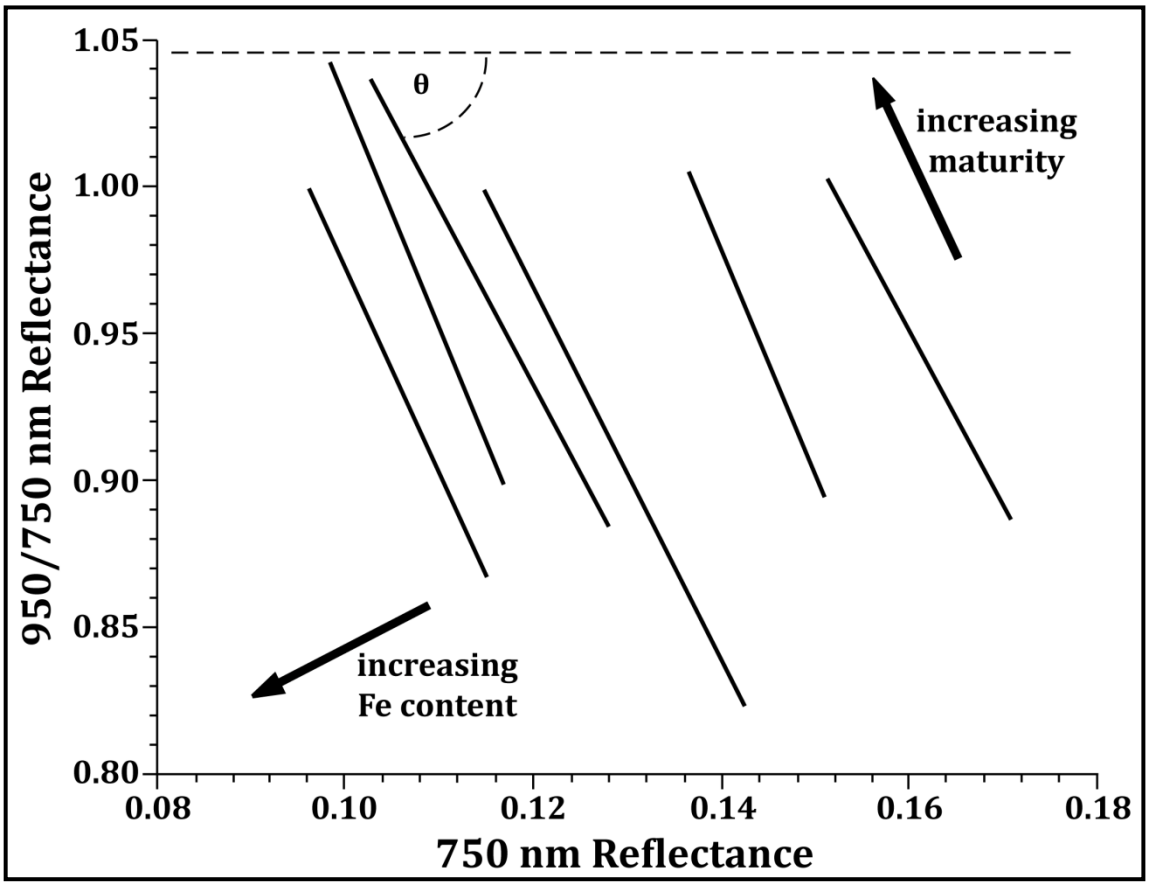

Figure 5.6. Example trends for craters in various mare areas illustrating the Wilcox method for separating maturity and FeO wt. % content trends and for calculating the iron-sensitive parameter (ρ). Most trends, like these, are linear and highly correlated (adapted from Wilcox et al., 2005).

Le Mouélic FeO

Le Mouélic et al. (2000) present an alternative method for quantitatively estimating the FeO content of lunar soils. This is based on the correlation between the maturity corrected 1 μm absorption depth (equation 5) and the slope of the continuum (equation 2) for areas with assumed constant FeO contents but different maturity levels. The depth of the corrected 1 μm absorption is linked to Fe^{2+} within un-weathered silicates and therefore this *mafic iron* includes Fe both within the current silicates as well as glassy particles; it is not sensitive to iron contained within oxides (of which ilmenite is the major one on the Moon). The difference between the FeO wt. % values returned from this algorithm and the Lucey et al. (2000b), Gillis et al. (2004) or Wilcox et al. (2005) methods is therefore related to the abundance of ilmenite/titanium, and as such a term is included in the final calculation

(equation 17) to deal with it (using the Lucey/Gillis algorithm to calculate the TiO_2 wt. %). This algorithm has a 1 σ error of 1.5 wt. %.

$$wt.\%\ FeO_{Le\ Mouelic} = 45.6 \times (corrected\ 1\ \mu m\ depth) - 3.8 + (0.9 \times TiO_2) \qquad (17)$$

Summary

In this chapter, the Wilcox et al. (2005) and Lucey et al. (2000b) algorithms for estimating FeO and TiO_2 wt. % contents respectively have been employed because they most reliably remove the effects of space weathering from mare reflectance spectra. Although the Lucey et al. (2000b) TiO_2 algorithm has a quoted estimated 1 σ error of 1 wt. %, later studies have cast doubts over its ability to accurately determine the true TiO_2 concentration of the lunar surface (Gillis et al., 2003; Gillis-Davis et al., 2006), and so the actual error may be somewhat larger. However, for this particular study, obtaining the absolute abundance of TiO_2 is less critical than ensuring that the differences in maturity of separate regions are properly accounted for and that their *relative* differences in TiO_2 content are significant.

Maturity parameters

The Lucey et al. (2000b) iron sensitive parameter (equation 7) is used to minimise the correlation between iron content and maturity; a complementary parameter, which is proportional to, and a measure of maturity also exists (Lucey et al., 2000c). This optical maturity parameter (OMAT; Grier et al., 1999) is the distance from the hypothetical mature end-member to each point on a plot of 950/750 nm versus 750 nm reflectance, and is defined in equation 18:

$$OMAT = \left((R_{750} - x_0)^2 + \left(\left(\frac{R_{950}}{R_{750}} \right) - y_0 \right)^2 \right)^{\frac{1}{2}} \qquad (18)$$

However, the Wilcox et al. (2005) FeO algorithm deals better with maturity effects than the Lucey et al. (2000b) algorithm, and as such they defined their own mare optical maturity parameter:

$$mOMAT = (R_{750}\cos\theta) - \left(\frac{R_{950}}{R_{750}}\sin\theta\right) \quad (19)$$

where values can range from -1.05 (most mature) to -0.65 (least mature) and θ has a value of 1.3885 radians.

5.2. Study area 1: Marius region (0°-15°N; 300°-315°W), Oceanus Procellarum

To begin this investigation, an area (Figure 5.7) was chosen that contains a significant number of individual lava flows within close proximity, as part of the widespread compositional diversity in Oceanus Procellarum (Hiesinger et al., 2003). As such, this region provides a suitable area to test the method of employing impact craters to probe subsurface lava flow stratigraphy. This area also contains the Reiner Gamma magnetic anomaly in the west of area (e.g. Hood & Williams, 1989; Hood et al., 2001) and the Marius Hills volcanic complex in the north of area (e.g. Whitford-Stark & Head, 1977; Weitz & Head, 1999).

The UV-Vis and NIR Clementine data were downloaded at full resolution (0.1 km/pixel) and in a simple cylindrical projection from the USGS Map-A-Planet website (www.mapaplanet.com) as radiometrically, geometrically and photometrically controlled .raw files (Eliason et al., 1999; Gaddis et al., 2007). These files were extracted and analysed using an in-house IDL (Interactive Data Language) code (written by K. Joy) in order to map the areas in terms of their composition.

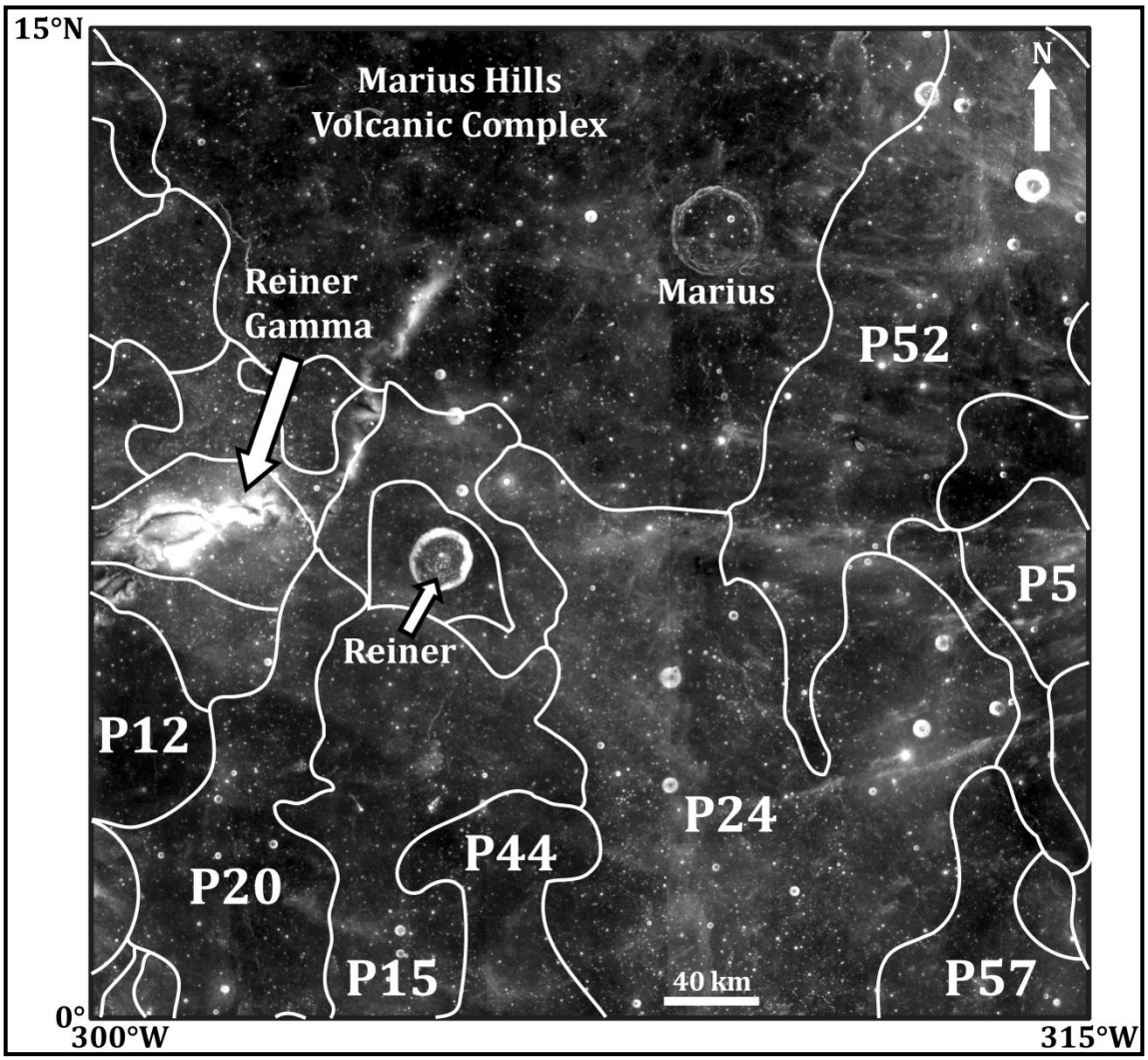

Figure 5.7. Clementine 750 nm image of the study area, indicating the major geological features of the region. Unit boundaries and nomenclature are taken from Hiesinger et al. (2003).

5.2.1. *Mafic mineralogy*

Figure 5.8 shows maps of the maturity corrected 1 μm and 2 μm absorption band depths for this region (see equations 5 and 6). These images should illustrate any large variations in mafic mineralogy. The lava flow boundaries as mapped by Hiesinger et al. (2003) are also shown. Fresh craters in Figure 5.8a are bright (albedo ~0.2) because they have excavated fresh material and their steep slopes prevent the products of space weathering from accumulating. There are no obvious large scale anomalous signatures relating to impact craters in this image. The depth of the 2 μm absorption band (corrected for maturity) shown in Figure 5.8b, allows pyroxene-rich and olivine-rich material to be distinguished. Pyroxenes, which exhibit a 2 μm absorption feature, have low values in this parameter and

should appear blue in Figure 5.8b; olivine does not exhibit this absorption, and so olivine-rich regions of the map should appear yellow/orange. The general mare surfaces in the map do not display notable colour variations. A single compositional anomaly is observed in the crater Marius towards the north of the map, and is marked by an arrow. This anomaly is discussed in section 5.2.3.

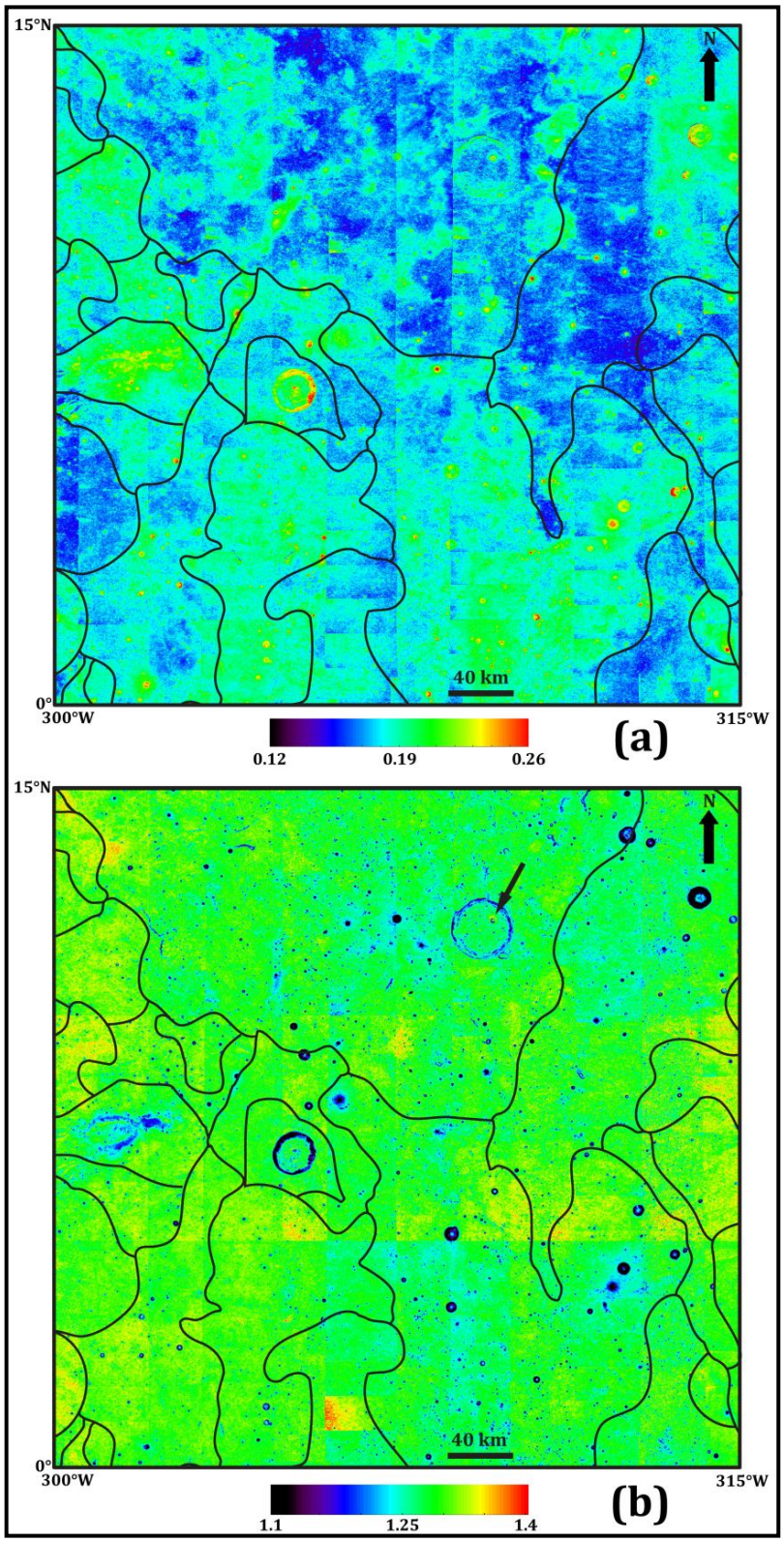

Figure 5.8. Maps of the (a) 1 µm and (b) 2 µm absorption depths, corrected for space-weathering spectral alterations (equations 5 and 6). High values (orange/red) in (a) represent fresh craters with steep interior slopes that prevent the accumulation of space-weathering products. The arrow to the north of the area, in (b), highlights a compositional anomaly associated with a small impact crater within the larger, older crater Marius. The unit boundaries are those mapped by Hiesinger et al. (2003).

5.2.2. *FeO & TiO_2 concentration*

Figure 5.9 displays maps of the estimated FeO and TiO_2 contents (wt. %), according to the algorithms of Wilcox et al. (2005) and Lucey et al. (2000b) respectively. The Hiesinger et al. (2003) unit boundaries closely approximate the colour variations of the TiO_2 wt. % content map (Figure 5.9b), which is expected due to the fact that their map was constructed using a false colour image that primarily reveals differences in the titanium content of mature basalts.

The TiO_2 concentration map (Figure 5.9b) reveals a number of craters within a particular lava flow unit (flow 'P52' of Hiesinger et al., 2003; immediately to the east of Marius Hills) that appear to be surrounded by haloes of material with a lower TiO_2 content (more blue) than the surrounding lava flow, and which approximate the extent of their continuous ejecta blankets. These craters are circled and numbered (1 to 13) in Figure 5.10, which shows a small subset of the area (a set of 18 craters with no discernable haloes are also shown and labelled 'A; to 'S' in Figure 5.10). It is hypothesised that these haloes evidence material with a lower TiO_2 abundance that has been excavated from a lithology beneath the surface flow ('P52'). A candidate for this lithology is the stratigraphically lower lava flow 'P24' (Hiesinger et al., 2003), which is TiO_2-poorer by ~3 wt. %.

To test this hypothesis, Clementine multispectral reflectance data for a number of pixels (see Table 5.1) within the continuous ejecta blankets of the haloed craters (these are assumed to extend for ~1 crater radius beyond the rim: Moore et al., 1974; Oberbeck et al., 1974; see Figure 5.11) were obtained, as well as for the inter-crater areas of lava flow units 'P52' and 'P24'. Figure 5.12 is a plot of mean FeO and TiO_2 wt. % abundances for (i) the ejecta of the thirteen craters with TiO_2-poor haloes identified in lava flow 'P52' and (ii) the mean lava flow compositions for 'P52' and 'P24'. It illustrates that the ejecta of the thirteen haloed craters have a distinct composition from that of lava flow 'P52' in which they are located and that the ejecta compositions are more similar to that of the proposed underlying unit, 'P24'.

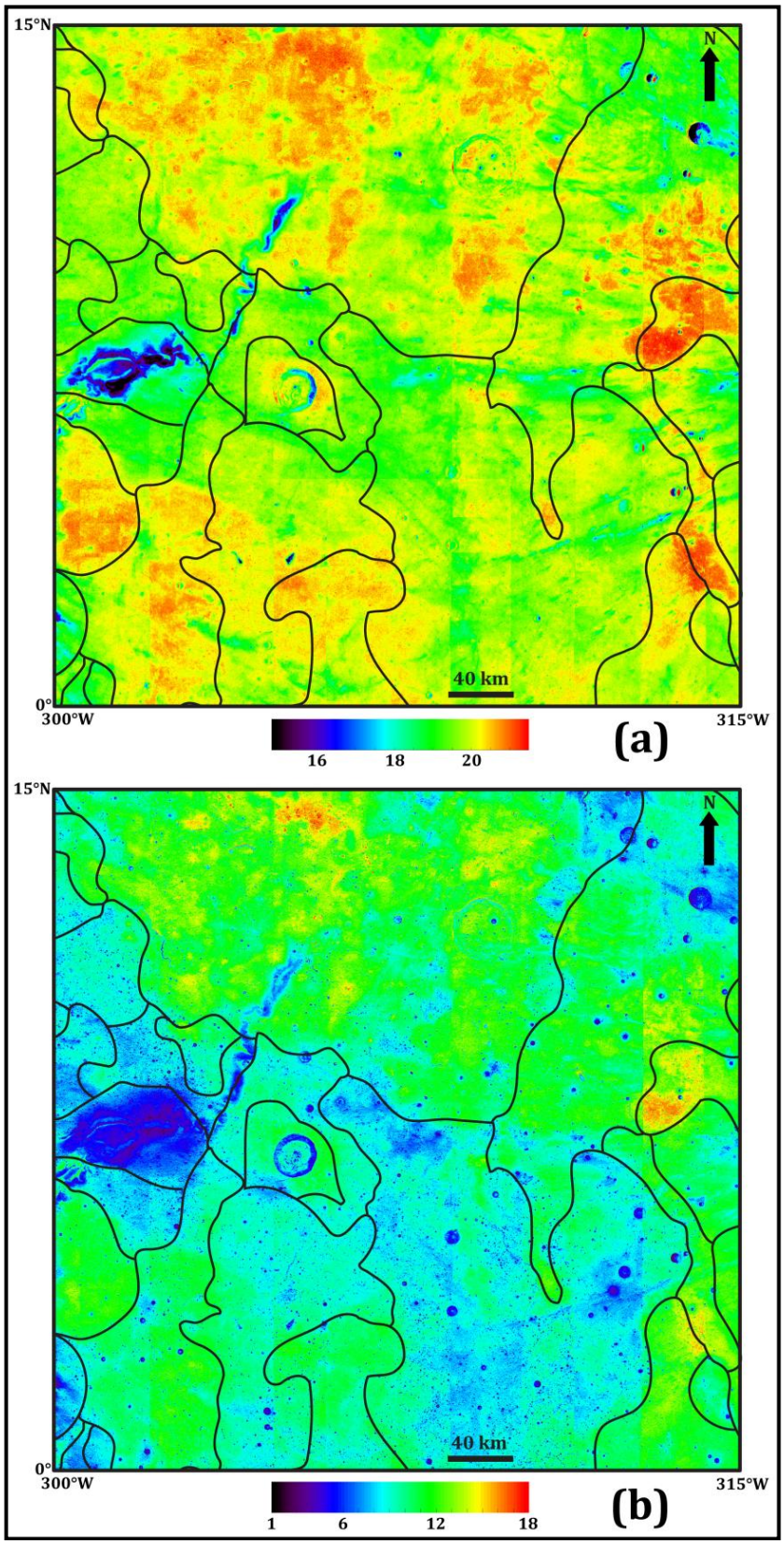

Figure 5.9. Maps of the (a) surface FeO content (in wt. %) according to the algorithm of Wilcox et al. (2005) and (b) surface TiO_2 content (in wt. %) according to the algorithm of Lucey et al. (2000b). Reiner Gamma appears to have a low FeO content, but this is probably an artefact of its anomalously high albedo. The unit boundaries are those mapped by Hiesinger et al. (2003).

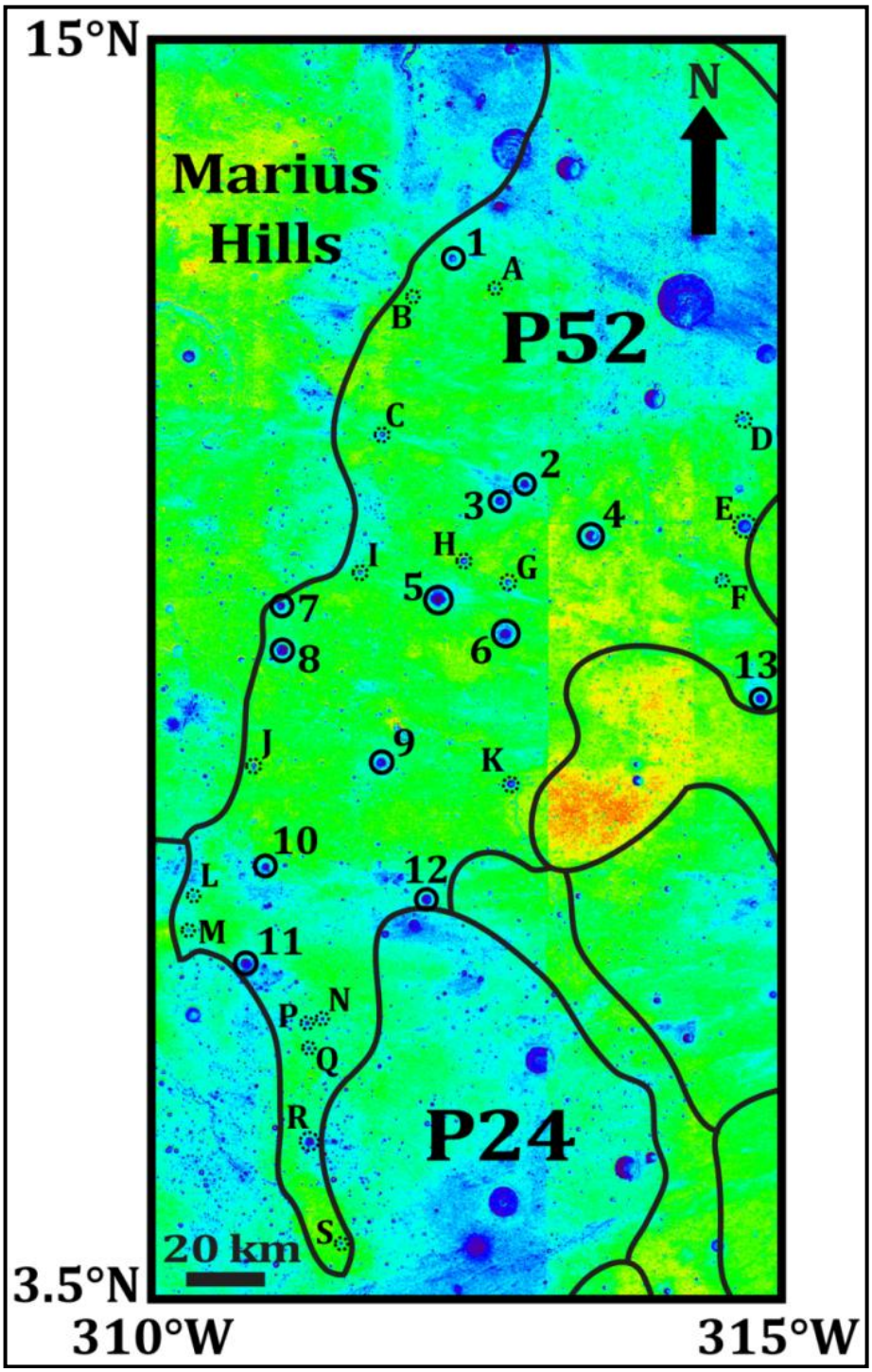

Figure 5.10. Surface TiO_2 wt. % composition (Lucey et al., 2000b algorithm) map for part of the Oceanus Procellarum study area (part of Figure 5.9b) around lava flow unit 'P52'. Indicated are (i) the thirteen impact craters with TiO_2-poor haloes (labelled 1 to 13) and (ii) additional impact craters in the same unit with no observable halo (labelled 'A' to 'S' and circled with dashed lines).

Table 5.1. List of craters and inter-craters areas for which measurements were obtained in the Oceanus Procellarum study area. Errors listed are 1 σ.

Area	No. pixels sampled	TiO_2 wt. %	mOMAT	Crater diameter (km)	Max. exc. depth (km)
Crater 1	23	8.22±0.78	-0.96±0.02	2.52	0.21
Crater 2	33	7.10±1.08	-0.94±0.04	2.91	0.24
Crater 3	24	7.68±0.52	-0.96±0.02	3.02	0.25
Crater 4	31	7.92±0.73	-0.95±0.01	4.23	0.35
Crater 5	24	7.88±1.10	-0.92±0.02	2.29	0.19
Crater 6	27	6.81±1.07	-0.94±0.03	3.20	0.27
Crater 7	21	8.23±0.61	-0.96±0.02	2.44	0.20
Crater 8	26	8.11±0.49	-0.97±0.02	3.50	0.29
Crater 9	24	7.57±0.64	-0.95±0.02	3.00	0.25
Crater 10	21	7.61±0.86	-0.94±0.02	2.28	0.19
Crater 11	35	6.67±0.50	-0.96±0.01	3.40	0.29
Crater 12	27	7.47±0.34	-0.96±0.01	3.63	0.30
Crater 13	23	7.80±1.25	-0.95±0.02	3.53	0.30
Crater A	10	9.54±0.55	-0.94±0.01	0.75	0.06
Crater B	10	10.27±0.56	-0.95±0.01	1.26	0.11
Crater C	10	8.98±0.60	-0.98±0.01	1.80	0.15
Crater D	15	9.27±0.34	-0.97±0.01	1.89	0.16
Crater E	18	10.61±0.64	-0.98±0.01	4.65	0.39
Crater F	7	9.70±0.68	-0.98±0.01	1.56	0.13
Crater G	10	10.55±0.67	-0.96±0.01	2.01	0.17
Crater H	13	10.22±0.57	-0.96±0.01	2.35	0.20
Crater I	11	9.71±0.50	$-0.98\pm4\times10^{-3}$	1.65	0.14
Crater J	11	10.53±1.46	-0.98±0.01	1.46	0.12
Crater K	20	10.12±0.50	-0.98±0.01	2.72	0.23
Crater L	9	9.20±0.25	$-0.98\pm4\times10^{-3}$	1.21	0.10
Crater M	9	9.00±0.25	-0.98±0.01	1.14	0.10
Crater N	8	8.91±0.52	-0.95±0.01	0.48	0.04
Crater P	7	9.10±0.42	-0.97±0.01	1.18	0.10
Crater Q	11	9.55±0.53	-0.98±0.01	1.00	0.08
Crater R	18	8.94±0.52	-0.97±0.01	2.67	0.22
Crater S	11	9.75±0.41	-0.97±0.01	0.93	0.08
'P24' inter-crater area	109	7.31±0.77	-0.97±0.02	-	-
'P52' inter-crater area	236	9.95±0.70	-0.97±0.01	-	-
Marius G interior	10	5.52±0.80	-0.92±0.02	-	-
Marius G ejecta	16	9.17±0.95	-0.97±0.02	-	-
Inner-Marius lava flow	34	11.22±0.93	-0.98±0.01	-	-
Outer-Marius lava flow	22	10.26±1.16	-0.99±0.01	-	-

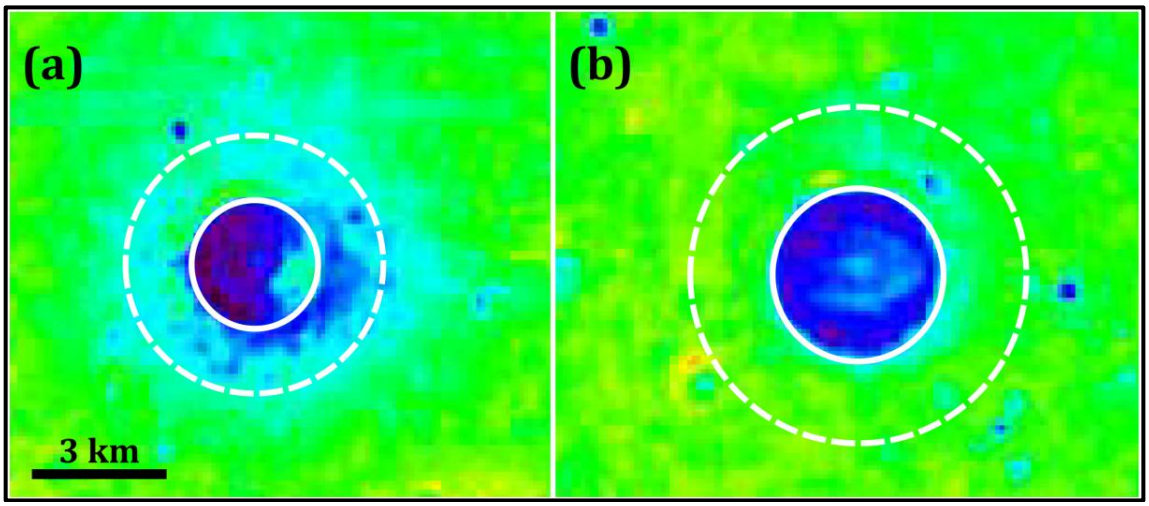

Figure 5.11. Examples of impact craters within lava flow unit 'P52', displayed in terms of TiO_2 wt. %. (a) Shows a crater with a TiO_2-poor halo and (b) without. The area between the solid (crater rim) and dashed (extent of continuous ejecta) lines is the region from which data for ejecta compositions were obtained. The ejecta limit does not always completely encompass the halo, but the fixed distance of 1 crater radius was chosen for the sake of consistency. The apparently low-TiO_2 crater interior (dark blue) is caused by bright, un-space weathered material on the steep slopes; asymmetries are caused by variations in illumination due to topography. The scale for both images is equal.

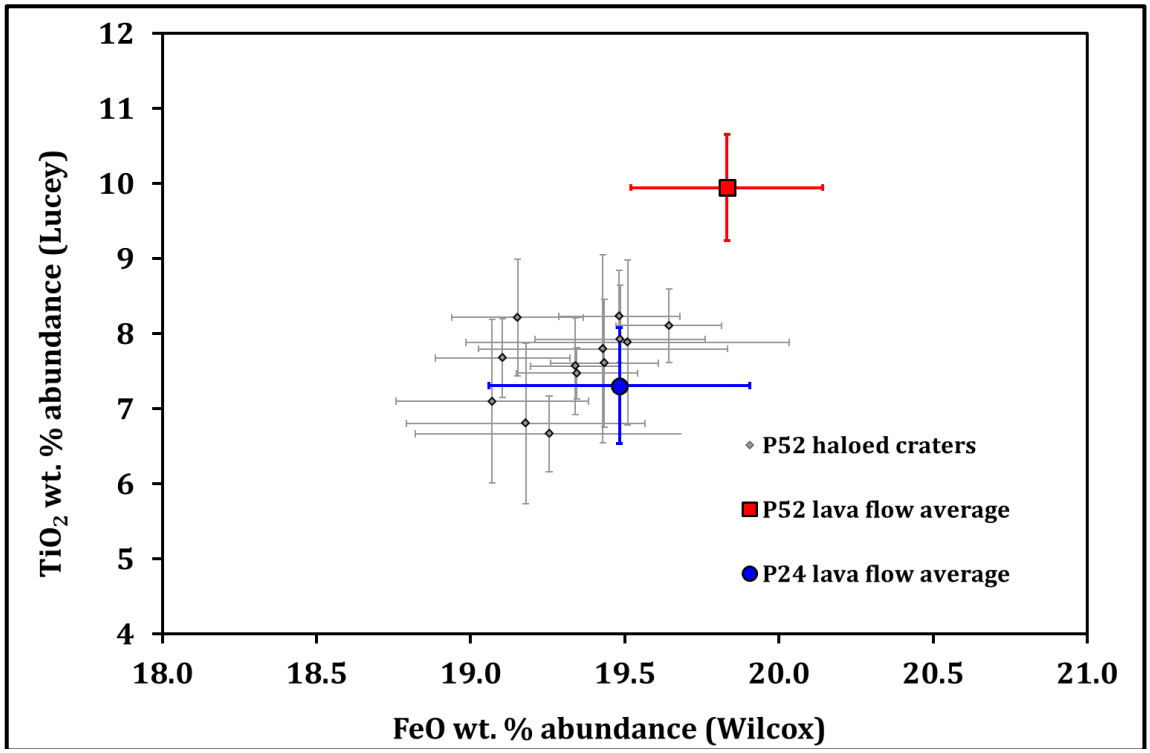

Figure 5.12. The mean FeO (according to the algorithm of Wilcox et al., 2005) and TiO_2 (according to the algorithm of Lucey et al., 2000b) wt. % contents for the ejecta of the thirteen haloed craters in lava flow unit 'P52', and mean inter-crater values for lava flows 'P52' and 'P24'. Error bars indicate 1 standard deviation of the individual pixel values used to produce the mean values.

The increase in nanophase iron in lunar soils due to space weathering causes a darkening of reflectance spectra, as does increased abundance of ilmenite (the major TiO_2 bearing opaque phase in lunar soils). It is therefore important to confirm that the apparent lower TiO_2 content of these crater ejecta is due to an actual compositional difference compared to the lava flow unit in which they are located, rather than to an unresolved maturity (albedo) issue. It is thought that the TiO_2-poor haloes are indeed evidence of a true compositional difference for a number of reasons illustrated in Figure 5.13:

(i) On a plot of the 415/750 nm reflectance ratio versus albedo (750 nm) the ejecta of the haloed craters in lava flow 'P52' form a distinct group from the ejecta of a set of craters with no haloes in the same lava flow (Figure 5.13a); the offset of these two groups follows a trend of increased TiO_2 content rather than one of increased maturity;

(ii) The majority of the craters (both with and without TiO_2-poor haloes) have a similar, narrow range of mature mOMAT values (Figure 5.13b), indicating that the craters which have been sampled all have a similar level of maturity; and

(iii) As a function of crater diameter, the two sets of craters display a clear distinction in TiO_2 wt. % values, but not in albedo (Figure 5.13c, d).

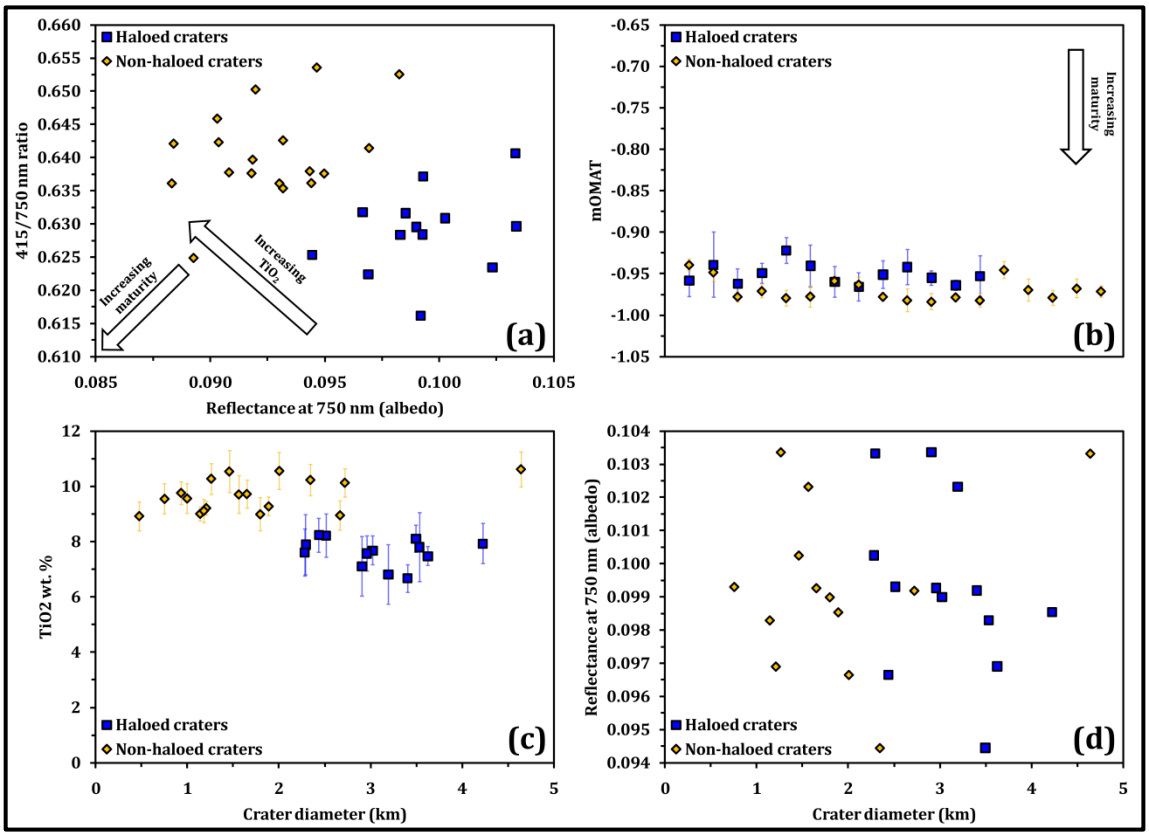

Figure 5.13. Graphs illustrating that the TiO_2-poor haloes of craters in lava flow unit 'P52' are caused by TiO_2 wt. % content variations rather than surface maturity issues. Data from craters with TiO_2-poor haloes are compared with neighbouring craters without such haloes. (a) 415/750 nm reflectance ratio vs. 750 nm reflectance (albedo) values for the haloed craters in lava flow 'P52'; the trend of the two groups is one for increased TiO_2 content rather than increased maturity. (b) mOMAT (according to the algorithm of Wilcox et al., 2005) values for both sets of craters; all the craters fall within a narrow range of mature values, there is considerable overlap between the two groups suggesting similar maturity levels. (c) Mean TiO_2 (according to the algorithm of Lucey et al., 2000b) wt. % values for the continuous ejecta of the haloed and non-haloed craters as a function of their diameter; there is a clear distinction in terms of TiO_2 abundance between the two subsets, with the haloed craters tending to be larger. (d) Albedo of both populations of craters, as a function of their diameter; the range of values for both groups is equal.

Given that the identified craters with TiO_2-poor haloes in lava flow 'P52' have indeed excavated material from a deeper, compositionally different lava flow (i.e. 'P24'), their diameters can be used to estimate their maximum depth of excavation and therefore constrain the thickness of the surficial lava flow ('P52'). The maximum excavation depth of simple craters (i.e. those with diameters <15 km) can be calculated using equations 20 and 21 (Melosh, 1989). These values are listed in Table 5.1.

$$D_t = 0.84 \times D \tag{20}$$

$$D_{exc} = \frac{1}{10} D_t \quad (21)$$

where D_t is the transient cavity diameter; D is the present diameter of the crater (rim to rim) and D_{exc} is the maximum excavation depth.

The maximum excavation depths of the TiO_2-poor haloed craters are used to provide an upper bound for the thickness of unit 'P52' where it overlies 'P24' in this area, whereas the excavation depths of the non-haloed craters provide a lower limit for this thickness. The maximum excavation depth estimates (in km) for the craters with and without TiO_2-poor haloes in lava flow 'P52' are shown in Figure 5.14. The results show that 'P24' is between ~100 m and 300 m below the surface of 'P52' in the area that has been investigated.

The total thickness of the mare basalt deposit within Oceanus Procellarum has previously been estimated using a variety of techniques. Morphometric crater relationships (Pike, 1974; 1977) and the heights of exposed rims were used to infer the burial depths of partially buried craters (De Hon, 1978; 1979). The isopach map produced by De Hon (1979) gives a total basalt thickness estimate in this study area of 500 – 1000 m. Craters which have excavated basement anorthositic material have been used to estimate the total thickness of the overlying basalt (Heather & Dunkin, 2002), and are in broad agreement with the earlier study by De Hon (1979). The new results presented here extend this approach by providing an estimate of the thickness of individual lava flows within a stack of temporally and compositionally distinct deposits. If 'P52' (with an estimated thickness of ~100 to 300 m) constitutes about half of the minimum estimated (i.e. 500 m) total depth of basaltic material in this region, then it is predicted that 'P24' has a similar thickness and completes the basin fill. However, if there is an additional, un-sampled flow(s) underlying 'P24', its true thickness would be smaller.

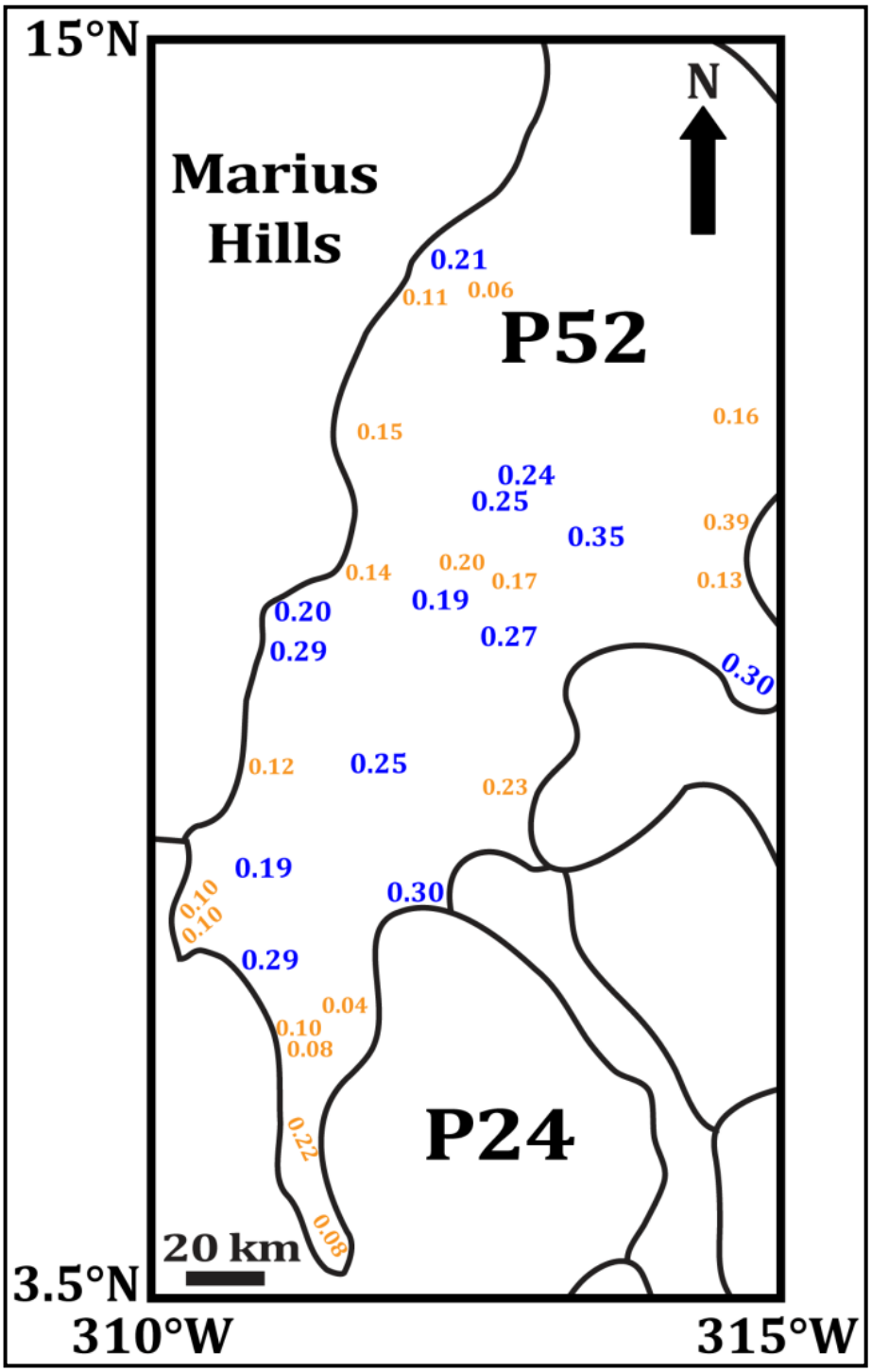

Figure 5.14. Maximum excavation depths (in km) for (i) the thirteen impact craters with TiO_2-poor haloes (blue) and (ii) the eighteen craters lacking compositional haloes (orange) in lava flow unit 'P52'. There is only limited overlap between the values of the two groups (see Figure 5.13c); this overlap is probably due to underlying topographic variations (e.g. buried craters) which cause local variations in the thickness of 'P52'.

5.2.3. *Marius Crater*

The arrow in Figure 5.8b (map of the space-weathering corrected 2 μm absorption depth for the study area) marks an anomalous region around a small impact crater (Marius G) within the larger crater Marius. Figure 5.15 is a map of the continuum slope (equation 2) for the area surrounding Marius and it illustrates a prominent ring of material (yellow/red) associated with its region of continuous ejecta. The anomalously high value in this parameter indicates that the material is more mature than its surroundings. However, this material should be ejecta of Marius G, and therefore younger than the adjacent surface; this conundrum warrants further investigation.

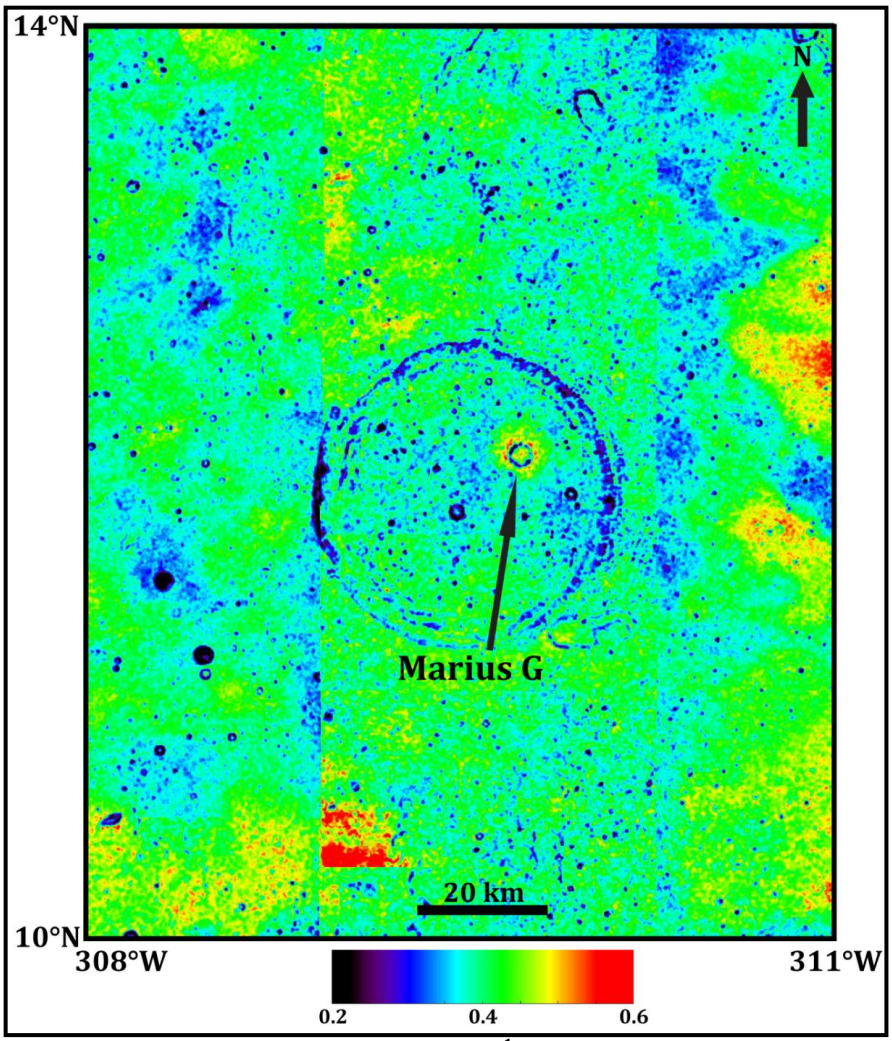

Figure 5.15. Map of the continuum slope value, in μm^{-1}, (equation 2) for the immediate area around Marius crater. The bright (yellow/red) ring of material around Marius G that coincides with the location of its continuous ejecta is clearly visible.

Figure 5.16 shows the same region around Marius, in terms of the space-weathering corrected depths of the 1 µm and 2 µm absorption features (equations 5 and 6). The ejecta of Marius G have a deeper mafic absorption (1 µm) than the surrounding material, which is due to its relative freshness, as well as a weaker 2 µm absorption that is indicative of either an olivine-rich basalt or anorthositic material. The TiO_2 (Figure 5.17a) and FeO (Figure 5.17b) content maps show that Marius G ejecta have a lower TiO_2 wt. % content than the adjacent environment, but the FeO abundance shows no significant change. The relatively constant and high iron abundance (~19 – 20 wt. %) negates the possibility of the ejecta containing abundant anorthosite. On the basis of these parameters, the ejecta of Marius G appear to consist of material excavated during its impact event, from an older and deeper lava flow with lower titanium and higher olivine content than the lithology currently exposed at the surface. Recent data from M^3 (Moon Mineralogy Mapper) also reveal olivine-rich signatures associated with fresh impact craters (including Marius G) within Marius (Besse et al., 2010).

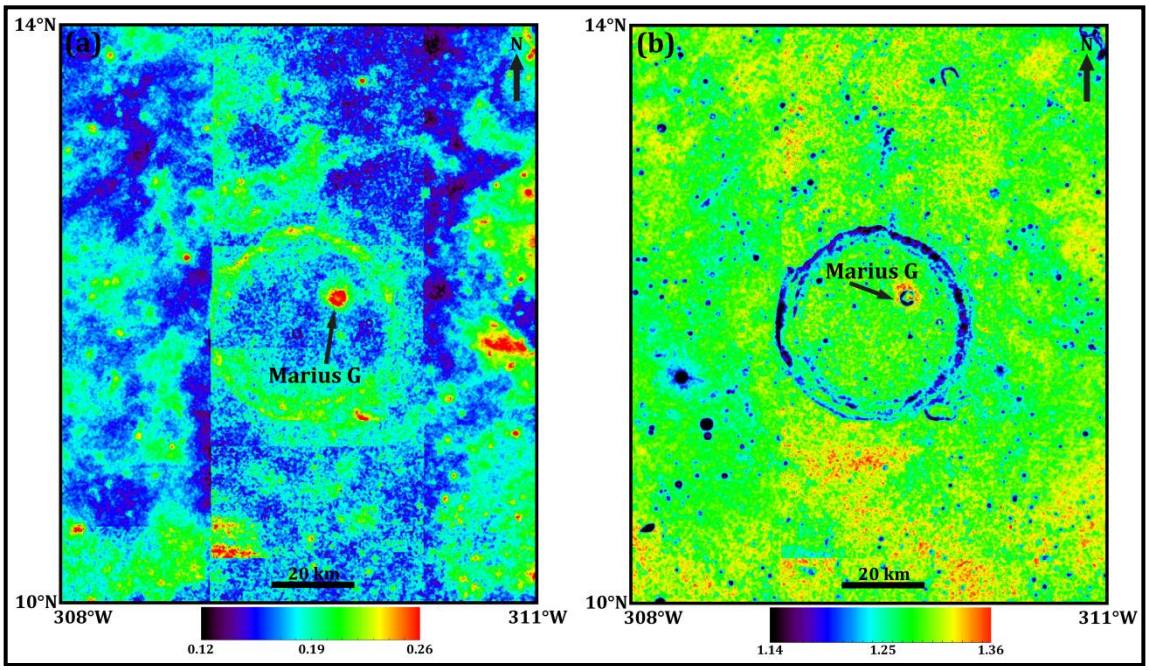

Figure 5.16. Maps of the space weathering corrected depths of the (a) 1 µm and (b) 2 µm absorption features (equations 5 and 6) for the immediate area around Marius. The 1 µm depth around Marius G is deeper than the rest of the interior of Marius, this is due to the relative freshness of the ejecta. Although the depth shown in (b) has a higher value in the Marius G ejecta than the surrounding lava flow, this represents a weaker 2 µm absorption depth (because of its definition as the 2000/1500 nm ratio) and is therefore indicative of material enriched in either olivine or anorthosite compared with its surroundings. Note that the colour scales for both images are not equal.

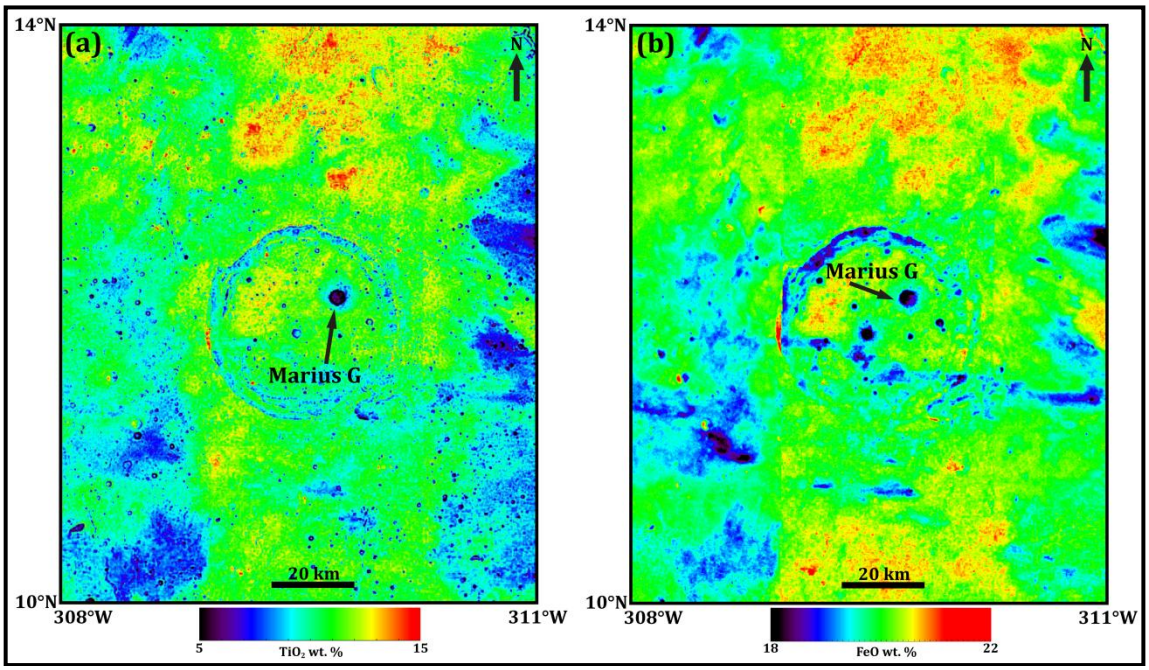

Figure 5.17. Maps of (a) TiO_2 and (b) FeO wt. % content (according to the algorithms of Lucey et al., 2000b and Wilcox et al., 2005 respectively) for the immediate area surrounding Marius.

In addition to these images, full resolution Clementine reflectance data were obtained for four separate regions around Marius and Marius G. The mean values of a number of pixels in each of these regions (Table 5.1) were used to produce the spectra shown in Figure 5.18. The four regions are: (i) the interior of Marius G; (ii) the continuous ejecta of Marius G; (iii) the Imbrian-aged (McCauley, 1967) surface lava flow within Marius; and (iv) the Eratosthenian-aged (McCauley, 1967) surface lava flow outside Marius.

The resultant spectral shapes of the Imbrian and Eratosthenian lava flows (blue and green lines in Figure 5.18) are very similar to each other, as well as to the slightly higher albedo signal from the Marius G ejecta. This shape, with weak absorption features, is representative of mature basalts, although the broad nature of the absorption around 1 µm and the apparent lack of one around 2 µm may suggest enrichment in olivine, or a relative lack of pyroxene. These findings are thus in keeping with those of Staid & Pieters (2001) and Staid et al. (2010) who observed that large regions of Oceanus Procellarum, covered by some of the youngest lunar basalts, have high-Ti contents and abundant olivine.

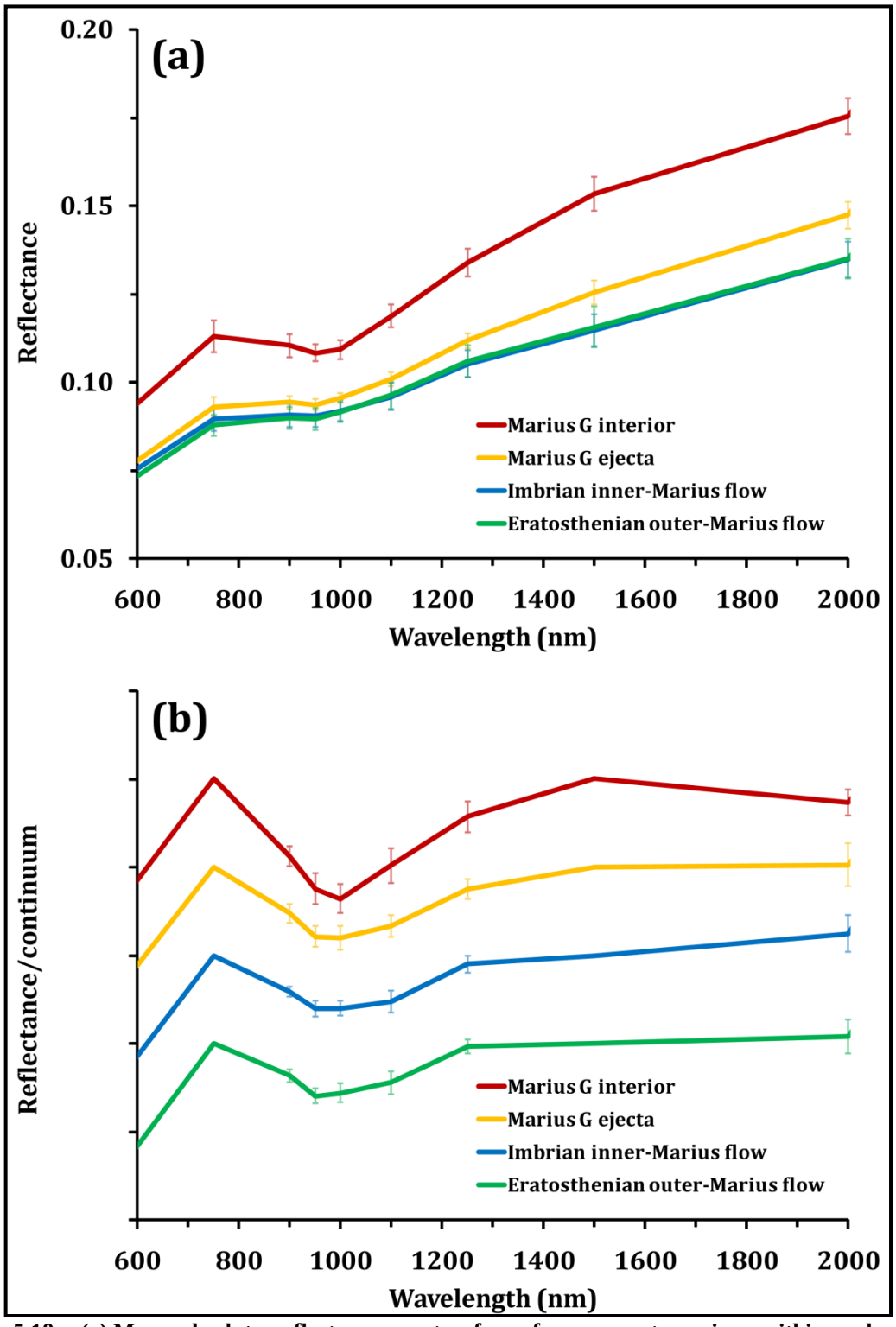

Figure 5.18. (a) Mean absolute reflectance spectra from four separate regions within and around Marius. (b) The same reflectance spectra divided by the line of the continuum slope (equation 2) in order to emphasise the absorption features; these spectra have been normalised to unity at 750 nm and 1250 nm, and offset for clarity (marks on the y-axis are at intervals of 0.1). Error bars indicate 1 standard deviation of the individual pixel values used to construct the mean spectra. The high albedo and relatively strong absorption features for the interior of Marius G are indicative of fresh material; the steep slopes of the crater cavity cause mass-wasting and prevent the products of space-weathering from accumulating.

A FeO vs. TiO_2 plot (Figure 5.19) shows that as well as being compositionally similar to each other, the Imbrian and Eratosthenian lava flows are also indistinguishable from the composition of lava flow unit 'P52'. This suggests that the Eratosthenian lava flow outside Marius (mapped by McCauley, 1967) and the lava flow 'P52' (mapped by Hiesinger et al., 2003) are actually the same lithology. Figure 5.19 compares the composition of the Marius G ejecta with the surrounding lava flows and indicates that material with a slightly lower TiO_2 content may have been excavated by the crater. If this is indeed the case, the diameter of Marius G (~3 km) can be used to constrain (using equations 20 and 21) the thickness of the Imbrian flow within Marius to <250 m.

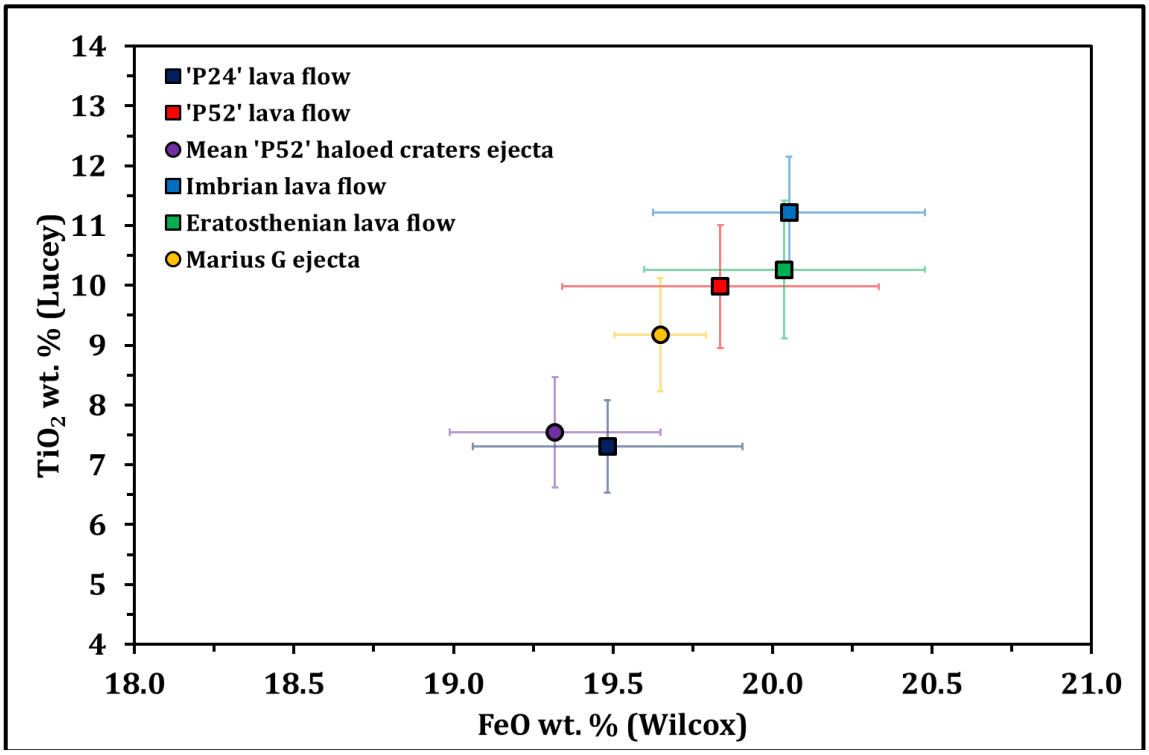

Figure 5.19. Mean FeO (according to the algorithm of Wilcox et al., 2005) and TiO_2 (according to the algorithm of Lucey et al., 2000b) wt. % contents for (i) the Imbrian and Eratosthenian lava flows, (ii) the ejecta of Marius G; and (iii) the compositions of lava flows 'P24' and 'P52' shown in Figure 5.12. Error bars indicate 1 standard deviation of the individual pixel values used to construct the mean values.

A hypothesised sequence of geologic events at the crater Marius can be formulated as follows (illustrated in Figure 5.20):

a) The impact crater Marius (diameter 41 km) is formed during the Lower Imbrian (Wilhelms et al., 1987), into anorthositic target material (likely primary lunar crust).

b) Later during the Imbrian (Wilhelms et al. 1987), at least one lava flow (~19.5 wt. % FeO; ~9 wt. % TiO_2) floods the area (basalt 1), and breaches the walls of Marius to flood its floor.

c) This Imbrian deposit is later (also during the Imbrian) overlain by the lava flow (basalt 2) that can now be seen at the surface within Marius (~20 wt. % FeO; ~11 wt. % TiO_2). The thickness of this lava flow is estimated to be <250 m from the depth constraint provided by Marius G.

d) Subsequently, a lava flow (basalt 3 with ~20 wt. % FeO; ~10 wt. % TiO_2) floods the area surrounding Marius during the Eratosthenian (Wilhelms et al., 1987), but it does not infiltrate the crater cavity.

e) Marius G (diameter ~3 km), a small young impact crater, forms on the floor of Marius and excavates older, previously buried material (Imbrian basalt) in the process.

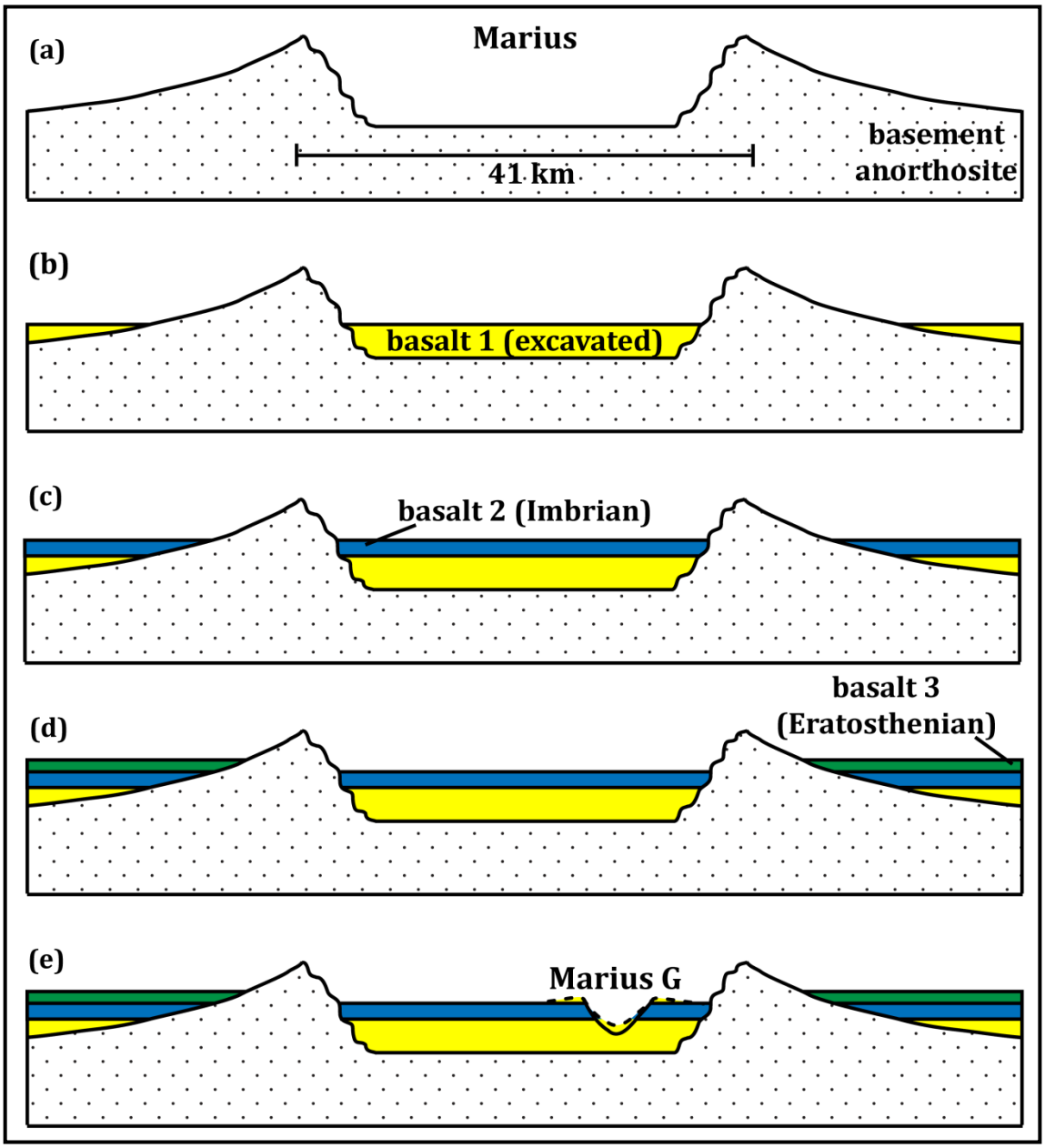

Figure 5.20. Cartoon cross-section through the crater Marius, illustrating various stages through its geologic history (see text for details).

5.3. Study area 2: central southern Mare Serenitatis (16° -33°N; 20° -26°E)

The Clementine multispectral reflectance data were also used to investigate the lava flow stratigraphy of an area in Mare Serenitatis (Figure 5.21). It was chosen because it coincides with published *Kaguya* radar tracks (Ono et al., 2009) that were used to infer the depth of a specific lava flow unit beneath the surface. The Clementine UV-Vis and NIR reflectance files were downloaded in the same format and extracted using the same IDL code as was employed for the first study area.

The TiO_2 abundance of the separate lava flow units in this area (whose boundaries and names are taken from Hiesinger et al., 2000) vary significantly, from very low-Ti basalts in the northwest, to high-Ti basalts in the southeast (Figure 5.22b). A total of 103 (simple) impact craters throughout the region were selected and their continuous ejecta blankets sampled in order to search for evidence of their excavating compositionally distinct material from beneath the surface.

Mean FeO and TiO_2 wt. % content values for the inter-crater areas of the eight lava flow units are shown in Figure 5.23. Although the difference in the composition of the southern units 'S11' and 'S18' compared with the more northern flows is clear, some of the units identified by Hiesinger et al. (2000) are indistinguishable based on this classification, which is not surprising because the earlier study used morphological features in addition to compositional differences to map the lava flow boundaries. Figure 5.24 shows a series of FeO vs. TiO_2 plots for each of the lava flow units that contain the craters sampled in this investigation, displaying the mean flow values as well as those for the craters within each particular unit. Details of the individual craters studied are given in Table 5.2 and the estimated absolute ages (Hiesinger et al., 2000) of the lava flows in Table 5.3.

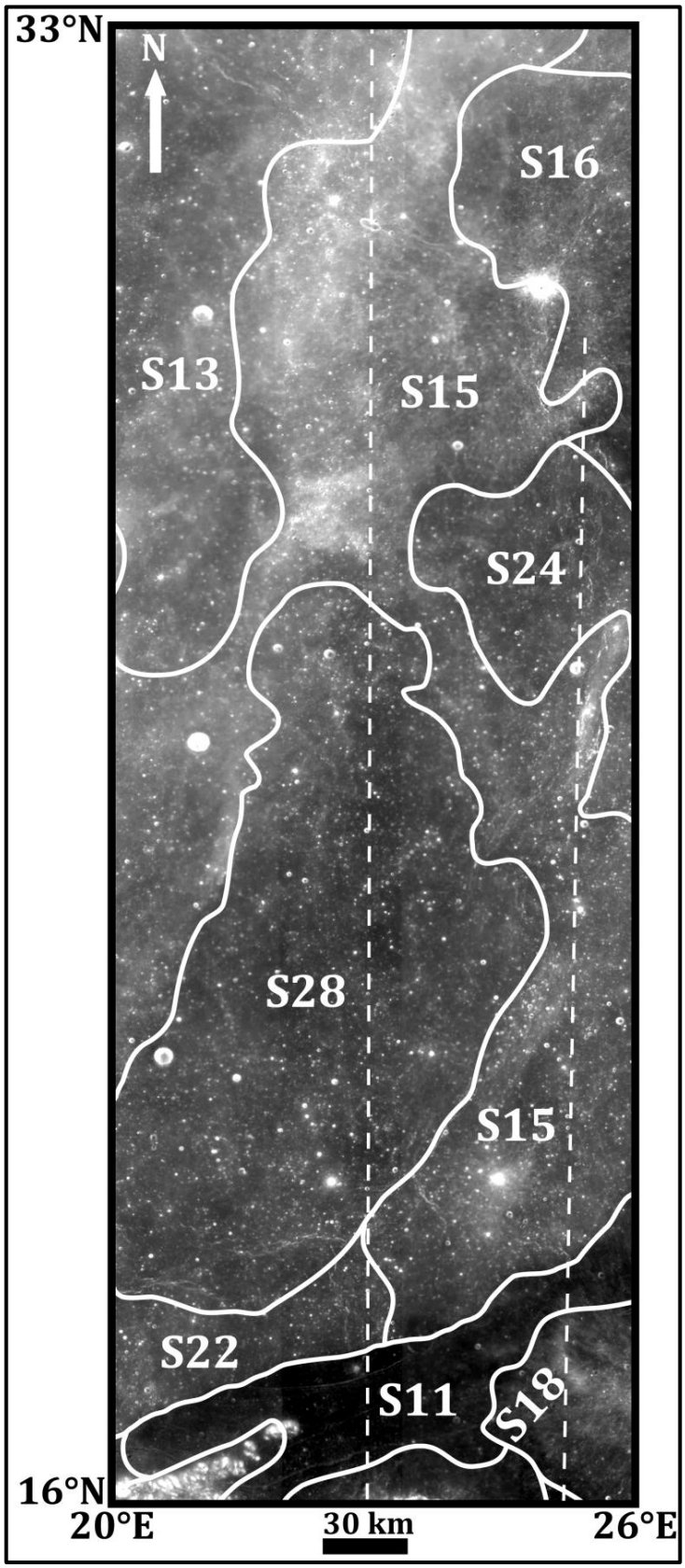

Figure 5.21. Clementine 750 nm reflectance (albedo) image for the Mare Serenitatis study area, indicating the lava flow boundaries and nomenclature of Hiesinger et al. (2000). Dashed lines show two tracks of LRS on *Kaguya* (Ono et al., 2009), results from which are discussed in section 5.3.2.

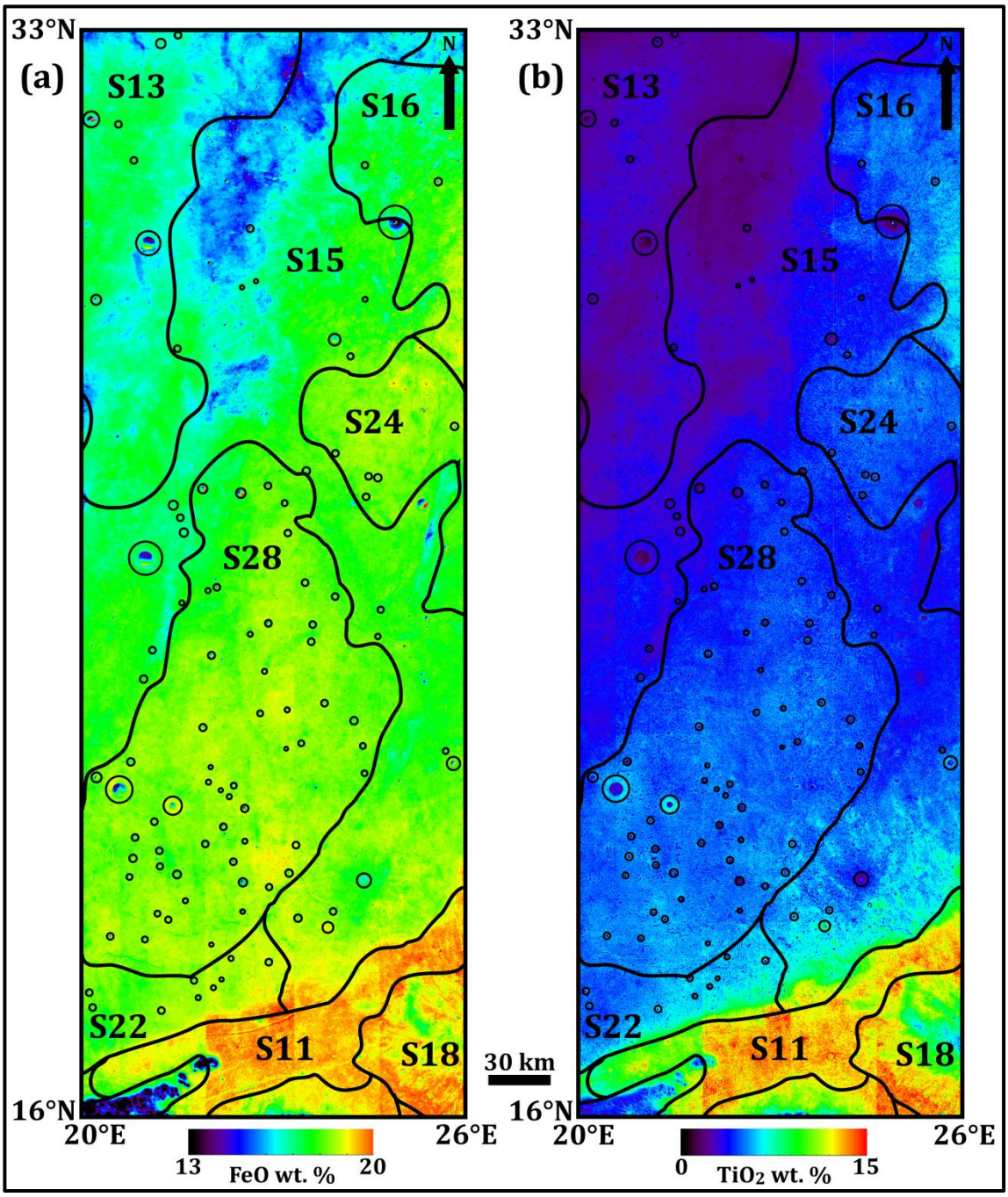

Figure 5.22. Maps of the Mare Serenitatis study area in terms of (a) FeO (according to the algorithm of Wilcox et al., 2005b) and (b)TiO_2 (according to the algorithm of Lucey et al., 2000b). The lava flow boundaries and names according to Hiesinger et al. (2000) are shown, and the 103 impact craters sampled in this investigation are circled.

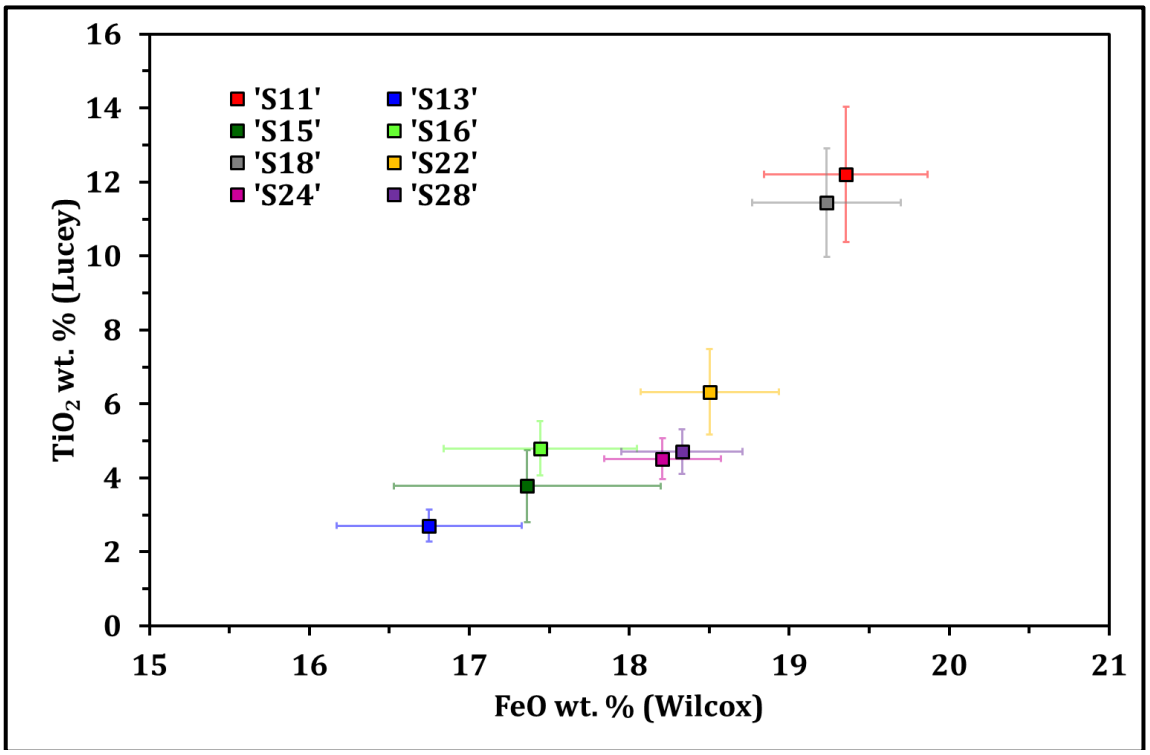

Figure 5.23. FeO (according to the algorithm of Wilcox et al., 2005) vs. TiO_2 (according to the algorithm of Lucey et al., 2000b) wt. % content values for the mean inter-crater areas of the eight lava flow units in the Mare Serenitatis study area. Although the pixels used for sampling the lava flows were chosen at random, an effort was made to avoid any obvious contamination by ejecta rays from distant craters. Error bars represent one standard deviation of the individual pixel values used to determine the mean.

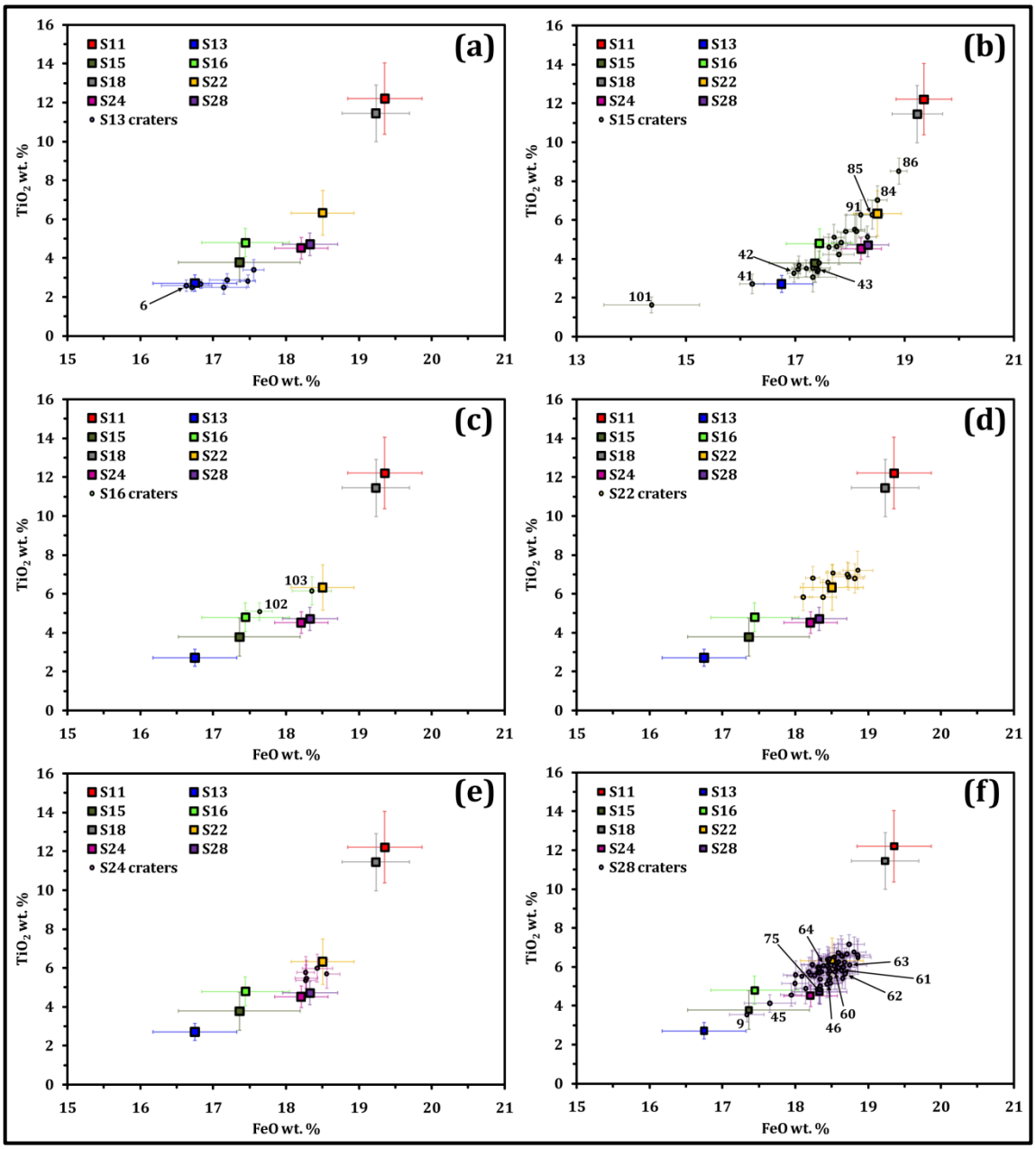

Figure 5.24. FeO wt. % (according to the algorithm of Wilcox et al., 2005) vs. TiO_2 wt. % (according to the algorithm of Lucey et al., 2000b) compositions for the mean inter-crater areas of the eight lava flow units in the Mare Serenitatis study area (Figure 5.23). Overlain on these lava flow compositions are: (a) the seven craters in lava flow unit 'S13' that all have a similar composition to the actual unit; (b) twenty-four craters in unit 'S15'. Some of these craters cluster around the composition for the actual unit, however a number of craters plot away from it. Crater 101 is much fresher than the rest of the craters; crater 41 has a composition similar to that of 'S13' and; several craters have more FeO and TiO_2-rich compositions than the flow itself; (c) two craters in unit 'S16'. Crater 102 plots close to the composition of 'S16' whereas crater 103 is more similar to the flow 'S22' with a higher FeO and TiO_2 content; (d) nine craters in unit 'S22'. All the craters cluster around the composition of the unit itself; (e) five craters in unit 'S24'. All these craters cluster close to the composition of the unit itself, however a deeper units with higher TiO_2 content, such as 'S22' may have been excavated; and (f) fifty-six craters in unit 'S28'. Many of the craters cluster close to the unit itself, however two deeper units (distributed laterally rather than vertically), one with a lower and one with a higher TiO_2 content seem to have been excavated by two sets of the craters.

Table 5.2. List of craters and inter-craters areas for which measurements were obtained in the Mare Serenitatis study area. Errors listed are 1 σ.

Lava flow / crater	No. pixels sampled	Crater found in lava flow	TiO_2 wt. %	mOMAT	Crater diameter (km)	Max. exc. depth (m)
S11	170	-	12.21±1.83	-1.02±0.02	-	-
S13	169	-	2.71±0.43	-0.99±0.01	-	-
S15	497	-	3.78±0.98	-0.98±0.01	-	-
S15	121	-	4.79±0.73	-0.99±0.02	-	-
S18	62	-	11.44±1.46	-0.98±0.01	-	-
S22	69	-	6.33±1.16	-1.00±0.01	-	-
S24	132	-	4.52±0.56	-0.98±0.01	-	-
S28	262	-	4.71±0.60	-0.99±0.01	-	-
Crater 1	21	S13	2.67±0.21	-1.00±0.01	1.29	109
Crater 2	31	S13	2.50±0.21	-1.00±0.01	1.47	124
Crater 3	32	S13	2.50±0.34	-0.95±0.02	3.81	320
Crater 4	17	S13	2.82±0.33	-1.00±0.01	0.80	67
Crater 5	22	S13	3.40±0.54	-0.96±0.01	0.91	76
Crater 6	31	S13	2.59±0.28	-0.98±0.01	6.97	585
Crater 7	34	S13	2.87±0.32	-1.00±0.02	2.31	194
Crater 8	17	S15	3.36±0.22	-0.98±0.01	0.55	46
Crater 9	30	S28	3.55±0.38	-0.97±0.01	2.78	234
Crater 10	17	S15	3.46±0.45	-0.98±0.01	1.77	149
Crater 11	20	S15	3.52±0.43	-0.96±0.01	0.69	58
Crater 12	18	S15	3.68±0.45	-0.96±0.01	0.72	61
Crater 13	55	S15	3.52±0.39	-0.96±0.01	8.07	678
Crater 14	18	S28	4.55±0.58	-0.97±0.02	0.68	57
Crater 15	22	S15	4.63±0.43	-0.95±0.02	0.65	55
Crater 16	22	S15	3.79±0.60	-0.94±0.02	0.53	44
Crater 17	28	S15	5.11±0.67	-0.98±0.02	1.81	152
Crater 18	35	S28	6.06±0.92	-0.99±0.01	1.28	107
Crater 19	24	S28	5.40±0.44	-0.95±0.01	1.44	121
Crater 20	37	S28	5.56±0.76	-0.97±0.02	2.01	169
Crater 21	74	S28	6.50±0.64	-0.98±0.01	6.84	574
Crater 22	56	S28	7.17±0.47	-0.97±0.01	2.78	234
Crater 23	26	S28	6.00±0.59	-0.98±0.01	0.84	71
Crater 24	22	S28	5.74±0.46	-0.98±0.01	0.96	80
Crater 25	31	S28	6.39±0.65	-0.99±0.01	1.54	129
Crater 26	25	S28	6.28±0.59	-0.97±0.01	0.96	81
Crater 27	24	S28	6.12±0.74	-0.97±0.02	1.37	115
Crater 28	25	S28	5.77±0.80	-0.98±0.01	1.26	106
Crater 29	26	S28	5.96±0.75	-0.98±0.01	1.31	110
Crater 30	33	S28	6.11±0.70	-0.99±0.01	2.16	182
Crater 31	22	S28	6.40±0.57	-0.97±0.02	0.87	73
Crater 32	24	S28	6.73±0.69	-0.99±0.01	0.94	79

Lava flow / crater	No. pixels sampled	Crater found in lava flow	TiO_2 wt. %	mOMAT	Crater diameter (km)	Max. exc. depth (m)
Crater 33	25	S28	6.67±0.51	-0.98±0.01	1.17	98
Crater 34	25	S28	6.24±0.75	-0.98±0.08	1.07	89
Crater 35	24	S28	6.48±0.86	-0.97±0.02	1.29	108
Crater 36	24	S22	5.83±0.90	-0.97±0.01	1.06	89
Crater 37	23	S22	5.83±0.70	-0.98±0.01	1.27	107
Crater 38	18	S22	7.07±0.46	-0.99±0.01	0.65	54
Crater 39	25	S22	6.81±0.60	-0.98±0.02	1.35	113
Crater 40	21	S22	6.59±0.59	-0.98±0.01	0.62	52
Crater 41	30	S15	2.71±0.49	-0.94±0.02	1.41	118
Crater 42	15	S15	3.26±0.47	-0.97±0.01	0.83	70
Crater 43	20	S15	3.42±0.35	-0.94±0.02	0.63	53
Crater 44	63	S15	4.23±0.52	-0.98±0.02	3.47	292
Crater 45	44	S28	4.13±0.45	-0.98±0.02	3.46	291
Crater 46	26	S28	5.12±0.71	-0.96±0.02	1.41	118
Crater 47	30	S15	5.51±0.75	-0.97±0.02	1.82	153
Crater 48	31	S24	5.77±0.81	-0.98±0.02	1.37	115
Crater 49	22	S28	5.02±0.92	-0.96±0.02	0.86	72
Crater 50	24	S28	5.16±0.69	-1.00±0.01	0.89	75
Crater 51	23	S28	4.89±0.79	-0.96±0.01	1.25	105
Crater 52	15	S28	5.36±0.53	-0.96±0.01	0.48	40
Crater 53	18	S28	5.16±0.57	-0.99±0.02	1.06	89
Crater 54	26	S28	5.67±0.75	-1.00±0.02	1.61	136
Crater 55	24	S28	5.75±0.74	-0.97±0.02	1.00	84
Crater 56	26	S28	5.52±0.61	-0.99±0.01	1.07	90
Crater 57	30	S28	5.58±0.92	-0.99±0.02	1.58	133
Crater 58	24	S28	5.69±0.66	-0.99±0.01	0.87	73
Crater 59	22	S28	5.31±0.67	-1.00±0.01	0.83	70
Crater 60	27	S28	5.87±0.76	-0.97±0.01	0.97	81
Crater 61	23	S28	6.00±0.76	-0.99±0.02	0.89	74
Crater 62	18	S28	5.64±0.79	-0.98±0.01	0.46	39
Crater 63	30	S28	6.24±0.71	-0.98±0.01	1.18	99
Crater 64	25	S28	6.07±0.60	-0.99±0.01	1.08	91
Crater 65	18	S28	5.97±0.67	-1.00±0.01	0.29	25
Crater 66	22	S28	5.92±1.02	-0.98±0.02	1.11	93
Crater 67	18	S28	5.78±0.72	-1.00±0.01	0.87	73
Crater 68	15	S28	6.00±0.61	-0.99±0.01	0.72	61
Crater 69	21	S28	5.96±0.71	-0.98±0.01	0.92	77
Crater 70	46	S28	6.09±0.55	-0.96±0.02	2.01	169
Crater 71	32	S28	5.41±0.52	-0.95±0.01	1.47	123
Crater 72	27	S28	6.05±0.59	-0.98±0.02	0.94	79
Crater 73	20	S28	6.76±0.79	-0.98±0.01	0.60	50

Lava flow / crater	No. pixels sampled	Crater found in lava flow	TiO_2 wt. %	mOMAT	Crater diameter (km)	Max. exc. depth (m)
Crater 74	31	S28	5.82±0.63	-0.94±0.02	1.15	96
Crater 75	40	S28	4.82±0.74	-0.90±0.03	1.47	123
Crater 76	26	S28	6.55±0.87	-0.98±0.02	1.79	150
Crater 77	33	S28	6.25±0.97	-0.99±0.01	1.29	108
Crater 78	24	S28	6.58±1.01	-0.96±0.02	0.93	78
Crater 79	16	S28	6.61±0.85	-0.98±0.01	0.35	30
Crater 80	27	S22	6.80±0.76	-0.98±0.01	0.57	48
Crater 81	24	S22	7.21±0.99	-0.96±0.01	1.29	108
Crater 82	18	S22	6.88±0.69	-0.98±0.02	0.44	37
Crater 83	22	S22	7.00±0.64	-0.99±0.02	0.79	67
Crater 84	38	S15	7.02±0.72	-0.98±0.01	1.13	95
Crater 85	35	S15	6.27±0.74	-0.96±0.02	0.99	83
Crater 86	28	S15	8.52±0.67	-0.98±0.01	1.73	145
Crater 87	66	S15	3.06±0.75	-0.85±0.04	1.29	109
Crater 88	22	S28	5.59±0.73	-0.98±0.01	0.93	78
Crater 89	30	S28	5.74±0.87	-0.97±0.01	1.32	111
Crater 90	30	S28	5.72±0.76	-0.99±0.01	1.85	156
Crater 91	42	S15	6.26±0.78	-0.99±0.02	2.66	224
Crater 92	26	S15	5.40±0.86	-0.99±0.01	1.36	114
Crater 93	21	S15	5.42±0.93	-0.97±0.02	0.54	45
Crater 94	22	S15	4.61±0.66	-0.98±0.01	1.19	100
Crater 95	31	S24	5.36±0.79	-0.98±0.01	1.34	113
Crater 96	24	S24	5.47±0.90	-0.99±0.02	1.16	97
Crater 97	28	S24	5.99±0.72	-0.99±0.02	1.50	126
Crater 98	23	S24	5.70±0.75	-0.98±0.01	1.29	108
Crater 99	19	S15	5.13±0.55	-0.97±0.01	0.55	462
Crater 100	13	S15	4.84±0.50	-0.97±0.01	0.91	76
Crater 101	30	S15	1.64±0.40	-0.72±0.01	2.26	190
Crater 102	17	S16	5.09±0.44	-0.98±0.01	0.76	64
Crater 103	27	S16	6.15±0.73	-0.96±0.02	1.17	98

Table 5.3. Estimated absolute ages for the lava flow units shown in Figure 5.21. Data are taken from Table 9 of Hiesinger et al. (2000).

Lava flow unit	Model age (Ga)	Error (Ga)
S28	2.84	+0.16 / -0.18
S24	3.21	+0.07 / -0.09
S22	3.28	+0.09 / -0.17
S18	3.42	+0.10 / -0.08
S16	3.43	+0.09 / -0.09
S15	3.44	+0.03 / -0.06
S13	3.49	+0.08 / -0.05
S11	3.55	+0.05 / -0.09

For the Oceanus Procellarum part of this study it was important to determine if the apparently TiO_2-poor ejecta haloes around selected impact craters were due to true compositional variations or unresolved maturity issues. For the craters in Mare Serenitatis, this issue is less important because most of the craters with compositionally anomalous ejecta appear to have excavated material rich in TiO_2 rather than poorer, and so the trends of maturity and composition are in opposition. The mOMAT (Wilcox et al., 2005) values of all 103 sampled craters are given in Table 5.2 and shown in Figure 5.25; the vast majority fall within a narrow band of mature values, with only three craters (75, 87 and 101) being more immature and fresh. Maximum excavation depths for these latter three craters are therefore ignored in making lava flow thickness estimates.

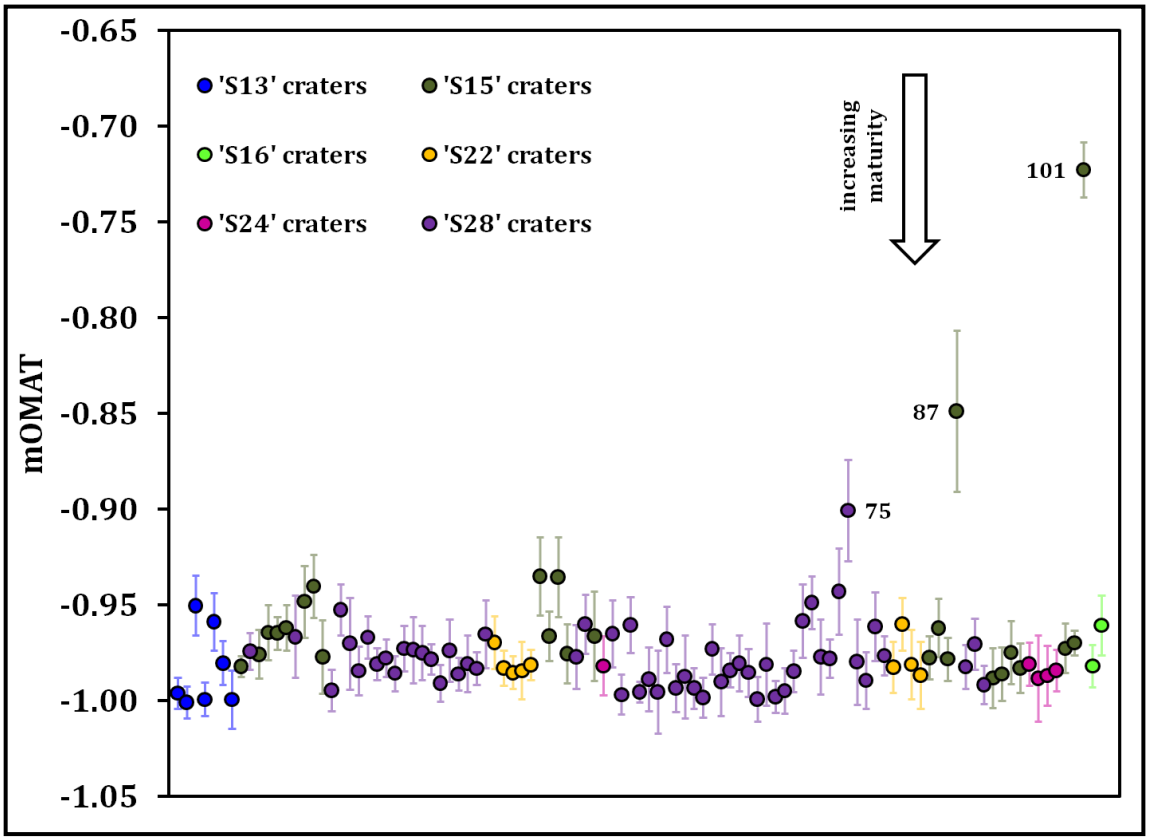

Figure 5.25. mOMAT (according to the algorithm of Wilcox et al., 2005) values for the 103 sampled craters in the Mare Serenitatis study area. All the craters fall within a narrow band of mature values except for the three craters that are labelled; these are fresher, immature craters and are not used in making estimations of lava flow thicknesses.

5.3.1. *Results*

In the following sections the results obtained for the various lava flow units (where the lava flow nomenclature is that of Hiesinger et al., 2000) are discussed.

Lava flow 'S13'

In terms of FeO and TiO_2 content, the ejecta compositions of the seven craters sampled in the small corner of 'S13' (Figure 5.24a) do not differ significantly from the lava flow itself. The crater diameters and their associated excavation depths therefore provide a lower bound for the thickness of 'S13' in this area; crater 6 is the largest and constrains the thickness of the unit to >585 m.

Lava flow 'S15'

Two craters in this unit (87 and 101) have higher mOMAT values (see Figure 5.25) than the vast majority of the 103 craters sampled within Mare Serenitatis (the freshness of crater 101 can explain its apparently low FeO and TiO_2 content; Figure 5.24b); these two craters were therefore not used in making lava flow thickness interpretations. For the other craters measured in 'S15', the ejecta compositions generally match that of the flow itself (Figure 5.24b). However, there is a subset that appears to have excavated older, compositionally distinct lithologies. Crater 41 seems to have excavated material from the underlying lava flow 'S13', and can therefore provide a thickness estimate of <120 m for 'S15' in the immediately surrounding area. Craters 42 and 43 are two smaller craters just to the south of crater 41 and they do not appear to have excavated the same material as it. The diameters of all three craters (41, 42 and 43) can therefore be used to constrain the 'S15' thickness estimate to between ~50 and ~120 m. Craters 84, 85 and 91 also appear to have excavated a separate unit underlying 'S15' that possesses a higher content of both FeO and TiO_2. Although on the basis of Figure 5.24b it would seem that 'S22' is a candidate for the excavated unit, this cannot be the case if the ages determined by Hiesinger et al. (2000) are correct and 'S22' is indeed *younger* than 'S15'. It is possible that these four craters have instead excavated a unit with a similar FeO and TiO_2 content to 'S22', but which has

no surface expression in this area; or that they have excavated 'S11' and that the average compositions of their ejecta represent a level of mixing between this older flow, which is richer in FeO and TiO_2, and 'S15' itself. These craters can still be used to constrain the thickness of 'S15' where it overlies such a lava flow to < ~225 m. In addition, the size of the craters in 'S15' whose ejecta lack any compositional anomalies, indicate that there is considerable variability in the thickness of 'S15' over the study area.

Lava flow 'S16'

Only two craters were sampled from 'S16', however a difference between their ejecta compositions is noted (Figure 5.24c). The composition of the ejecta from crater 102 resembles that of 'S16', whereas that from crater 103 has a higher content of both FeO and TiO_2. As for unit 'S15' it is not possible for crater 103 to have excavated material from the younger units 'S18', 'S22', 'S24' or 'S28' and so there is the potential for craters 103 (in 'S16') and 84, 85 and 91 (in 'S15') to have all sampled an unidentified underlying unit, or 'S11'. In the case of 'S11' having been excavated, the ejecta composition of crater 103 would represent a mixture of 'S16' and the older, more FeO and TiO_2-rich flow. Using the diameters of the craters 102 and 103, the thickness of this part of lava flow unit 'S16' is estimated to be between ~65 and ~100 m.

Lava flow 'S22'

All of the nine craters sampled within lava flow unit 'S22' have ejecta that match the composition of the unit itself (Figure 5.24d). As such they provide only a lower bound for the thickness of 'S22'; it is estimated to be at least ~100 m thick in this region.

Lava flow 'S24'

The ejecta of the five craters sampled in 'S24' (Figure 5.24e) have slightly elevated TiO_2 contents compared to that of the lava flow itself, suggesting that material from an older lithology such as 'S22', or the unidentified unit potentially sampled by craters in 'S15' and 'S16', has been excavated. Given the position of 'S24' next to units 'S15' and 'S16' and

removed from 'S22', the second option is perhaps more likely. It is also possible that the craters in 'S24' have ejecta compositions that are mixtures of the surface lava flow and an older lava flow such as 'S11' or 'S18'. If this set of craters has indeed excavated material from a separate lava flow, the thickness of 'S24' above it can be constrained to < ~125 m.

Lava flow 'S28'

Crater 75, within lava flow unit 'S28' (Figure 5.24f) has a higher mOMAT value than the majority of the craters sampled in this study (Figure 5.25) and therefore is disregarded in estimating the thickness of 'S28'. Craters 9 and 45, in the north of 'S28' appear to have excavated material from the neighbouring unit, 'S15'. Their sizes, along with that of nearby crater 46, are used to constrain the thickness of 'S28' where it overlies 'S15' in this region to between ~120 and ~290 m. About half of the craters in 'S28' have ejecta with distinct composition to that of the lava flow, and appear to have excavated material from a unit with higher FeO and TiO_2 contents, such as 'S11', 'S18' or 'S22'. Craters 61, 63, 64 all have ejecta with compositions different to 'S28', whereas neighbouring craters 60, 62, 90 and 89 do not. The thickness of 'S28' is thus estimated to be between ~40 and ~100 m where it overlies 'S22' (or a similarly FeO and TiO_2 enriched lava flow in this region). Craters 89 and 90 do not have compositionally anomalous haloes, and are larger than the three craters that do, possibly indicating local variations in the surface unit thickness that may be caused by the underlying topography. A large number of craters within the southernmost third of 'S28' have compositionally anomalous ejecta deposits and appear to have excavated material from lava flow 'S22' (or perhaps 'S11' / 'S18'). There are considerable variations in the depth estimates provided by these craters that are probably due to local topographical changes, but for a small area around craters 23 – 27, for example, the thickness of 'S28' is estimated at ~80 m.

A summary of these findings is illustrated in Figure 5.26. All 103 craters are shown and those that are noteworthy are labelled with their number. Those craters whose ejecta have excavated a subsurface lithology are represented by circles of the colour corresponding to the lava flow from which it is proposed the material originated; black circles mark craters without compositional anomalies. The three yellow circles represent the craters with

immature mOMAT values. Figure 5.27a shows the estimated maximum excavation depths (in metres) for all the sampled impact craters (other than the three with high mOMAT values); Figure 5.27b shows the approximated thickness estimates (in metres) for the surface flows that have been made based on these excavation depth constraints.

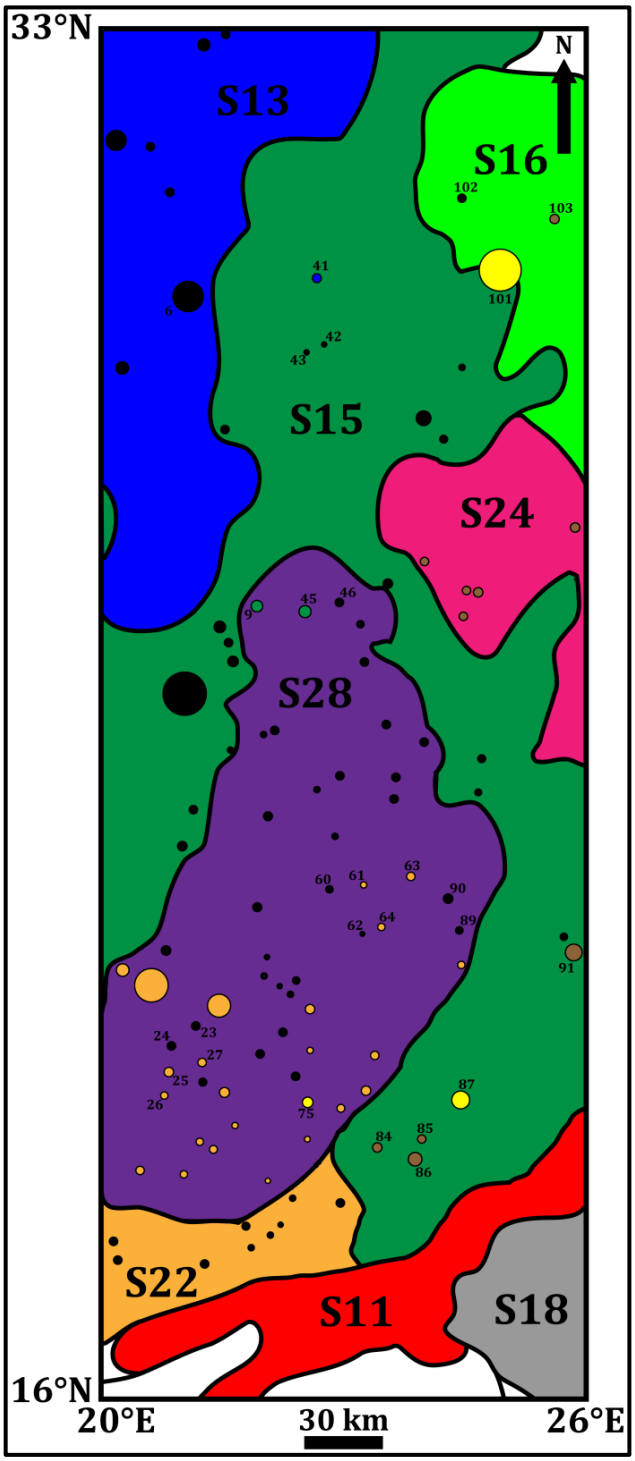

Figure 5.26. Map of the Mare Serenitatis study area with the separate lava flow units and each of the 103 impact craters investigated. Circles indicate the sampled impact craters; those which are black have no discernable compositional difference between their ejecta and the lava flow in which they lie; those which appear to have excavated material from a different lithology have been filled with a colour that matches the proposed source. Those in brown have either excavated material from an unidentified deeper lava flow unit with a similar FeO and TiO_2 content to that of 'S22', or whose ejecta are a mixture of the surface lava flow and either 'S11' or 'S18'.. The three yellow craters are those which have been identified as fresher than the rest of the population on the basis of their mOMAT value (see Figure 5.25). The size of the circles is proportional to the diameter (present day rim to rim) of the craters.

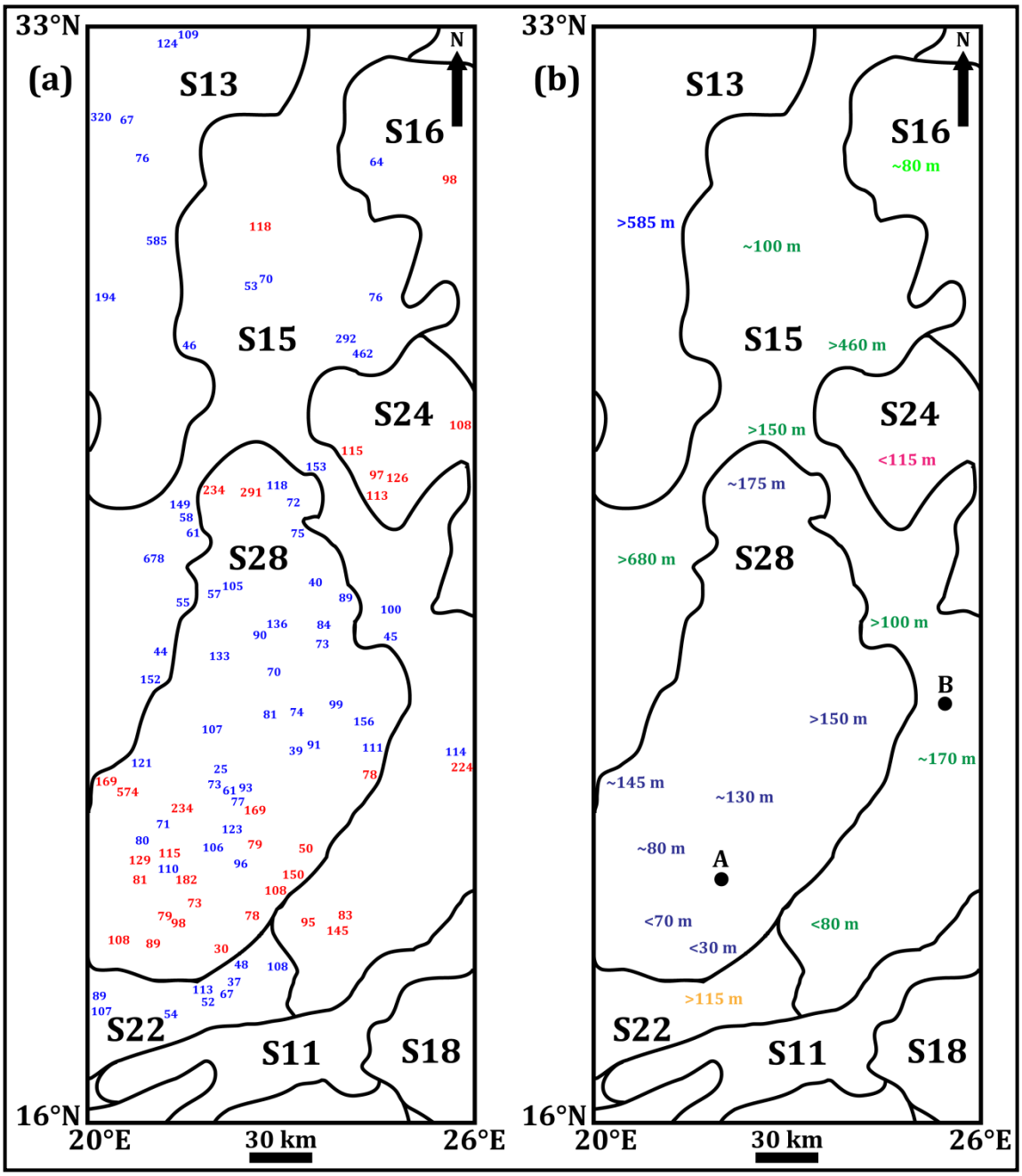

Figure 5.27. (a) Estimated maximum excavation depths (in metres) of the sampled craters in Mare Serenitatis. Red numbers are for those crater whose ejecta have originated from a deeper lava flow unit and therefore provide upper bounds for the thickness of the surface lithology (i.e. the surface lava flow must be thinner than the crater's excavation depth). Blue numbers are for craters whose ejecta compositions match the lava flow in which they are found and therefore provide lower bounds for the thickness of the surface unit (i.e. the surface lava flow must be thicker than the crater's excavation depth). (b) Surface lava flow unit thickness estimates (in metres) for various points around the study area. These estimates are based on the crater excavation depths shown in (a) and are formulated using crude averages and mid-points. Points A and B are locations cited in Ono et al. (2009) where they state that lava flow 'S11' lies at a depth of ~175 m below the surface (at both locations).

5.3.2. *Comparisons with other studies*

The Lunar Radar Sounder (LRS) on the Japanese Kaguya spacecraft was a high-frequency imaging radar instrument, which allowed the lunar sub-surface stratigraphy and tectonic features to be probed, with global coverage (Ono et al., 2009; Pommerol et al., 2010). The 5 MHz frequency permitted sub-surface data to be obtained to a depth of several kilometres (Ono et al., 2009), with an estimated vertical resolution ranging between 25 and 40 m (Pommerol et al., 2010). This technique specifically detects differences in the dielectric constant of the sub-surface materials, which is affected on the Moon by factors such as porosity and composition.

On the basis of the LRS data, Ono et al. (2009) observe a sub-surface reflector at a depth of ~175 m at point A (20°N, 23.3°E) in Figure 5.27b. They interpret this reflector as a high porosity deposit (buried regolith rather than a pyroclastic deposit or ejecta deposits) on the top of unit 'S11' which they can trace to where it outcrops at the surface. This interpretation is possibly in agreement with the new estimates made here, if 'S22' lies between the surface flow 'S28' and the reflector which marks the top of 'S11'. The craters in 'S28' which appear to have excavated material from 'S22' constrain the thickness of 'S28' at this point to ~75 m. 'S22' must therefore be ~100 m thick at this point. This fits well with the constraints provided by the craters in 'S22' that do not excavate a deeper lithology. Ono et al. (2009) do not observe a sub-surface boundary corresponding to the top of 'S22', but this may be because such a boundary at a depth of only 75 m is below their resolution. The deeper 'S11' boundary may also be more pronounced than for 'S22' because of its greater TiO_2 content (Pommerol et al., 2010). Ono et al., (2009) also identify the top of 'S11' at a similar depth (~175 m) beneath 'S15' at point B (19°N, 25.5°E) in Figure 5.27b. The craters in this part of 'S15' suggest that an older lava flow does exist at around this depth, but the composition of the ejecta do not obviously indicate that it is 'S11'. These ejecta do have higher TiO_2 (and FeO) contents than that of 'S15', but they do not appear to match any of the lava flow units currently exposed at the surface in Mare Serenitatis. These compositions could therefore represent an additional sub-surface lava flow (the top of which has been detected by Ono et al. (2009) and misidentified by them as

'S11'), or be due to mixing between the high FeO and TiO_2 contents of 'S11' and the surface lava flow 'S15' in the crater ejecta blankets.

The total thickness of mare fill within the Serenitatis basin has previously been estimated to be ~4 km (Williams & Zuber, 1998), although larger (~8.5 km; Solomon & Head, 1980) and smaller (~3.5 km; De Hon 1974; 1979; De Hon & Waskom, 1976) estimates have also been made. The surface lava flows whose thicknesses have been estimated in this study therefore contribute only a fraction of the total mare fill.

5.4. Synthesis

It is important to understand the thickness of the mare basalts and the individual lava flow units of which they consist so that the total volume of volcanic material at the lunar surface can be determined. This allows the evolution of the lunar interior to be investigated, for example the extent of partial melting of the mantle with time.

Table 5.4 shows estimated (and approximate) values for various parameters relating to the lava flow units studied in both Oceanus Procellarum and Mare Serenitatis. Using the estimated average thickness of the flows, for which this has been determined, and their surface area (Hiesinger et al., 2000; 2003), an approximate minimum volume for the units can be determined. A maximum time interval in which the individual flows were emplaced can be constrained from the difference in absolute ages of the flow in question and the unit immediately older than it in the stratigraphy (Hiesinger et al., 2000; 2003). This enables an average 'flux' of magma eruption to be calculated. Of course, the actual length of time over which these flows erupted would have been essentially instantaneous on these timescales, so the flux derived here is purely a measure of the amount of material that reached the surface within each several million year interval. Even for these gross averages there are several caveats: (i) the apparent (absolute) age dating of the lava flow units by cratering counting inherently involves large errors; (ii) extrapolation of the thickness of a whole lava flow from only a few spot estimates may be problematic; (iii) the areas of the surface flows, and especially the older flows, as given by Hiesinger et al (2000; 2003) are likely to be underestimated due to coverage by subsequent flows; and (iv) the TiO_2

abundances upon which our thickness estimates are based are estimated from an algorithm (Lucey et al., 2000b) which has a 1 σ error of at least 1 wt. %. Although this algorithm may over or underestimate the true TiO_2 wt. % content of the regolith by up to ~5 wt. % in some areas (Gillis et al., 2003), it is the *relative* difference between the values from different deposits that is important in this study, as well as the suppression of any maturity effects.

Table 5.4. Estimated volumes and fluxes for the lava flow units in Oceanus Procellarum (units 'P…') and Mare Serenitatis (units 'S…') for which depth estimates have been made. The flow areas and time intervals over which the flows were emplaced are taken from Hiesinger et al. (2000; 2003). The estimated flow thicknesses are established from the spot values shown in Figure 5.27b.

Lava flow unit	Estimated average thickness (km)	Area (km^2)	Approximate volume (km^3)	Maximum interval of emplacement (Ma)	Approximate average flux (km^3/Ma)
'P24'	0.25	6300	1575	70	22.5
'P52'	0.25	4075	1020	120	8.5
'S13'	0.60	10173	6100	30	203
'S15'	0.50	9089	4545	50	91
'S16'	0.08	4363	350	10	35
'S22'	0.10	3415	340	20	17
'S24'	0.10	6201	620	20	31
'S28'	0.10	3927	390	60	6.5

Knowledge of the flux of lunar volcanism can help refine the understanding of mare basalt petrogenesis and the relationship between the basalts and the Moon's magmatic and thermal evolution (e.g. Head & Wilson, 1992; Zhong et al., 1999; Parmentier et al., 2000; Wieczorek & Phillips, 2000; Wilson & Head, 2001; Shearer et al., 2006). The precise shape of the lunar mare basalt flux curve (Figure 5.28) is still uncertain; different shapes are derived from various methods (see discussion in Head & Wilson, 1992). The determination of individual lava flow thicknesses and fluxes in different lunar maria would improve the overall accuracy to which this curve is known (Hiesinger et al., 2003).

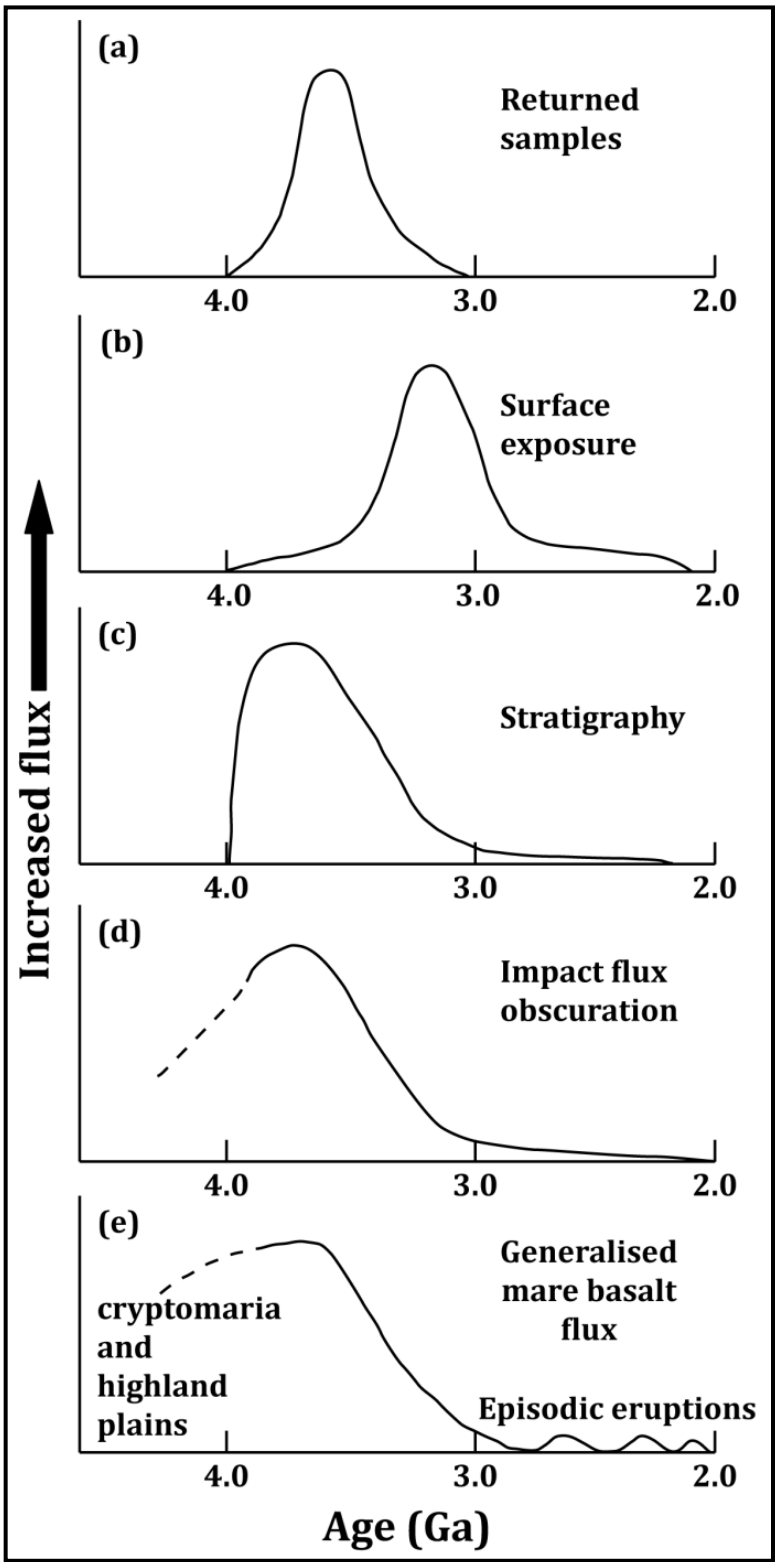

Figure 5.28. Estimated lunar mare basalt flux curves, based on different approaches (adapted from Head & Wilson, 1992). (a) shows the flux as determined from returned lunar samples; (b) using the surface area exposure of units, a similar curve is derived, albeit wider and shifted towards younger ages; (c) stratigraphic investigations of the mare basalts yields a more asymmetric curve with a peak at ~3.8 Ga; (d) shows an extrapolated curve for the period of volcanism that is likely to have been obscured by the proposed heavy bombardment and; (e) is the curve based on a combination of these approaches.

Figure 5.29a illustrates the estimated flux for the lava flow units in this study (from Oceanus Procellarum and Mare Serenitatis) as a function of their crater-count age. Although the number of data points is quite small, the overall shape of the curve produced is similar to the generalised mare basalt flux of Head & Wilson (1992), which is based on a combination of approaches (e.g. data from returned samples and remote sensing); it is shown in Figure 5.28e and superimposed for comparison in Figure 5.29a.

Giguere et al. (2000) investigated the apparent dichotomy between the bimodal distribution of lunar basalts in terms of TiO_2 content according to sample data, and the more unimodal distribution suggested by remote sensing data. They conclude that of the mare basalts, the low-Ti basalts are the most spatially abundant. If the flux of the lava flow units presented here is used as a proxy for their total abundance, then the trend observed in Figure 5.29b can be compared to the work of Giguere et al. (2000), with which it appears to agree. Figure 5.29b shows that the flux of the low-Ti basalt units tends to be greater than that of the high-Ti units, i.e. the vertical variation in the abundance of different basalt types shown here is similar to the lateral (surface) variation previously identified.

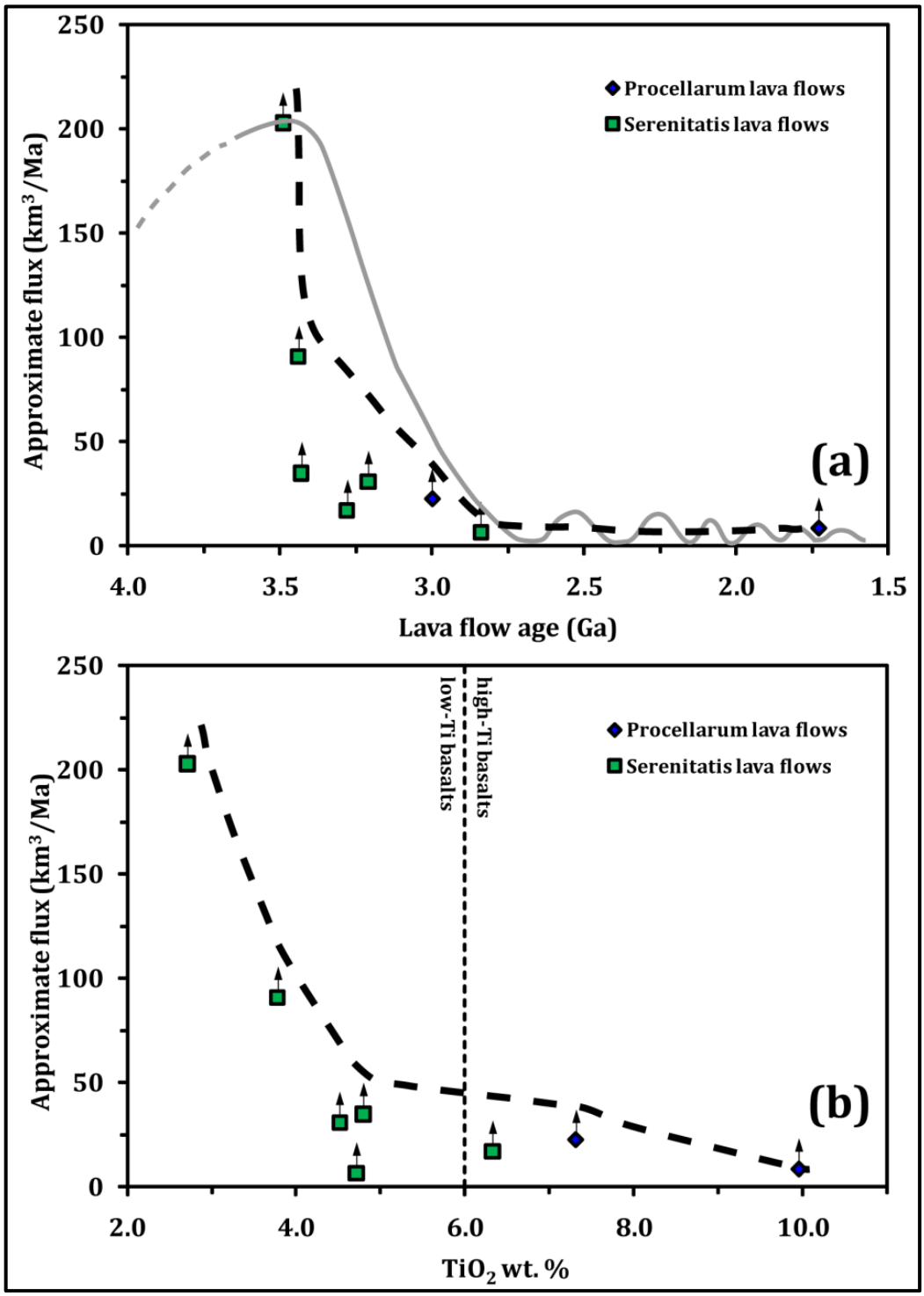

Figure 5.29. The estimated flux of each of the lava flow units listed in Table 5.4, as a function of (a) their crater counting age and (b) their mean TiO_2 wt. % content (according to the algorithm of Lucey et al., 2000b). Arrows from the data points indicate that the flux values given are likely to be lower limits due to coverage by younger lava flows. The shape of the curve in (a) which indicates the change of flux with time (dashed line) compares well with the generalised mare basalt flux model of Head & Wilson (1992) (grey line), especially considering that the actual flux of many of the data points may be considerably higher. The curve shown in (b) illustrates that the flux of the low-Ti basalts is generally higher than that of the high-Ti basalts (i.e. the volumetric variation in the abundance of different basalt types shown here is similar to the surface variation previously identified). High and low-Ti basalt classification is taken from Neal & Taylor (1992).

5.5. Conclusions

The integration of Clementine UV-Vis and NIR data provides a more complete understanding of the mineralogical nature of the lunar surface than the original five UV-Vis bands can alone. However, even by employing all the available Clementine multispectral wavebands, it has not been possible to unequivocally distinguish between lava flows in Oceanus Procellarum with varying abundances of olivine and pyroxene. Instead, the FeO and TiO_2 contents of impact crater ejecta in two study areas (in Oceanus Procellarum and Mare Serenitatis) have led to the identification of crater populations which have excavated material from deeper, compositionally distinct lava flows. The depth-diameter relationship of simple craters allows some constraints to be placed on the thickness of the surface units. Being able to constrain the depth of lava flows in this way allows the volcanic history of the area to be better understood, and by extrapolation allows lava flow volumes and fluxes to be estimated. This information in turn allows a more detailed view of spatial and temporal variations in the thermal history of the Moon.

The results presented are in broad agreement with previous work on lava flow thicknesses, and with recent radar sounding results. It would therefore be of value to extend this method to wider areas of the maria, and to employ newer, higher quality datasets. Data from the Spectral Profiler (SP) onboard *Kaguya* (500 m spatial footprint; 296 spectral channels covering wavelengths between 0.5 and 2.6 µm; Matsunaga et al., 2008) and the Moon Mineralogy Mapper (M^3) onboard Chandrayaan-1 (80 m spatial footprint; up to 260 spectral channels covering wavelengths between 0.42 and 3.0 µm; Pieters et al., 2009a), will be especially valuable in this respect.

Chapter 6: Summary and recommendations for future work

This summary gives an overview of the previous chapters, as well as discussing outstanding issues and recommendations for future work which have arisen from the research described in this thesis.

6.1. Introduction

The introduction to this thesis outlined the datasets which are available for studying the Moon. These include: (i) the returned rock and soil samples from the Apollo and Luna missions; (ii) results from the surface experiments conducted during the manned Apollo landing missions as well other landing robotic probes; and (iii) remote sensing datasets from Apollo (and its precursors) in the 1960s and 1970s, Galileo, Clementine and Lunar Prospector in the 1990s and the most recent set of satellites Kaguya, Change'1, Chandrayaan-1 and Lunar Reconnaissance Orbiter. The current major theories relating to lunar formation, evolution and geology, e.g. the giant impact and magma ocean hypotheses, which have arisen from lunar research were also described and discussed. The processes of UV-Vis-NIR, gamma-ray and XRF spectrometry (the geochemical remote sensing techniques employed in this thesis) were examined and the existing lunar datasets of these kinds from previous missions were presented. The literature review provides the lunar context and coherency for the multiple threads of my research.

6.2. C1XS

This chapter was focused on the C1XS instrument: its design, detector system, pre-flight calibration campaign in the RESIK facility at RAL, as well as the steps in its data processing. The range and nature of the C1XS XRF dataset was presented and the methodology of the RAL abundance algorithm, which converts X-ray flux data to elemental abundance estimates, was discussed (the algorithm was verified with laboratory XRF data in chapter 3 and used on C1XS data in chapter 4). Due to the low solar activity during the mission, together with its premature end, the C1XS dataset is smaller in size than it might have been given more ideal conditions. However, the success of the instrument

itself meant that the limited dataset includes lunar XRF data from flares up to two orders of magnitude weaker than it had been designed to detect. The instrument was easily capable of resolving the characteristic lines of the major rock forming elements (most notably Mg, Al and Si), as shown in Figure 6.1. The technologies employed in the C1XS instrument have thus been successfully proven; further developments may include the use of a new generation of large are SCDs (Holland & Pool, 2008).

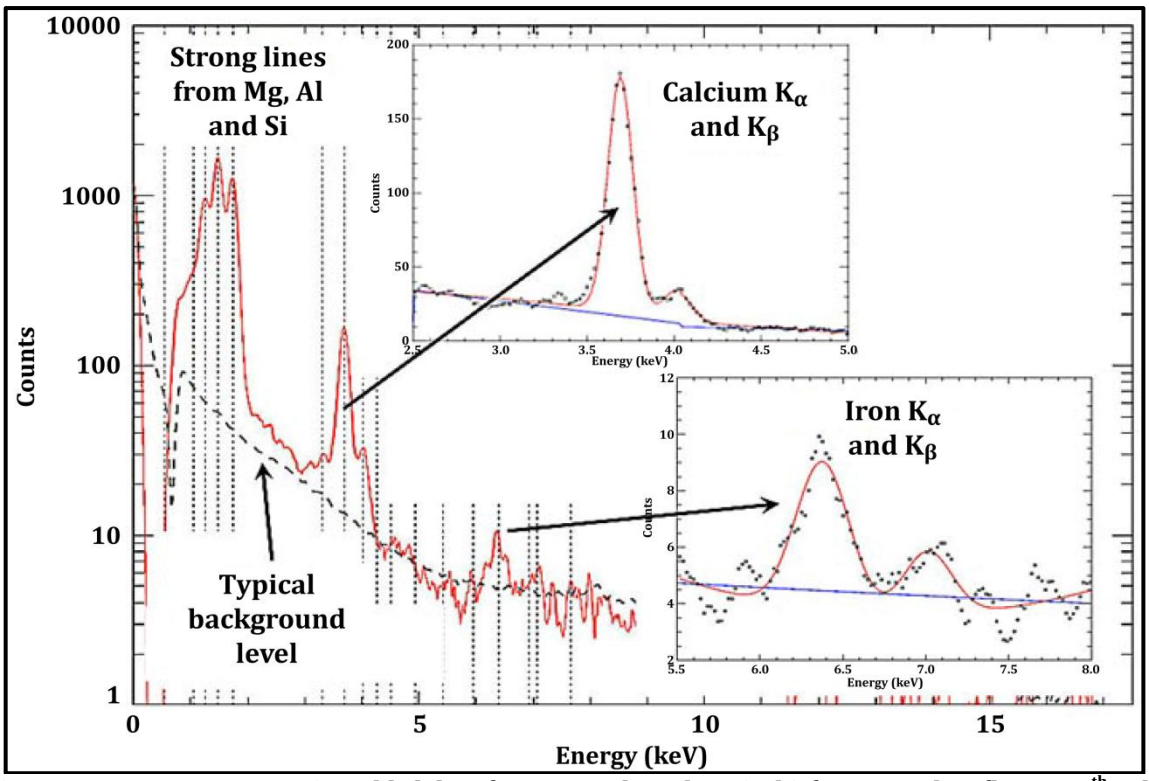

Figure 6.1. C1XS spectrum (co-added data from several 100 km pixels) from a C-class flare on 5th July 2009 (07:13 UT), with a ground track in the southern nearside highlands. The spectrum shows the clearly resolved, strong lines of Mg, Al and Si, as well as higher energy lines characteristic of Ca and Fe (iron can be detected at this flare level using cumulative data). Adapted from http://www.isro.org/chandrayaan/htmls/ImageMoon_C1XS.htm.

6.3. Laboratory XRF experiments

The bulk of the work presented in chapter 3 has been submitted (Weider et al., in review) and provided an account of laboratory experiments that were conducted as an analogue to planetary XRF missions, in order to investigate the role of changing phase angle geometry and sample grain-size on the intensity of XRF from regolith-like samples. The data obtained provide evidence of a grain-size effect (XRF line intensity decreases with

increasing sample grain-size), as well as an almost ubiquitous increase in XRF line intensity above phase angles of ~60°. XRF data for a lunar regolith simulant (JSC-1A) are used to test the accuracy of the RAL abundance algorithm (whose methodology is described in section 2.5.1), which is used to estimate the major element abundance of the lunar surface from C1XS XRF data. In ideal situations (i.e. when the input spectrum is well-defined and the XRF spectrum has a sufficient signal to noise ratio) the algorithm can recover a known rock composition to within 1.0 elemental wt. % (1 σ).

Preliminary experiments, using lithological samples were conducted using a desktop vacuum chamber setup at Brunel University, but the viewing geometry capabilities were limited; the incidence and emergence angles of observation could not be varied independently. The more extensive RESIK campaign allowed the incidence angle to be altered whilst keeping a fixed emergence angle (0°), thus allowing the phase angle effect to be measured. Improvements to the sample preparation techniques were also made in these later experiments, and a wider range of compositionally homogeneous and heterogeneous samples were measured.

The major findings of these experiments include:

(i) XRF line intensity generally decreases with increasing grain-size. The homogeneous, mono-oxide samples show no energy dependence for the grain-size effect, whereas the heterogeneous rock samples do. The results from Brunel agree with previous studies (e.g. Maruyama et al., 2008; Näränen et al., 2008) and indicate that the magnitude of the grain-size effect is larger for lower energy elements; however the RESIK data for lunar regolith simulant JSC-1A indicate the opposite. Enhanced fluorescence of lighter elements caused by the XRF from the heavier elements in the heterogeneous (multiple elements in minerals), complex sample is proposed as an explanation for this discrepancy. The RESIK JSC-1A data have been adjusted to account for the relative proportions of its chemical constituents, whereas the Brunel data for other lithologies (and the results in the previous studies) have not, and it is these relative proportions which are key in determining the energy direction of the grain-size effect magnitude, as shown with the simple oxide mixture samples.

(ii) Within real planetary XRF situations, the grain-size effect may become important when trying to discern true chemical heterogeneities across the surface of the planet or asteroid. If the effect is not accounted for properly, then apparent differences in geochemistry may, in part, be due to grain-size (or surface roughness) differences in the regolith. This issue is particularly important for complex and heterogeneous regoliths, for example those on the surface of asteroids (e.g. Saito et al., 2006; see Figure 6.2).

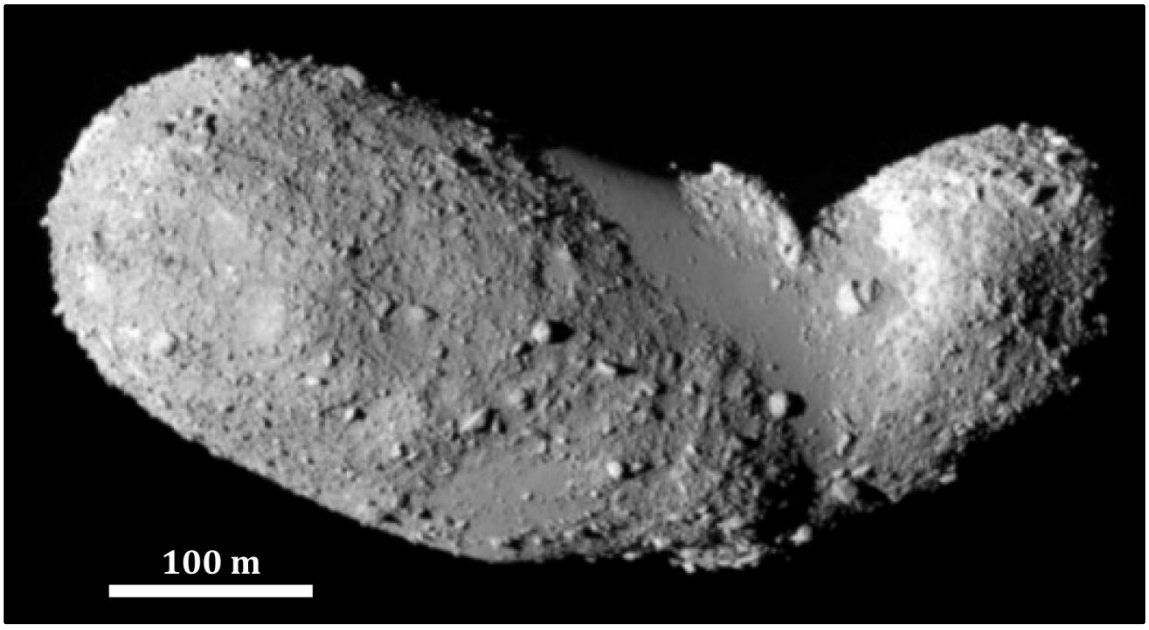

Figure 6.2. Global image of asteroid Itokawa from the JAXA satellite Hayabusa (image no. ST2448357351). The asteroid's surface is covered by numerous conspicuous boulders (up to ~10 m in size); smooth terrains which lack boulders can also be discerned (Saito et al., 2006).

(iii) XRF line intensity increases with phase angle, in a manner that approaches a cosine law, thus becoming significant at angles greater than about 50° or 60°. The homogeneous samples do not exhibit an energy dependent phase angle effect, but the more heterogeneous simple oxide mixture samples do; the magnitude of the relative rise in XRF intensity at higher phase angles is greater for higher energy elements and this is consistent with the findings of previous studies (e.g. Näränen et al., 2008). This is an example of a matrix effect, where the relative proportions of the different sample components is important. The JSC-1A samples show very little phase angle effect, but this is likely due to the small range of phase angles at which the samples were measured.

(iv) It is important to constrain the likely magnitude of the phase angle effect, so that planetary XRF measurements made at high phase angles (either by a nadir-pointing instrument operating at high-latitude or by a non-nadir pointing instrument, such as the XRS on NEAR, that operate at large phase angles) can provide accurate elemental abundance estimates. The energy dependence of this effect is also likely to be problematic if the results (for phase angles greater than 50° or 60°) are expressed as ratios of two elements which vary significantly in energy (e.g. Fe and Si; Okada, 2002).

Several recommendations for future experimental campaigns of this kind are made:

(i) Detectors that are able to operate efficiently down to energies of ~1 keV are required so that both the sample XRF and the incident X-ray spectra can be measured accurately and with good spectral resolution. SCDs are able to achieve this better than other traditional detectors such as Si-PIN diodes. New SDDs (silicon drift detectors) are also being developed (e.g. Carini et al., 2009) to have low-energy detection capabilities for planetary XRF spectrometers, including MIXS (Mercury Imaging X-ray Spectrometer) on BepiColombo (Treis et al., 2010).

(ii) Ideally the input X-ray spectrum would imitate the solar spectrum (perhaps at a number of different temperature flare states), however this might not be feasible. Strong lines at (or just above) the energy (K_α) of major rock forming elements should be avoided wherever possible.

(iii) The experimental configuration should allow a full range of phase angles to be measured; at least 0° – 90°, and even more if possible. It must be capable of altering the incidence and emergence angles independently and measurements with emergence angles ≠ 0° should be conducted.

(iv) Samples should be constructed in a (standardised) manner that preserves (or replicates) regolith characteristics such as porosity and surface roughness.

(v) These samples could include: (a) additional mono-oxides such as Ca and Ti (it is important that these differ only in composition and not in their grain-shape or surface texture); (b) further simple oxide mixtures samples, made with a number of variables taken into account: grain-size (this could vary between the different components), the relative proportion of the different components, and the number of components;

(c) other heterogeneous rock samples, for example a highlands regolith simulant and perhaps mixtures of this and JSC-1A. The simple oxide mixture samples are set to be the main focus of a new experimental campaign of this nature, to be conducted at Brunel University using the same equipment as in the previous study.

(vi) All the samples should be made at a variety of grain-sizes (or surface roughness), with more size fractions (including smaller grains) than employed in the experiments described in chapter 3.

(vii) It is important that all the samples are fully characterised in terms of their chemistry, relative component proportions, surface coverage, porosity, grain texture, grain-size, grain shape and surface roughness.

The simple oxide mixture samples may be particularly important in providing a simple system, relevant to planetary XRF, on which to test modelling codes such as the RAL abundance algorithm. Whereas in the real rock samples, each grain is made up of a complex mix of minerals, the oxide mixtures separate the different compositions into different grains. This may provide a more faithful (although simplified) analogue of a planetary regolith, where grains of different rock types (e.g. basalt and anorthosite), with characteristic major element chemistries, are mixed in varying proportions. Matrix effects, caused by characteristic X-rays interacting with atoms different from which they originated are thus likely to occur on an inter-grain scale as well as on a finer, intra-granular scale. It is important to test the XRF modelling codes on examples such as this because they are currently built to deal with single rock types (therefore matrix effects occurring only on the fine, intra-granular scale) rather than mixtures.

6.4. C1XS flare analyses

Two ground tracks of C1XS solar flare data were analysed in chapter 4, with predominantly basaltic footprints through Mare Serenitatis (from an A-class flare on 12th December 2008) and Oceanus Procellarum (from a B-class flare on 10th February 2009). The RAL abundance algorithm was employed to fit the X-ray spectra and provide quantitative elemental estimates. These results were expressed as MgO/SiO_2 and Al_2O_3/SiO_2 ratios for different regions along the two ground tracks. Although Na lines are often present within

the X-ray spectra, their presence is thought to be due to scattered solar X-ray lines rather than XRF.

The modelled XRF results, in combination with Clementine-based estimates of the TiO_2 and FeO contents of the C1XS regions, are generally in good agreement with the compositions of returned mare basalt samples. Appropriate levels of mixing between mare basalt and ferroan anorthosite compositions can be invoked to explain small variations between the regions. However, in at least one region the relatively low abundance of Al is harder to explain. The Al content may have been underestimated by C1XS, but more likely is that the mixing models employed are not complex enough and require at least one more end-member (e.g. a norite). Although the MgO/SiO_2 and Al_2O_3/SiO_2 C1XS ratios agree well with sample compositions, there is a significant discrepancy between Lunar Prospector gamma-ray data for the same regions, especially in terms of MgO/SiO_2. This may be explained by the overestimation of Mg abundances by Lunar Prospector, or by inherent differences in the techniques of XRF and gamma-ray spectroscopy . These differences may allow different layers within a compositionally stratified regolith to be sampled, and in addition, regolith matrix effects only concern XRF. Discrepancies between XRF and gamma-ray spectroscopy results have been noted before from NEAR (Lim & Nittler, 2009) and thus it seems that this issue is not isolated to the C1XS results and warrants further investigation. This must involve new (e.g. gamma-ray data from Kaguya) and future (e.g. from MESSENGER and BepiColombo for Mercury) datasets.

The work carried out in chapter 4 involved only two (but the only basaltic areas of the Moon observed by C1XS) of ~30 flare periods from which XRF data were obtained by C1XS. The majority of these flares took place within in a short four day period towards the end of the mission, with ground tracks in the southern nearside highlands. The C-class flare (5^{th} July 2009) whose summed spectrum is shown in Figure 6.1 is being analysed in a forthcoming paper (Narendranath et al., forthcoming). Therefore, there is still much work to do on fulfilling the scientific harvest from the C1XS yield. Ideally, an investigation of the C1XS flare data would have been conducted with a focus on possible phase angle effects, to complement the laboratory investigation conducted in this thesis. However, due to the limited dataset this has not been possible. This project would require multiple

observations of the same lunar regions, illuminated with similar flare conditions, but with a variety of phase angles. The only real phase angle variations within the C1XS data are along single flare ground tracks and are thus caused by the changing latitude of observation (therefore different regions being measured) rather than observations occurring for the same area with different solar angles (i.e. at different times of the month).

6.5. Clementine study: lava flow stratigraphy

Multispectral reflectance data from the lunar Clementine mission were used in this chapter (most of which is included within Weider et al., 2010) to investigate the impact ejecta deposits of simple craters in two separate lunar mare basalt regions, one in Oceanus Procellarum and one in Mare Serenitatis. Different (published) mineralogical and compositional algorithms were described and discussed, including those employed in the investigation. Using the UV-Vis and NIR datasets in tandem does not generally reveal (mafic) mineralogical differences between impact crater ejecta and surficial lava flow units in Oceanus Procellarum. However, an anomalous signal in Marius crater may be evidence of olivine-rich material having been excavated from depth. From both regions, a total of >100 craters were studied, and for a number there are significant differences between the TiO_2 (and FeO) contents of their ejecta deposits and the lava flow units in which they are located. These differences, coupled with morphometric crater relationships that provide maximum crater excavation depths, allowed the sub-surface lava flow stratigraphy to be examined.

Average thicknesses for a number of lava flow units in the two study regions were estimated to range from ~80 m to ~600 m. In the case of the Serenitatis area, the results are consistent with the presence of sub-surface horizons inferred from recent radar sounding measurements from the JAXA Kaguya spacecraft (Ono et al., 2009). The average lava flow thicknesses obtained were used to make estimates of the average flux of volcanic material in these regions. These are in broad agreement with previous studies, suggesting that the variation in mare basalt types observed at depth is similar to the lateral variations already identified at the surface.

This study employed Clementine data with five UV-Vis bands and 100 m spatial resolution. These spectral and/or spatial resolutions have been now been superceded by more recent datasets. The Spectral Profiler instrument on Kaguya had an energy range of 0.5 – 2.6 μm covered by 296 spectral channels, and a spatial footprint of 500 m (Matsunaga et al., 2008); the Moon Mineralogy Mapper (M^3) on Chandrayaan-1 had an energy range of 0.42 – 3.0 μm and operated in two modes: low resolution spectroscopic data were obtained with 86 spectral channels and with a spatial resolution of 140 m/pixel, high resolution science data were obtained with 260 spectral channels and at 80 m/pixel (Pieters et al., 2009a).

Future studies, either in the same, or different, mare basalt regions could be conducted using these newer, more powerful data. In some cases, it might be possible to utilise slightly smaller craters, but it is the increased spectral resolutions that should really be advantageous. Additional and more reliable compositional and mineralogical differentiation between different deposits should enable the variability of the lunar lava flows to be highlighted further. New high resolution imagery from LROC will also allow the regions, craters and their morphologies (e.g. Figure 6.3) to be mapped in unprecedented detail. In order to accelarate the process of crater identification in such studies, it would be useful to employ a suitable automatic crater detection tool, e.g. that of Kramer (2010).

Although it is difficult to conduct the same studies with C1XS and Clementine data, due to their diverse spatial resolutions, the two investigations conducted in chapter 4 and chapter 5 of this thesis are complementary to one another and highlight the kind of large and small scale studies that can be used to understand the diversity (both laterally and with depth) of the lunar maria.

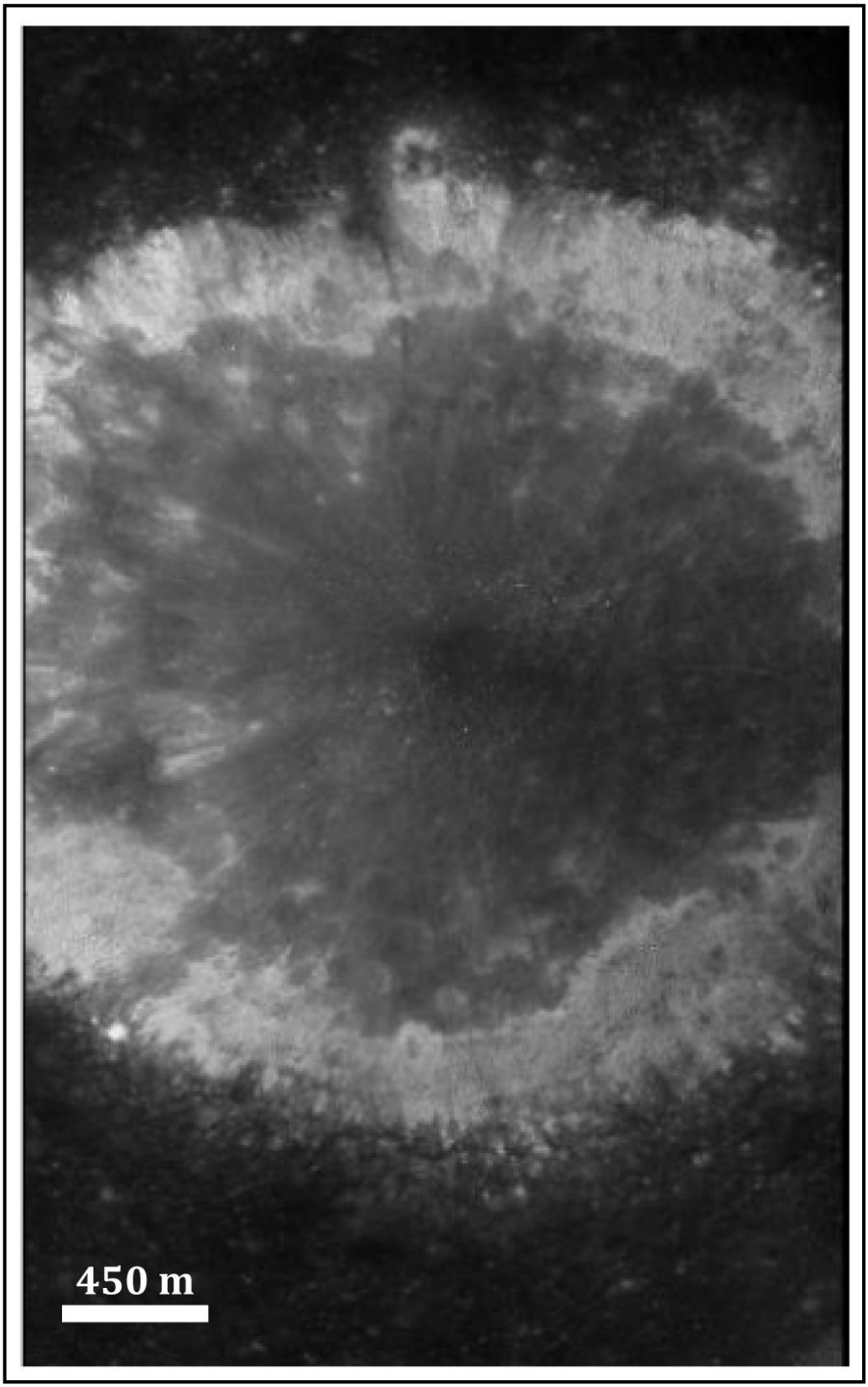

Figure 6.3. LROC narrow angle camera (NAC) image (M122543543LE) of the crater Marius G within the larger Marius crater (not map projected), which is shown to have a compositional anomaly associated with its ejecta in section 5.2.3. The internal structure of this small (~3 km diameter) crater can be seen clearly for the first time (image courtesy of: NASA/GSFC/Arizona State University).

6.6. Future of planetary XRF

Planetary XRF spectroscopy is a complex process, with many issues which need to be understood properly in order for accurate compositions to be derived. One of the most important of these issues is the incident solar spectrum. The precise position of the characteristic lines in the spectrum is now known (unlike the thinking of Clark & Trombka, 1997) to be important in the modelling of the resultant XRF spectra and it is therefore important that the solar models have the highest spectral resolution possible. The current models however are not perfect. In chapter 4, the *atomdb* model was employed, which uses astronomical abundances for the flare modelling and can only generate models at certain quantised temperatures. The other commonly used solar model, CHIANTI (e.g. Lim & Nittler, 2009; Narendranath et al., forthcoming), is limited as it does not extend to low energies (i.e. ~0.5 keV, the lower limit of SCD detection), including the K_α line energy of the important rock forming element Na. A study of the resulting difference in terms of the XRF results derived by using these solar models is thus required in order to demonstrate if the choice between different solar models is actually significant. With the C1XS technology it has been possible to obtain data from very weak solar flares (i.e. A-class flares), and future XRF instruments with similar, or better, capabilities should be able to do the same. Accurate solar models, with energy ranges that reach down to ~0.5 keV are thus required at all flare states.

There currently exist a number of different planetary XRF modelling algorithms, e.g. the RAL abundance algorithm and that of Narendranath et al. (forthcoming) that are used in analysing C1XS data, and those of Lim & Nittler (2009) and Okada et al. (2006) which are used to model the XRS data from NEAR and Hayabusa respectively. It is suggested that inter-code comparisons between these different methodologies be conducted, using a set of common XRF and incident spectra (both planetary data and laboratory analogue data).

A global lunar XRF dataset is still lacking. The success of C1XS has proven that high quality XRF spectral data can be obtained from lunar orbit, but a new mission (flown at, or around, solar maximum) with an XRF payload will be required in order to fulfil the original scientific aims and goals of C1XS (Crawford et al., 2009). Future lunar (or other planetary)

landing missions could carry miniaturised XRF spectrometers (as did the two Lunokhod rovers; Abdrakhimov & Basilevsky, 2010), and accompanying X-ray sources and would thus exclude the uncertainties in elemental modelling that derive from the lack of understanding of the solar spectrum.

The lessons learnt from the past lunar and asteroidal XRF missions will be of immediate use and relevance to the analysis of data from the XRF spectrometers on the current NASA MESSENGER (due to reach orbit in March 2011) and the forthcoming ESA BepiColombo (due to be launched in 2014 and reach orbit in 2020) missions to Mercury. The MESSENGER XRS (Figure 6.4a) consists of three gas-filled proportional counters (see section 1.4.1) which will measure the XRF from Mercury's surface (with a 12° FOV, that provides a spatial resolution of 42 km at periapsis and 3200 km at apoapsis) and an accompanying Si-PIN diode that will act as a solar monitor (Schlemm et al., 2007). Although this instrument owes much of its heritage to the XRF on the NEAR mission (Starr et al., 2000), the proposed instrument on BepiColombo, MIXS (Mercury Imaging X-ray Spectrometer), will be one of the new generation of solid-state detector XRF spectrometers (Figure 6.4b). It will consist of two components: a collimated channel (MIXS-C) which will provide measurements at scales of 70 – 270 km (from the elliptical orbit) and an imaging X-ray telescope (MIXS-T) which will measure the abundance of major elements at scales of <10 km during solar flares (Fraser et al., 2010).

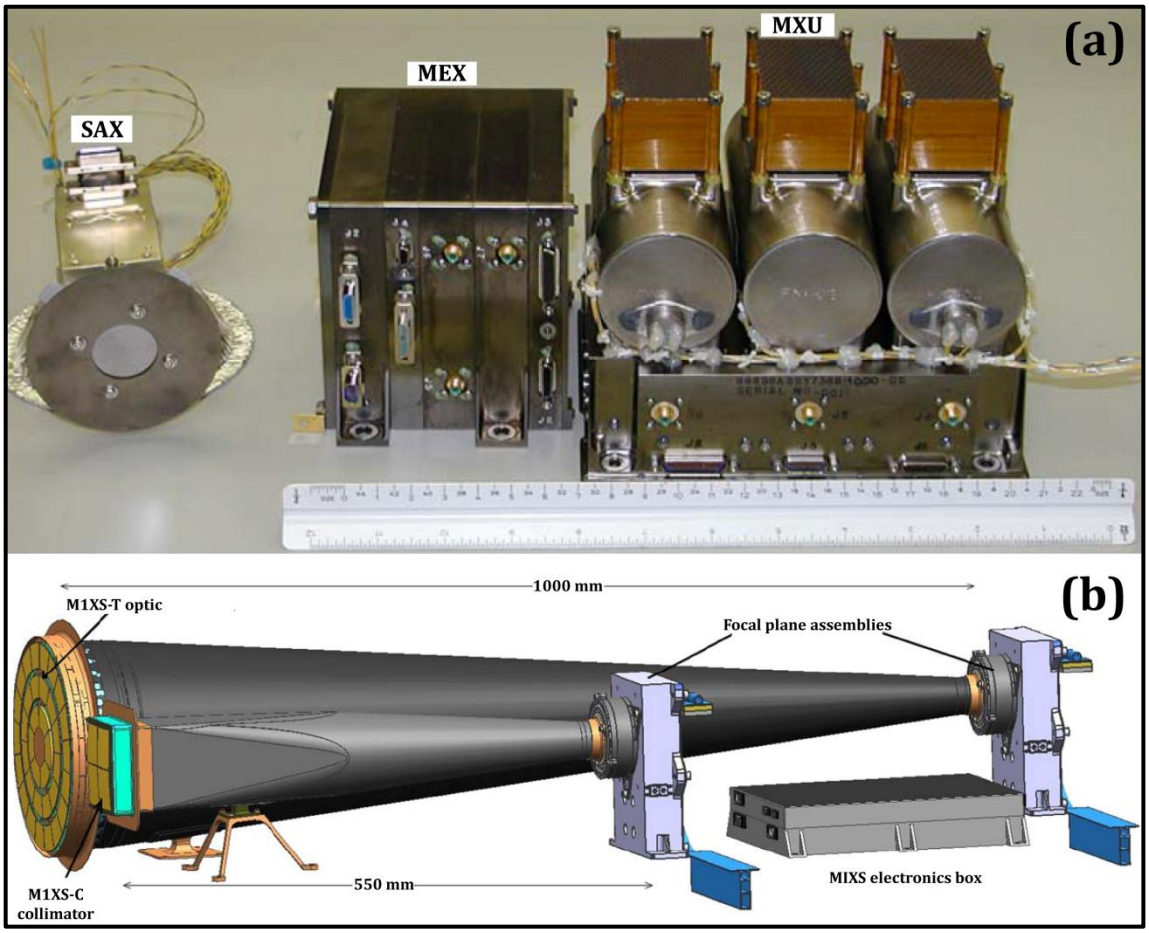

Figure 6.4. (a) The XRS flight instrument onboard MESSENGER, showing its three physical units: the planetary detectors and measurement circuitry which comprise the Mercury X-ray Unit (MXU), the Main Electronics for X-rays (MEX) unit, and the Solar Assembly for X-rays (SAX) which measures the solar X-rays (taken from Schlemm et al., 2007). (b) A schematic illustration of MIXS depicting the adjacent MIXS-C and MIXS-T components (taken from Fraser et al., 2010).

6.7. Future lunar exploration

The Moon continues to be a focus of planetary exploration. LRO (see section 1.2.6) continues to orbit the Moon, collecting scientific data which are reshaping lunar science. For example, the very recently published results from the LCROSS (Lunar Crater Observation and Sensing Satellite) mission indicate water ice may be present in permanently shadowed craters of the Moon (Colaprete et al., 2010). Future NASA lunar missions will include GRAIL (Gravity Recovery and Interior Laboratory) which will determine the structure of the lunar interior by conducting high-quality gravity field mapping to provide insights into the Moon's thermal evolution, and LADEE (Lunar Atmosphere and Dust Environment Explorer) which is designed to characterise the Moon's

tenuous atmosphere and dust environment from orbit. Other space agencies and nations are also reaching for the Moon. China have just launched their second lunar probe, Change'2; India are also planning a second lunar mission, Chandrayaan-2, which will carry the Large Area Soft X-ray Spectrometer (CLASS) as part of its scientific payload (website reference 2).

With the recent abundance of data obtained from lunar remote sensing missions, the understanding of the Moon is changing and it has become clear that the returned sample collection from the Apollo and Luna missions does not adequately represent the global heterogeneity and complexity of the Moon. In this thesis it has been demonstrated that combining different geochemical remote sensing datasets can be difficult, either due to their methodologies (e.g. atomic versus mineralogic detection) or to their different spatial and depth scales. However, these available datasets are complementary to one another and allow comparisons to be conducted globally. These comparisons can highlight gaps in our knowledge of the techniques employed and thus focus future research and development. However, differences will probably only be ultimately resolved after a series of new sampling missions (robotic or manned), at diverse locations across the lunar surface which provide additional geological ground truth information, and that also inspire the wider, lay public.

References

Abdrakhimov, A.M. & Basilevsky, A.T., 2010. Re-examination of Lunokhod sites: panoramas and aims for LROC investigations. *Proceedings of the Lunar and Planetary Science Conference XXXXI*, abstract #2173.

Adams, J.B., 1974. Visible and near-infrared diffuse reflectance spectra of pyroxenes as applied to remote sensing of solid objects in the solar system. *Journal of Geophysical Research*, 79, 4829-4836.

Adler, I., Gerard, J., Trombka, J., Schmadebeck, R., Lowman, P., Blodget, H., Yin, L., Eller, E., Lamothe, R., Gorenstein, P., Bjorkholm, P., Harris, B. & Gursky, H., 1972a. The Apollo 15 X-ray fluorescence experiment. *Proceedings of the Lunar Science Conference III*, *Geochimica et Cosmochimica Acta Supplement*, 3, 2157-2178.

Adler, I., Trombka, J., Gerard, J., Lowman, P., Schmadebeck, R., Blodget, H., Eller, E., Yin, L., Lamothe, R., Gorenstein, P. & Bjorkholm, P., 1972b. Apollo 15 geochemical X-ray fluorescence experiment: preliminary report. *Science*, 175, 436-440.

Adler, I., Trombka, J., Gerard, J., Lowman, P., Schmadebeck, R., Blodget, H., Eller, E., Yin, L., Lamothe, R., Osswald, G., Gorenstein, P., Bjorkholm, P., Gursky, H. & Harris, B., 1972c. Apollo 16 geochemical X-ray fluorescence experiment: preliminary report. *Science*, 177, 256-259.

Adler, I., Trombka, J., Gerard, J., Lowman, P., Schmadebeck, R., Blodget, H., Eller, E., Yin, L., Lamothe, R., Osswald, G., Gorenstein, P., Bjorkholm, P., Gursky, H., Harris, B., Golub, L. & Harnden, F.R., Jr., 1972d. X-ray fluorescence experiment. *Apollo 16: Preliminary Science Report*, NASA SP-315, 19.1-19.14.

Adler, I., Trombka, J.I., Lowman, P., Schmadebeck, R., Blodget, H., Eller, E., Yin, L., Lamothe, R., Osswald, G., Gerard, J., Gorenstein, P., Bjorkholm, P., Gursky, H., Harris, B.,

Arnold, J., Metzger, A. & Reedy, R., 1973. Apollo 15 and 16 results of the integrated geochemical experiment. *The Moon*, 7, 487-504.

Alibert, C., Norman, M.D. & McCulloch, M.T., 1994. An ancient Sm-Nd age for a ferroan noritic anorthosite clast from lunar breccia 67016. *Geochimica et Cosmochimica Acta*, 58, 2921-2926.

Allen, C.C., Morris, R.V., Lauer, H.V., Jr. & McKay, D.S., 1993. Microscopic iron metal on glass and minerals – a tool for studying regolith maturity. *Icarus*, 104, 291-300.

Allen, C.C., Morris, R.V. & McKay, D.S., 1996. An experimental analog to maturing lunar soil. *Proceedings of the Lunar and Planetary Science Conference XXVII*, 13-14.

Andre, C.G., Bielefeld, M.J., Eliason, E., Soderblom, L.A., Adler, I. & Philpotts, J.A., 1977. Lunar surface chemistry: a new imaging technique. *Science*, 197, 986-989.

Arai, T., Takeda, H., Yamaguchi, A. & Ohtake, M., 2008. A new model of lunar crust: asymmetry in crustal composition and evolution. *Earth Planets Space*, 60, 433-444.

Araki, H., Tazawa, S., Noda, H., Ishihara, Y., Goossens, S., Sasaki, S., Kawano, N., Kamiya, I., Otake, H., Oberst, J. & Shum, C., 2009. Lunar global shape and polar topography derived from Kaguya-LALT laser altimetry. *Science*, 323, 897-900.

Bambynek, W., Crasemann, B., Fink, R.W., Freund, H.-U., Mark, H., Swift, C.D., Price, R.E. & Venugopala Rao, P., 1972. X-ray fluorescence yields, Auger, and Coster-Kronig transition probabilities. *Reviews of Modern Physics*, 44, 716-813.

Basaltic Volcanism Study Project (BVSP), 1981. *Basaltic volcanism on the terrestrial planets*, Pergamon Press.

Basilevsky, A.T., Keller, H.U., Nathues, A., Mall, U., Hiesinger, H. & Rosiek, M., 2004. Scientific objectives and selection of targets for the SMART-1 Infrared Spectrometer (SIR). *Planetary and Space Science*, 52, 1261-1285.

Becker, T., Weller, L., Gaddis, L., Cook, D., Archinal, B., Rosiek, M., Isbell, C., Hare, T. & Kirk, R., 2008. Lunar Orbiter mosaic of the Moon. *Lunar and Planetary Science Conference XXXIX*, abstract #2357.

Belton, M.J.S., Veverka, J., Thomas, P., Helfenstein, P., Simonelli, D., Chapman, C., Davies, M.E., Greeley, R., Greenberg, R., Head, J., Murchie, S., Klaasen, K., Johnson, T.V., McEwen, A., Morrison, D., Neukum, G., Fanale, F., Anger, C., Carr, M. & Pilcher, C., 1992. Galileo encounter with 951 Gaspra: first pictures of an asteroid. *Science*, 257, 1647-1652.

Berezhnoy, A.A., Hasebe, N., Kobayashi, M., Michael, G.G., Okudaira, O. & Yamashita, N., 2005. A three end-member model for petrologic analysis of lunar prospector gamma-ray spectrometer data. *Planetary and Space Science*, 53, 1097-1108.

Berry, P.F., Furuta, T. & Rhodes, J.R., 1969. Particle size effects in radioisotope X-ray spectrometry. *Advances in X-ray Analysis*, 12, 612-632.

Besse, S., Sunshine, J.M., Pieters, C.M., Petro, N.E., Staid, M., Deepak, D., Head, J.W., Isaacson, P.J. & The M^3 Team, 2010. New observations of the Marius Hills Complex from Moon Mineralogy Mapper (M^3). *Proceedings of the Lunar and Planetary Science Conference XLI*, abstract #1361.

Binder, A.B., 1998. Lunar Prospector: overview. *Science*, 281, 1475-1476.

Bogard, D.D. & Johnson, P., 1983. Trapped noble gases indicate lunar origin for Antarctic meteorite. *Geophysical Research Letters*, 10, 801-803.

Borg, J., Chaumont, J., Langevin, Y., Maurette, M. & Jouret, C., 1980. Solar wind radiation damage in lunar dust grains and the characteristics of the ancient solar wind. In: *The Ancient Sun: fossil record in the earth, moon and meteorites*, Pergamon, 431-461.

Borg, L., Norman, M., Nyquist, L., Bogard, D., Snyder, G., Taylor, L. & Lindstrom, M., 1999. Isotopic studies of ferroan anorthosite 62236: a young lunar crustal rock from a light rare-earth-element-depleted source. *Geochimica et Cosmochimica Acta*, 63, 2679-2691.

Borg, L.E., Shearer, C.K., Asmerom, Y. & Papike, J.J., 2004. Prolonged KREEP magmatism on the Moon indicated by the youngest dated lunar igneous rock. *Nature*, 432, 209-211.

Bourdon, B., Touboul, M., Caro, G. & Kleine, T., 2008. Early differentiation of the Earth and the Moon. *Philosophical Transactions of the Royal Society A*, 366, 4105-4128.

Bouwer, S.D., 1983. Intermediate-term epochs in solar soft X-ray emission. *Journal of Geophysical Research*, 88 (A10), 7823-7830.

Bryant, R., Moran, M.S., Thoma, D.P., Holifield Collins, C.D., Skirvin, S., Rahman, M., Slocum, K., Starks, P., Bosch, D. & González Dugo, M.P., 2007. Measuring surface roughness height to parameterize radar backscatter models for retrieval of surface soil moisture. *IEEE Geoscience and Remote Sensing Letters*, 4, 137-141.

Burhop, E.H.S., 1952. *The Auger effect and other radiationless transitions*, Cambridge University Press.

Burns, R.G., 1993. *Mineralogical applications of crystal field theory*, Cambridge University Press.

Bussey, D.B.J. & Spudis, P.D., 2000. Compositional studies of the Orientale, Humorum, Nectaris, and Crisium lunar basins. *Journal of Geophysical Research*, 105 (E2), 4234-4243.

Cahill, J.T., Lucey, P.G., Gillis, J.J. & Steutel, D., 2004. Verification of quality and compatibility of the newly calibrated Clementine NIR data set. *Lunar and Planetary Science Conference XXXV*, abstract #1469.

Cameron, A.G.W., 2000. Higher-resolution simulations of the giant impact. In: Canup, R.M. & Righter, K. (Eds.) *Origin of the Earth and Moon*, University of Arizona Press, 133-144.

Cameron, A.G.W. & Ward, W.R., 1976. The origin of the Moon. *Proceedings of the Lunar Science Conference VII*, 120-122.

Campbell, B.A. & Hawke, B.R., 2005. Radar mapping of lunar cryptomaria east of Orientale basin. *Journal of Geophysical Research*, 110, E09002, doi: 10.109/2005JE002425.

Canup, R.M., 2004. Dynamics of lunar formation. *Annual Review of Astronomy and Astrophysics*, 42, 441-475.

Canup, R.M., Levison, H.F. & Stewart, G.R., 1999. Evolution of a terrestrial multiple-moon system. *The Astronomical Journal*, 117, 603-620.

Carini, G.A., Chen, W., De Geronimo, G., Gaskin, J.A., Keister, J.W., Li, Z., Ramsey, B.D., Rehak, P. & Siddons, D.P., 2009. Performance of a thin-window silicon drift detector X-ray fluorescence spectrometer. *IEEE Transactions on Nuclear Science*, 56, 2843-2849.

Carlson , R.W. & Lugmair, G.W., 1988. The age of ferroan anorthosite 60025: oldest crust on a young Moon? *Earth and Planetary Science Letters*, 90, 119-130.

Charette, M.P., McCord, T.B., Pieters, C. & Adams, J.B., 1974. Application of remote spectral reflectance measurements to lunar geology classification and determination of titanium content of lunar soils. *Journal of Geophysical Research*, 79, 1605-1613.

Claisse, F. & Samson, C., 1962. Heterogeneity effects in X-ray analysis. *Advances in X-ray Analysis*, 5, 335-354.

Clark, P.E., 1979. Correction, correlation and theoretical consideration of lunar X-ray fluorescence intensity ratios, PhD thesis, University of Maryland.

Clark, P.E. & Adler, I., 1978. Utilization of independent solar flux measurements to eliminate nongeochemical variation in X-ray fluorescence data. *Proceedings of the Lunar and Planetary Science Conference IX*, 3029-3036.

Clark, P.E. & Hawke, B.R., 1981. Compositional variations in the Hadley Apennine region. *Proceedings of the Lunar and Planetary Science Conference XII*, B, 727-749.

Clark, P.E., Hawke, B.R. & Basu, A., 1990. The relationship between orbital, Earth-based, and sample data for lunar landing sites. *Proceedings of the Lunar and Planetary Science Conference XX*, 147-160.

Clark, P.E. & Trombka, J.I., 1997. Remote X-ray spectrometry for NEAR and future missions: modeling and analyzing X-ray production from source to surface. *Journal of Geophysical Research*, 102, 16,361-16,384.

Clark, R.N., 2009. Detection of adsorbed water and hydroxyl on the Moon. *Science*, 326, 562-564.

Clayton, R.N. & Mayeda, T.K., 1975. Genetic relations between the Moon and meteorites. *Proceedings of the Lunar Science Conference VI*, 1761-1769.

Colaprete, A., Schultz, P., Heldmann, J., Wooden, D., Shirley, M., Ennico, K., Hermalyn, B., Marshall, W., Ricco, A., Elphic, R.C., Goldstein, D., Summy, D., Bart, G.D., Asphaug, E., Korycansky, D., Landis, D. & Sollitt, L., 2010. Detection of water in the LCROSS ejecta plume. *Science*, 330, 463-468.

Crawford, I.A., Fagents, S.A. & Joy, K.H., 2007. Full moon exploration. *Astronomy and Geophysics*, 48 (3), 18-21.

Crawford, I.A., Joy, K.H., Kellett, B.J., Grande, M., Anand, M., Bhandari, N., Cook, A.C., d'Uston, L., Fernandes, V.A., Gasnault, O., Goswami, J., Howe, C.J., Huovelin, J., Koschny, D., Lawrence, D.J., Maddison, B.J., Maurice, S., Narendranath, S., Pieters, C., Okada, T., Rothery, D.A., Russell, S.S., Sreekumar, P., Swinyard, B., Wieczorek, M. & Wilding, M., 2009. The scientific rationale for the C1XS X-ray Spectrometer on India's Chandrayaan-1 mission to the Moon. *Planetary and Space Science*, 57, 725-734.

Crosby, N.B., Aschwanden, M.J. & Dennis, B.R., 1993. Frequency distribution and correlations of solar X-ray flare parameters. *Solar Physics*, 143, 275-299.

Dalrymple, G.B. & Ryder, G., 1996. Argon-40/argon-39 age spectra of Apollo 17 highlands breccia samples by laser step heating and the age of the Serenitatis basin. *Journal of Geophysical Research*, 101 (E11), 26,069-26,084.

Davis, P.A., Jr., 1980. Iron and titanium distribution on the Moon from orbital gamma ray spectrometry with implications for crustal evolutionary models. *Journal of Geophysical Research*, 85 (B6), 3209-3224.

De Hon, R.A., 1974. Thickness of mare material in the Tranquillitatis and Nectaris basins, *Proceedings of the Lunar Science Conference I*, 53-59.

De Hon, R.A., 1978. Maximum thickness of materials in the western mare basins. *Proceedings of the Lunar and Planetary Science Conference IX*, 229-231.

De Hon, R.A., 1979. Thickness of the western mare basalts, *Proceedings of the Lunar and Planetary Science X*, 2935-2955.

De Hon, R.A. & Waskom, J.D., 1976. Geologic structure of the eastern mare basins. *Proceedings of the Lunar Science Conference VII*, 2729-2746.

Delano, J.W., 1986. Pristine lunar glasses: criteria, data and implications. *Lunar and Planetary Science Conference XVI, Journal of Geophysical Research*, 91 (B4), D201-D213.

Donnelly, R.F., 1976. Empirical models of solar flare X-ray and EUV emission for use in studying their E and F region effects. *Journal of Geophysical Research*, 81, 4745-4753.

Dunham, D.W., Cudnik, B., Palmer, D.M., Sada, P.V., Melosh, J., Beech, M., Frankenberger, R., Pellerin, L., Venable, R., Asher, D., Sterner, R., Gotwols, B., Wun, B. & Stockbauer, D., 2000. The first confirmed video recordings of lunar meteor impacts. *Lunar and Planetary Science Conference XXXI*, abstract #1547.

Dunkin, S.K., Grande, M., Casanova, I., Fernandes, V., Heather, D.J., Kellett, B., Muinonen, K., Russell, S.S., Browning, R., Waltham, N., Parker, D., Kent, B., Perry, C.H., Swinyard, B., Perry, A., Feraday, J., Howe, C., Phillips, K., McBride, G., Huovelin, J., Muhli, P., Hakala, P.J., Vilhu, O., Thomas, N., Hughes, D., Alleyne, H., Grady, M., Lundin, R., Barabash, S., Baker, D., Clark, P.E., Murray, C.D., Guest, J., d'Uston, L.C., Maurice, S., Foing, B., Christou, A., Owen, C., Charles, P., Laukkanen, J., Koskinen, H., Kato, M., Sipila, K., Nenonen, S., Holmstrom, M., Bhandari, N., Elphic, R. & Lawrence, D., 2003. Scientific rationale for the D-CIXS X-ray spectrometer on board ESA's SMART-1 mission to the Moon. *Planetary and Space Science*, 51, 435-442.

Eliason, E., Isbell, C., Lee, E., Becker, T., Gaddis, L., McEwen, A. & Robinson, M., 1999. The Clementine UVVIS global lunar mosaic. *NASA Planetary Data System CD-ROM Archive*, CL_4001-4078.

Eliason, E.M., Lee, E.M., Becker, T.L., Weller, L.A., Isbell, C.E., Staid, M.I., Gaddis, L.R., McEwen, A.S., Robinson, M.S., Duxbury, T., Steutel, D., Blewett, D.T. & Lucey, P.G., 2003. A near-infrared (NIR) global multispectral map of the Moon from Clementine. *Lunar and Planetary Science Conference XXXIV*, abstract #2093.

Elphic, R.C., Lawrence, D.J., Feldman, W.C., Barraclough, B.L., Maurice, S., Binder, A.B. & Lucey, P.G., 2000. Lunar and rare earth element distribution and ramifications for FeO and TiO_2: Lunar Prospector neutron spectrometer observations. *Journal of Geophysical Research*, 105 (E8), 20,333-20,345.

Evensen, N.M., Hamilton, P.J. & O'Nions, R.K., 1978. Rare-earth abundances in chondritic meteorites. *Geochimica et Cosmochimica Acta*, 42, 1199-1212.

Fagents, S.A., Rumpf, M.E., Crawford, I.A. & Joy, K.H., 2010. Preservation potential of implanted solar wind volatiles in lunar palaeoregolith deposits buried by lava flows. *Icarus*, 207, 595-604.

Feldman, W.C., Ahola, K., Barraclough, B.L., Belian, R.D., Black, R.K., Elphic, R.C., Everett, D.T., Fuller, K.R., Kroesche, J., Lawrence, D.J., Lawson, S.L., Longmire, J.L., Maurice, S., Miller, M.C., Prettyman, T.H., Storms, S.A. & Thornton, G.W., 2004. Gamma-ray, neutron, and alpha-particle spectrometers for the Lunar Prospector mission. *Journal of Geophysical Research*, 109, E07S06.

Feldman, W.C., Maurice, S., Binder, A.B., Barraclough, B.L., Elphic, R.C. & Lawrence, D.J., 1998. Fluxes of fast and epithermal neutrons from Lunar Prospector: evidence for water ice at the lunar poles. *Science*, 281, 1496-1500.

Fernandes, V.A., Burgess, R. & Morris, A., 2009. ^{40}Ar-^{39}Ar age determinations of lunar basalt meteorites Asuka 881757, Yamato 793169, Miller Range 05035, La Paz Icefield 02205, Northwest Africa 479, and basaltic breccia Elephant Moraine 96008. *Meteoritics and Planetary Science*, 44, 805-821.

Fernandes, V.A., Burgess, R. & Turner, G., 2003. ^{40}Ar-^{39}Ar chronology of lunar meteorites Northwest Africa 032 and 773. *Meteoritics and Planetary Science*, 38, 555-564.

Fischer, E.M. & Pieters, C.M., 1994. Remote determination of exposure degree and iron concentration of lunar soils using VIS-NIR spectroscopic methods. *Icarus*, 111, 475-488.

Fischer, E.M. & Pieters, C.M., 1996. Composition and exposure age of the Apollo 16 Cayley and Descartes regions from Clementine data: normalizing the optical effects of space weathering. *Journal of Geophysical Research*, 101 (E1), 2225-2234.

Fitton, G., 1997. X-ray fluorescence spectrometry. In: Gill, R. (Ed.) *Modern Analytical Geochemistry*, Addison Wesley Longman Ltd.

Foing, B.H., Racca, G.D., Marini, A., Evrard, E., Stagnaro, L., Almeida, M., Koschny, D., Frew, D., Zender, J., Heather, J., Grande, M., Huovelin, J., Keller, H.U., Nathues, A., Josset, J.L., Malkki, A., Schmidt, W., Noci, G., Birkl, R., Iess, L., Sodnik, Z. & McManamon, P., 2006. SMART-1 mission to the Moon: status, first results and goals. *Advances in Space Research*, 37, 6-13.

Fraser, G.W., Carpenter, J.D., Rothery, D.A., Pearson, J.F., Martindale, A., Huovelin, J., Treis, J., Anand, M., Anttila, M., Ashcroft, M., Benkoff, J., Bland, P., Bowyer, A., Bradley, A., Bridges, J., Brown, C., Bulloch, C., Bunce, E.J., Christensen, U., Evans, M., Fairbend, R., Feasey, M., Giannini, F., Hermann, S., Hesse, M., Hilchenbach, M., Jorden, T., Joy, K., Kaipiainen, M., Kitchingman, I., Lechner, P., Lutz, G., Malkki, A., Muinonen, K., Näränen, J., Portin, P., Prydderch, M., San Juan, J., Sclater, E., Schyns, E., Stevenson, T.J., Strüder, L., Syrjasuo, M., Talboys, D., Thomas, P., Whitford, C. & Whitehead, S., 2010. The mercury imaging X-ray spectrometer (MIXS) on BepiColombo. *Planetary and Space Science*, 58, 79-95.

Fruland, R.M., 1983. *Regolith breccia workbook*, JSC 19045, NASA Johnson Space Center, Houston.

Gaddis, L., Isbell, C., Staid, M., Eliason, E., Lee, E.M., Weller, L., Sucharski, T., Lucey, P., Blewett, D., Hinrichs, J. & Steutel, D., 2007. The Clementine NIR Global Lunar Mosaic. *NASA Planetary Data System DVD*, Archive, CL_5001-5078.

Gasnault, O., Forni, O., Diez, B., d'Uston, C., Hasebe, N., Okudaira, O., Yamashita, N., Kobayashi, S., Karouji, Y., Hareyama, M., Shibamura, E., Kobayashi, M.N., Reedy, R.C.

& the Selene GRS team. Preliminary analysis of SELENE GRS data – the iron case. *Proceedings of the Lunar and Planetary Science Conference XL*, abstract #2253.

Giguere, T.A., Taylor, G.J., Hawke, B.R. & Lucey, P.G., 2000. The titanium contents of lunar mare basalts. *Meteoritics and Planetary Science*, 35, 193-200.

Gillis, J.J., Haskin, L.A. & Spudis, P.D., 1999. An empirical calibration to calculate thorium abundances from the Lunar Prospector gamma-ray data. *Lunar and Planetary Science Conference XXX*, abstract 1699.

Gillis, J.J., Jolliff, B.L. & Elphic, R.C., 2003. A revised algorithm for calculating TiO_2 from Clementine UVVIS data: a synthesis of rock, soil, and remotely sensed TiO_2 concentrations. *Journal of Geophysical Research*, 108 (E2), 5009, doi:10.1029/2001JE001515.

Gillis, J.J., Jolliff, B.L. & Korotev, R.L., 2004. Lunar surface geochemistry: global concentrations of Th, K, and FeO as derived from Lunar Prospector and Clementine data. *Geochimica et Cosmochimica Acta*, 68, 3791-3805.

Gillis-Davis, J.J., Lucey, P.G. & Hawke, B.R., 2006. Testing the relation between UV-vis color and TiO_2 content of the lunar maria. *Geochimica et Cosmochimica Acta*, 70, 6079-6102.

Glotch, T.D., Lucey, P.G, Bandfield, J.L., Greenhagen, B.T., Thomas, I.R., Elphic, R.C., Bowles, N., Wyatt, M.B., Allen, C.C., Donaldson Hanna, K. & Paige, D.A., 2010. Highly silicic compositions on the Moon. *Science*, 329, 1510-1513.

Goldsten, J.O., Rhodes, E.A., Boynton, W.V., Feldman, W.C., Lawrence, D.J., Trombka, J.I., Smith, D.M., Evans, L.G., White, J., Madden, N.W., Berg, P.C., Murphy, G.A., Gurnee, R.S., Strohbehn, K., Williams, B.D., Schaefer, E.D., Monaco, C.A., Cork, C.P., Del Eckels, J., Miller, W.O., Burks, M.T., Hagler, L.B., DeTeresa, S.J. & Witte, M.C.,

2007. The MESSENGER gamma-ray and neutron spectrometer. *Space Science Reviews*, 131, 339-391.

Gnos, E., Hofmann, B.A., Al-Kathiri, A., Lorenzetti, S., Eugster, O., Whitehouse, M.J., Villa, I.M., Jull, A.J.T., Eikenberg, J., Spettel, B., Krähenbühl, U., Franchi, I.A. & Greenwood, R.C., 2004. Pinpointing the source of a lunar meteorite: implications for the evolution of the Moon. *Science*, 305, 657-659.

Goldreich, 1966. History of the lunar orbit. *Reviews of Geophysics*, 4, 411-439.

Goswami, J.N. & Annadurai, M., 2009. Chandrayaan-1: India's first planetary science mission to the moon. *Current Science*, 96, 486-491.

Gow, J., Smith, D.R., Holland, A.D., Maddison, B., Howe, C., Grande, M., Sreekumar, P. & Huovelin, J., 2008. Radiation study of swept-charge devices for the Chandrayaan-1 X-ray Spectrometer (C1XS) instrument. *Proceedings of SPIE*, 7021, abstract# 70211A.

Grande, M., 2001. The D-CIXS X-ray spectrometer on ESA's SMART-1 mission to the Moon. *Earth, Moon and Planets*, 85-86, 143-152.

Grande, M., Browning, R., Waltham, N., Parker, D., Dunkin, S.K., Kent, B., Kellett, B., Perry, C.H., Swinyard, B., Perry, A., Feraday, J., Howe, C., McBride, G., Phillips, K., Huovelin, J., Muhli, P., Hakala, P.J., Vilhu, O., Laukkanen, J., Thomas, N., Hughes, D., Alleyne, H., Grady, M., Lundin, R., Barabash, S., Baker, D., Clark, P.E., Murray, C.D., Guest, J., Casanova, I., d'Uston, L.C., Maurice, S., Foing, B., Heather, D.J., Fernandes, V., Muinonen, K., Russell, S.S., Christou, A., Owen, C., Charles, P., Koskinen, H., Kato, M., Sipila, K., Nenonen, S., Holmstrom, M., Bhandari, N., Elphic, R. & Lawrence, D., 2003. The D-CIXS X-ray mapping spectrometer on SMART-1. *Planetary and Space Science*, 51, 427-433.

Grande, M., Kellett, B.J., Howe, C., Perry, C.H., Swinyard, B., Dunkin, S., Huovelin, J., Alha, L., D'Uston, L.C., Maurice, S., Gasnault, O., Couturier-Doux, S., Barabash, S., Joy, K.H., Crawford, I.A., Lawrence, D., Fernandes, V., Casanova, I., Wieczorek, M., Thomas,

N., Mall, U., Foing, B., Hughes, D., Alleyne, H., Russell, S., Grady, M., Lundin, R., Baker, D., Murray, C.D., Guest, J. & Christou, A., 2007. The D-CIXS X-ray spectrometer on the SMART-1 mission to the Moon – first results. *Planetary and Space Science*, 55, 494-502.

Grande, M., Maddison, B.J., Howe, C.J., Kellett, B.J., Sreekumar, P., Huovelin, J., Crawford, I.A., d'Uston, C.L., Smith, D., Anand, M., Bhandari, N., Cook, A., Fernandes, V., Foing, B., Gasnault, O., Goswami, J.N., Holland, A., Joy, K.H., Kochney, D., Lawrence, D., Maurice, S,. Okada, T., Narendranath, S., Pieters, C., Rothery, D., Russell, S.S., Shrivastava, A., Swinyard, B., Wilding, M. & Wieczorek, M., 2009. The C1XS X-ray Spectrometer on Chandrayaan-1. *Planetary and Space Science*, 57, 717-724.

Greenhagen, B.T., Lucey, P.G., Wyatt, M.B., Glotch, T.D., Allen, C.C., Arnold, J.A., Bandfield, J.L., Bowles, N.E., Donaldson Hanna, K.L., Hayne, P.O., Song, E., Thomas, I.R. & Paige, D.A., 2010. Global silicate mineralogy of the Moon from the Diviner Lunar Radiometer. *Science*, 1507-1509.

Grier, J.A., McEwen, A.S., Lucey, P.G., Milazzo, M. & Strom, R.G., 1999. The optical maturity of ejecta from large rayed craters: preliminary results and implications. *Proceedings of Workshop on New Views of the Moon II: Understanding the Moon Through the Integration of Diverse Datasets*, abstract #8057.

Hall, R.C., 1977. *Lunar impact: a history of project Ranger*, NASA SP-4210, Washington, D.C.

Hapke, B., 1977. Interpretation of optical observations of Mercury and the Moon. *Physics of the Earth and Planetary Interiors*, 15, 264-274.

Hapke, B., Cassidy, W. & Wells, E., 1975. Effects of vapor-phase deposition processes on the optical, chemical, and magnetic properties of the lunar regolith. *The Moon*, 13, 339-353.

Hartmann, W.K. & Davis, D.R., 1975. Satellite-sized planetesimals and lunar origin. *Icarus*, 24, 504-515.

Haruyama, J., Matsunaga, T., Ohtake, M., Morota, T., Honda, C., Yokota, Y., Torii, M., Ogawa, Y. & the LISM Working Group, 2008a. Global lunar-surface mapping experiment using the Lunar Imager/Spectrometer on SELENE. *Earth Planets Space*, 60, 243-255.

Haruyama, J., Ohtake, M., Matsunaga, T., Morota, T., Honda, C., Yokota, Y., Pieters, C.M., Hara, S., Hioki, K., Saiki, K., Miyamoto, H., Iwasaki, A., Abe, M., Ogawa, Y., Takeda, H., Shirao, M., Yamaji, A. & Josset, J.-L., 2008b. Lack of exposed ice inside lunar south pole Shackleton crater. *Science*, 322, 938-939.

Haskin, L.A., 1998. The Imbrium impact event and the thorium distribution at the lunar highlands surface. *Journal of Geophysical Research*, 103 (E1), 1679-1689.

Haskin, L.A., Gillis, J.J., Korotev, R.L. & Jolliff, B.L., 2000. The materials of the lunar Procellarum KREEP Terrane: a synthesis of data from geomorphological mapping, remote sensing, and sample analyses. *Journal of Geophysical Research*, 105 (E8), 20,403-20,415.

Hawke, B.R., Peterson, C.A., Blewett, D.T., Bussey, D.B.J., Lucey, P.G., Taylor, G.J. & Spudis, P.D., 2003. Distribution and modes of occurrence of lunar anorthosite. *Journal of Geophysical Research*, 108 (E6), 5050.

Hawthorne, A.R. & Gardner, R.P., 1978. A proposed model for particle-size effects in the X-ray fluorescence analysis of heterogeneous powders that includes incidence angle and non-random packing effects. *X-ray Spectrometry*, 7, 198-205.

He, F., & Van Espen, P.J., 1991. General approach for quantitative energy dispersive X-ray fluorescence analysis based on fundamental parameters. *Analytical Chemistry*, 63, 2237-2244.

Head, J.W., III, 1976. Lunar volcanism in space and time. *Reviews of Geophysics and Space Physics*, 14, 265-300.

Head, J.W., Murchie, S., Mustard, J.F., Pieters, C.M., Neukum, G., McEwen, A., Greeley, R., Nagel, E & Belton, M.J.S., 1993. Lunar impact basins: new data for the western limb and far side (Orientale and South Pole-Aitken basins) from the first Galileo flyby. *Journal of Geophysical Research*, 98 (E9), 17,149-17,181.

Head, J.W., III & Wilson, L., 1992. Lunar mare volcanism: stratigraphy, eruption conditions, and the evolution of secondary crusts. *Geochimica et Cosmochimica Acta*, 56, 2155-2175.

Heather, D.J. & Dunkin, S.K., 2002. A stratigraphic study of southern Oceanus Procellarum using Clementine multispectral data. *Planetary and Space Science*, 50, 1299-1309.

Henke, B.L., Gullikson, E.M. & Davis, J.C., 1993. X-ray interactions: photoabsorption, scattering, transmission and reflection at E = 50-30,000 eV, Z = 1-92. *Atomic Data and Nuclear Data Tables*, 54, 181-342.

Hess, P.C., 1994. Petrogenesis of lunar troctolites. *Journal of Geophysical Research*, 99 (E9), 19,083-19,093.

Hess, P.C. & Parmentier, E.M., 1995. A model for the thermal and chemical evolution of the Moon's interior: implications for the onset of mare volcanism. *Earth and Planetary Science Letters*, 134, 501-514.

Hiesinger, H. & Head, J.W., III, 2006. New views of lunar geosciences: an introduction and overview. *Reviews in Mineralogy and Geochemistry*, 60, 1-81.

Hiesinger, H., Head, J.W., III, Wolf, U., Jaumann, R. & Neukum, G., 2003. Ages and stratigraphy of mare basalts in Oceanus Procellarum, Mare Nubium, Mare Cognitum, and Mare Insularum. *Journal of Geophysical Research*, 108 (E7), 5065, doi: 10.1029/2002JE001985.

Hiesinger, H., Head, J.W., Wolf, U., Neukum, G. & Jaumann, R., 2008. Ages of mare basalts on the lunar nearside: a synthesis. *Proceedings of the Lunar and Planetary Science Conference XXXIX*, abstract #1269.

Hiesinger, H., Jaumann, R., Neukum, G. & Head, J.W., III, 2000. Ages of mare basalts on the lunar nearside. *Journal of Geophysical Research*, 105 (E12), 29,239-29,275.

Holland, A.D., Hutchinson, I.B., Smith, D.R., & Pool, P., 2004. Proton damage in the E2V swept charge device. *Nuclear Instruments and Methods in Physics Research A*, 521, 393-398.

Holland, A. & Pool, P., 2008. A new family of swept charge devices (SCDs) for X-ray spectroscopy. *Proceedings of SPIE*, 7021, abstract #702117.

Hood, L.L. & Williams, C.R., 1989. The lunar swirls: distribution and possible origins. *Proceedings of the Lunar and Planetary Science Conference XIX*, 99-113.

Hood, L.L., Zakharian, A., Halekas, J., Mitchell, D.L., Lin, R.P., Acuña, M.H. & Binder, A.B., 2001. Initial mapping and interpretation of lunar crustal magnetic anomalies using Lunar Prospector magnetometer data. *Journal of Geophysical Research*, 106 (E11), 27,825-27,839.

Hörz, F., Grieve, R., Heiken, G., Spudis, P. & Binder, A., 1991. Lunar surface processes. In: Heiken, G.H., Vaniman, D.T. & French, B.M. (Eds.) *Lunar sourcebook: a user's guide to the Moon*, Cambridge University Press, 61-120.

Howe, C.J., Drummond, D., Edeson, R., Maddison, B., Parker, D.J., Parker, R., Shrivastava, A., Spencer, J., Kellett, B.J., Grande, M., Sreekumar, P., Huovelin, J., Smith, D.R., Gow, J., Narendranath, S. & d'Uston, L., 2009. Chandrayaan-1 X-ray Spectrometer (C1XS) – Instrument design and technical details. *Planetary and Space Science*, 57, 735-743.

Huovelin, J., Alha, L., Andersson, H., Andersson, T., Browning, R., Drummond, D., Foing, B., Grande, M., Hämäläinen, K., Laukkanen, J., Lämsä, V., Muinonen, K., Murray, M., Nenonen, S., Salminen, A., Sipilä, H., Taylor, I., Vilhu, O., Waltham, N. & Lopez-Jorkama, M., 2002. The SMART-1 X-ray solar monitor (XSM): calibrations for D-CIXS and independent coronal science. *Planetary and Space Science*, 50, 1345-1353.

Ida, S., Canup, R.M. & Stewart, G.R., 1997. Lunar accretion from an impact-generated disk. *Nature*, 389, 353-357.

James, O.B., 1980. Rocks of the early lunar crust. *Proceedings of the Lunar and Planetary Science Conference XI*, 365-393.

James, O.B. & Flohr, M.K., 1983. Subdivision of the Mg-suite noritic rocks into Mg-gabbronorites and Mg-norites. *Proceedings of the Lunar and Planetary Science Conference XIII*, *Journal of Geophysical Research*, 88 (supplement), A603-A614.

Jenkins. R., 1974. *An introduction to X-ray spectrometry*, Heyden & Sons Ltd, London.

Jerde, E.A., Morris, R.V. & Warren, P.H., 1990. In quest of lunar regolith breccias of exotic provenance: a uniquely anorthositic sample from the Fra Mauro (Apollo 14) highlands. *Earth and Planetary Science Letters*, 98, 90-108.

Jerde, E.A., Warren, P.H., Morris, R.V., Heiken, G.H. & Vaniman, D.T., 1987. A potpourri of regolith breccias: "new" samples from the Apollo 14, 16 and 17 landing sites. *Proceedings of the Lunar and Planetary Science Conference XVII*, *Journal of Geophysical Research*, 92 (B4), E526-E536.

Johnson, J.R., Larson, S.M. & Singer, R.B., 1991. Remote sensing of potential lunar resources 1. near-side compositional properties. *Journal of Geophysical Research*, 96 (E3), 18,861-18,882.

Jolliff, B.L., Floss, C., McCallum, I.S. & Schwartz, J.M., 1999. Geochemistry, petrology, and cooling history of 14161,7373: a plutonic sample with textural evidence of granitic-fraction separation by silicate-liquid immiscibility. *American Mineralogist*, 84, 821-837.

Jolliff, B.L., Gillis, J.J., Haskin, L.A., Korotev, R.L. & Wieczorek, M.A., 2000. Major lunar crustal terranes: surface expressions and crust-mantle origins. *Journal of Geophysical Research*, 105 (E2), 4197-4216.

Jolliff, B.L., Korotev, R.L., Zeigler, R.A. & Prettyman, T.H., 2009. Connecting lunar meteorite Dhofar 961 to the South Pole-Aitken Basin through Lunar Prospector gamma-ray data. *Lunar and Planetary Science Conference XL*, abstract #2555.

Jones, J.H. & Palme, H., 2000. Geochemical constraints on the origin of the Earth and Moon. In: Canup, R.M. & Righter, K. (Eds.) *Origin of the Earth and Moon*, University of Arizona Press, 197-216.

Josset, J.-L., Beauvivre, S., Cerroni, P., De Sanctis, M.C., Pinet, P., Chevrel, S., Langevin, Y., Barucci, M.A., Plancke, P., Koschny, D., Almeida, M., Sodnik, Z., Mancuso, S., Hofmann, B.A., Muinonen, K., Shevchenko, K., Shkuratov, Yu., Ehrenfreund, P. & Foing, B.H., 2006. Science objectives and first results from the SMART-1/AMIE multicolour micro-camera. *Advances in Space Research*, 37, 14-20.

Joy, K.H., Crawford, I.A., Anand, M., Greenwood, R.C., Franchi, I.A. & Russell, S.S., 2008. The petrology and geochemistry of Miller Range 05035: a new lunar gabbroic meteorite. *Geochimica et Cosmochimica Acta*, 72, 3822-3844.

Joy, K.H., Crawford, I.A., Rothery, D.A., Weider, S.Z. & Nittler, L.R., 2010. Planetary X-ray fluorescence: data product requirements for meaningful planetary geological interpretation. *Proceedings of the X-ray Fluorescence Spectroscopy in Planetary Remote Sensing Workshop*, ESA SP-687.

Kaula, W.M. & Yoder, C.F., 1976. Lunar orbit evolution and tidal heating of the Moon. *Proceedings of the Lunar and Planetary Science Conference VII*, 440-442.

Kay, H.R.M., Harra, L.K., Matthews, S.A., Culhane, J.L. & Green, L.M., 2003. The soft X-ray characteristics of solar flares, both with and without associated CMEs. *Astronomy and Astrophysics*, 400, 779-784.

Keller, L.P. & McKay, D.S., 1993. Discovery of vapor deposits in the lunar regolith. *Science*, 261, 1305-1307.

Keller, L.P. & McKay, D.S., 1997. The nature and origin of rims on lunar soil grains. *Geochimica et Cosmochimica Acta*, 61, 2331-2341.

Kellett, B., 2008. C1XS calibration in the RAL RESIK facility. *RAL Publication*, C1-C1X-RAL-RP-0031.

Kiran Kumar, A.S., Roy Chowdhury, A., Banerjee, A., Dave, A.B., Sharma, B.N., Shah, K.J., Murali, K.R., Joshi, S.R., Sarkar, S.S. & Patel, V.D., 2009. Terrain Mapping Camera: a stereoscopic high-resolution instrument on Chandrayaan-1. *Current Science*, 96, 492-495.

Kleine, T., Palme, H., Mezger, K. & Halliday, A.N., 2005. Hf-W chronometry of lunar metals and the age and early differentiation of the Moon. *Science*, 310, 1671-1674.

Koeberl, C., 2006. The record of impact processes on the early Earth: a review of the first 2.5 billion years. *Geological Society of America*, Special Paper, 405, 1-22.

Koppes, C.R., 1982. JPL and the American space program: a history of the Jet Propulsion Laboratory, *Yale University Press*.

Korchak, A.A., 1971. On the origin of solar flare X-rays. *Solar Physics*, 18, 284-304.

Korotev, R.L., 1996. On the relationship between the Apollo 16 ancient regolith breccias and feldspathic fragmental breccias, and the composition of the prebasin crust in the central highlands of the Moon. *Meteoritics and Planetary Science*, 31, 403-412.

Korotev, R.L., 1997. Some things we can infer about the Moon from the composition of the Apollo 16 regolith. *Meteoritics and Planetary Science*, 32, 447-478.

Korotev, R.L., 2000. The great lunar hot spot and the composition and origin of the Apollo mafic ("LKFM") impact-melt breccias. *Journal of Geophysical Research*, 105 (E2), 4317-4345.

Korotev, R.L., 2005. Lunar geochemistry as told by lunar meteorites. *Chemie der Erde*, 65, 297-346.

Korotev, R.L. & Gillis, J.J., 2001. A new look at the Apollo 11 regolith and KREEP. *Journal of Geophysical Research*, 106 (E6), 12,339-12,353.

Korotev, R.L., Jolliff, B.L., Zeigler, R.A., Gillis, J.J. & Haskin, L.A., 2003. Feldspathic lunar meteorites and their implications for compositional remote sensing of the lunar surface and the composition of the lunar crust. *Geochimica et Cosmochimica Acta*, 67, 4895-4923.

Korotev, R.L., Zeigler, R.A., Jolliff, BL., Irving, A.J. & Bunch, T.E., 2009. Compositional and lithological diversity among brecciated lunar meteorites of intermediate iron concentrations. *Meteoritics and Planetary Science*, 44, 1287-1322.

Kramer, G.Y., 2010. Characterizing bedrock lithologies using small crater rims and ejecta probing (SCREP). *Advances in Space Research*, 45, 1257-1267.

Lang, J., Brown, C.M., Magraw, J.E. & Payne, J., 1993. The laboratory calibration of the Yohkoh Bragg crystal spectrometer. *RAL-93-035*, CCLRC.

Lawrence, D.J., Elphic, R.C., Feldman, W.C., Prettyman, T.H., Gasnault, O. & Maurice, S., 2003. Small-area thorium features on the lunar surface. *Journal of Geophysical Research*, 108 (E9), 5102, doi: 10.1029/2003JE002050.

Lawrence, D.J., Feldman, W.C., Barraclough, B.L., Binder, A.B., Elphic, R.C., Maurice, S. & Thomsen, D.R., 1998. Global elemental maps of the Moon: the Lunar Prospector gamma-ray spectrometer. *Science*, 281, 1484-1489.

Le Mouélic, S., Langevin, Y., Erard, S., Pinet, P., Chevrel., S. & Daydou, Y., 2000. Discrimination between maturity and composition of lunar soils from integrated Clementine UV-visible/near-infrared data: application to the Aristarchus Plateau. *Journal of Geophysical Research*, 105 (E4), 9445-9455.

Lee, D.-C., Halliday, A.N., Snyder, G.A. & Taylor, L.A., 1997. Age and origin of the Moon. *Science*, 278, 1098-1103.

Lemoine, F.G., Smith, D.E., Zuber, M.T., Neumann, G.A. & Rowlands, D.D., 1997. A 70th degree lunar gravity model (GLGM-2) from Clementine and other tracking data. *Journal of Geophysical Research*, 102 (E7), 16,339-16,359.

Lim, L.F. & Nittler, L.R., 2009. Elemental composition of 433 Eros: new calibration of the NEAR-Shoemaker XRS data. *Icarus*, 200, 129-146.

Lindstrom, M.M., Knapp, S.A., Shervais, J.W. & Taylor, L.A., 1984. Magnesian anorthosites and associated troctolites and dunite in Apollo 14 breccias. *Proceedings of the Lunar and Planetary Science Conference XV, Journal of Geophysical Research*, 89 (supplement), C41-C49.

Lindstrom, M.M. & Lindstrom, D.J., 1986. Lunar granulites and their precursor anorthositic norites of the early lunar crust. *Proceedings of the Lunar and Planetary Science Conference XVI, Journal of Geophysical Research*, 91 (B4), D263-D276.

Longhi, J., 1977. Magma oceanography 2: chemical evolution and crustal formation. *Proceedings of the Lunar Science Conference VIII*, 601-621.

Longhi, J., 2003. A new view of lunar ferroan anorthosites: postmagma ocean petrogenesis. *Journal of Geophysical Research*, 108 (E8), 5083.

Longhi, J. & Ashwal, L.D., 1985. Two-stage models for lunar and terrestrial anorthosites: petrogenesis without a magma ocean. *Proceedings of the Lunar and Planetary Science Conference XV, Journal of Geophysical Research*, 90 (supplement), C571-C584.

Lowe, B.G., Holland, A.D., Hutchinson, I.B., Burt, D.J. & Pool., 2001. The swept charge device, a novel CCD-based EDX detector: first results. *Nuclear Instruments and Methods in Physical Research A*, 458, 568-579.

Lucey, P.G., 2004. Mineral maps of the Moon. *Geophysical Research Letters*, 31, L08701, doi: 10.1029/2003GL019406.

Lucey, P.G., 2006. Radiative transfer modeling of the effect of mineralogy on some empirical methods for estimating iron concentration from multispectral imaging of the Moon. *Journal of Geophysical Research*, 111, E08003, doi: 10.1029/2005JE002661.

Lucey, P.G., Blewett, D.T., Eliason, E.M., Weller, L.A., Sucharski, R., Malaret, E., Hinrichs, J.L. & Owensby, P.D., 2000a. Optimized calibration constants of the Clementine NIR camera. *Lunar and Planetary Science Conference XXXI*, abstract #1273.

Lucey, P.G., Blewett, D.T. & Hawke, B.R., 1998. Mapping the FeO and TiO_2 content of the lunar surface with multispectral imagery. *Journal of Geophysical Research*, 103 (E2), 3679-3699.

Lucey, P.G., Blewett, D.T., Johnson, J.L., Taylor, G.J. & Hawke, B.R., 1996. Lunar titanium content from UV-VIS measurements. *Proceedings of the Lunar and Planetary Science Conference XXVII*, 781-782.

Lucey, P.G., Blewett, D.T. & Jolliff, B.L., 2000b. Lunar iron and titanium abundance algorithms based on final processing of Clementine ultraviolet-visible images. *Journal of Geophysical Research*, 105 (E8), 20,297-20,305.

Lucey, P.G., Blewett, D.T., Taylor, G.J. & Hawke, B.R., 2000c. Imaging of lunar surface maturity. *Journal of Geophysical Research*, 105 (E8), 20,377-20,386.

Lucey, P.G., Hinrichs, J.L. & Malaret, E., 1997. Progress toward calibration of the Clementine NIR camera data set. *Lunar and Planetary Science Conference XXVIII*, abstract #1401.

Lucey, P., Korotev, R.L., Gillis, J.J., Taylor, L.A., Lawrence, D., Campbell, B.A., Elphic, R., Feldman, B., Hood, L.L., Hunten, D., Mendillo, M., Noble, S., Papike, J.J., Reedy, R.C., Lawson, S., Prettyman, T., Gasnault, O. & Maurice, S., 2006. Understanding the lunar surface and space-moon interactions. *Reviews in Mineralogy and Geochemistry*, 60, 83-219.

Lucey, P.G., Taylor, G.J. & Malaret, E., 1995. Abundance and distribution of iron on the Moon. *Science*, 268, 1150-1153.

Margot, J.L., Campbell, D.B., Jurgens, R.F. & Slade, M.A., 1999. Topography of the lunar poles from radar interferometry: a survey of cold trap locations. *Science*, 284, 1658-1660.

Maruyama, Y., Ogawa, K., Okada, T. & Kato, M., 2008. Laboratory experiments of particle size effect in X-ray fluorescence and implications to remote X-ray spectrometry of lunar regolith surface. *Earth Planets Space*, 60, 293-297.

Matsunaga, T., Ohtake, M., Haruyama, J., Ogawa, Y., Nakamura, R., Yokota, Y., Morota, T., Honda, C., Torri, M., Abe, M., Nimura, T., Hiroi, T., Arai, T., Saiki, K., Takeda, H., Hirata, N., Kodama, S., Sugihara, T., Demura, H., Asada, N., Terazono, J. & Otake, H., 2008. Discoveries on the lithology of lunar crater central peaks by SELENE Spectral Profiler. *Geophysical Research Letters*, 35, L23201, doi: 10.1029/2008GL035868.

Matsunaga, T., Ohtake, M., Hirahara, Y. & Haruyama, J., 2001. Development of a visible and near infrared spectrometer for Selenological and Engineering Explorer (SELENE). *Proceedings of SPIE,* 4151, 32-39.

McCauley, J.F., 1967. Geologic map of the Hevelius region of the Moon. *USGS*, I-491.

McEwen, A.S., Gaddis, L.R., Neukum, G., Hoffman, H., Pieters, C.M. & Head, J.W., 1993. Galileo observations of post-Imbrium lunar craters during the first Earth-Moon flyby. *Journal of Geophysical Research*, 98 (E9), 17,207-17,231.

McKay, D.S., Bogard, D.D., Morris, R.V., Korotev, R.L., Johnson, P. & Wentworth, S.J., 1986. Apollo 16 regolith breccias: characterization and evidence for early formation in the mega-regolith. *Proceedings of the Lunar and Planetary Science Conference XVI, Journal of Geophysical Research*, 91 (B4), D277-D303.

McKay, D.S., Bogard, D.D., Morris, R.V., Korotev, R.L., Wentworth, S.J. & Johnson, P., 1989. Apollo 15 regolith breccias: window to a KREEP regolith. *Proceedings of the Lunar and Planetary Science Conference IXX*, 19-41.

McKay, D.S., Carter, J.L., Boles, W.W., Allen, C.C. & Allton, J.H., 1994. JSC-1: a new lunar soil simulant. *Engineering, Construction, and Operation in Space IV.* American Society of Civil Engineers, 857-866.

McKay, D.S., Fruland, R.M. & Heiken, G.H., 1974. Grain size and the evolution of lunar soils. *Proceedings of the Lunar Science Conference V, Geochimica et Cosmochimica Acta* (supplement 5), 1, 887-906.

McKay, D.S., Heiken, G., Basu, A., Blanford, G., Simon, S., Reedy, R., French, B.M. & Papike, J., 1991. The lunar regolith. In: Heiken, G.H., Vaniman, D.T. & French, B.M. (Eds.) *Lunar Sourcebook: a user's guide to the moon*, Cambridge University Press, 285-356.

Melendrez, D.E., Johnson, J.R., Larson, S.M. & Singer, R.B., 1994. Remote sensing of potential lunar resources 2. high spatial resolution mapping of spectral reflectance ratios and implications for nearside mare TiO_2 content. *Journal of Geophysical Research*, 99 (E3), 5601-5619.

Melosh, H.J., 1989. *Impact cratering: a geologic process*. Oxford University Press.

Melosh, H.J., 1990. Giant impacts and the thermal state of the early Earth. In Newsom, H.E. & Jones, J.H. (Eds.) *Origin of the Earth*, Oxford University Press, 69-83.

Melosh, H.J., 2009. An isotopic crisis for the giant impact origin of the Moon? *72nd Meteoritical Society Meeting*, abstract #5104.

Metzger, A.E., 1993. Composition of the Moon as determined from orbit by gamma ray spectroscopy. In: Pieters, C.M. & Englert, P.A.J. (Eds.) *Remote geochemical analysis: elemental and mineralogical composition*, Cambridge University Press, 341-365.

Metzger, A.E. & Parker, R.E., 1979. The distribution of titanium on the lunar surface. *Earth and Planetary Science Letters*, 45, 155-171.

Moore, H.J., Hodges, C.A. & Scott, D.H., 1974. Multiringed basins – illustrated by Orientale and associated features. *Proceedings of the Lunar Science Conference V*, 1, 71-100.

Morris, R.V., 1976. Surface exposure indices of lunar soils: a comparative FMR study. *Proceedings of the Lunar and Planetary Science Conference VII*, 315-335.

Morris, R.V., 1978. *In situ* reworking (gardening) of the lunar surface: evidence from the Apollo cores. *Proceedings of the Lunar and Planetary Science Conference IX*, 1801-1811.

Morris, R.V., Score, R., Dardano, C. & Heiken, G., 1983. *Handbook of lunar soils*, JSC 19069, NASA Johnson Space Center, Houston.

Namiki, N., Iwata, T., Matsumoto, K., Hanada, H., Noda, H., Goossens, S., Ogawa, M., Kawano, N., Asari, K., Tsuruta, S.-I., Ishihara, Y., Liu, Q., Kikuchi, F., Ishikawa, T., Sasaki, S., Aoshima, C., Kurosawa, K., Sugita, S. & Takano, T., 2009. Farside gravity field of the Moon from four-way doppler measurements of SELENE (Kaguya). *Science*, 323, 900-905.

Näränen, J., Carpenter, J., Parviainen, H., Muinonen, K., Fraser, G., Peura, M. & Kallonen, A., 2009. Regolith effects in planetary X-ray fluorescence spectroscopy: laboratory studies at 1.7-6.4 keV. *Advances in Space Research*, 44, 313-322.

Näränen, J., Parviainen, H., Muinonen, K., Carpenter, J., Nygård, K. & Peura, M., 2008. Laboratory studies into the effect of regolith on planetary X-ray fluorescence spectroscopy. *Icarus*, 198, 408-419.

Narendranath, S., Athiray, P.S., Sreekumar, P., Kellett, B.J., Alha, L., Howe, C.J., Joy, K.H., Grande, M., Huovelin, J., Crawford, I.A., Unnikrishnan, U., Lalita, S., Subramaniam, S., Weider, S.Z., Nittler, L.R., Gasnault, O., Rothery, D., Fernandes, V.A., Bhandari, N., Goswami, J.N., Wieczorek, M.A. & the C1XS team, forthcoming. Lunar X-ray fluorescence observations by the Chandrayaan-1 X-ray Spectrometer (C1XS): results from a lunar highland region.

Narendranath, S., Sreekumar, P., Maddison, B.J., Howe, C.J., Kellett, B.J., Wallner, M., Erd, C. & Weider, S.Z., 2010. Calibration of the C1XS instrument on Chandrayaan-1. *Nuclear Instruments and Methods in Physical Research A*, 621, 344-353.

National Research Council, 2007. *The scientific context for exploration of the Moon: final report*, The National Academies Press, Washington D.C.

Neal, C.R. & Taylor, L.A., 1992. Petrogenesis of mare basalts: a record of lunar volcanism. *Geochimica et Cosmochimica Acta*, 56, 2177-2211.

Nemchin, A., Timms, H., Pidgeon, R., Geisler, T., Reddy, S. & Meyer, C., 2009. Timing of crystallization of the lunar magma ocean constrained by the oldest zircon. *Nature Geoscience*, 2, 133-136.

Neukum, G. & Ivanov, B.A., 1994. Crater size distributions and impact probabilities on Earth from lunar, terrestrial-planet, and asteroid cratering data. In Gehrels, T., Matthews, M.S. & Schumman, A. (Eds.) *Hazards due to comets and asteroids*, University of Arizona Press.

Nicholis, M.G. & Rutherford, M.J., 2005. Pressure dependence of graphite-C-O phase equilibria and its role in lunar mare volcanism. *Lunar and Planetary Science Conference XXXVI*, abstract #1726.

Nittler, LR., Starr, R.D., Lim, L., McCoy, T.J., Burbine, T.H., Reedy, R.C., Trombka, J.I., Gorenstein, P., Squyres, S.W., Boynton, W.V., McClanahan, T.P., Bhangoo, J.S., Clark, P.E., Murphy, M.E. & Killen, R., 2001. X-ray fluorescence measurements of the surface elemental composition of asteroid 433 Eros. *Meteoritics and Planetary Science*, 36, 1673-1695.

Norman, M.D., Borg, L.E., Nyquist, L.E. & Bogard, D.D., 2003. Chronology, geochemistry, and petrology of a ferroan noritic anorthosite clast from Descartes breccia 67215: clues to the age, origin, structure, and impact history of the lunar crust. *Meteoritics and Planetary Science*, 38, 645-661.

Nozette, S., Lichtenberg, C.L., Spudis, P., Bonner, R., Ort, W., Malaret, E., Robinson, M. & Shoemaker, E.M., 1996. The Clementine bistatic radar experiment. *Science*, 274, 1495-1498.

Nozette, S., Rustan, P., Pleasance, L.P., Horan, D.M., Regeon, P., Shoemaker, E.M., Spudis, P.D., Acton, C.H., Baker, D.N., Blamont, J.E., Buratti, B.J., Corson, M.P., Davies, M.E., Duxbury, T.C., Eliason, E.M., Jakosky, B.M., Kordas, J.F., Lewis, I.T., Lichtenberg, C.L., Lucey, P.G., Malaret, E., Massie, M.A., Resnick, J.H., Rollins, C.J., Park, H.S.,

McEwen, A.S., Priest, R.E., Pieters, C.M., Reisse, R.A., Robinson, M.S., Simpson, R.A., Smith, D.E., Sorenson, T.C., Vorder Breugge, R.W. & Zuber, M.T., 1994. The Clementine mission to the Moon: scientific overview. *Science*, 266, 1835-1839.

Nyquist, L.E. & Shih, C.-Y., 1992. The isotopic record of lunar volcanism. *Geochimica et Cosmochimica Acta*, 56, 2213-2234.

Oberbeck, V.R., Morrison, R.H., Hörz, F., Quaide, W.L. & Gault, D.E., 1974. Smooth plains and continuous deposits of craters and basins. *Proceedings of the Lunar Science Conference V*, 1, 111-136.

Ohtake, M., Haruyama, J., Matsunaga, T., Yokota, Y., Morota, T., Honda, C. & LISM Team, 2008. Performance and scientific objectives of the SELENE (Kaguya) Multiband Imager. *Earth Planets Space*, 60, 257-264.

Ohtake, M., Matsunaga, T., Haruyama, J., Yokota, Y., Morota, T., Honda, C., Ogawa, Y., Torii, M., Miyamoto, H., Arai, T., Hirata, N., Iwasaki, A., Nakamura, R., Hiroi, T., Sugihara, T., Takeda, H., Otake, H, Pieters, C.M., Saiki, K., Kitazato, K., Abe, M., Asada, N., Demura, H., Yamaguchi, Y., Sasaki, S., Kodama, S., Terazono, J., Shirao, M., Yamaji, A., Minami, S., Akiyama, H. & Josset, J.-L., 2009. The global distribution of pure anorthosite on the Moon. *Nature*, 461, 236-241.

Okada, T., 2002. Surface elemental composition of Asteroid 433 Eros: discussions on the results of the NEAR/XGRS. *Proceedings of the 35th ISAS Lunar Planetary Symposium*, 120-123.

Okada, T., 2004. Particle size effect in X-ray fluorescence at a large phase angle: importance of elemental analysis of asteroid Eros (433). *Proceedings of the Lunar and Planetary Science Conference XXXV*, abstract #1927.

Okada, T., Shirai, K., Yamamoto, Y., Arai, T., Ogawa, K., Hosono, K. & Kato, M., 2006. X-ray fluorescence spectrometry of asteroid Itokawa by Hayabusa. *Science*, 312, 1338-1341.

Okada, T., Shirai, K., Yamamoto, Y., Arai, T., Ogawa, K., Shiraishi, H. & Iwasaki, M., 2008. X-ray fluorescence experiments on the SELENE (Kaguya) Spacecraft. *Lunar and Planetary Science Conference XXXIX*, abstract #1960.

Ono, T., Kumamoto, A., Nakagawa, H., Yamaguchi, Y., Oshigami, S., Yamaji, A., Kobayashi, T., Kasahara, Y. & Oya, H., 2009. Lunar radar sounder observations of subsurface layers under the nearside maria of the Moon. *Science*, 323, 909-912.

Ortiz, J.L., Sada, P.V., Bellot Rubio, L.R., Aceituno, F.J., Aceituno, J., Gutiérrez, P.J. & Thiele, U., 2000. Optical detection of meteoroidal impacts on the Moon. *Nature*, 405, 921-923.

Oshigami, S., Yamaguchi, Y., Yamaji, A., Ono, T., Kumamoto, A., Kobayahsi, T. & Nakagawa, H., 2009. Distribution of the subsurface reflectors of the western nearside maria observed from Kaguya with Lunar Radar Sounder. *Geophysical Research Letters*, 36, L18202.

Owens, A., Beckhoff, B., Fraser, G., Kolbe, M., Krumrey, M., Mantero., A., Mantler, M., Peacock, A., Pia, M.G., Pullan, D., Schneider, U.G. & Ulm, G., 2008. Measuring and interpreting X-ray fluorescence from planetary surfaces. *Analytical Chemistry*, 80, 8398-8405.

Pahlevan, K. & Stevenson, D.J., 2009. Chemical fractionation after the Moon-forming giant impact. *Lunar and Planetary Science Conference XL*, abstract #2392.

Paige, D.A., Foote, M.C., Greenhagen, B.T., Schofield, J.T., Calcutt, S., Vasavada, A.R., Preston, D.J., Taylor, F.W., Allen, C.C., Snook, K.J., Jakosky, B.M., Murray, B.C., Soderblom, L.A., Jau, B., Loring, S., Bulharowski, J., Bowles, N.E., Thomas, I.R.,

Sullivan, M.T., Avis, C., De Jong, E.M., Hartford, W. & McCleese, D.J., 2009. The Lunar Reconnaissance Orbiter Diviner Lunar Radiometer experiment. *Space Science Reviews*, 150, 125-160.

Papike, J.J., Ryder, G. & Shearer, C.K., 1998. Lunar samples. *Reviews in Mineralogy*, 36, 5.1-5.234.

Parmentier, E.M., Zhong, S. & Zuber, M.T., 2000. On the relationship between chemical differentiation and the origin of lunar asymmetries. *Proceedings of the Lunar and Planetary Science Conference XXXI*, abstract #1614.

Parry, S.J., 1997. Neutron activation analysis. In: Gill, R. (Ed.) *Modern Analytical Geochemistry*, Addison Wesley Longman Ltd.

Pieters, C.M., 1978. Mare basalt types on the front side of the moon: a summary of spectral reflectance data. *Proceedings of the Lunar and Planetary Science Conference IX*, 2825-2849.

Pieters, C.M., 1986. Composition of the lunar highland crust from near-infrared spectroscopy. *Reviews of Geophysics*, 24, 557-578.

Pieters, C.M., Boardman, J., Buratti, B., Chatterjee, A., Clark, R., Glavich, T., Green, R., Head, J., III, Isaacson, P., Malaret, E., McCord, T., Mustard, J., Petro, N., Runyon, C., Staid, M., Sunshine, J., Taylor, L., Tompkins, S., Varanasi, P. & White, M., 2009a. The Moon Mineralogy Mapper (M^3) on Chandrayaan-1. *Current Science*, 96, 500-505.

Pieters, C.M., Boardman, J., Buratti, B., Clark, R., Combe, J.-P., Green, R., Goswami, J.N., Head, J.W., III., Hicks, M., Isaacson, P., Klima, R., Kramer, G., Kumar, S., Lundeen, S., Malaret, E., McCord, T.B., Mustard, J., Nettles, J., Petro, N., Runyon, C., Staid, M., Sunshine, J., Taylor, L., Tompkins, S. & Varanasi, P., 2009b. Mineralogy of the lunar crust in spatial context: first results from the Moon Mineralogy Mapper (M^3). *Lunar and Planetary Science Conference XL*, abstract #2052.

Pieters, C.M., Fischer, E.M., Rode, O. & Basu, A., 1993b. Optical effects of space weathering: the role of the finest fraction. *Journal of Geophysical Research*, 98 (E11), 20,817-20,824.

Pieters, C.M., Goswami, J.N., Clark, R.N., Annadurai, M., Boardman, J., Buratti, B., Combe, J.-P., Dyar, M.D., Green, R., Head, J.W., Hibbitts, C., Hicks, M., Isaacson, P., Klima, R., Kramer, G., Kumar, S., Livo, E., Lundeen, S., Malaret, E., McCord, T., Mustard, J., Nettles, J., Petro, N., Runyon, C., Staid, M., Sunshine, J., Taylor, L.A., Tompkins, S. & Varanasi, P., 2009c. Character and spatial distribution of OH/H_2O on the surface of the Moon seen by M^3 on Chandrayaan-1. *Science*, 326, 568-572.

Pieters, C.M., Head, J.W., III., Gaddis, L., Jolliff, B. & Duke, M., 2001. Rock types of South Pole-Aitken basin and extent of basaltic volcanism. *Journal of Geophysical Research*, 106 (E11), 28,001-28,022.

Pieters, C.M., Head, J.W., Sunshine, J.M., Fischer, E.M., Murchie, S.L., Belton, M., McEwen, A., Gaddis, L., Greeley, R., Neukum, G., Jaumann, R. & Hoffman, H., 1993a. Crustal diversity of Moon: compositional analysis of Galileo solid state imaging data. *Journal of Geophysical Research*, 98 (E9), 17,127-17,148.

Pieters, C., Shkuratov, Y., Kaydash, V., Stankevich, D. & Taylor, L., 2006. Lunar soil characterization consortium analyses: pyroxene and maturity estimates derived from Clementine image data. *Icarus*, 184, 83-101.

Pike, R.J., 1974. Depth/diameter relations of fresh lunar craters: revision from spacecraft data. *Geophysical Research Letters*, 1, 291-294.

Pike, R.J., 1977. Size-dependence in the shape of fresh impact craters on the moon. In: *Impact and explosion cratering: planetary and terrestrial implications, Proceedings of the Symposium on Planetary Cratering Mechanics*, Pergamon Press, 489-509.

Pommerol, A., Kofman, W., Audouard, J., Grima, C., Beck, P., Mouginot, J., Herique, A., Kumamoto, A., Kobayashi, T. & Ono, T., 2010. Detectability of subsurface interfaces in lunar maria by the LRS/SELENE sounding radar: influence of mineralogical composition. *Geophysical Research Letters*, 37, L03201.

Prettyman, T.H., Hagerty, J.J., Elphic, R.C., Feldman, W.C., Lawrence, D.J., McKinney, G.W. & Vaniman, D.T., 2006. Elemental composition of the lunar surface: analysis of gamma ray spectroscopy data from Lunar Prospector. *Journal of Geophysical Research*, 111, E12007, doi: 10.1029/2005JE002656.

Racca, G.D., Marini, A., Stagnaro, L., van Dooren, J., di Napoli, L., Foing, B.H., Lumb, R., Volp, J., Brinkmann, J., Grünagel, R., Estublier, D., Tremolizzo, E., McKay, M., Camino, O., Schoemaekers, J., Hechler, M., Khan, M., Rathsman, P., Andersson, G., Anflo, K., Berge, S., Bodin, P., Edfors, A., Hussain, A., Kugelberg, J., Larsson, N., Ljung, B., Meijer, L., Mörtsell, A., Nordebäck, T., Persson, S. & Sjöberg, F., 2002. SMART-1 mission description and development status. *Planetary and Space Science*, 50, 1323-1337.

Rajmon, D. & Spudis, P., 2004. Distribution and stratigraphy of basaltic units in Maria Tranquillitatis and Fecunditatis: a Clementine perspective. *Meteoritics and Planetary Science*, 39, 1699-1720.

Rhodes, J.M. & Blanchard, D.P., 1981. Apollo 11 breccias and soils: aluminous mare basalts or multi-component mixtures? *Proceedings of the Lunar and Planetary Science Conference XII*, 607-620.

Rickman, D., 2007. Characterization summary of JSC-1A bulk lunar mare regolith simulant (draft). http://www.orbitec.com/store/JSC-1A_Bulk_data_Characterization.pdf.

Righter, K., 2010. The lunar meteorite compendium, NASA, http://curator.jsc.nasa.gov/antmet/lmc/index.cfm.

Riner, M.A., Robinson, M.S., Eckart, J.M. & Desch, S.J., 2008. Global survey of color variations on 433 Eros: implications for regolith processes and asteroid environments. *Icarus*, 198, 67-76.

Ringwood, A.E. & Kesson, S.E., 1976. A dynamic model for mare basalt petrogenesis. *Proceedings of the Lunar Science Conference VII*, 1697-1722.

Robinson, M., McEwen, A., Eliason, E., Jolliff, B., Hiesinger, H., Malin, M., Thomas, P., Turtle, E & Brylow, S., 2006. NASA's Lunar Reconnaissance Orbiter Cameras (LROC). *36th COSPAR Scientific Assembly*.

Röntgen, W.C., 1896. On a new kind of rays. *Nature*, 53, 274-276.

Russell, C.T., Luhmann, J.G. & Jian, L.K., 2010. How unprecedented a solar minimum? *Reviews of Geophysics*, 48, RG2004.

Ryder, G., 1976. Lunar sample 15405: remnant of a KREEP basalt-granite differentiated pluton. *Earth and Planetary Science Letters*, 29, 255-268.

Ryder, G., 1987. Petrographic evidence for nonlinear cooling rates and a volcanic origin for Apollo 15 KREEP basalts. *Proceedings of the Lunar and Planetary Science Conference XVII, Journal of Geophysical Research*, 92 (B4), E331-E339.

Ryder, G., Stoeser, D.B. & Wood, J.A., 1977. Apollo 17 KREEPy basalt: a rock type intermediate between mare and KREEP basalts. *Earth and Planetary Science Letters*, 35, 1-13.

Saito, J., Miyamoto, H., Nakamura, R., Ishiguro, M., Michikami, T., Nakamura, A.M., Demura, H., Sasaki, S., Hirata, N., Honda, C., Yamamoto, A., Yokota, Y., Fuse, T., Yoshida, F., Tholen, D.J., Gaskell, R.W., Hashimoto, T., Kubota, T., Higuchi, Y., Nakamura, T., Smith, P., Hiraoka, K., Honda, T., Kobayashi, S., Furuya, M., Matsumoto,

N., Nemoto, E., Ykishita, A., Kitazato, K., Dermawan, B., Sogame, A., Terazono, J., Shinohara, C. & Akiyama, H., 2006. *Science*, 312, 1341-1344.

Schlemm, C.E., II., Starr, R.D., Ho, G.C., Bechtold, K.E., Hamilton, S.A., Boldt, J.D., Boynton, W.V., Bradley, W., Fraeman, M.E., Gold, R.E., Goldsten, J.O., Hayes, J.R., Jaskulek, S.E., Rossano, E., Rumpf, R.A., Schaefer, E.D., Strohbehn, K., Shelton, R.G., Thompson, R.E., Trombka, J.I. & Williams, B.D., 2007. The X-ray Spectrometer on the MESSENGER spacecraft. *Space Science Reviews*, 131, 393-415.

Scott, D.H., McCauley, J.F. & West, M.N., 1977. Geologic map of the west side of the Moon. *USGS*, I-1034.

Shearer, C.K., Hess, P.C., Wieczorek, M.A., Pritchard, M.E., Parmentier, E.M., Borg, L.E., Longhi, J., Elkins-Tanton, L.T., Neal, C.R., Antonenko, I., Canup, R.M., Halliday, A.N., Grove, T.L., Hager, B.H., Lee, D.-C. & Wiechert, U., 2006. Thermal and magmatic evolution of the Moon. *Reviews in Mineralogy and Geochemistry*, 60, 365-518.

Shearer, C.K. & Papike, J.J., 1993. Basaltic magmatism on the Moon: a perspective from volcanic picritic glass beads. *Geochimica et Cosmochimica Acta*, 57, 4785-4812.

Shearer, C.K. & Papike, J.J., 1999. Magmatic evolution of the Moon. *American Mineralogist*, 84, 1469-1494.

Shearer, C.K. & Newsom, H.E., 2000. W-Hf isotope abundances and the early origin and evolution of the Earth-Moon system. *Geochimica et Cosmochimica Acta*, 64, 3599-3613.

Shervais, J.W. & McGee, J.J., 1998. Ion and electron microprobe study of troctolites, norite, and anorthosites from Apollo 14: evidence for urKREEP assimilation during petrogenesis of Apollo 14 Mg-suite rocks. *Geochimica et Cosmochimica Acta*, 62, 3009-3023.

Shih, C.-Y., Nyquist, L.E., Bansal, B.M. & Wiesmann, H., 1992. Rb-Sr and Sm-Nd chronology of an Apollo 17 KREEP basalt. *Earth and Planetary Science Letters*, 108, 203-215.

Shih, C.-Y., Nyquist, L.E., Dasch, E.J., Bogard, D.D., Bansal, B.M. & Wiesmann, H., 1993. Ages of pristine noritic clasts from lunar breccias 15455 and 15455. *Geochimica et Cosmochimica Acta*, 57, 915-931.

Simon, S.B., Papike, J.J., Gosselin, D.C. & Laul, J.C., 1985. Petrology and chemistry of Apollo 12 regolith breccias. *Proceedings of the Lunar and Planetary Science Conference XVI, Journal of Geophysical Research*, 90, D75-D86.

Smith, D.R. & Gow, J., 2009. The effect of protons on the performance of swept-charge devices. *Nuclear Instruments and Methods in Physical Research A*, 604, 177-179.

Smith, D.R., Gow, J. & Holland, A.D., 2007. Proton irradiation of swept-charge devices for the Chandrayaan-1 X-ray Spectrometer (C1XS). *Nuclear Instruments and Methods in Physics Research A*, 583, 270-277.

Snyder, G.A., Borg, L.E., Nyquist, L.E. & Taylor, L.A., 2000. Chronology and isotopic constraints on lunar evolution. In: Canup, R.M. & Righter, K. (Eds.) *Origin of the Earth and Moon*, University of Arizona Press, 361-395.

Snyder, G.A., Neal, C.R., Taylor, L.A. & Halliday, A.N., 1995a. Processes involved in the formation of magnesian-suite plutonic rocks from the highlands of the Earth's Moon. *Journal of Geophysical Research*, 100 (E5), 9365-9388.

Snyder, G.A., Taylor, L.A. & Halliday, A.N., 1995b. Chronology and petrogenesis of the lunar highlands alkali suite: cumulates from KREEP basalt crystallization. *Geochimica et Cosmochimica Acta*, 59, 1185-1203.

Solomon, S.C. & Head, J.W., 1980. Lunar mascon basins: lava filling, tectonics, and evolution of the lithosphere, *Reviews of Geophysics and Space Physics*, 18, 107-141.

Solomon, S.C. & Longhi, J., 1977. Magma oceanography: 1. Thermal evolution. *Proceedings of the Lunar Science Conference VIII*, 583-599.

Spudis, P.D., 1996. *The once and future moon*. Smithsonian Institution Press, Washington.

Spudis, P., Nozette, S., Bussey, B., Raney, K., Winters, H., Lichtenberg, C.L., Marinelli, W., Crusan, J.C. & Gates, M.M., 2009. Mini-SAR: an imaging radar experiment for the Chandrayaan-1 mission to the Moon. *Current Science*, 96, 533-539.

Spudis, P. & Pieters, C., 1991. Global and regional data about the Moon. In: Heiken, G.H., Vaniman, D.T. & French, B.M. (Eds.) *Lunar Sourcebook: a user's guide to the moon*, Cambridge University Press, 595-632.

Spudis, P.D., Reisse, R.A. & Gillis, J.J., 1994. Ancient multiring basins on the Moon revealed by Clementine laser altimetry. *Science*, 266, 1848-1851.

Stacy, N.J.S., Campbell, D.B. & Ford, P.G., 1997. Arecibo radar mapping of the lunar poles: a search for ice deposits. *Science*, 276, 1527-1530.

Staid, M.I. & Pieters, C.M., 2000. Integrated spectral analysis of mare soils and craters: application to eastern nearside basalts. *Icarus*, 145, 122-139.

Staid, M.I. & Pieters, C.M., 2001. Mineralogy of the last lunar basalts: results from Clementine. *Journal of Geophysical Research*, 106 (E11), 27,887-27,900.

Staid, M.I., Pieters, C.M., Boardman, J., Head, J.W., Sunshine, J., Taylor, L.A., Isaacson, P., Besse, S., Klima, R., Kramer, G. & Dhingra, D., 2010. Regional and temporal variations in the western mare basalts: new observations from the Moon Mineralogy Mapper. *Proceedings of the Lunar and Planetary Science Conference XLI*, abstract #2002.

Starr, R., Clark, P.E., Murphy, M.E., Floyd, S.R., McClanahan, T.P., Nittler, L.R., Trombka, J.I., Evans, L.G., Boynton, W.V., Bailey, S.H., Bhangoo, J., Mikheeva, I., Brückner, J., Squyres, S.W., McCartney, E.M., Goldsten, J.O. & McNutt, R.L., Jr., 2000. Instrument calibrations and data analysis procedures for the NEAR X-ray spectrometer. *Icarus*, 147, 498-519.

Stöffler, D., Knöll, H.D., Marvin, U.B., Simonds, C.H. & Warren, P.H., 1980. Recommended classification and nomenclature of lunar highland rocks – a committee report. *Proceedings of the Conference on the Lunar Highlands Crust*.

Stöffler, D. & Ryder, G., 2001. Stratigraphy and isotope ages of lunar geologic units: chronological standard for the inner solar system. *Space Science Reviews*, 96, 9-54.

Stöffler, D., Ryder, G., Ivanov, B.A., Artemieva, N.A., Cintala, M.J. & Grieve, R.A.F., 2006. Cratering history and lunar chronology. *Reviews in Mineralogy and Geochemistry*, 60, 519-596.

Strüder, L., Lutz, G., Lechner, P., Soltau, H. & Holl, P., 2004. X-ray detectors. In: Tsuji, K., Injuk, J. & Van Grieken, R. (Eds.) *X-ray spectrometry: recent technological advances*, John Wiley & Sons Ltd, 134-275.

Suggs, R.M., Cooke, W.J., Suggs, R.J., Swift, W.R. & Hollon, N., 2008. The NASA lunar impact monitoring program. *Earth Moon Planet*, 102, 293-298.

Sunshine, J.M., Farnham, T.L., Feaga, L.M., Groussin, O., Merlin, F., Milliken, R.E. & A'Hearn, M.F., 2009. Temporal and spatial variability of lunar hydration as observed by the deep impact spacecraft. *Science*, 326, 565-568.

Swinyard, B.M., Joy, K.H., Kellett, B.J., Crawford, I.A., Grande, M., Howe, C.J., Fernandes, V.A., Gasnault, O., Lawrence, D.J., Russell, S.S., Wieczorek, M.A., Foing, B.H. & The SMART-1 team, 2009. X-ray fluorescence observations of the Moon by

SMART-1/D-CIXS and the first detection of Ti Kα from the lunar surface. *Planetary and Space Science*, 57, 744-750.

Swinyard, B., Kellett, B., Weider, S., Joy, K., Crawford, I. & The C1XS Team, 2010. C1XS spectral analysis method. *Proceedings of the X-ray Fluorescence Spectroscopy in Planetary Remote Sensing Workshop*, ESA SP-687.

Tandberg-Hanssen, E. & Emslie, A., 1988. *The physics of solar flares*, Cambridge University Press.

Taylor, G.J., Warren, P., Ryder, G., Delano, J., Pieters, C. & Lofgren, G., 1991. Lunar rocks. In: Heiken, G.H., Vaniman, D.T. & French, B.M. (Eds.) *Lunar sourcebook: a user's guide to the moon*, Cambridge University Press, 183-284.

Taylor, S.R., 1975. *Lunar Science: a post Apollo view*, Pergamon.

Taylor, S.R., 1982. *Planetary science: a lunar perspective*. Lunar and Planetary Institute, Houston, TX.

Terada, K., Anand, M., Sokol, A.K., Bischoff, A. & Sano, Y., 2007. Cryptomare magmatism 4.35 Gyr ago recorded in lunar meteorite Kalahari 009. *Nature*, 450, 849-853.

Tompkins, S. & Pieters, C.M., 1999. Mineralogy of the lunar crust: results from Clementine. *Meteoritics and Planetary Science*, 34, 25-41.

Tonks, W.B. & Melosh, H.J., 1990. The physics of crystal settling and suspension in a turbulent magma ocean. *Proceedings of the Conference on the Origin of the Earth*, 151-174.

Touboul, M., Kleine, T., Bourdon, B., Palme, H. & Wieler, R., 2007. Late formation and prolonged differentiation of the Moon inferred from W isotopes in lunar metals. *Nature*, 450, 1206-1209.

Touma, J. & Wisdom, J., 1994. Evolution of the Earth-Moon system. *The Astronomical Journal*, 108, 1943-1961.

Treis, J., Andricek, L., Aschauer, F., Heinzinger, K., Herrman, S., Hilchenbach, M., Lauf, T., Lechner, P., Lutz, G., Majewski, P., Porro, M., Richter, R.H., Schaller, G., Schnecke, M., Schopper, F., Soltau, H., Stefanescu, A., Strüder, L. & de Vita, G., 2010. MIXS on BepiColombo and its DEPFET based focal plane instrumentation. *Nuclear Instruments and Methods in Physics Research A*, 624, 540-547.

Vaniman, D., Dietrich, J., Taylor, G.J. & Heiken, G., 1991. Exploration, samples, and recent concepts of the Moon. In: Heiken, G.H., Vaniman, D.T. & French, B.M. (Eds.) *Lunar Sourcebook: a user's guide to the moon*, Cambridge University Press, 5-26.

Walker, D., 1983. Lunar and terrestrial crust formation. *Proceedings of the Lunar and Planetary Science Conference XIV, Journal of Geophysical Research*, 88 (supplement), B17-B25.

Warner, J.L., Simonds, C.H. & Phinney, W.C., 1976. Genetic distinction between anorthosites and Mg-rich plutonic rocks. *Proceedings of the Lunar and Planetary Science Conference VII*, 915-917.

Warren, P.H., 1985. The magma ocean concept and lunar evolution. *Annual Review of Earth and Planetary Sciences*, 13, 201-240.

Warren, P.H., 1988. The origin of pristine KREEP: effects of mixing between urKREEP and the magmas parental to the Mg-rich cumulates. *Proceedings of the Lunar and Planetary Science Conference XVIII*, 233-241.

Warren, P.H., 1990. Lunar anorthosites and the magma-ocean plagioclase-flotation hypothesis: importance of FeO enrichment in the parent magma. *American Mineralogist*, 75, 46-58.

Warren, P.H., 1993. A concise compilation of petrologic information on possibly pristine nonmare Moon rocks. *American Mineralogist*, 78, 360-376.

Warren, P.H., 2005. "New" lunar meteorites: implications for composition of the global lunar surface, lunar crust, and the bulk Moon. *Meteoritics and Planetary Science*, 40, 477-506.

Warren, P.H., Jerde, E.A. & Kallemeyn, G.W., 1991. Pristine Moon rocks: Apollo 17 anorthosites. *Proceedings of the Lunar and Planetary Science Conference XXI*, 51-61.

Warren, P.H. & Wasson, J.T., 1977. Pristine nonmare rocks and the nature of the lunar crust. *Proceedings of the Lunar Science Conference XIII*, 2215-2235.

Warren, P.H. & Wasson, J.T., 1978. Compositional petrographic investigation of pristine nonmare rocks. *Proceedings of the Lunar and Planetary Conference IX*, 185-217.

Warren, P.H. & Wasson, J.T., 1979. The origin of KREEP. *Reviews of Geophysics and Space Physics*, 17, 73-88.

Warren, P.H. & Wasson, J.T., 1980. Early lunar petrogenesis, oceanic and extraoceanic. *Proceedings of the conference on the lunar highlands crust*, 81-99, Pergamon.

Weidenschilling, S.J., Greenberg, R., Chapman, C.R., Herbert, F., Davis, D.R., Drake, M.J., Jones, J. & Hartmann, W.K., 1986. Origin of the Moon from a circumterrestrial disk. *Proceedings of the Conference on the Origin of the Moon, Kona, HI*, 731-762.

Weider, S.Z., Crawford, I.A., Joy, K.H., 2010. Individual lava flow thicknesses in Oceanus Procellarum and Mare Serenitatis determined from Clementine multispectral data. *Icarus*, 209, 323-336.

Weider, S.Z., Swinyard, B.M., Kellett, B.J., Howe, C.J., Joy, K.H., Crawford, I.A., Gow, J. & Smith, D.R., in review 2010. Planetary X-ray fluorescence analogue laboratory

experiments and an elemental abundance algorithm for C1XS. *Submitted to Planetary and Space Science*.

Weitz, C.M. & Head, J.W., III, 1999. Spectral properties of the Marius Hills volcanic complex and implications for the formation of lunar domes and cones. *Journal of Geophysical Research*, 104 (E8), 18,933-18,956.

Wetherill, G.W., 1990. Formation of the Earth. *Annual Review of Earth and Planetary Sciences*, 18, 205-256.

Whitford-Stark, J.L. & Head, J.W., 1977. The Procellarum volcanic complexes: contrasting styles of volcanism. *Proceedings of the Lunar Science Conference VIII*, 2705-2724.

Wiechert, U., Halliday, A.N., Lee, D.-C., Snyder, G.A., Taylor, L.A. & Rumble, D., 2001. Oxygen isotopes and the Moon-forming giant impact. *Science*, 294, 345-348.

Wieczorek, M.A., Jolliff, B.L., Khan, A., Pritchard, M.E., Weiss, B.P., Williams, J.G., Hood, L.L., Righter, K., Neal, C.R., Shearer, C.K., McCallum, I.S., Tompkins, S., Hawke, B.R., Peterson, C., Gillis, J.J. & Bussey, B., 2006. The constitution and structure of the lunar interior. *Reviews in Mineralogy and Geochemistry*, 60, 221-364.

Wieczorek, M.A. & Phillips, R.J., 2000. The "Procellarum KREEP Terrane": implications for mare volcanism and lunar evolution. *Journal of Geophysical Research*, 105 (E8), 20,417-20,430.

Wieler, R., Kehm, K., Meshik, A.P. & Hohenberg, C.M., 1996. Secular changes in the xenon and krypton abundances in the solar wind recorded in single lunar grains. *Nature*, 384, 46-49.

Wilcox, B.B., Lucey, P.G. & Gillis, J.J., 2005. Mapping iron in the lunar mare: an improved approach. *Journal of Geophysical Research*, 110, E11001, doi: 10.1029/2005JE002512.

Wilhelms, D.E., 1993. *To a rocky Moon: a geologist's history of lunar exploration*. University of Arizona Press.

Wilhelms, D.E. & McCauley, J.F., 1971. Geologic map of the nearside of the Moon, USGS, I-703.

Wilhelms, D.E., McCauley, J.F. & Trask, N.J., 1987. *The Geologic History of the Moon*, U.S. Geological Survey, Washington D.C.

Williams, K.K. & Zuber, M.T., 1998. Measurement and analysis of lunar basin depths from Clementine altimetry. *Icarus*, 131, 107-122.

Wilson, L. & Head, J.W., 2001. Ascent and eruption of mare basalts on the Moon. *Proceedings of the Lunar and Planetary Science Conference XXXII*, abstract #1297.

Wöhler, C., Berezhnoy, A. & Evans, R., 2011. Estimation of elemental abundances of the lunar regolith using Clementine UVVIS+NIR data, *Planetary and Space Science*, 59, 92-110.

Wood, J.A., 1986. Moon over Mauna Loa: a review of hypotheses of formation of Earth's Moon. In: Hartmann, W.K., Phillips, R.J. & Taylor, G.J. (Eds.) *Origin of the Moon*, Lunar and Planetary Institute, Houston, 17-55.

Wood, J.A., Dickey, J.S., Jr., Marvin, U.B. & Powell, B.N., 1970. Lunar anorthosites and a geophysical model of the moon. *Proceedings of the Apollo 11 Lunar Science Conference*, 965-988.

Yin, L.I., Trombka, J.I., Adler, I. & Bielefeld, M., 1993. X-ray remote sensing techniques for geochemical analysis of planetary surfaces. In: Pieters, C.M. & Englert, P.A.J. (Eds.) *Remote geochemical analysis, elemental and mineralogical composition*, Cambridge University Press, 199-212.

Zheng, Y., Ouyang, Z., Li, C., Liu, J. & Zou, Y., 2008. China's lunar exploration program: present and future. *Planetary and Space Science*, 56, 881-886.

Zhong, S., Parmentier, E.M. & Zuber, M.T., 1999. Early lunar evolution and the origin of asymmetric distribution of mare basalts. *Proceedings of the Lunar and Planetary Science Conference XXX*, abstract #1789.

Zhong, S., Parmentier, E.M. & Zuber, M.T., 2000. A dynamic origin for the global asymmetry of lunar mare basalts. *Earth and Planetary Science Letters*, 177, 131-140.

Zuber, M.T., Smith, D.E., Lemoine, F.G. & Neumann, G.A., 1994. The shape and internal structure of the Moon from the Clementine Mission. *Science*, 266, 1839-1843.

Website References

(1) http://nssdc.gsfc.nasa.gov/planetary/lunar/lunarussr.html (last accessed 12th November 2010)

(2) http://www.isro.org/pressrelease/scripts/pressreleasein.aspx?Aug30_2010 (last accessed 12th November 2010).